Technische Universität München

Physik Department E21

Arbeitsgebiet stark korrelierte Elektronensysteme

Magnetic and Structural Properties of Fe and MnSi Thin Films Investigated by Scattering Techniques

Birgit Maria Wiedemann, M.Sc.

Vollständiger Abdruck der von der
Fakultät für Physik der Technischen Universität München
zur Erlangung des akademischen Grades eines

Doktors der Naturwissenschaften (Dr. rer. nat.)

genehmigten Dissertation.

Vorsitzender:		Univ.-Prof. Dr. Martin Zacharias
Prüfer der Dissertation:	1.	Univ.-Prof. Dr. Peter Böni
	2.	Univ.-Prof. Jonathan J. Finley, Ph.D.

Die Dissertation wurde am 03.09.2014 an der Technischen Universität München eingereicht
und durch die Fakultät für Physik am 25.11.2014 angenommen.

List of Abbreviations

AFM antiferromagnetism

CVD chemical vapor deposition

DC direct current

DM Dzyaloshinskii-Moriya interaction

EBSD electron backscattering diffraction

EXAFS extended X-Ray absorption fine structure

FC field cooling

FIB focused ion beam

FM ferromagnetism

FWHM full width half maximum

GISANS grazing incidence small-angle scattering

GMR giant magnetoresistance

HF hydrofluoric acid

HFC high field cooling

HV high vacuum

LCP left circular polarization

LEED low-energy electron diffraction

LT low temperature

MBE molecular beam epitaxy

MC master chopper

MEED medium-energy electron diffraction

MFM magnetic force microscopy

ML monolayer

MOKE magneto-optic Kerr effect

MR magnetoresistance

NM nanomartensite

NR neutron reflectometry

OSR off-specular reflectometry

PGISANS polarized grazing incidence small angle scattering

PLD pulsed laser deposition

PM paramagnetism

PNR polarized neutron reflectometry

RCP right circular polarization

RF radio frequency

RT room temperature

SA spin asymmetry

SC slave chopper

SDW spin-density wave

Skx skyrmion phase

SLD scattering length density

SPA-LEED spot profile analysis low-energy electron diffraction

SPE solid-phase epitaxy

SP-STM spin-polarized scanning tunneling microscope

SQUID superconducting quantum interference device

STM scanning tunneling microscope

TD thermal deposition

TEM transmission electron microscope

THE topological Hall effect

TOF time of flight

UHV ultra high vacuum

VSM vibrating sample magnetometry

XANES X-ray absorption near edge structure

XMCD X-ray magnetic circular dichroism

XRD X-Ray diffraction

XRR X-ray reflectometry

ZFC zero-field cooling

Contents

Chapter 1

Introduction

The properties of thin films differ strongly from those of the bulk. The reduced dimensionality results in a reduction of symmetry, which can influence several types of phenomena: geometrical structure, electronic properties, and magnetism [1]. The combination of materials in epitaxial multilayers can also alter the properties, as the surfaces and interfaces play a crucial role. Epitaxy is the growth of a layer adopting the crystal structure of the substrate [2]. Epitaxial layers can therefore form new artificial materials with properties, that can be tailored for a required purpose for devices such as sensors, photovoltaic cells, or electronic components.

Combining different materials as a heterostructure led, for example, to the observation of giant magnetoresistence (GMR) in 1988 [3]. GMR or tunneling magnetoresistence (TMR) has played the central role in the development of read heads of solid-state drives [4] over the last two decades. A new generation of read heads utilizing, for example, spin transfer torque is currently under development. Aside from read heads, magnetic thin films are of course widely used as storage media. With the steadily increasing demand for even higher storage densities, new material systems and properties are required. Although the magnetic domains need to shrink, the magnetic bits should be nonvolatile and easy to manipulate. These highly demanding requirements will challenge researchers for the next decades.

This thesis focuses on magnetic thin films, in particular Fe thin films grown on Cu(100) and MnSi(111) thin films. Although bulk Fe is an ordinary ferromagnet, the structural and magnetic properties are a complex function of Fe thickness in ultrathin films. Several studies of Fe films deposited by MBE or PLD revealed that fcc Fe can be grown on Cu(100) as ultrathin layer, which also influences the magnetic properties [5–7]. However, there are only a few studies on sputtered films. Consequently, the atomic and magnetic structure of sputtered Fe/Cu(100) films are still unknown. For this reason, we developed an *in-situ* sputtering system, which enabled us to investigate magnetic properties during growth. The sputtering system was specifically designed for *in-situ* polarized neutron reflectometry (PNR). This combination constitutes a unique technique. With the addition of focusing optics installed

at the neutron reflectometer Amor, known as Selene setup, we established this technique as a powerful tool. Using it, we measured the evolution of the magnetization as a function of Fe thickness almost in real time. However, the structural evolution could not be clarified within the scope of this thesis.

Bulk MnSi was found to be a helimagnet with a complex phase diagram. With a helical phase in the ground state, it also forms complex magnetic structures under the application of a magnetic field — the skyrmions [8]. Since a skyrmion is a very stable magnetic structure that can be manipulated by tiny electric currents [9], they are of particular interest. The existence of the sykrmions in MnSi(111) films is controversially discussed. It is known that the magnetic properties of these films also differ strongly from the bulk and depend sensitively on the magnetic field direction [10–13]. Using grazing incidence small-angle scattering (GISANS) and off-specular reflectivity (OSR) combined with PNR, our study advances the understanding of the magnetic structure of MnSi films — especially for an in-plane magnetic field. Further research needs to be undertaken before the magnetic structure in an out-of-plane field can be definitely identified.

In Chapter 2, I will introduce the scattering techniques which are of profound relevance for the characterization of the magnetic films. Chapter 3 focuses on the Fe/Cu(100) material system. It includes a literature review, an introduction to the sputtering and Selene system, a description of *ex-situ* characterizations, and, most importantly, the results of *in-situ* PNR measurements, followed by a conclusion. Chapter 4 focuses on MnSi(111) thin films. A literature review is followed by a description of the growth and quality of the samples and of the setup used at the neutron beamlines. The presentation and discussion of the results precedes a conclusion. Finally, Chapter 5 draws upon the findings of the entire thesis and provides an outlook.

Chapter 2

Scattering Techniques

This chapter introduces the scattering techniques that were used for the investigation of the two material systems: Fe/Cu(100) (Chapter 3) and MnSi(111) thin films (Chapter 4). The structure of these films was investigated using X-ray reflectometry (XRR) and diffraction (XRD). These techniques are described in Section 2.1. The magnetic properties are investigated by grazing incidence small-angle neutron scattering (GISANS) and neutron reflectometry. The latter includes polarized neutron reflectometry (PNR) and off-specular reflectometry (OSR). These techniques are presented in Section 2.2. Note that the fundamental scattering processes are equal and the techniques very similar for X-rays and neutrons. With the exception of PNR, the neutron scattering techniques mentioned also exist for X-rays, i.e. GISAXS and OSR. However, those methods were not applied in this thesis and are therefore not discussed in this chapter.

2.1 X-ray Scattering Techniques

X-rays interact with the shell electrons of atoms via the electromagnetic interaction and are therefore scattered by matter. XRD and XRR are common techniques used for the structural characterization of samples. Usually, a conventional laboratory X-ray diffractometer is sufficient. While XRD is sensitive to the atomic distances (Section 2.1.1), XRR (Section 2.1.2) is sensitive to the layer thickness and roughness of thin films. The scan type for both methods is the same, as will be described in the following sections.

2.1.1 X-ray Diffraction

X-rays have a wavelength of the order of the atomic lattice parameters of crystal structures. Therefore, X-rays are diffracted by powders, polycrystals, and monocrystals. The correspond-

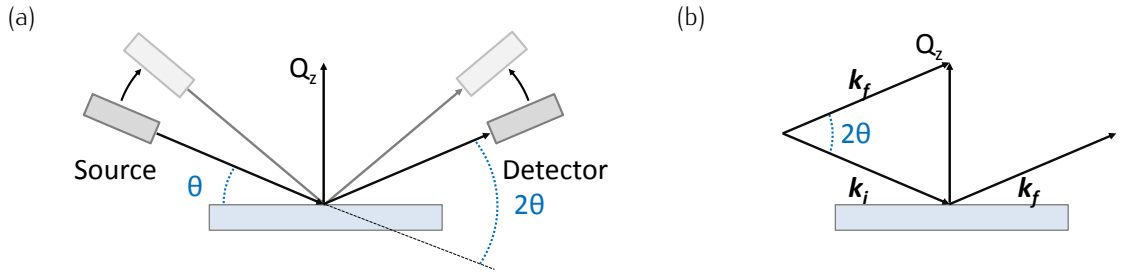

Fig. 2.1: *(a) XRD θ-2θ-scan: the X-ray source and detector move simultaneously with the angle of incidence equal to the angle of reflection. (b) Scattering triangle defining the scattering wavevector* $\boldsymbol{Q} = \boldsymbol{k_i} - \boldsymbol{k_f}$*, with* $\boldsymbol{k_i}$ *and* $\boldsymbol{k_f}$ *the wavevectors of the incoming and of the reflected beam, respectively.*

ing diffraction patterns reveal the atomic structure. Using the Bragg equation [14], one can calculate the distance of crystal planes d:

$$n\lambda = 2d \cdot \sin(\theta), \tag{2.1}$$

where λ is the wavelength of the X-ray source, n an integer, and θ the angle of incidence relative to the sample surface.

We used the two-circle diffractometer D5000 (Siemens) equipped with a standard X-ray tube with a Cu anode, producing Kα radiation of $\lambda = 1.5406\,\text{Å}$. With this instrument, one can perform so called θ-2θ-scans, as shown in Figure 2.1a. The source and the detector move simultaneously such that the angle of incidence is always equal to the angle of reflection. The scattering vector $\boldsymbol{Q}$ is defined by $\boldsymbol{Q} = \boldsymbol{k_i} - \boldsymbol{k_f}$ [15] with $\boldsymbol{k_i}$ and $\boldsymbol{k_f}$ the wavevectors of the incoming and reflected beam as shown in Figure 2.1b. Using $|\boldsymbol{k_i}| = |\boldsymbol{k_f}|$ and $k = 2\pi/\lambda$ one can derive:

$$Q_z = \frac{4\pi}{\lambda} \sin(\theta). \tag{2.2}$$

If the angle of incidence is equal to the angle of reflection and the scattering is elastic, the scattering wavevector $\boldsymbol{Q}$ is always perpendicular to the surface with a pure z component. As a result, the measurement is only sensitive to the vertical lattice parameter. This type of measurement is therefore often referred to as out-of-plane XRD.

If a Bragg peak is found, it is also possible to perform so-called rocking scans, as illustrated in Figure 2.2. Here, the source and the detector are fixed, i.e. 2θ is constant, while the sample is tilted using θ. For rocking scans, this angle is also sometimes referred to as ω.

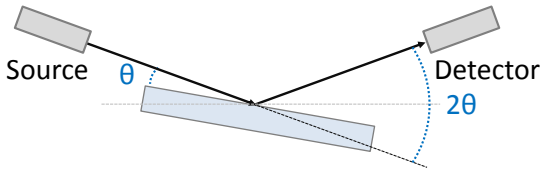

Fig. 2.2: *XRD rocking scan, i.e. a θ-scan with 2θ = constant.*

Performing only out-of-plane XRD is often not sufficient. To prove monocrystalline growth or to verify a specific structure it may be necessary to investigate crystal planes that are not parallel to the surface. This can be done by using a four-circle diffractometer, i.e. in our case a D500 (Siemens). Besides the circles for θ and 2θ, two more angles are needed (Figure 2.3a): χ, which is used to rotate the sample in a plane perpendicular to the scattering plane and φ, which rotates the sample around the surface normal. For $\chi \neq 0$, $\boldsymbol{Q}$ is not parallel to the surface normal anymore. Therefore, we will refer to this type of measurement as off-surface XRD. To align, for example, a cubic crystal with a (100) surface to a {110} plane, χ has to be rotated by 45°, as shown in Figure 2.3b. Angles between cubic crystal planes can be calculated, for example, using the website [16]. Subsequently, the crystal has to be rotated about the surface normal, here, the <100> direction to find a {110} plane. Note that the surface normal, and thus also the axis of φ rotation, moves with χ and is not parallel to $\boldsymbol{Q}$ anymore. In a 360° φ-scan, four {110} planes pass the Bragg condition every 90° with Q_z || <110>. In Figure 2.3b, φ is already correctly adjusted.

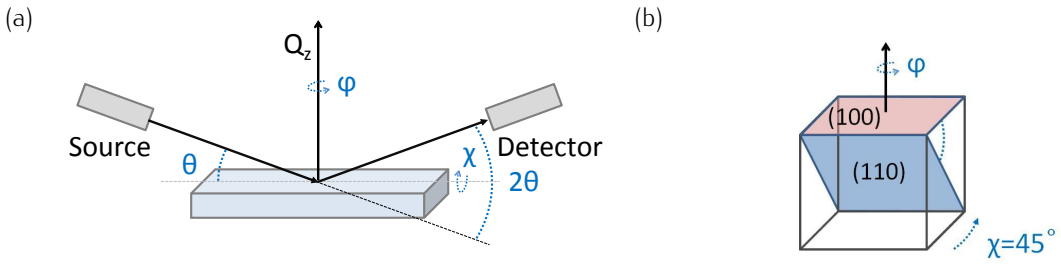

Fig. 2.3: *(a) XRD geometry at a four-circle diffractometer, with two additional angles χ and φ to align the Q-vector perpendicular to a crystal plane other than the surface plane. (b) Example for the alignment of a (110) crystal plane in the case of a (100) surface plane of a cubic lattice: χ has to be rotated by 45°, while φ is already correct.*

2.1.2 X-ray Reflectometry

The 2θ angles used for XRD are typically 20–80°. In contrast, the angles of incidence used for X-ray reflectometry (XRR) are, with $2\theta < 10°$, much smaller. In this regime, one probes not the distance of lattice planes but larger distances up to typically 300 nm: the layer thickness. The scan type is the same as for XRD, as shown in Figure 2.1a with the Q-vector being parallel to the surface normal, i.e. the z-direction.

Figure 2.4a shows typical reflectivity curves of Si substrate as a function of Q_z simulated using the program Parratt32 [17]. For small values of Q_z, the intensity is totally reflected by the sample before it drops steeply. The critical wavevector below which total reflection occurs is proportional to the scattering length density (SLD) of the sample with $Q_{z,c} = 4\sqrt{\pi \cdot \mathrm{SLD}}$ [15]. For zero roughness of the Si surface, i.e. $\sigma_{Si} = 0\,\text{Å}$ [15], the decrease of the reflectivity for $Q_z > Q_{z,c}$ is proportional to Q_z^{-4}. For greater roughnesses, the reflectivity drops more steeply as shown for $\sigma_{Si} = 5\,\text{Å}$ and $\sigma_{Si} = 10\,\text{Å}$ in the figure. The Si substrate is too thick to observe interference fringes by XRR. Figure 2.4b shows the reflectivity of a 50 nm Cu layer deposited on a Si substrate. From the interface and surface reflected waves interfere with each other and form oscillations in the reflectivity. These are known as Kiessig fringes [18]. From Equations 2.1 and 2.2 one can derive $\Delta Q_z \approx 2\pi/d$ to estimate the thickness d using the peak-to-peak distance ΔQ_z. Figure 2.4b compares the reflectivities for different roughness ratios of the Si substrate and the Cu layer. As is also shown in Figure 2.4a, the roughness has a huge impact on the curve. The reflectivity curves become more complicated when more

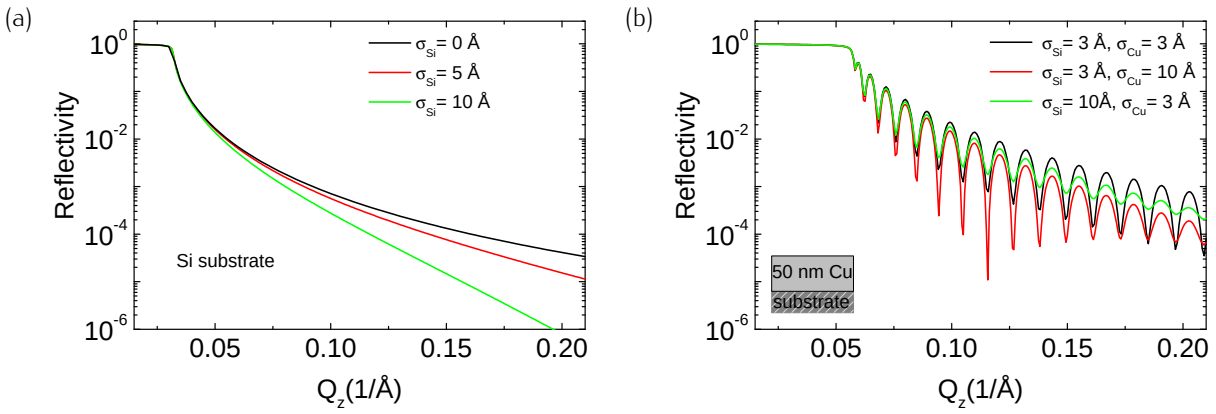

Fig. 2.4: *(a) Reflectivity of a Si substrate as a function of Q_z. For values below the critical edge, the incident beam is totally reflected. For larger values of Q_z, it drops steeply. Here, it drops even more steeply for increasing surface roughnesses of $\sigma_{Si} = 5\,\text{Å}$ and $\sigma_{Si} = 10\,\text{Å}$. (b) Reflectivity curves of 50 nm Cu layer deposited on a Si substrate. The critical edge is shifted to higher Q_z values than for a pure Si substrate. The reflectivity oscillates, resulting in so-called Kiessig fringes that emerge from interference between the Cu/Si and Cu/air interfaces. The curves differ strongly for different ratios of surface roughness σ_{Cu} and interface roughness σ_{Si}.*

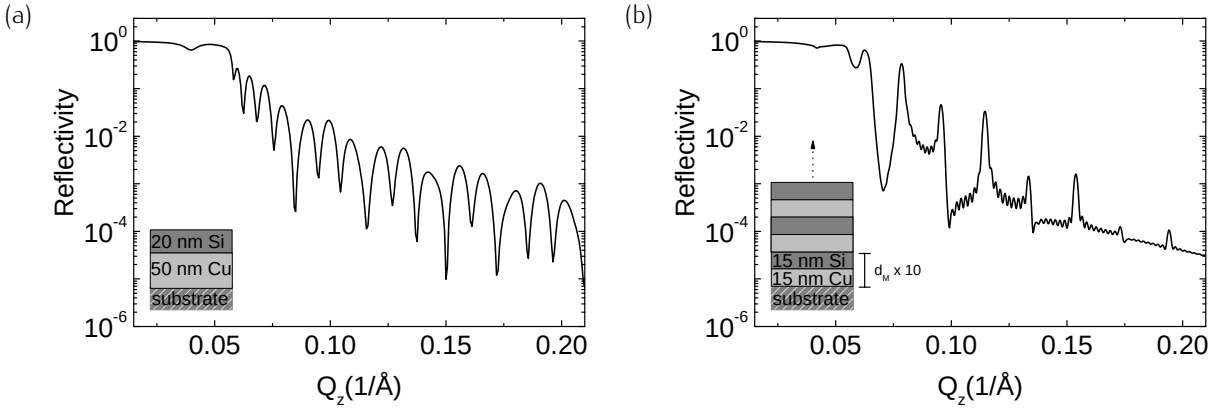

Fig. 2.5: *(a) Reflectivity curve as a function of Q_z for a Cu/Si bilayer deposited on a Si substrate. The critical edge of Cu appears at a larger Q_z than for Si. The latter is visible as small dip in the region of total reflection. The superposition of Kiessig fringes emerging from the Cu and Si layers result in a complicated reflectivity curve. (b) Reflectivity curve of a $[Cu(15\,nm)/Si(15\,nm)]_{10}$ multilayer as a function of Q_z. Alongside the Kiessig fringes, additional high intensity Bragg peaks emerge owing to the repeat distance $d_M = 30\,nm$ of the bilayer.*

layers are involved. Figure 2.5a shows the reflectivity of a Si/Cu bilayer deposited on a Si substrate. Here, the thickness estimation is not as straightforward as for a single layer. The critical edges of both materials are visible in the curve: the first small dip in the region of total reflection corresponds to the Si edge, while the Cu edge appears at larger Q_z values due to its higher SLD. The reflectivity curve of a $[Cu(15\,nm)/Si(15\,nm)]_{10}$ multilayer with a tenfold repetition of the Si/Cu bilayer is shown in Figure 2.5b. In addition to the Kiessig fringes of the total layer thickness $d = 300\,nm$, high intensity Bragg peaks, corresponding to the bilayer thickness of $d_M = 30\,nm$, also emerge.

Using programs like Parratt32 [17] or SimulReflec [19], a measured reflectivity curve has to be fitted to determine the thickness and roughness of each layer. Such programs are based on the Parratt algorithm [17], which recursively calculates the Fresnel coefficients for transmission and reflection of each interface.

Before fitting, the x-component of the reflectivity curve is converted from 2θ into Q_z using Equation 2.2. For very small angles the footprint of the X-rays is smaller than the sample surface. To account for this, the data is corrected by multiplying the factor $C(\theta) = w/(l \cdot \sin\theta)$ for $C > 1$, with w the width of the beam and l the sample length [20]. Finally, the region of total reflection is normalized to one.

2.2 Neutron Scattering Techniques

The formulas introduced in Section 2.1 for X-rays also apply for neutrons. Neutrons are neutral particles that are not affected by the electrons in matter. The neutrons interact with

the nucleus via the strong nuclear force. This interaction is short-ranged [15]. In terms of characterization techniques, the advantage of neutrons are their magnetic moment. They interact with magnetic atoms due to the magnetic dipole–dipole interaction. As a result, the neutrons are also scattered by a magnetic structure of a material. The neutron wavelength used for the experiments in this thesis are in the range of 3–15 Å. These neutrons are called cold neutrons.

2.2.1 Small-Angle Neutron Scattering

Small-angle neutron scattering (SANS) is used to probe structures with a size of 10 to 1000 Å [21]. Bulk samples are usually investigated in transmission and the Bragg peaks are detected using a 2D detector to measure Q_y and Q_z as shown in Figure 2.6. Similar to reflectometry, $\boldsymbol{Q}$ is small compared to $\boldsymbol{k_i}$ and $\boldsymbol{k_f}$ for SANS. In contrast, owing to the 2D detector, the scattering wavevector is not limited to Q_z only. The collimation sections and sample–detector distance are several meters long in order to provide a good angular resolution of the small Q-vectors of a Bragg peak appearing at small angles at the 2D detector. To find a Bragg peak, the sample has to be tilted, i.e. a rocking scan is performed, using χ and ω as defined in Figure 2.6. Since neutrons possess a magnetic moment, this method is also sensitive to magnetic structures. This advantage will be exploited for the investigations of the MnSi thin films.

Grazing incidence small-angle scattering (GISANS) is used to measure diffuse scattering, with the aim of determining the lateral correlation length of nanostructured surfaces. A 2D detector is required to simultaneously detect diffuse scattering over a wide Q-range. The term grazing incidence refers to the fact, that $\boldsymbol{k_i}$ is almost parallel to the surface of the film, but with a small angle of incidence similar to a reflectometry setup. Then, the reflected beam also appears on the detector. This is in contrast to SANS applied to bulk samples, where the beam does not usually hit a surface. Here, the intrinsic structures are looked at, rather than

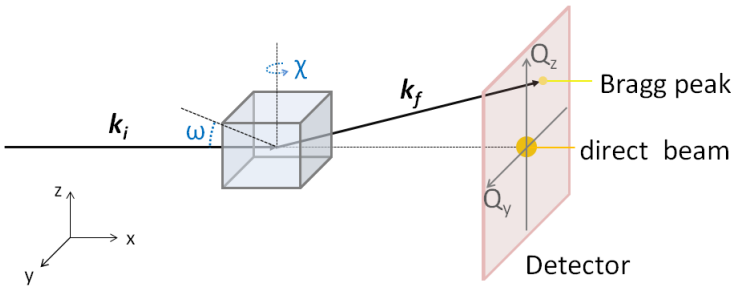

Fig. 2.6: SANS geometry with the sample investigated in transmission. Bragg peaks appear at the 2D detector measuring Q_y and Q_z. To find the maximum of a Bragg peak, the sample has to be rocked using χ and ω.

diffuse scattering, i.e. lateral correlations of nanostructured surfaces.

In this thesis, I will describe how we measured the wavevector of a magnetic structure of MnSi thin films. We had to rock the sample to find a Bragg peak. Thus, the sample was inclined during the measurement in order to fulfill the Bragg condition. Then, the reflected beam imperatively appeared at the detector. Hence, we refer to this type of measurement as GISANS, but the focus is the same as for SANS: the determination of the intrinsic magnetic structure. The detailed setup and a description of data treatment can be found in Section 4.3.1.

2.2.2 Polarized Neutron Reflectometry

Unpolarized neutron reflectometry is similar to XRR, which was described in Section 2.1.2. The scattering length densities of materials are, however, one order of magnitude smaller for neutrons than for X-rays. Again, the neutron's spin can be exploited to measure the magnetization of each layer by performing polarized neutron reflectometry (PNR). PNR provides the magnetic depth profile. In order to measure the reflectivity of polarized neutrons, a polarizer and a flipper must be installed in front of the sample, as shown in Figure 2.7. The scattering amplitude depends on the neutron's polarization relative to the magnetization, $\boldsymbol{M}$, of the sample. The scattering length for a polarization parallel or antiparallel to $\boldsymbol{M}$ is

$$b_{total} = b_{nuclear} \pm b_{magnetic}. \tag{2.3}$$

This results in the reflectivities R+ and R- for spin-up and spin-down polarization, respectively. The spin polarization is parallel to the external field for R+ and antiparallel for R-. With the installation of another flipper and analyzer after the sample, four spin channels can be measured with R++ and R- - being the non-spin-flip channels (Figure 2.7). R+- and R-+ are known as spin-flip channels, since only neutrons can be detected when the sample flips their spins. This happens for a magnetization component perpendicular to the spin polarization (not shown in Figure 2.7). In general, the reflectivity is only sensitive to components of the magnetization $\boldsymbol{M}$ perpendicular to $\boldsymbol{Q}$. In common with XRR, the reflectivities have to be fitted with Parratt32 [17] or SimulReflec [19]. Using the latter program, it is possible to fit R+, R-, and the spin asymmetry (SA) simultaneously. The SA can be defined by:

$$SA = \frac{R^- - R^+}{R^+ + R^+}. \tag{2.4}$$

In the case of an additional analyzer, R+ and R- have to be substituted by R++ and R- -.

Since R+ and R- measure only the magnetization parallel to the neutron polarization, the corresponding fits provide a magnetic depth profile which is a projection of the magnetization along $\boldsymbol{M}$.

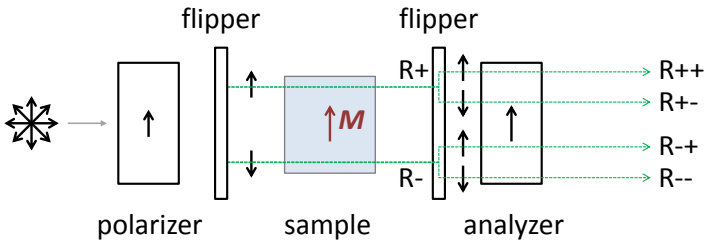

Fig. 2.7: Schematic of a polarized beam reflectometer used for PNR. The polarizer and flipper in front of the sample define the spin polarization before the neutrons are reflected from the sample. The reflected intensities are referred to as R+ and R-, which are different for a magnetized sample. With the installation of an additional flipper and analyzer after the sample, the spin-flip channels R+- and R-+ can also be measured. R++ and R-- are referred to as non-spin-flip channels.

2.2.3 Off-specular Reflectometry

So far, I have only discussed reflectometry with a scattering vector with a pure z component parallel to the surface normal. This holds for angles with $\theta_i = \theta_f$, i.e. the initial angle of incidence is equal to the final angle of reflection. This type of reflection is called specular reflection. We also measured the reflectivity that accounts also for final angles with $\theta_i \neq \theta_f$. Then, the scattering vector comprises a x-component, which is sensitiv to lateral correlations. Figure 2.8 shows the scattering triangle for an arbitrary $\boldsymbol{k_f}$ with $\theta_i \neq \theta_f$. The Q-vector is not parallel to the z-direction but exhibits an x and a z-component. This type of reflectometry is referred to as off-specular reflectometry. In contrast to GISANS, one measures not Q_y, because reflectometers have a very coarse Q_y resolution. Here again, a 2D detector is of great advantage.

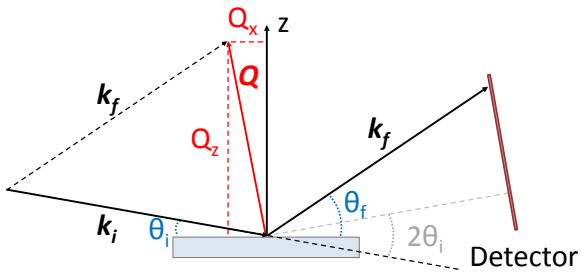

Fig. 2.8: Scattering triangle measuring off-specular reflectometry using a 2D detector. For $\theta_i \neq \theta_f$, $\boldsymbol{Q}$ is not longer parallel to the surface, but exhibits an x and z component.

The following relations, similar to Equation 2.2, can be deduced [22]:

$$Q_x = \frac{2\pi}{\lambda}\left(\cos(\theta_f) - \cos(\theta_i)\right) \tag{2.5}$$

$$Q_z = \frac{2\pi}{\lambda}\left(\sin(\theta_f) + \sin(\theta_i)\right). \tag{2.6}$$

Figure 2.9a shows a typical off-specular intensity map as a function of θ_i and θ_f. The scattering map was calculated for a $[\mathrm{Cu}(15\,\mathrm{nm})/\mathrm{Si}(15\,\mathrm{nm})]_{10}$ multilayer in [22]. The specular reflection (red diagonal line) appears for $\theta_i = \theta_f$. As a result of the large total thickness of $d = 300\,\mathrm{nm}$, the Kiessig fringes in the specular reflection are hardly visible. The two Yoneda wings at $\theta_i = \theta_f = \theta_c$ are indicated as green lines. Three Bragg sheets corresponding to the first, second, and third order emerge as lines perpendicular to the specular line owing to the multilayer reflection peaks like those shown in Figure 2.5b. As a result of refraction effects for θ_i and θ_f close to the angle of total reflection, the first Bragg sheet (dark-blue line) is strongly bent. The second is slightly bent, while the third Bragg sheet (light-blue line) is straight. Here, the roughness of all layers is fully correlated, i.e. the roughness is replicated from layer to layer. For perfectly smooth layers or layers with uncorrelated roughness no Bragg sheets would be visible [22]. Note that the Kiessig fringes, like the Bragg sheets, can also be extended to the off-specular regime for rough layers. However, the intensity of the Kiessig fringes is low compared to that of the multilayer Bragg peaks and sheets. Figure 2.9b shows the scattering map with the angles converted in Q_x and Q_z values using Equations 2.5 and 2.6.

OSR can also be used to exploit the magnetic moment of the neutron by measuring magnetic layers. For example, a multilayer stack consisting of magnetic sheets separated by a non-magnetic layer will result in a magnetic Bragg sheet corresponding to the thickness of the bilayer composed of the magnetic and non-magnetic layers.

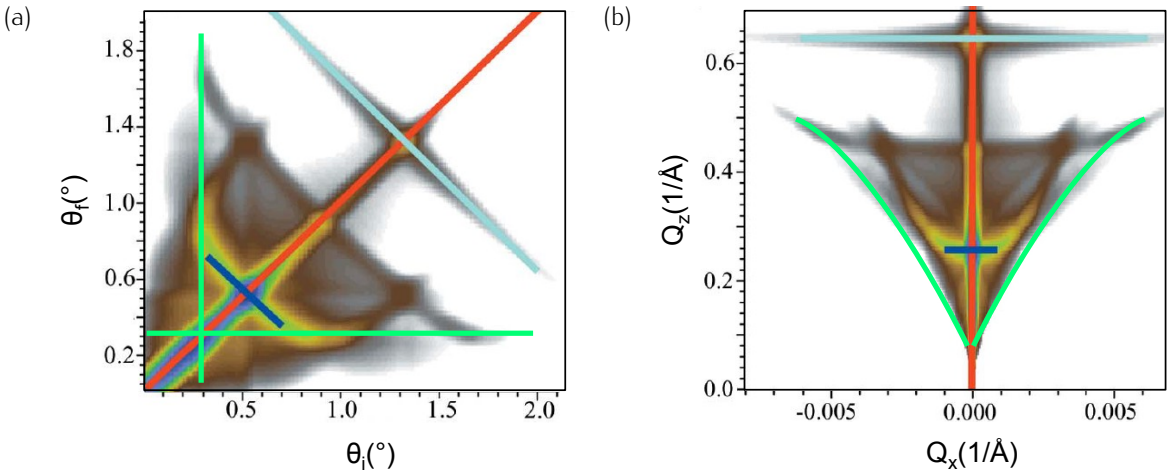

Fig. 2.9: *(a) Simulated off-specular scattering map of a $[Cu(15\,nm)|Si(15\,nm)]_{10}$ multilayer as a function of θ_i and θ_f. The specular reflection at $\theta_i = \theta_f$ is indicated as a red diagonal line. The Yoneda wings (green lines) appear at $\theta_i = \theta_f = \theta_c$. Three Bragg sheets of first, second, and third order emerge as lines perpendicular to the specular line owing to the multilayer reflection peaks like those in Figure 2.5b. The first Bragg sheet (dark-blue line) is strongly bent as a result of refraction effects at small angles, while the third Bragg sheet (light-blue line) is straight. (b) Same scattering map, but with the angles θ_i and θ_f converted into Q_x and Q_z. (adapted from [22])*

Chapter 3

Structural and Magnetic Properties of Ultrathin Fe Films on Cu(100)

Magnetic layers and heterostructures form the basis of many magneto-electronic devices, the development of which aspires towards smaller and more complex systems. Therefore it is important to be aware that magnetic and structural properties can change as a result of reduced dimensionality or the influence of interfaces by e.g. inducing strain. These properties often evolve as a function of layer thickness or when layers of different materials are added. An additional factor that strongly influences the properties of thin films is the growth mode itself, which can be controlled by the deposition method, the substrate, and the deposition conditions. All these factors can, for example, cause different orientations of the magnetization, different T_c values, or even different types of magnetism. Monitoring the structural and magnetic properties during growth in vacuum allows the comparison of properties for different thicknesses on the same sample and under the same growth conditions. As a consequence, each change of measurement signal can be directly attributed to the newly added layer and one can abandon the very time-consuming preparation of several samples with different layer thicknesses. Furthermore, keeping the sample in a vacuum prevents surface pollution or oxidation.

On this basis, the *in-situ* sputtering system specifically designed for neutron reflectometry was developed and realized in a collaboration between the Universität Augsburg and Technische Universität München as TRR 80 project. This system allows one to measure the magnetic and structural properties after every layer deposition. This method was established as a powerful tool by performing *in-situ* polarized neutron reflectometry during the sputtering of Fe/Cu(100) thin films. The bilayer is of great interest, as fcc Fe can be stabilized as an ultrathin layer on a Cu(100) surface at room temperature. The fcc structure is expected to give rise to different magnetic properties. The growth was found to be very complex and accompanied by an equally complex magnetic behavior as a function of Fe thickness. Although this system has been studied for several decades, little work has been done on sputtered films.

Section 3.1 reviews the literature on the structural and magnetic properties of Fe/Cu(100) as a function of layer thickness. Section 3.2 presents advanced techniques exceeding the standard methods described in Chapter 2: the *in-situ* sputtering system used for the Fe/Cu(100) growth and the neutron focusing system Selene. The latter was used for the most recent and very successful beamtime at AMOR. The sample preparation process and the results of initial *ex-situ* structural investigations of sputtered Fe/Cu(100) films are described in Section 3.3. Initial *ex-situ* magnetic characterizations are presented in Section 3.4. Section 3.5 discusses the findings that emerged from the *in-situ* polarized neutron reflectometry measurements of three beamtimes at the neutron sources Forschungsreaktor München II (FRM II), Heinz Maier-Leibnitz Zentrum (MLZ), Munich and at the SINQ, Paul Scherrer Institut (PSI), Villigen (Switzerland). The final section (Section 3.6) of this first chapter of my thesis provides a conclusion.

3.1 Fe Thin Films Deposited on Cu(100) — a Literature Review

Bulk face-centered-cubic (fcc) Fe, also called γ-iron or austenite, exists only at temperatures between 912–1394 °C. In contrast, fcc Fe can be stabilized as precipitates in a Cu matrix [23] or by epitaxial growth on an fcc substrate. The latter has attracted interest over several decades, because ultrathin Fe films show different magnetic phases depending on their structure. As early as 1930s, Bethe and Slater [24] postulated that the direct exchange interaction was a function of atomic spacing. Later, several authors calculated the magnetic properties of iron directly as a function of the lattice constant [25, 26]. Complex magnetic behavior, including non-magnetic, antiferromagnetic (AFM), and ferromagnetic (FM) states, accommodated by instabilities was predicted. Many different conditions of the Fe thin film growth, such as the growth method and growth temperature, can tailor the lattice spacing and morphology. Further, many different substrates were used to grow epitaxial Fe, such as Pt(110) [27], Ag(100) [28], Fe_xMn_{1-x} [29], fcc Pt [30], Ni(111) [31] and Au(111) [32]. Vaz *et al.* [33] provide an overview of different substrates used for Fe deposition and reviews the structural and magnetic properties of the different systems. The most common substrate for Fe deposition, and the one that is exclusively discussed here, is a Cu(100) substrate — either as an epitaxially grown seed layer on Si(100) or as a single crystal. Cu has a lattice constant of 3.61 Å, which is only slightly smaller than the that of fcc Fe of 3.65 Å. In contrast, the lattice constant of bcc Fe of 2.87 Å is much smaller than that of Cu. The extrapolated lattice spacing of fcc Fe of 3.59 Å at room temperature (RT) leads to a lattice mismatch to the Cu substrate of only −0.7% [2]. Furthermore, the lattice constant of Cu is in the range of Fe lattice constants for which different magnetic states for Fe are predicted to be very close. Fe was usually grown by thermal deposition for these studies. However, little work has been done on sputtered Fe films, which is technologically a very important technique and is the focus of this thesis.

In this chapter, I will summarize the experimental results of the magnetic properties of thin

Fe/Cu(100) films and their correlation to the atomic structure. The magnetic (Section 3.1.1) and structural properties (Section 3.1.2) of Fe films deposited by thermal deposition at room temperature (RT) on Cu(100) single crystals will be presented in detail. Both are directly correlated and depend sensitively on the Fe thickness. Those properties are found to be unstable against temperature and H_2 adsorption, as described in Section 3.1.3. To conclude, I will give an overview of which growth conditions may influence the structural and magnetic characteristics of various Fe films (Section 3.1.4). The whole chapter is summarized and discussed in Section 3.1.5.

3.1.1 Magnetic Behavior

Thomassen *et al.* [35] were among the first to study the magnetic signal as a function of Fe thickness in great detail. They performed magneto-optical Kerr effect (MOKE) measurements on Fe thin films deposited on Cu(100) single crystals by thermal evaporation at room temperature. The evolution of the Kerr ellipticity measured in the polar and longitudinal geometry between 110 K$< T < T_c$, on the basis of which the saturation value was extrapolated to 0 K, shows three distinct magnetic regions as a function of Fe thickness (upper panel of Figure 3.1a) — similar to the MEED signal (bottom panel), which will be discussed in the next paragraph. The out-of-plane Kerr ellipticity accessible in the polar geometry increases in

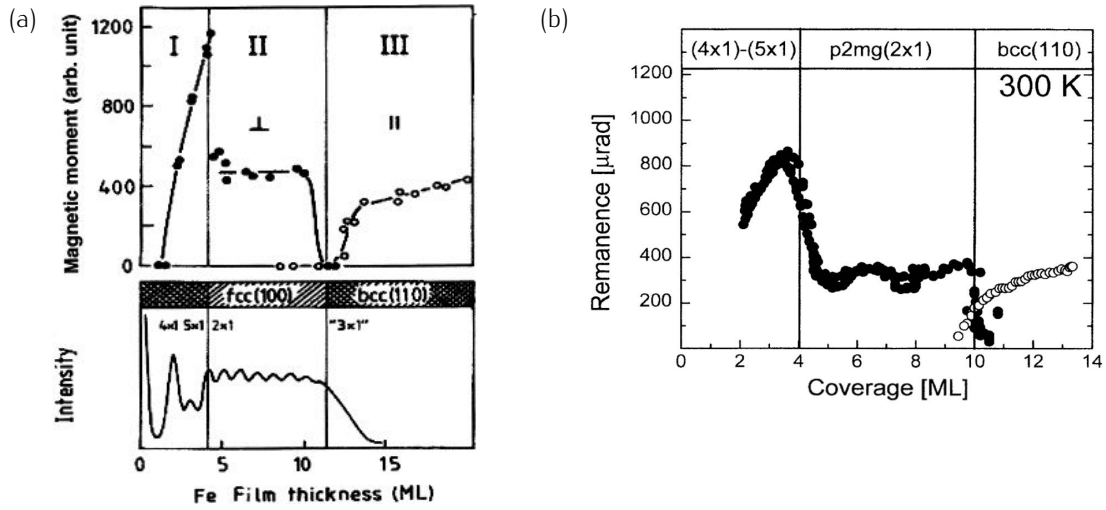

Fig. 3.1: *Kerr ellipticities as a function of Fe thickness, measured in the polar (solid circles) and in the longitudinal geometry (open circles). Samples were deposited at RT. (a) Upper curve: saturated signal of Fe thin films at temperatures >110 K (Source: [2]). (b) Remanence of Fe wedge-like films measured at 166 K (Source: [34]). Both curves can be classified according to their slopes into three regions. The lower curve in (a) shows the MEED intensity of the specular beam as a function of Fe thickness, which also alters its curve shape at the boundaries of the three regions.*

region I almost linearly with increasing Fe thickness up to 4 monolayers (ML). Around 4 ML, i.e. the transition to region II, the Kerr ellipticity suddenly drops by more than half and remains constant up to 10 ML, after which it vanishes. Instead of an out-of-plane moment, an in-plane moment measured in the longitudinal geometry starts to arise (region III), where again the signal linearly increases above 11 ML. Note that the higher ellipticity in region I and II is due to the higher sensitivity in the polar geometry. Since a linear dependence is typical for ferromagnetism, Thomassen *et al.* [35] regard region I and III as ferromagnetic (FM). In region II, i.e. between 4 ML and 11 ML, they consider that the signal belongs to a constant number of ferromagnetic top layers with either underlying paramagnetic layers or antiferromagnetic (AFM) layers with a Neel temperature (T_N) below 110 K. Similar results were published by their collaborators Müller *et al.* [34]. They measured a wedge-like Fe film deposited on Cu(100) at room temperature. Figure 3.1b shows the ellipticity of the MOKE signal in the polar and longitudinal geometry measured at remanence.

I will now discuss the correlation between this magnetic behavior and the structure, followed by a description of the unclear magnetic behavior in region II. The evolution of the Curie temperature as a function of thickness is discussed in the final part of this section.

Correlation with Structure. Wuttig and Liu [2] (originally published in 1992 in [35]) provide powerful evidence for the direct correlation between magnetic behavior and the morphology of Fe/Cu(100) by measuring the intensity of medium-energy electron diffraction (MEED) beams. The bottom panel of Figure 3.1a shows the intensity variation of the specular beam as a function of Fe-layer thickness. Region II definitely exhibits a different behavior than region I and region III, with the zone boundaries being exactly the same as those of the magnetic signal. In this region, the intensity oscillates, which is a fingerprint of layer-by-layer growth [2], due, however, to the small oscillation amplitude in a 2D island way rather than in absolutely filled layers. In region III, the intensity drops exponentially indicating the growth of 3D islands. Similar MEED results were found by Qian *et al.* [6, 36] and Li *et al.* [5].

Anomaly in Region II. While the existence of these structurally distinct regions of Fe/Cu(100) are confirmed by several authors [37, 38] and the ferromagnetic nature of regions I and III are widely accepted [39–42], the magnetic properties of region II are still unclear.

Li *et al.* [5] observed an oscillatory behavior of the Kerr signal at remanence of an Fe wedge exhibiting two maxima at around 7.5 ML and 10 ML (Figure 3.2a). Those maxima become even more pronounced as the temperature decreases and vanish above 200 K. Owing to the absence of a longitudinal Kerr signal up to 11 ML, they exclude spin canting. Further, they attribute this effect, as Thomassen *et al.* have already suggested [35], to a ferromagnetic surface located on top of antiferromagnetic layers, the total number of which changes from odd to even with increasing thickness leading to the oscillation of the magnetization.

Qian *et al.* [6, 36] carried out MOKE measurements on Fe thin films at 70 K and also found an oscillation in the Kerr signal (Fig. 3.2b), but with a maximum at 6 ML and at 8 ML. Additional T-sweeps of the 6th and 8th ML (not shown) revealed a steplike increase of the magnetic

(a) (b)

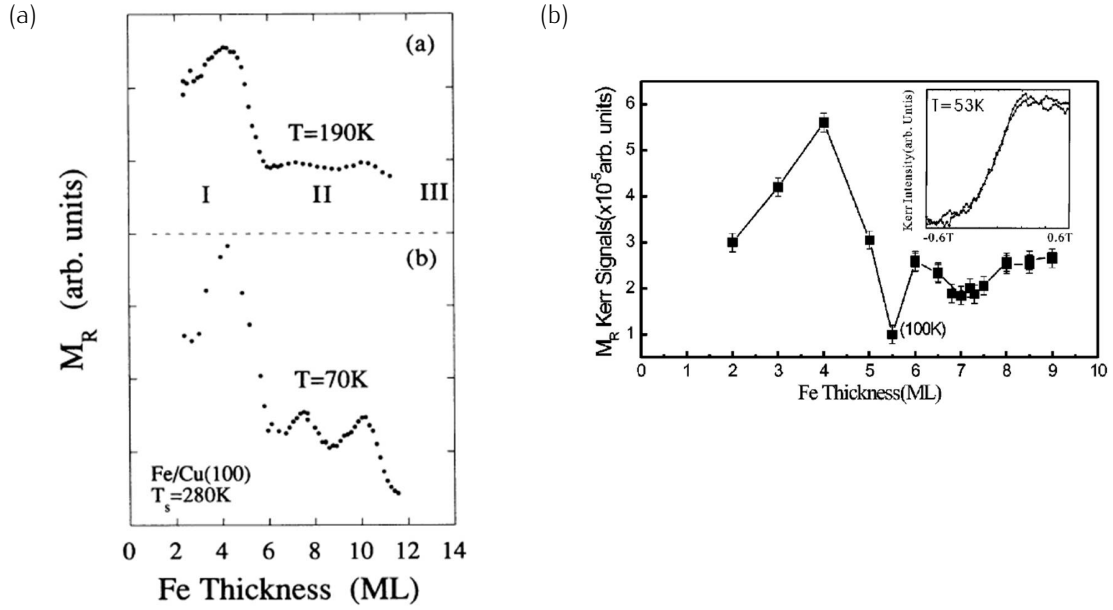

Fig. 3.2: *Kerr signals as a function of Fe thickness, measured in the polar geometry at remanence. (a)) Fe wedge grown at 280 K and measured at 190 K (upper curve) and 70 K (lower curve) (Source: [5]). (b) Fe thin films grown at 300 K and measured at 70 K (Source: [36]). The magnetic behavior can again be divided into three regions in close accordance with Figure 3.1. In contrast, the magnetic signal of the Fe wedge and film oscillates in region II for $T < 200$ K.*

signal for decreasing temperature at around 200 K, i.e. the Neel temperature, indicating an arising exchange interaction between the top FM layers and the AFM underlayers. Further, they concluded that a spin-density wave (SDW) exists with a strong coupling to the FM top layers and determined the wavelength to be 2.7 ML, which is similar to the separation of the maxima of Li *et al.* Although the signal in Figure 3.1b also shows a small oscillation in region II, Müller *et al.* [34] regard the signal as constant.

The same constant behavior is described by Thomassen *et al.* [35], but here, perhaps owing to a lack of data points, no oscillation is prominent (Figure 3.1a). Oscillations were also observed by Vollmer and Kirschner [41], with maxima at 6.2 ML and 8.8 ML. Wuttig and Liu [2] reviewed this anomaly below 200 K in literature and summarized results of theoretical studies in which the moments of the Fe sheets are collinearly aligned (Table 3.1). The first study [43] predicts a maximum in region II at 6 ML, the second study [44] at 7 ML and 9 ML, and the third study [45] at 5 ML. While those studies predict a collinearity of the spins, Qian *et al.* refer to the experimental study of Fe particles in a Cu matrix, in which an incommensurate spin density wave (SDW) is determined [46]. Spišák and Hafner [47] reveal that collinear configurations are energetically preferred to spin-density-wave configurations. Wuttig and Liu further argue that this anomalous behavior could also be caused by the magnetic ordering of bcc clusters, which are predicted to exist in [48]. Another possibility for those oscillations is that a slight structural change occurs below 200 K.

Thickness (ML)	1	2	3	4	5	6	7	8	9
Results of [43]	u	uu	uuu	uudd	uuddd	uuddduu			
Results of [44]	u	uu	uuu	uudd	uuddd	uuddduu	uuuddduu	uudduudd	uudududuu
Results of [45][1]	u	uu	udu	uddu	uuduu	uuddduu	uuddduu	uddduuddu	uuddudduu

Table 3.1: *Summary of theoretical results for the magnetic ground-state of fcc Fe/Cu(100) films. Up (u) and down (d) indicate the spin orientations starting at the free surface. (adapted from [2]) [1] The calculations were based on Fe/Cu(001) superlattices with an ideal fcc Cu structure.*

Curie Temperature. Corresponding to Figure 3.1a, measurements were performed by Thomassen *et al.* [35] to determine the Curie Temperature T_c of Fe/Cu(100) as a function of Fe-layer thickness. In region I, T_c increases above 350 K, while at 3 ML – 4 ML T_c drops again till it remains constant in region II then suddenly jumps at around 11 ML (region III) to a value above 500 K (Figure 3.3). Li *et al.* [5] estimated T_c of the Fe wedge to be 250 K±20 K. They do not mention the thickness range included in their measurements, but state that the results are in good agreement with the results presented in Figure 3.3. A few years later, Zharnikov *et al.* [49] confirmed the behavior of T_c published by [35]. They mentioned in addition the unexpected drop of T_c between 3 ML and 4 ML. In ultrathin ferromagnetic films T_c should increase with increasing thickness provided that no structural change occurs. Since the transition observed by MOKE does not occur before 4 ML, the decrease of T_c at 3 ML is a first hint that an additional and temperature-driven structural transition occurs in 4 ML films. This is discussed in detail in section 3.1.2.

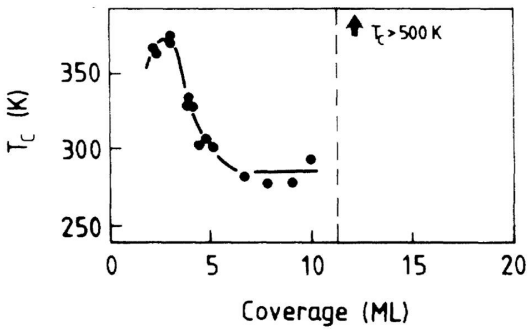

Fig. 3.3: *Curie Temperature as a function of Fe thickness determined by MOKE (Source: [2], originally published in [35]).*

3.1.2 Detailed Study of Structure and Growth

From Section 3.1.1, it is clear that the complex magnetic behavior of Fe/Cu(100) thin films is due to structural changes during growth. The exact growth modes of each region (I–III) are widely discussed in the literature and are summarized in this section.

Region I. In region I, Biedermann *et al.* [37] as well as Rajeswari *et al.* [50] found intermixing of Cu and Fe in the first two ML. By scanning tunneling microscopy (STM) on a 0.2 ML film Fe, Biedermann *et al.* [37] found Fe atoms embedded into the substrate as well as small circular Fe islands, the edges of which are covered by Cu atoms creating large Cu islands.

Low-energy electron diffraction (LEED) patterns, together with the LEED I/V curves (Intensity vs. Energy) of one of the LEED pattern spots, are a powerful tool for investigating superstructures. Figure 3.4a shows LEED patterns recorded in each region, revealing a (5x1) superstructure in region I, a (2x1) superstructure in region II, and a (3x1) superstructure in region III [2]. In addition to the (5x1) superstructure in region I, Wuttig *et al.* [2] observed

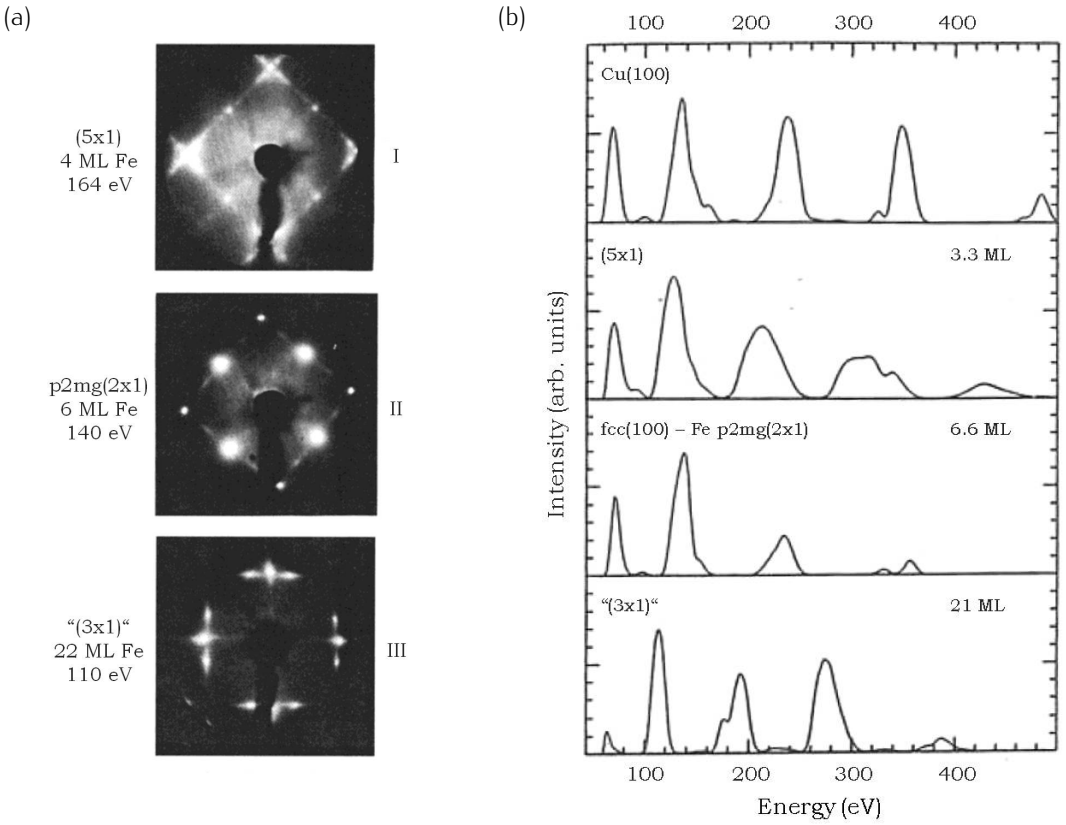

Fig. 3.4: *(a) LEED patterns of Fe/Cu(100) measured in region I–III with the Fe thickness increasing from 4 to 22 ML (from top to bottom) (Source: [2]). (b) Corresponding LEED I/V curves compared to the I/V curve of Cu(100) (Source: [2]).*

an additional (4x1) superstructure at 2–2.4 ML. I/V curves corresponding to Figure 3.4a are compared to fcc Cu in Figure 3.4b. The I/V curve of region II is in good agreement with the Cu I/V curve, indicating an fcc(100) superstructure, while the curve of region III is totally different, indicating a bcc lattice. The (4x1) (not shown) and (5x1) I/V curves are very similar to Cu, both exhibiting the same features as the I/V curve of fcc Cu(100). However, the peaks of the (5x1) pattern are somewhat shifted at larger energies compared to Cu, which suggests vertical disorder with a tetragonal expansion of the interlayer spacing [2]. This behavior corresponds to the results of the extended X-ray absorption spectroscopy (EXAFS) studies by Magnan *et al.* [51], who regard this phase as fcc-like or as a tetragonally distorted fcc phase (fct). Heinz *et al.* [34, 52] performed detailed LEED measurements together with a full dynamic analysis and found buckling of the atoms with displacements in plane up to 0.5 Å as well as in the vertical direction up to 0.4 Å. Their fits revealed a layer spacing enlarged by an average of 5% as compared to the ideal bulk fcc Fe. They explain the observed ferromagnetism in region I by the displacements, as these lead to an increase of the atomic volume to 12.1 $Å^3$, at which ferromagnetism is theoretically predicted.

Although they observed similar LEED patterns, in particular a mixture of (1x4), (1x5) and (1x6) superstructures, Biedermann *et al.* [37, 53, 54] obtained completely different results of the structural properties in region I. Detailed investigations of STM images revealed a 14°–15° shear angle for 2–5 ML films, as illustrated in the center image of Figure 3.5, which indicates a (110) bcc structure ordered in the Pitsch orientation instead of a distorted fcc or fct lattice. The figure also compares the Pitsch orientation to fcc and bcc structures, where the ideal bcc structure has a shear angle of 19.5°. The Pitsch structure is strained, forming a zigzag deformation of the atom rows with a spatial wavelength of 5–6 atoms, which also leads to an enlarged atomic volume, as described by Heinz *et al.* The sheared lattice can be described by a 9% tensile strain along the zigzag chain direction and a 3% tensile strain in the perpendicular direction, which fits with the fcc lattice [53]. This bcc-like structure covers the surface by about 90% for a 2.7 ML film, decreases to about 20% for 4.5 ML film, and

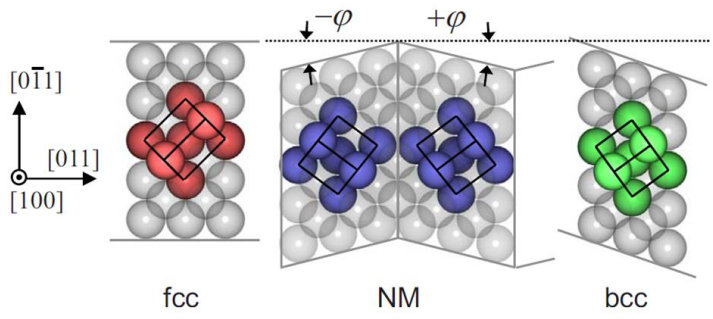

Fig. 3.5: *Top view of the nanomartensitic (NM) crystal structure corresponding to the Pitsch orientation in comparison to the fcc(100) and bcc(110) structure. The shear angle φ of NM is 14°–15° (Source: [53]).*

almost vanishes for films with thicknesses above 5 ML. Biedermann *et al.* call this structure nanomartensitic (NM) bcc phase and explain the ferromagnetism as a direct consequence of the ferromagnetic bcc structure, rather than of the enlarged volume of the fcc lattice. The rest of the area consists of fcc Fe but is widely limited to the 4th ML. This additional structural transition explains the drop of T_c at 4 ML mentioned in the last section (3.1.1).

Wuttig and Liu [2] query the growth of nanomartensite, as bcc structures usually grow as 3D islands and align their spins in plane, whereas Biedermann *et al.* reported smooth films and out-of-plane magnetization. Biedermann *et al.*'s statement was supported a few months later by Hammer *et al.* [1], who collaborate with Wuttig: a re-analysis of the LEED data for the (4x1) reconstruction used in their earlier publication [34] showed that they could equally fit the data satisfactorily with the model of the nanomartensite.

Regions II and III. The Pitsch orientation of Fe, visualized by [55] in Figure 3.6 in the case of a Cu(100) seed layer grown on a MgO substrate, was also observed in thicker Fe layers. Myagkov *et al.* [55] proved this growth mode for an 800 nm Fe layer by in-plane XRD measurements of the Fe(211) planes, performing a 360° φ-scan around the surface normal. This showed that the corresponding peaks coincide in φ, either with Cu(113) or shifted by ±19.5°. Another group [56] found the footprint of the Pitsch orientation in RHEED patterns of Fe/Cu(100) films as 20 Å $< d_{Fe} <$ 1500 Å. The (3x1) superstructure observed in LEED patterns of region III were interpreted as resulting from the bcc Pitsch orientation [57]. The same authors found an in-plane magnetic anisotropy behavior with the easy axis ±9.7° shifted relatively to the Cu<110> axis of the substrate for a 25 ML Fe film, here coated with 20 ML Cu, which could be a measure of the Pitsch shear angle.

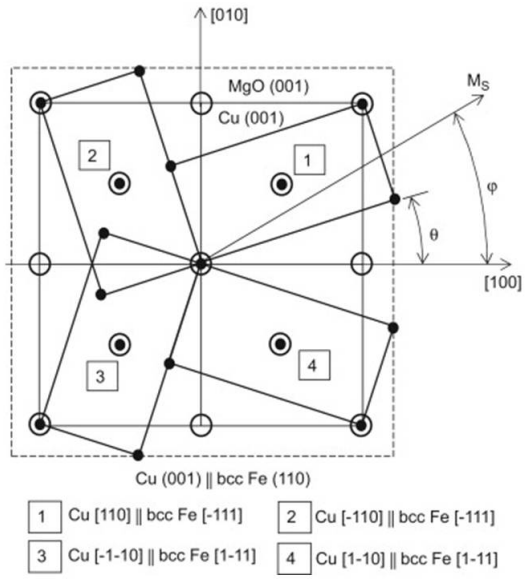

Fig. 3.6: *Four equivalent variations of the Pitsch orientation relationship between Cu(001), here deposited on MgO (open circles) and Fe(110) (filled circles) (Source: [55]).*

Additionally, post-growth SPALEED (high-resolution analysis LEED) was used by Wuttig and Liu [2] for further investigation of the growth mode in region II and III. Using this method, the islands in region II were found to grow as 2D islands, with a step height of 1.74 Å ± 0.04 Å, close to the value for strained fcc Fe. In region III, the step height of 2.02 ±0.04 Å in 3D mode indicated a different structure. Those results were confirmed by STM (scanning tunneling microscopy) images, in which large 2D islands were observed in region II, and in region III a high roughness was seen. In addition, Kief *et al.* [38] described the growth of Fe at RT between 2 and 10 ML as being almost layer-by-layer.

Further studies hint at the structure in region II and III. Interdiffusion experiments [58] showed that during annealing more diffusion of Cu atoms occurs towards the top in region III than in region II, despite the increased Fe thickness, which ought to form a barrier. This shows the existence of additional diffusion channels, which form due to misfit locations.

There is a controversy over the interpretation of the LEED patterns in region II regarding the surface structure of the Fe layer, which is responsible for the ferromagnetism. Wuttig *et al.* [2] regard the I/V curves of the (2x1) pattern in region II (Figure 3.4b) as fcc-like, exhibiting no vertical disorder, but the (2x1) LEED pattern (Figure 3.4a) indicates a parallel displacement of adjacent atoms in the top layer. A full dynamic LEED calculation fitted this displacement to 0.14 Å ± 0.09 Å and the interlayer spacing of the top layer to 1.88 Å ± 0.02 Å, compared to the 1.77 ± 0.04 Å spacing of deeper layers. The latter corresponds to the expected layer spacing for strained fcc Fe(100). The top layer is expected to be responsible for the ferromagnetic signal, while the buried layers order antiferromagnetically. The same group observed the (2x1) superstructure above 7 ML only at 150 K, whereas at room temperature a (1x1) pattern occurred [2].

In contrast, Biedermann *et al.* [37, 59] investigated 6 ML and 7 ML films in detail by STM and high-standard quantitative LEED analysis. Both methods exhibited a higher sensitivity than the standard LEED analysis used by Wuttig *et al.* [1]. While Biedermann *et al.* also assumed the structure of the Fe sublayers to be fcc, they do not consider the surface to be strained fcc. At 150 K they found a superposition of 70% of the p4g(2x2) and 30% of the p2mg(1x2) superstructures. Both could be attributed to an fcc structure at first sight. At RT, their fit results were not as significant as at low temperature (LT), since fluctuation of the domain boundaries distorted the measurement. Here, a pure (1x1), (2x1), (2x2), and a mixed phase gave almost equal results, but they revealed the best fit for 60% p4g(2x2) and 40% p2mg(1x2). However, the surface was dominated by the (2x2) reconstruction at both temperatures rather than the (2x1) reconstruction posulated by Wuttig *et al.* and exhibited a very similar surface reconstruction to the bcc(100) surface. Biedermann *et al.* fitted the enhanced interlayer distance to very similar results as [2]. However, for an enlarged fcc lattice, the interatomic distances also have to be enlarged. This was not the case, but they fitted the interatomic distance close to the bcc value and concluded that the (2x2) reconstruction belonged to a bcc surface. As for the bcc phase below 4 ML, they postulated that the ferromagnetism of the top layers was a direct consequence of the bcc structure.

3.1.3 Stability of the Phases

I have only discussed Fe/Cu(100) films measured at low temperatures and under similar conditions. However, it was found that the conditions during the measurement can change the structural and magnetic properties. The cooling history, the H_2 dose, and an applied magnetic field can influence the measurements. This is discussed in the following section. Note that these parameters were first applied during the measurement but not during growth. The Fe/Cu(100) films are still deposited at RT.

Cooling Cycles. Qian *et al.* [36] found that the Fe films grown at 300 K with a thickness between 9 ML and 11 ML are unstable with cooling. As discussed above, the samples exhibited the fcc-like phase when measured at LT, whereas after cooling to 70 K and warming again to 300 K STM, LEED and MOKE measurements proved a bcc-like phase. This phase was observed either when cooled slowly already during cooling or not until reheating. Similar observations were made by Biedermann *et al.* [37] using STM. Indeed, they report this instability already for 7–8 ML films. The bcc Fe content for a 8 ML film was determined to be less than 1% at 300 K and around 10% at 80 K. They were even able to reach a total transformation to the bcc (nanomartensitic) phase after two temperature cycles. Vollmer and Kirschner [41] used MOKE and IV-LEED and found the instability for 8–10 ML films.

H_2 Dose. As well as temperature changes, hydrogen exposure also strongly influences the phase stability. This was first discovered in [60]. Whereas the first 3 ML of an RT-grown Fe wedge were stable against H_2 exposure, 4 ML were not [41]. The exposure to H_2 for a dose of 2 L (Langmuir, $1\,\mathrm{L} = 1,33 \cdot 10^{-6}\mathrm{mbar} \cdot \mathrm{s}$) led to an increase of the MOKE ellipticity as well as to a structural change observed in the LEED I/V curves. This suggests that the transition to region II occurs 1 ML later than without H_2 exposure. This delayed phase transition was found to be reversible by heating to above 320–330 K, at which temperature-driven H_2 desorption occurs. However, an instability around 4 ML was observed even without H_2 exposure: a 4 ML film exhibited a reduced T_c [49] and an increased coercive field H_c [41, 61]. This is explained by the coexistence of the structure of region I and region II. As a result, the region around 4 ML differs from region I and region II, which explains why the instability only occurs here. Note that this additional structure is not visible in the remanence or in the saturation values.

This coexistence of phases and instability was recently confirmed by Biedermann [53]. He found that a 3 ML film is fully nanomartensitic, which is the characteristic feature of region I as discussed in section 3.1.2. A 4 ML film can, however, consist of both phases: Figure 3.7 compares the nanomartensitic fraction determined by STM as a function of H_2 dose for different temperatures.

Magnetic Field. Lastly, Hembree *et al.* [62] demonstrated that a magnetic field can also influence the stability of a 3.5 ML film. By applying an out-of-plane magnetic field of 9 kOe, they suppressed the out-of-plane magnetization, perhaps owing to a magnetoelastic effect. This process was reversible by heating above RT or by applying an in-plane magnetic field. However, they also reported that the rotation of magnetization already occured at 3.5 ML,

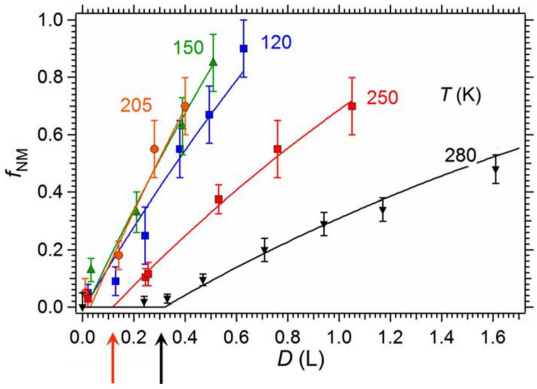

Fig. 3.7: Nanomartensitic fraction of a 4 ML film as a function of H_2 dose measured at different temperatures (Source: [53]). The arrows mark the strong delay of the onset at 250 K and 280 K.

although the Fe was deposited at RT, which contradicts the findings of several authors [5, 34, 35]. As they seem to imply a different structure, their results cannot be directly compared to other instability studies around 4 ML. Furthermore, Fowler *et al.* [40] could not reproduce the spin reorientation by applying a perpendicular magnetic field of 1.1 T for 2–4 ML films.

3.1.4 Influence of Growth Conditions

So far, I have only considered room-temperature growth of Fe/Cu(100) in UHV by thermal deposition, i.e. by MBE, resistive evaporation or e-beam evaporation. However, it is known that the structure of all thin films is closely dependent on the growth conditions. In this section, I will report what has been observed for the Fe/Cu(100) system when growth conditions, i.e. CO dose or substrate temperature, changed or when a different deposition method, such as PLD or sputtering, was applied.

CO Dose. Thomassen *et al.* [35] found that a pressure of $7 \cdot 10^{-8}$ Pa CO during growth shifts the transition from region II to region III from 11 to 13 ML.

Substrate Temperature. Steigerwald *et al.* [63] were the first to extensively study the structural dependence of 1–2 ML Fe films on the substrate temperature. They found that below 200 K Fe was poorly ordered, but above 200 K Fe agglomerated into clusters. Above 300 K Cu segregation occured and led to intermixing of Fe and Cu, which was even more dominant for substrate temperatures above 360 K.

Besides their RT-grown samples (Figure 3.2a and 3.1b), Li *et al.* [5], as well as Müller *et al.* [34], also investigated the magnetic behavior for different growth temperatures T_S. The Kerr signals as a function of the layer thickness of Fe wedges grown at low temperature are shown in Figure 3.8. The thickness range of the fcc phase (region II) becomes smaller at $T_S = 260$ K and vanishes completely at $T_S = 190$ K (Figure 3.8a) as well as at $T_S = 100$ K

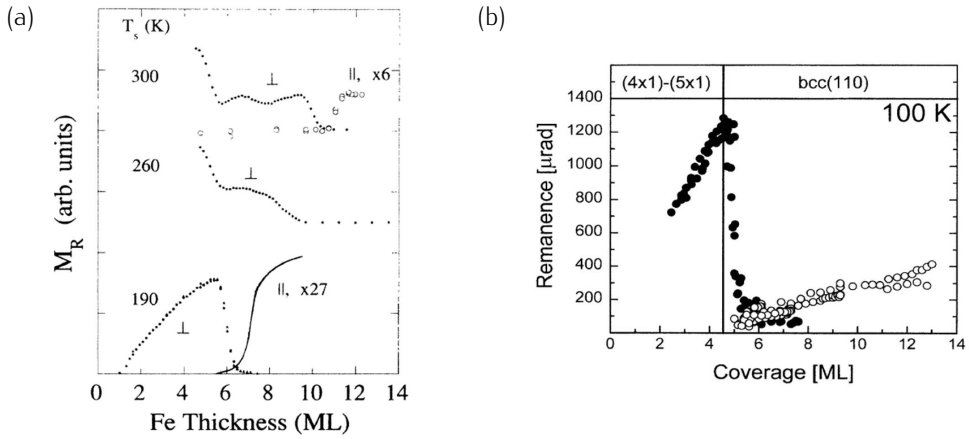

Fig. 3.8: *Kerr signals at remanence of Fe wedges as a function of Fe thickness measured in the polar (curves at lower thicknesses) and longitudinal geometry (curves at higher thicknesses). (a) Fe grown at 300 K, 260 K and 190 K and measured at 110–140 K (Source: [5]). (b) Fe grown at 100 K and measured at 166 K (Source: [34]).*

(Figure 3.8b). Further, the first phase transition is shifted by about 1 to ca. 5 ML and is accompanied by a out-of-plane magnetization rotation between 5 and 6 ML. T_c of the measurements corresponding to Figure [34] were determined as $> RT$ for $d_{Fe} > 5\,ML$ [2].

Similar results for the onset of the out-of-plane magnetization were found by several authors [40, 64]. Li *et al.* regard this phase transition as different from the phase transition at 11 ML for RT-grown films, because they did not observe the "3x1" LEED pattern characteristic of bcc films. However, it is widely accepted that bcc Fe forms above 5 ML, and thus it is similar to region III of RT-grown films. This was proved by LEED and I/V curves [34].

Pappas *et al.* [65] found the magnetization rotation at 6.1 ML and proved that the magnetization of a 6 ML film can be manipulated by temperature: below 180 K the magnetization is aligned out of plane, while above 200 K it is mainly in plane.

Vollmer and Kirschner [41] found a similar phase transition to bcc between 5 and 6 ML, by growing Fe at room temperature in an H_2 atmosphere of $5x10^{-8}$ mbar. They suggest this effect may be at least partly responsible for the difference between low- and room-temperature-grown Fe films discussed above.

Growth by PLD. In addition to the conventional method of thermal deposition, physical laser deposition (PLD) was used to deposit Fe on Cu(100). Both the magnetic and the structural properties were substantially different from those when Fe was deposited thermally. The magnetic evolution was rather complex, as depicted in Figure 3.9 (lower panel) [7, 42]. The intensity of the MOKE signal increases linearly with Fe thickness up to 4 ML, indicating uniformly magnetized films (regions I and II). Afterwards, the signal decreases monotonically with thickness (region IV), except between 5 ML and 7 ML (region III), at which the signal remains constant.

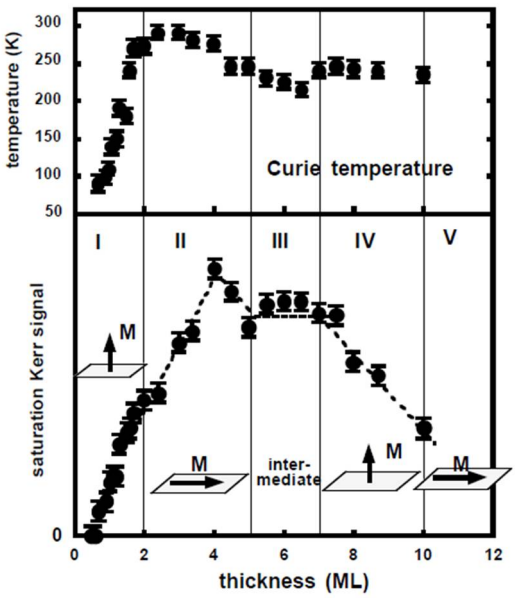

Fig. 3.9: *Curie temperature (upper panel) and saturation magnetization (lower panel) of Fe/Cu(100) deposited by PLD and measured using MOKE. This exhibits a complex behavior as a function of thickness. The direction of magnetization is illustrated in the insets. (Source [42])*

The spin orientation also exhibits very complex behavior with increasing thickness. Whereas in region I the spins are aligned out of plane, they become in plane in region II. In region III, the spins are either canted or two different phases coexist, as a MOKE signal is observed in the longitudinal as well in the polar geometry. In region IV, the sample is again magnetized perpendicular and, in region V, parallel to the surface. The magnetic anisotropy is sensitively influenced by strain and the structure of the surface and interfaces. Therefore it is rather difficult to explain this complex magnetic anisotropy behavior. In principle, two main processes are in competition: the surface anisotropy leading to perpendicular magnetization and the shape anisotropy leading to parallel magnetization. T_c is determined to be ≈RT at 3 ML, whereas it is below RT in the residual Fe thickness regions (Figure 3.9 upper panel).

STM images revealed a layer-by-layer growth starting already in the submonolayer regime [7, 42], while the films with $d_{Fe} > 10$ ML grew very roughly, suggesting a transition to bcc Fe. LEED patterns measured by the same group exhibited only a clear (1x1) superstructure between 2 ML and 10 ML, indicating an fcc structure [7], whereas Weinelt *et al.* [66] described similar LEED patterns as it was observed for TD films indicating a more complex structure. Recent STM studies revealed, alongside the fcc structure, a nanomartensitic fraction for 2–5 ML with its maximum at 3 ML [67]. The 6 ML and the 7 ML films were in contrast almost entirely fcc. The surface of the 6–7 ML films showed the p2mg(1x2) or p4g(2x2) reconstruction, implying bcc-like bond angles.

From this, the complex magnetic behavior (Figure 3.9) can be explained. As in TD films, the

magnetization rises (regions I and II) owing to the increasing nanomartensitic bcc fraction up to 3 ML. Afterwards, for $d_{Fe} > 4$ ML, the magnetization drops again. Since the 6 ML and 7 ML films are almost entirely fcc with a bcc-like surface, the magnetization remains constant (region III), owing to the antiferromagnetically ordered fcc sublayers and the magnetic bcc surface layer. The magnetization drop of region IV is still not understood. Shen *et al.* [7] suggested that above 4 ML the films already start the fcc-to-bcc transitions, forming bcc precipates, which absorb the strain in the film. As a consequence, some parts of the strained fcc that was ferromagnetic can relax to bulk-like paramagnetic fcc. However, that strained fcc is ferromagnetic is disputed by several authors [37, 67], who claim that only bcc contributes to the ferromagnetism signal observed in Fe/Cu(100) layers.

At all growth stages, the Cu content was significantly higher than in TD-grown films, since the high ion energies during deposition lead to Fe implantation into the surface [67].

Growth by Sputtering. The growth of Fe/Cu(100) by sputtering was less common and was mainly used to grow Fe/Cu multilayers [69–73] in which the Cu mostly appeared to be polycrystalline. However, it was demonstrated in [74] that Cu(100) can be grown epitaxially by magnetron sputtering on HF etched Si(100). Further, Clemens *et al.* [68] performed *in-situ* grazing incidence X-ray scattering (GIXS) measurements on Fe/Cu(100) and identified the fcc Fe(220) peak as the shoulder of the Cu(220) peak, growing from 3 to 16 ML in Fe thickness. Afterwards, the intensity of the shoulder remained constant. They observed the increase of the Fe(222) Pitsch peak from 10 to 40 ML simultaneously with the increase of the Bain Fe(200)

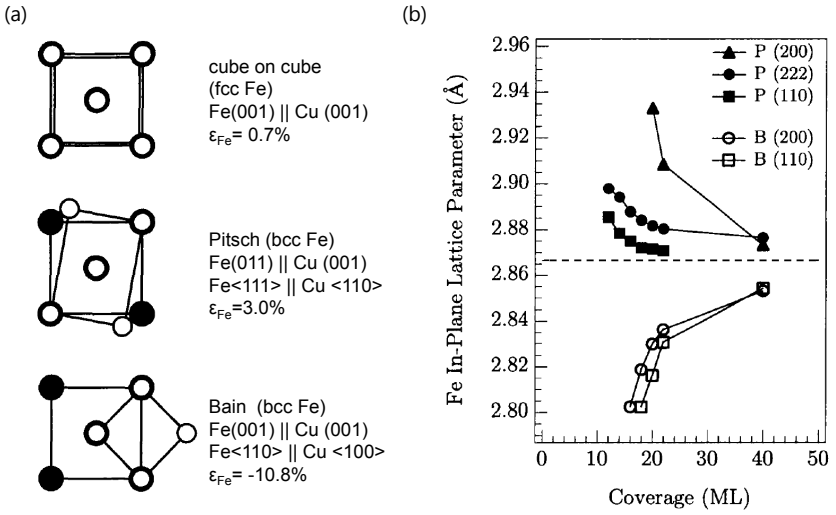

Fig. 3.10: *(a) Lattice orientations identified for the growth of Fe (open atoms) on Cu(001) (filled atoms) with ϵ_{Fe} as the lattice mismatch between Fe and Cu. (b) In-plane lattice parameters as a function of Fe thickness for P and B, the Pitsch and Bain orientations, respectively. The lattice parameters approach the lattice constant of bulk Fe of 2.87 Å (horizontal dashed line) for increasing Fe thickness. (Source: [68])*

peak from 14 to 40 ML, indicating tandem growth of the Fe Pitsch and Fe Bain orientation.

Figure 3.10a illustrates both structures compared to fcc Fe grown cube on cube on Cu(100), which provides the minimal lattice mismatch ϵ_{Fe}, while ϵ_{Fe} is increased for the Pitsch and Bain orientation. In the latter, Fe growth occurs with a 45° rotation on Cu. The in-plane lattice parameters of both structures are plotted for several directions in Figure 3.10b as a function of Fe thickness. All lattice parameters approach the lattice constant of bulk bcc (horizontal dashed line) for increasing thickness.

3.1.5 Summary and Discussion

In the first two sections of this chapter (Sections 3.1.1, 3.1.2), I showed that the magnetic and structural behavior at RT of TD-grown Fe/Cu(100) films can be divided into three different regions as a function of Fe-layer thickness: region I up to 4 ML [34, 35] or 5 ML [5, 6] exhibits ferromagnetism with the magnetization aligned perpendicular to the surface. Region II ranges up to 11 ML, showing an oscillatory net magnetic signal with the same orientation. The ferromagnetic region III [35] shows an in-plane magnetization [5, 34].

While some authors regard the distorted fcc lattice with an enlarged volume [2, 34, 51, 52] to be responsible for the ferromagnetism in region I, Biedermann *et al.* [37, 53, 54] recently found that Fe grows partially as bcc Fe in the Pitsch orientation (nanomartensitic phase). This stucture is strained, forming a zigzag pattern to fit to the underlying fcc lattice. It also results in an enlarged volume. Only the 4th ML was found to exhibit large portions of fcc structures. From this, one may infer that the ferromagnetism is a direct consequence of the bcc structure and not of a distorted fcc lattice. Similar observations have been made for region II. It is accepted that the buried Fe layers possess either a non-magnetic or antiferromagnetic fcc structure with a magnetic live surface layer [2, 5, 36, 41, 53, 67]. Biedermann *et al.* state that the ferromagnetic top layer is due to a bcc surface construction and not to a strained fcc layer.

In region II, the magnetic signal oscillates as a function of Fe-layer thickness explained by the number of buried AFM layers being odd or even [2, 41] with a Neel temperature of $\approx$ 200 K [5, 6]. The exact AFM behavior in region II is still unclear. It may be caused by a SDW [36] or by collinear magnetic sheets [35]. Also, the location of the maxima and of the minima of the magnetic signal was not the same in all studies.

Further, it is widely accepted that region III is ferromagnetic owing to its bcc structure, which is suspected to grow in the Pitsch orientation in [55–57].

The authors found Fe implantation in the substrate, forming islands of Fe and Cu atoms in the first 2 ML, followed by a layer-by-layer growth [53] in region I, an almost layer-by-layer growth in region II and a 3D island growth in region III [5, 6, 34, 35]. T_c was found to increase with increasing Fe thickness to 350 K at 3 ML, to drop again at 4 ML, which is probably due

to the non-magnetic fcc structure occurring at 4 ML, and to remain constant in region II. In region III, T_c suddenly increased to a value above 500 K [35].

In Section 3.1.3, I discussed the limits of the stability of such structures, which can be altered by specific cooling processes, exposure to H_2, or by applying a strong magnetic field. More importantly, the structural and magnetic properties alter dramatically with a change of growth conditions or deposition technique (Section 3.1.4). As well as the LT growth, which suppressed region II for sufficient low temperatures, PLD-grown or sputtered films exhibiedt a completely different behavior to thermal deposited films. Although all growth methods result in the onset of pure bcc growth at $d_{Fe} > 10$ ML and in a structure dominated by fcc Fe growth for smaller thicknesses, the structural details seem to differ strongly. This is reflected in the complex magnetization reorientation as a function of Fe thickness and the decrease of magnetization from 7 to 10 ML for films produced by PLD. In general, magnetization is expected to be reduced for PLD-grown films, as a higher Cu content appears in the top layers than for TD films [67]. For sputtered films, neither a magnetic nor a detailed STM study exists, but the simultaneous growth of Fe in the Pitsch and Bain structure [68] has not been reported for PLD- or TD-grown films. Nevertheless, detailed STM studies revealed nanomartensitic fractions for 2–5 ML for PLD- and TD-grown films, but with different fractions for each growth method and a bcc-like magnetic top layer in the region of constant magnetization. Similar structures may therefore also be present in sputtered films.

The different properties of the films grown by TD, PLD, or sputtering are mainly due to the different kinetic energies of the deposition atoms produced by each method. Atoms produced by PLD have energies in the range of 40–200 eV [67] and in the range of 5–50 eV when produced by sputtering, while atoms produced by TD typically have energies of only 0.1 eV [42]. Further, PLD differs from TD and sputtering in the pulsed deposition rate. Although the average rate is in the same order of magnitude ($\approx$ 1 ML/s), the instantaneous rate is about 1000 ML/min, during which many atoms arrive simultaneously at the substrate, resulting in a high nucleation density [42]. On these grounds, one may expect that the growth mode for sputtering differs from TD as well as from PLD deposition, owing to the difference in kinetic energy of the deposition atoms and the nucleation density, respectively.

Compared to the studies on TD- and PLD-grown Fe/Cu(100) films, only a little work has been done on sputtered films [68]. This Ph.D. thesis will therefore focus on the magnetic and structural properties of sputtered Fe/Cu(100) films using our *in-situ* sputtering system specifically designed for neutron experiments in order to monitor those properties directly during growth.

3.2 Advanced Techniques

Alongside the standard techniques described in Chapter 2, we also used two very unique techniques for our neutron experiments: a sputtering system for *in-situ* neutron reflectometry to monitor the growth (Section 3.2.1) and the Selene concept (Section 3.2.2) to reduce the measurement time. Combining both methods, we establish a step towards an *in-situ* neutron experiment in which the measurement takes place on a similar time scale as the growth.

3.2.1 *In-Situ* Sputtering System

It is often of great importance to investigate the properties of thin films as a function of layer thickness, to tailor materials with a desired property, and to understand the fundamental mechanism during growth as described for Fe/Cu(100) films in Section 3.1. Owing to the sensitive growth of thin films and their complex structural and magnetic properties, which can be altered dramatically by slight changes of the growth conditions, the monitoring of these properties during growth brings tremendous advantages. It allows several layers to be sputtered on the same substrate and under the same growth conditions instead of several samples with different thicknesses being produced with time-consuming preparation. Additionally, it avoids surface oxidation or pollution.

The sputtering chamber dedicated to *in-situ* neutron reflectometry was developed through cooperation within the TRR 80 between Prof. Böni's group (chair of Experimentalphysik für Neutronenstreuung E21, Technische Universität München) and Prof. Mannhart's group (at that times: chair of Experimentalphysik VI, Universität Augsburg). Andreas Schmehl, Alexander Herrnberger, and Thomas Mairoser from Prof. Mannhart's group realized the sputtering system technically, while Wolfgang Kreuzpaintner and I from Prof. Böni's group were responsible for technical maintenance and the neutron experiments.

For this work, we used the sputtering system to monitor the evolution of the magnetic and structural properties of ultrathin Fe layers by polarized neutron reflectometry (PNR). PNR can measure the magnetic moment of the sample as a function of layer depth as well as the layer thickness and roughness for all layers, including the buried layers (Section 2.2.2). This offers great advantages over X-ray methods such as XMCD, which integrate over the film depth. Additionally, neutron reflectometry allows monitoring of the evolution of very thick layers and moreover to distinguish between different isotopes. And because, polarized neutron reflectometry is only sensitive to a specific magnetization direction, vector magnetometry is very simple compared to XMCD. The sputtering chamber can also be used for GISANS or PGISANS, which also allows the possibility of determining the structural and magnetic correlation length of the films.

Two *in-situ* chambers already exist for neutron facilities. There is an MBE system at NIST [75] and an e-beam evaporation system at HZB [76]. The latter uses a transfer rod to change the sample from the deposition position to the measurement position within the deposition

chamber. In this case, the sample has to be realigned every time, so the orientation of the sample at the measuring position cannot be always replicated. However, the *in-situ* system built by the University of Augsburg uses a deposition technique very common in industry — magnetron sputtering. Here, the sample position is kept fixed for deposition and measurement.

Setup. The sputtering system is depicted in Figure 3.11. The sputtering chamber (center) is shown with the neutron exit window towards the front. The neutron entrance window on the back side allows the neutrons to pass through the chamber by reflection from the sample surface. A gas rack (left) provides argon or oxygen, which can be injected into the chamber for non-reactive and reactive sputtering, respectively. Two racks equipped with power supplies (one of them is shown on the right) and a computer (right) are used to control the sputtering process. For further details please refer to Thomas Mairoser's Ph.D. thesis [77]. For the measurement, the sample table can be translated parallel to the beam (x-direction) as well as vertically to the sample surface (z-direction) and rotated around the y-axis to change the angle of incidence θ. The sample table is mounted on the left flange with a rotary feedthrough and with x-y stepping motors. Three sputter guns [78] for 2″ targets are located on top of the chamber. The top flange as well as the guns themselves are tilted by 20° to provide the maximum spacing between the guns to prevent cross-contamination. The flange with the sputtering guns is rotatable, so that one gun is always located above the sample. This design allows the deposition material to be changed without breaking the vacuum. The guns can

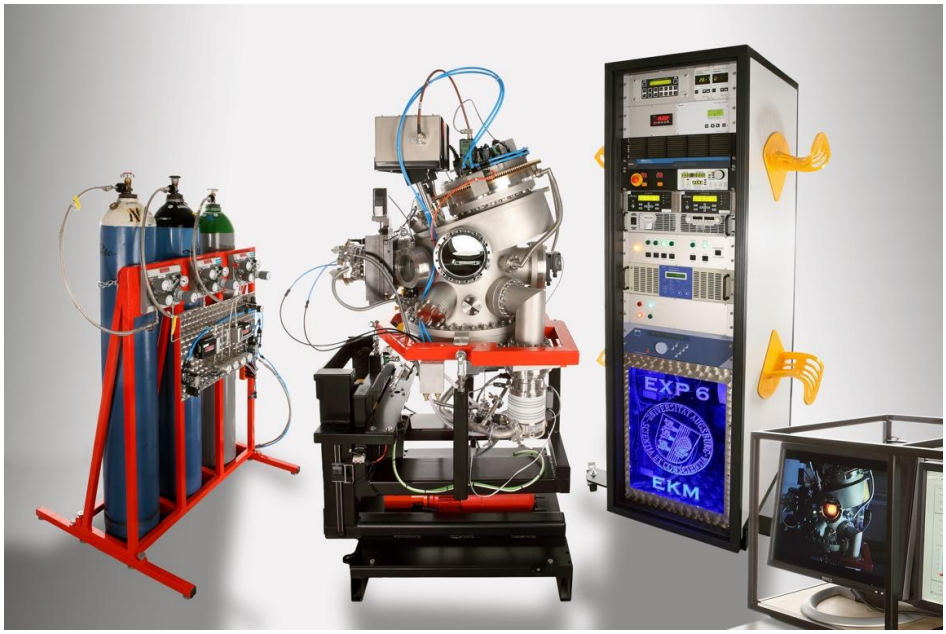

Fig. 3.11: *Photo of the sputtering system with the mobile components: the sputtering chamber in the center, the gas rack on the left, and the electronic rack and the computer on the right. (Source: [77])*

be operated using DC or RF. The match box of the RF power supply is fixed on top of the chamber to provide the correct impedance of the cable to connect the gun. The total chamber can be lifted for a rough alignment to the neutron beam, while the exact alignment of the sample height is done by the sample table.

The chamber was specifically designed to be very compact, with dimensions of 1.6 m x 1 m x 1.5 m (L x B x H) and a footprint of 1 m x 1 m in its demounted state, to fit the sample position at REFSANS. Moreover, the sputtering system is fully mobile, with most of the components fixed at the chamber or its frame. Deinstallation and installation take about 5 h, respectively. As this setup is used for neutron experiments, it was important to use materials without Co, preventing activation for parts that could come into contact with neutrons. Further, it was essential to reduce diffuse scattering of neutrons, which was achieved by using materials containing boron with a high absorption cross-section. Thus, the sample table, the slits and the gun shields are either made of boron silicate or B_4C. In contrast, the chamber windows are from boron-free window glass to reduce any absorption. For further details see [77].

A schema of the chamber cross-section and the neutron path (yellow beam) inside the chamber (Figure 3.12a) and a detailed view of it (Figure 3.12b) were illustrated by Andreas Schmehl and Alexander Herrnberger. The sample table with integrated heater for temperatures up to 700°C and the shutter are mounted on the left flange, while the Helmholtz coils are mounted on the right flange (Figure 3.12a). Since the Helmholtz coils were built at a later stage during the design of the sputtering chamber, they were not mounted in the photo in Figure 3.11. To perform PNR measurements, we installed several guide field yokes and provided a magnetic field at the sample position by applying current to the Helmholtz coils, which produces a magnetic field up to 35 mT. The sample must be able to be positioned freely for the dedicated sputtering height and should not be blocked by the coils during deposition.

(a) (b)

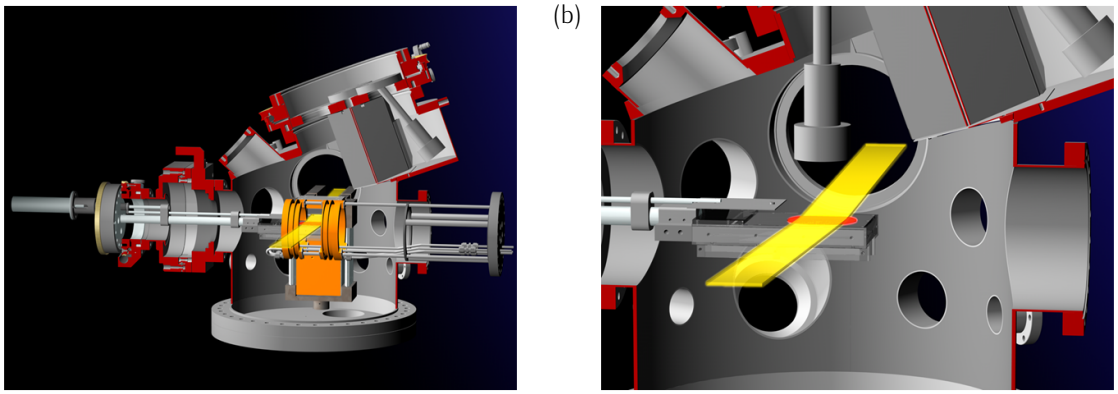

Fig. 3.12: Schema of the sputtering chamber. (a) A cross-section with the sample manipulator mounted on the left flange, the sample being in the center exposed by neutrons (yellow beam) and the movable coils on the right flange. The three sputter sources are located on the top flange and are separated by shields. (b) Zoom of the sample table with integrated heater and shutter with a sputtering gun positioned above the sample. (Source: Andreas Schmehl)

The coils can therefore be moved from the sample position for sputtering and moved back again for the measurement using a translation table with a welded bellow. The tilted flange and only one out of three sputter guns are depicted at the top of Figure 3.12a. We installed a slit directly in front of the sample, visible in Figure 3.12a and partially hidden behind the coils to control the footprint of the beam, hence, reducing diffuse background and improving the angular resolution. External slits mounted on the chamber frame outside the chamber (not shown) can be used to block the direct beam. Further details about the heater, the Helmholtz coils, the yokes, the internal slits, and the external slits can be found in [77].

The sputtering process is controlled by a LabVIEW program, developed and realized by Thomas Mairoser [77]. The pressure is determined by two pressure sensors — a capacitive sensor working at pressures down to 10^{-3} mbar and a full range sensor working down to $5 \cdot 10^{-9}$ mbar. A turbo and a scroll pump evacuate the chamber to a base pressure of $3 \cdot 10^{-7}$ mbar. Starting from ambient pressure, the chamber is evacuated firstly by the scroll pump through a bypass valve. Below a pressure of 10 mbar, a gate valve located before the turbo pump is opened, while the bypass valve is closed. If the turbo pump is started, the scroll pump then operates as backing pump. After evacuating for typically 6 to 12 h, a sufficient base pressure of $p_0 < 10^{-6}$ mbar is reached. Before starting the sputtering process, one has to select the gun with the desired material by rotating the top flange, then move the sample to a specific z position, and insert Ar or O_2 gas. The gas pressure is regulated by the position of the motorized gate valve and the gas flux. Afterwards, the plasma can be started by applying a constant power. For presputtering, the shutter is closed to sputter the oxide layer off the target and to control all sputter parameters. When the plasma is stable, the shutter can be opened for a specific time, controlling the thickness of the sputtered layer.

During the research for my PhD-Thesis, we used the sputter system for two beamtimes at REFSANS (FRM II) in February 2012 and August 2012 as well as for one beamtime at Amor (PSI) in November 2013. After each beamtime and in preparation for the next upcoming beamtimes, we generally found ways to improve and upgrade the sputtering system.

Upgrade 1. After the beamtime in February 2012 at REFSANS, it became necessary to reduce the diffuse scattering, because the measurement times were, with 27 h per spin state and layer, very long. As the heater function of the sample table was not required, we decided to reduce the size of the sample table to match the sample size of 2 cm x 2 cm. In this way, less material was exposed to the neutron beam, reducing diffuse scattering. The new sample table was built by Thomas Mairoser and Alexander Herrnberger. The top of the sample table was covered with boron carbide [77] to reduce scattering of the sample table itself. During sputtering the neutron exit window was covered with sputtered material, and this too was suspected to contribute to the diffuse scattering and to decrease the signal intensity. Thomas Mairoser and Alexander Herrnberger therefore built a shutter for the exit window, which can be closed during sputtering and opened again for the measurement. However, because of the need to characterize the polarizer during the beamtime of August 2012, we installed an additional guide field up to the analyzer to maintain the neutron polarization. As a consequence, there was no longer sufficient space to install the new window shutter.

Upgrade 2. After the beamtime in August 2012, we found that the sputtering parameters were not reproducible for a constant valve position of the motorized gate valve: to maintain constant sputtering pressure, different flux values had to be used and still, this did not result in reproducible plasma voltages. There was no obvious trend of pressure and voltage as a function of flux or base pressure. We concluded that either the pressure sensor did not work properly or that the chamber had a leak. Therefore and to achieve a better sample quality, we decided to upgrade from HV to UHV, by sealing all flanges and feedthroughs with Cu instead of viton gaskets wherever possible. The viton-sealed viewports of the two neutron windows were changed to CF-sealed fused silica windows. The only remaining viton gaskets are in the rotary feedthroughs of the top flange and in the sample table, realized as two-stage differential pumping system. The viton-sealed quick-access door with a viewport, necessary to change the sample, was separated by an additional gate valve from the main chamber to pump here differentially, too.

We also added a separate turbo pump to evacuate the second stage of the differential pumping system, instead of using the main turbo pump for both stages. To prevent further possible leaks, the previously installed standard gas inlet needle valve was substituted with a UHV precision valve and the viton-sealed pressure-relief valve by a CF burst disk. The flange of the sample table had a welded seam and was replaced by a new flange. While implementing the upgrade, we found a leakage in the oxygen gas valve. Since, we had not planned to sputter reactively at this time and the oxygen leakage could have been the reason for the non reproducible sputtering process, we disconnected the oxygen gas station for the next beamtime. To obtain the best possible vacuum during sputtering, we also decided to sputter with the position valve fully open instead of half opened.

As well as the upgrade to UHV, the full range sensor was replaced by a new sensor. In addition, we reconstructed the sample shutter, since there was not enough space at the Amor beamline on the side where the pneumatic motor of the shutter protrudes from the chamber frame. We chose to mount a rotatable half-open hollow cylinder as a shutter on the opposite flange inside the coils, instead of a linear shutter moving forward and backward to the same side. In the original design, one could not guarantee the same exposure times for the full sample area. In contrast, by using a rotating shutter, which always moves in the same direction, each part of the sample is exposed for the same time. The new shutter system required sputtering to occur at a different sample height closer to the axis of the shutter rotation, to avoid the shutter crashing into the sample holder. The new sample position is therefore $z = -4\,\mathrm{mm}$, 19 mm higher than compared to the previous position of $z = -23\,\mathrm{mm}$. As a result, the sample-target distance was reduced to 70 mm, which suggests an increase in deposition rate at the sample position. Investigations of the rate homogeneity as a function of sample-target distance and radial distance were carried out in [79] with a 2″ target used for RF magnetron sputtering of Si. From this, we infer that a homogeneous film within 2 cm radial distance of the target center with a rate dropping from 0 to 2 cm by $<<20\%$ can still be deposited.

After upgrade 2, we achieved a base pressure of $1.8 \cdot 10^{-8}\,\mathrm{mbar}$ when the precision valve

was closed and the coils were not installed. When the precision valve was open, we reached a pressure of $1 \cdot 10^{-7}$ mbar, indicating either a leakage in the gas rack or a low pumping efficiency for the gas-supply tube due to its low cross-section. When the coils were installed, we reached a pressure of $1.2 \cdot 10^{-6}$ mbar, but we could not determine any leakage. Rather, we suspect the materials of the coverage of the coils itself to outgas into the vacuum.

3.2.2 Selene for Neutron Optics

In order to measure the reflectivity from small samples, a highly efficient reflectometer is required. Especially for small samples the recording of the reflectivity is usually very time-consuming. This is even worse when one wants to record a set of measurements for varying external parameters, such as temperature or magnetic field. Then, the samples are exposed to air for a long time, making an oxidation of the surface probable, which alters the reflected signal. The Selene concept realized by Jochen Stahn at PSI, based on a concept of Frederic Ott [81], can provide an intensity gain of at least one order of magnitude by using focusing optics, resulting in a small footprint on the sample and a highly divergent beam instead of a collimated beam [82, 83]. A collimated beam used in conventional neutron reflectometry experiments provides only a small range of angles of incidence $\Delta\theta$, which corresponds to a small Q_z-range defined by $Q_z = 4\pi/\lambda \cdot sin(\theta)$ as illustrated in Figure 3.13a by Jochen Stahn. By contrast, a divergent beam with a large $\Delta\theta$ allows to measure a wide Q_z-range simultaneously (Figure 3.13b). The angular resolution $\Delta\theta$ is determined in the first case by the divergence of the incoming beam and in the second case by the resolution of the detector. A disadvantage of the high divergence is an enhanced background, which is counterbalanced, however, by the increased intensity. In the following section, I will introduce the Selene optics operated in the TOF mode, as used at the Amor beamline at the Paul Scherrer Institute (PSI). This additionally provides a broad wavelength band of typically 4–14 Å increasing the intensity further.

For the Selene setup, two elliptically-shaped focusing reflectors have to be installed at a reflectometer, as shown in Figure 3.14a (illustrations from Jochen Stahn), with the sample

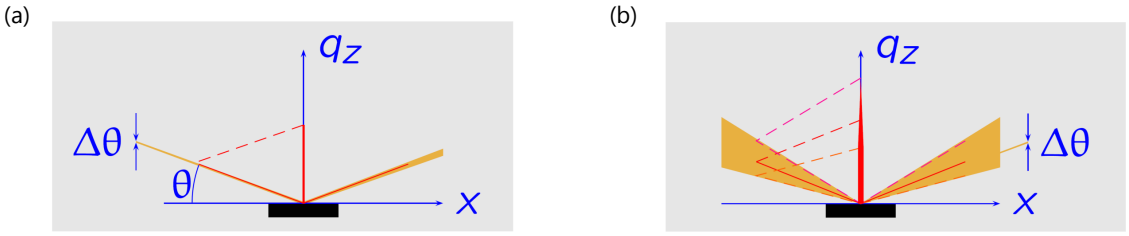

Fig. 3.13: (a) Conventional reflectometry setup with collimated beam. (b) High intensity reflectometry setup with divergent beam. (Source: [80])

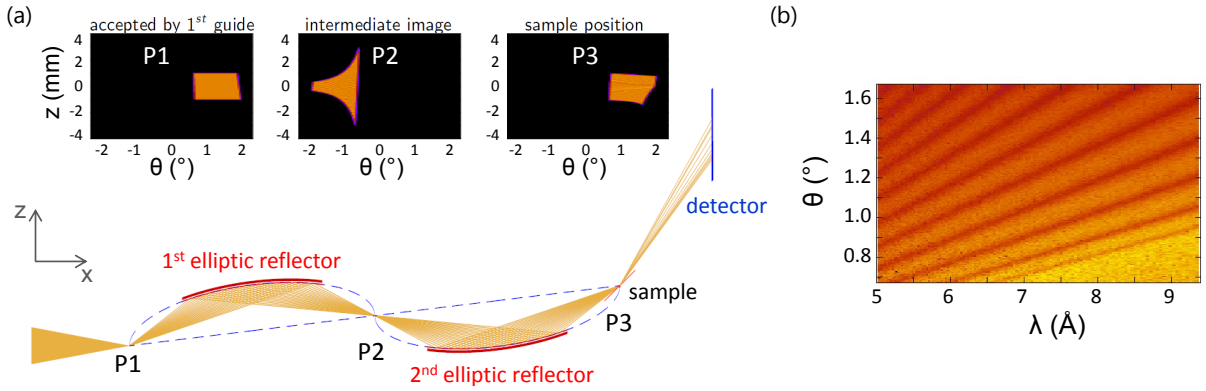

Fig. 3.14: (a) Bottom: Selene concept with two elliptic reflectors to focus the neutron beam on a small sample providing a large divergence. Top: Images as they appear in focal points P1, P2 and P3. The second reflector corrects the coma aberration responsible for the distorted intermediate image in P2. (b) Exemplary intensity map I(λ, θ) measured for a thin film. Diagonal lines of high intensity represent Kiessig fringes. (adopted from: [80, 84])

located in the focal point P3, providing a divergence of $> 1°$. The two elliptical reflectors are needed to correct the coma aberration, which causes off-axis points imaged as lines. They are positioned such that the focal points of both reflectors coincide in P2. Figure 3.14a depicts the real image in P1 that is accepted by the 1st reflector and is strongly distorted in P2, while it is almost completely restored after the second reflector in the image at P3. Note that the beam is focused not only in the x-z-plane but also in the x-y-plane to further increase the flux on the sample. To achieve this, another pair of reflectors is adjoined to the first pair, forming an L-shaped cross-section, i.e. a Montel mirror [85].

To obtain a reflectivity curve from the detector image, the z-channel of the detector is converted into θ and the time of flight (TOF) of the neutrons from chopper to detector into λ. This results in an intensity map $I(\lambda, \theta)$ as plotted exemplarily in Figure 3.14b for a thin film sample. The triangle of high intensity in the lower right corner corresponds to the region of total reflection, while the diagonal stripes of high intensity are the Kiessig fringes (Section 2.1.2). Each point can be assigned to a Q_z value by $Q_z = 4\pi/\lambda \cdot sin(\theta)$. The intensity map then reduces to $I(Q_z)$, which represents a reflectivity curve.

A photo of the Selene setup tested at the BOA beamline (PSI) is shown in Figure 3.15. Each Montel mirror consists of two elements. On the left is the first Montel mirror element with the L-shaped profile. On the right is the final installation with the same guide element shown in the opposite direction, this time with the viewer looking towards the detector. Guide fields for maintaining the polarization were mounted on the top and on the bottom of the guides. So was the second Montel mirror element of the first Montel mirror, separated by knife edges to block neutrons, which are not reflected from the guide. The second Montel mirror, the sample, and the detector can be seen at the back.

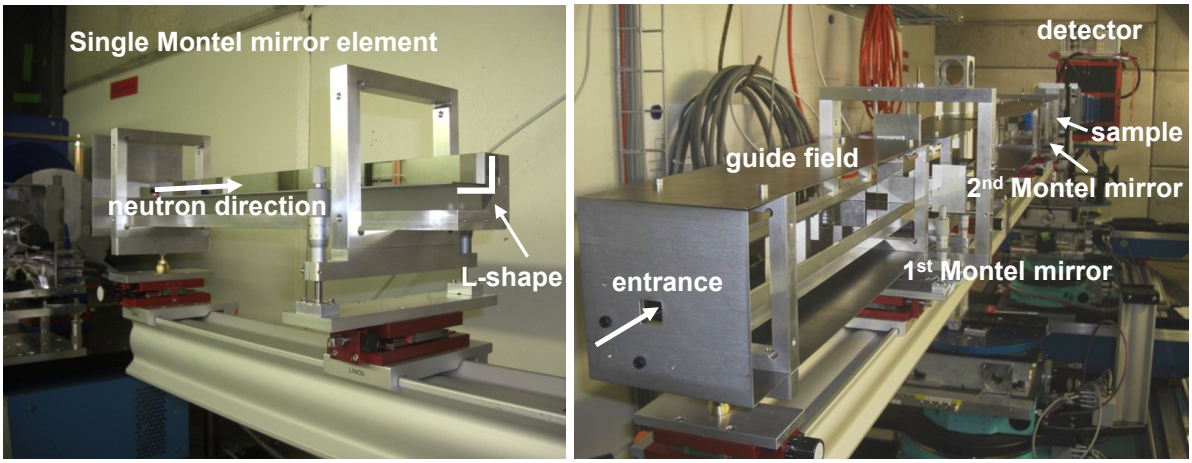

Fig. 3.15: Photos of the setup. Left: first guide element, i.e. a Montel mirror, in an early installation stage, showing the L-shaped profile with the view to the neutron source. Right: total setup in the final installation stage with the view towards the detector. All four guide elements with guide field, the sample and the detector vessel are installed.

3.3 Sample Growth and Structural Characterization

All Cu/Fe bilayers investigated within the scope of this thesis were fabricated using the *in-situ* sputtering system presented in Section 3.2.1 — for samples measured *in situ* during growth when the chamber was installed at a neutron beamline, as well as for samples grown with the chamber installed in the laboratory for calibration and *ex-situ* characterization. In Section 3.3.1, I will introduce the sample preparation and the sputtering parameters used for Cu, Fe, and Si. The latter was used as protective capping layer. The samples are structurally characterized in Section 3.3.2 – 3.3.4 using XRR and XRD to determine the deposition rate of each sputtered material as well as the layer thicknesses, roughnesses, and the crystal growth of the samples. The X-ray measurements are complemented by TEM (Section 3.3.5) and XANES (Section 3.3.6). The structure is summarized in Section 3.3.7.

3.3.1 Sample Growth

We used Si(100) wafers as substrate, which were pre-cut in 2 x 2 cm^2 or 1 x 1 cm^2 squares. Tests to find the optimal cleaning procedure showed that an ultrasonic bath enhances the roughness by 1–2 Å. This confirmed similar observations made by others [86]. Wiping with KIMTECH wipers increased the roughness by 3 Å. Rinsing the samples with acetone or isopropanol and drying them again using compressed air did not provide a dust-free surface, since a clean room for sample preparation was not available. We had to etch the surface anyway to remove the SiO_2 layer using 4–5% diluted hydrofloric acid (HF), which, as I will show in Section 3.3.3, ensures the epitaxial growth of Cu(200). Potential protective resist

or dirt is removed during this process. Thus, to ensure the least possible roughness, we omitted substrate cleaning and put the samples directly into the acid for 60 s after removing the protective foil.

Substrates ordered from Crystec showed a very high and varying surface roughness of 4–12 Å after etching. We therefore used Si(100) substrates from Si-Mat with a roughness of only 2.5–3.5 Å after etching. These samples are labeled with numbers > #47. The etching process itself, with etching times between 15 s and 3 min, did not increase the roughness systematically. Once only, an etching time of 2 min increased the roughness from 4 Å to 8 Å. However, a similar sample had the same roughness before and after 2 min of etching. Nevertheless, we decided to etch all Si substrates for 60 s, which always produced good results. Afterwards, the samples were rinsed two times in deionized water. If the total substrate surface became hydrophobic, the SiO_2 layer was completely removed and terminated by H atoms covalently bonded to the Si surface atoms [87]. This hydrogen termination prevents surface reoxidation for some time. While one group reports on experiments that showed that 7 days in air are necessary to form a complete oxide layer [88], another group [89] described the passivation as being stable after several minutes in air and of several hours in vacuum. However, we tried to limit the time from etching to sample mounting and evacuating the chamber to 5 min.

In general, the chamber was evacuated for a minimum of 5 hours and a maximum of 24 hours before the deposition was started. First, Cu was sputtered to form a seed layer. This process was followed by Fe sputtering and finally by Si sputtering to form a protective layer preventing oxidation of the Fe layer. While Cu and Si were sputtered using DC, Si was sputtered by RF. One sputtering step was performed by starting with the shutter closed, providing a high Ar flux at a fixed valve position such that the plasma easily started by applying 50 W. Afterwards, we reduced the power to the desired value and presputtered for 2 min to 5 min to remove the oxide layer from the target until the voltage remained constant. Then, the Ar flux had to be adjusted manually to reach the desired Ar pressure p_1. Once all parameters were constant, we started the deposition by opening the shutter for a specific time. After each step of sputtering, the power at the guns was switched off, the Ar valve was closed, the valve was fully opened, and the sputter guns were rotated to the next target. Once the base pressure p_0 restabilized, we restarted the plasma using the same procedure as above to deposit the next layer.

The upgrades of the sputter chamber as discussed in Section 3.2.1 may have influenced the rate or the growth mode as well. Upgrade 2 in particular is assumed to have had a strong impact, since the chamber was sealed with Cu gaskets, improving the base pressure. In addition, the shutter was replaced, which required a new sample position closer to the sputtering target. Accompanying upgrade 2 was the decision to sputter with a fully open valve to ensure the best possible vacuum. We sputtered several series of samples with different Fe thickness to determine the sputtering rate and to investigate the structural and magnetic properties of Fe as a function of thickness. The first and second sample series were #42–46 and #65–75.

Sample Series 1–2, Before Upgrade 2

	Sample	Cu	Fe	Si
Valve position	general	500	430	200
Power (W)	general	20 (DC)	20 (DC)	50 (RF)
Flow (sccm)	#38, 42-46	6.5 – 6.8	4.4 – 4.7	3.8 – 4.0
	#62	3.3 – 4.5 (instable)	4.6 – 4.8	10
	#65-75	4.6 – 5.0	3.5 – 4.1	3.3 – 3.8
p_1 (E-3mbar)	#38, 42-46	6.0 – 6.3		10.9 – 11.7
	#62	4.4 – 5.0 (instable)	6.9 – 7.3	52.3
	#65-75	5.7 – 6.0		10.6 – 11.7
Voltage (V)	#38, 42-46	338	324 – 332	416 – 426
	#62	355 - 384 (instable)	330 – 333	unknown
	#65-75	346 - 351	335 – 342	412 - 417
Sputtering time (s)	#38, 42-46	150	2 – 18	150
	#62	330	11	180
	#65-75	330	2 – 23	150

Table 3.2: *Sputtering parameters before upgrade 2 with a partially open valve position (1000 open, 0 closed), a sample height of -23 mm and a base pressure of* $4 \cdot 10^{-7}$–$9 \cdot 10^{-7}$ *mbar.*

These were produced before the second upgrade of the sputtering chamber, while the third series, #91–99, was sputtered after the upgrade. The parameters used for those series are summarized in Table 3.2 (for before upgrade 2) and in Table 3.3 (for after upgrade 2) together with the samples sputtered for *in-situ* PNR experiments, #38 and #62 at REFSANS and #83 and #89 at Amor. As mentioned, the main difference between the parameters in both tables is the fully open valve position of 1000 (Table 3.3), which allowed us to sputter at a reduced Ar flux and a reduced Ar pressure p_1. The base pressure p_0 was $4 \cdot 10^{-7}$–$9 \cdot 10^{-7}$ mbar before upgrade 2. Afterwards, it has improved to $8 \cdot 10^{-8}$–$5 \cdot 10^{-7}$ mbar. If we had pumped for several days, we could have reached a pressure of $1.8 \cdot 10^{-8}$ mbar. Nevertheless, we would have increased the risk of substrate reoxidation and we were therefore able to save time by pumping for a maximum of 24 h. The Fe layer of sample series 3 was sputtered in steps of 1.5 s to provide the same growth conditions as for the *in-situ*-measured samples #83 and #89 (Section 3.5.4). The base pressure for sample #83 increased to a value of

Sample Series 3, After Upgrade 2

	Sample	Cu	Fe	Si
Valve position	general	1000	1000	1000
Power (W)	general	20 (DC)	20 (DC)	50 (RF)
Flow (sccm)	#83	13	11	–
	#89, 91-99	13	25.4 – 26.1	16.3
p_1 (E-3mbar)	#83	3.1	2.7	–
	#89, 91-99	3.0 - 3.1	4.5	3.5
Voltage (V)	#83	358	369 – 371	–
	#89, 91-99	355 – 358	302 – 318	396 – 441
Sputtering time (s)	#83	200	11 x1.5s	0
	#89, 91-99	200	2 – 15 x1.5s	0s, 8s or 50s

Table 3.3: *Sputtering parameters after upgrade 2 with a fully open valve position of 1000, a sample height of -4 mm being closer to the sputter target and an improved base pressure of* $8 \cdot 10^{-8}$–$5 \cdot 10^{-7}$ *mbar. In contrast, owing to the installation of the coils, the base pressure for sample #83 was only* $1 \cdot 10^{-6}$–$4 \cdot 10^{-6}$ *mbar.*

$p_0 = 1 \cdot 10^{-6}$–$4 \cdot 10^{-6}$ mbar. It seems the coils had either a leakage or outgassed. The corresponding measurement was therefore excluded from the rate determination in the next section, but will be discussed in Section 3.5 when compared with PNR data. Note that we changed the supplier of the Si(100) substrates from Crystec to Si-Mat after series 1 to ensure less substrate roughness as already mentioned above.

3.3.2 XRR

The thickness, roughness, and crystalline quality of the samples introduced in Section 3.3.1 are investigated in this section using X-rays. The measurements are complemented with results from TEM and XANES.

XRR measurements (Section 2.1.2) were performed to determine the layer thickness and roughness. Some typical reflectivity curves of each sample series are depicted in Figure 3.16a as a function of Q_z. The reflectivities of series 1 associated with sample #42 drop more steeply and have Kiessig fringes that stop earlier, owing to very rough Si-substrates with $\sigma_{sub} = 9\,\text{Å} \pm 3\,\text{Å}$. For series 2 and 3, we used the new substrates with a roughness of $2.5\,\text{Å} < \sigma_{sub} < 3.2\,\text{Å}$. The Kiessig fringes of sample #42 are broader, since the Cu

thickness $d_{Cu} = 221\,\text{Å} \pm 9\,\text{Å}$ of series 1 is smaller than that of series 2 and 3 associated with sample #67 and sample #92, respectively. These have a Cu thickness of $d_{Cu} = 444\,\text{Å} \pm 11\,\text{Å}$ and $d_{Cu} = 469\,\text{Å} \pm 4\,\text{Å}$. Series 3 of sample #92 has Kiessig fringes ranging at least to $Q_z = 0.5\,\text{Å}^{-1}$, which can be attributed to a thinner and smoother Si capping layer. The reflectivity curves were fitted (black lines) using Parratt32 [17]. Good fits were obtained by adding a rough intermediate layer between the substrate and Cu layer, where Cu_3Si probably is formed. The formation of Cu_3Si was also observed in [20]. The fits also included an upper oxide layer of either FeO or, when a Si capping layer was sputtered, SiO_2. In the case of the FeO top layer, an effective Fe thickness was calculated by including also the Fe atoms in the FeO layer.

The Fe thickness determined by the fits is plotted for each sample series as a function of sputtering time in Figure 3.16b. Series 2 was fitted by Patrick Ziegler. The corresponding fits can be found in his Diploma thesis [90]. The curves of Figure 3.16b were fitted by a straight line $d_{Fe}(t) = R_{Fe} \cdot t + d_{Fe}(0)$ using the intersection with the y-axis $d_{Fe}(0)$ as a free parameter, because the Fe atoms may not adhere or grow as islands at the very beginning of the deposition process, which resulted in an extrapolation to $d_{Fe}(0) \neq 0$.

series 1 (#38, 42–46): $d_{Fe} = (0.99 \pm 0.12)\text{Å}/s \cdot t + (3.3 \pm 1.7)\text{Å}$
series 2 (#65–75): $d_{Fe} = (0.76 \pm 0.03)\text{Å}/s \cdot t + (0.8 \pm 0.4)\text{Å}$
series 3 (#89, 91–99): $d_{Fe} = (1.58 \pm 0.14)\text{Å}/s \cdot t - (2.5 \pm 1.8)\text{Å}$

As expected, the slope R_{Fe} of the straight line, that is, the sputtering rate of Fe, clearly increased for the last series after upgrade 2 as a result of the reduced sample-target distance.

Although the Fe sputtering pressure p_1 for series 1 and 2 was similar (Table 3.2), the rates

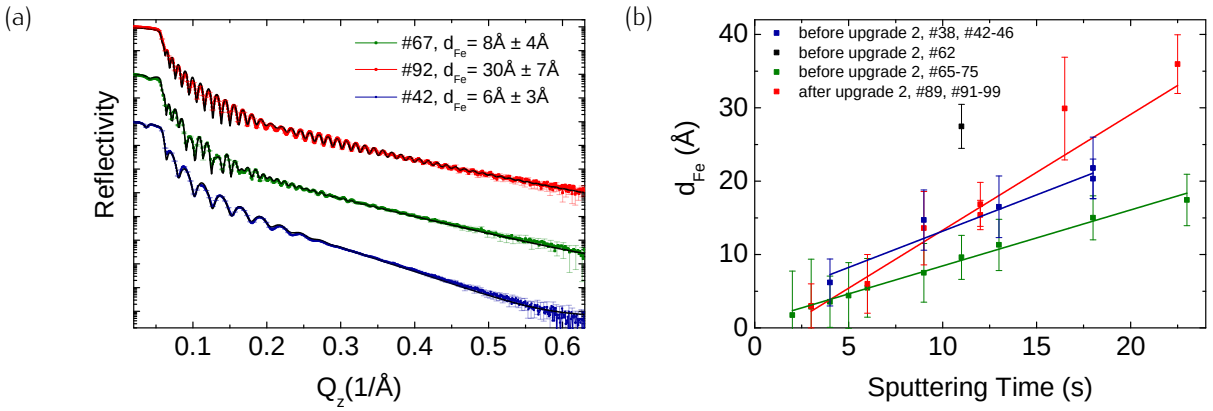

Fig. 3.16: *(a) Reflectivity measured by X-rays and plotted vs. Q_z together with fits (black lines) for three samples, each representing one sample series. (b) Fe thickness determined from the fits as in (a) as a function of sputtering time for all sample series. All data series are fitted by a linear slope (lines).*

differ by 30%. For series 2, we had to reduce the Ar flow to reach the same pressure p_1. We do not fully understood why. It could be the result of a leakage in the O_2 supply (Section 3.2.1) or of pressure p_1 not being at equilibrium, although the pressure reading was constantly at 10^{-4} mbar. If the pressure sensor did not work properly and the pressure p_1 was indeed reduced as a result of the reduced Ar flow, the sputtering rate of Fe for series 2 would have increased. A similar relationship was shown for $p_1 > 0.001$ mbar for tungsten in [91]. In the case of a smaller Ar pressure, fewer deposition atoms scatter with Ar ions so that they can reach the sample more easily. However, the rate decreased compared to series 1, hence this effect seems to be small compared to other effects.
Additionally, the sputtering voltage increased from 329 V±1V in series 1 to 338 V±5 V in series 2. This is probably due to the reduction of the target thickness, which reduces the target's resistance. The power remained constant, so this should not have affected the sputtering rate. We also have to consider that, according to their density, different Fe targets can be responsible for different sputtering rates [92]. Unfortunately, we did not number our two Fe targets and did not note when they were changed.

The extrapolation of the linear fit to 0 s sputtering time, i.e. $d_{Fe}(0)$, is also different for each series. Series 1 with $d_{Fe}(0) = 3.3$ Å has the highest point of intersection with the y-axis. This series also has the highest Cu roughness. Islands may have formed, perhaps alongside defects or Cu atoms at the surface as observed for PLD-grown films (Section 3.1.4), which would result in an increased mean thickness of the first few monolayers. Series 3 exhibits a negative point of intersection of $d_{Fe}(0) = -2.5$ Å. This series has the highest sputtering rate, since it was closer to the sputtering target. Consequently, the Fe atoms deposited with higher energy on the Cu surface, being mobile enough to arrange themselves as complete layers growing layer by layer. The energy may even have been too high for the Fe atoms to nucleate at the beginning and be resputtered or reevaporated, which could explain the negative value of $d_{Fe}(0)$.

Sample #62 was measured *in situ* at REFSANS. The Fe layer was sputtered in four steps and was much thicker than expected from series 1 or 2 (Figure 3.16b), with very similar sputter parameters for Fe. Here, to obtain a very smooth Cu layer, we tried to reduce the pressure for Cu sputtering by reducing the Ar flux: this had been successful in test measurements. Even so, the plasma was unstable and went out after a few seconds, which was probably a result of a non equilibrated base pressure, although p_1 remained constant until the plasma went out. The plasma had to be restarted three times by increasing the Ar flux. However, the Cu layer still grew much smoother than other samples with $\sigma_{Cu} = 4\,\text{Å} \pm 2\,\text{Å}$, which may have altered the Fe growth mode and thus the thickness. Nevertheless, the deviation of the Fe rate is large and the result does also not fit to the PNR data, which are presented later (Section 3.5). We therefore considered the measurement itself or the fit to be erroneous, although the latter seemed to be very unambiguous.

All parameters obtained from the fits are summarized in Table 3.4. As well as the Fe sputtering rate, the Cu and Si rates also increased by a factor of 1.3–2.0 for series 3. This was a result

sample	d_{Fe}(Å)	σ_{Fe}(Å)	d_{Cu}(Å)	σ_{Cu}(Å)	R_{Cu} (Å/s)	d_{Si}(Å)	σ_{Si}	R_{Si} (Å/s)
#42-46	6 – 27	4 ± 1	221 ± 9	12 ± 6	1.47 ± 0.06	231 ± 8	13 ± 2	1.54 ± 0.05
#38	22 ± 4	10 ± 3	198 ± 4	10 ± 5	1.32 ± 0.03	215 ± 13	12 ± 6	1.43 ± 0.09
#62	28 ± 3	4 ± 2	431 ± 5	4 ± 2	1.31 ± 0.02	52 ± 7	12 ± 7	0.29 ± 0.04
#65-75	0 – 17	12 ± 2	444 ± 11	10 ± 3	1.35 ± 0.03	177 ± 4	12 ± 3	1.18 ± 0.03
#83	33 ± 4	12 ± 9	483 ± 7	13 ± 4	2.40 ± 0.05			
#91-99	3 – 36	13 ± 4	469 ± 4	11 ± 5	2.34 ± 0.02	20 ± 3	11 ± 6	2.41 ± 0.31
#89	29 ± 5	14 ± 5	460 ± 5	6 ± 1	2.30 ± 0.03			

Table 3.4: *Sample parameters obtained from XRR fits, where d is the thickness, σ the roughness and $R = d/t$ an estimation for the sputtering rate.*

of the decreased sample-target distance and the reduced Ar pressure p_1. The Cu and Si rates are estimated by the ratio of the layer thickness and the sputtering time $R = d/t$. For a better comparison, the Cu thickness and the Si thickness of Table 3.4 already include the intermediate layer formed on the substrate, probably Cu_3Si, and the SiO_2 of the first few top layers, respectively. Note that samples measured *in situ* at Amor, i.e. #83 and #89, have no Si capping layer.

3.3.3 Out-of-plane XRD

To investigate the structure of the Cu and Fe layer, we recorded typical XRD patterns obtained by performing 2θ-θ-scans (Section 2.1.1) using our two-circle X-ray diffractometer D5000. Here, the scattering wavevector $\boldsymbol{Q}$ is parallel to the surface normal.

Cu layer. Figure 3.17a shows XRD patterns of samples used for PNR measurements, which will be presented in Section 3.5, are compared to the pattern of sample #57, which has the thickest Cu thickness of 1294 Å. The absolute intensities are not comparable, owing to different intensities of the primary beam. However, sample #57 shows the most intense Cu(200) Bragg peak at $2\theta = 50.49°$. Sample #38, with the thinnest Cu thickness, shows, along with sample #62, the smallest Cu(200) peak. Sample #62 exhibits the additional Bragg peak of Cu(111) at $2\theta = 43.32°$, indicating that this sample grew in a polycrystalline structure. For Cu powder, the Cu(111) Bragg peak is more intense by a factor of 2 than the Bragg peak of Cu(200) and the most intense peak at all. Therefore, if the Cu(111) peak is not visible in the XRD pattern, it is a strong hint that the sample grew epitaxially on the Si(100) substrate with the Cu(200) parallel to the surface plane, as is the case for all samples, except #62, shown in Figure 3.17a. Sample #62 is suspected to have reoxidized after substrate etching, since it was positioned in the evacuated chamber for several days before we could start the Fe deposition. The latter was delayed as a result of technical problems.

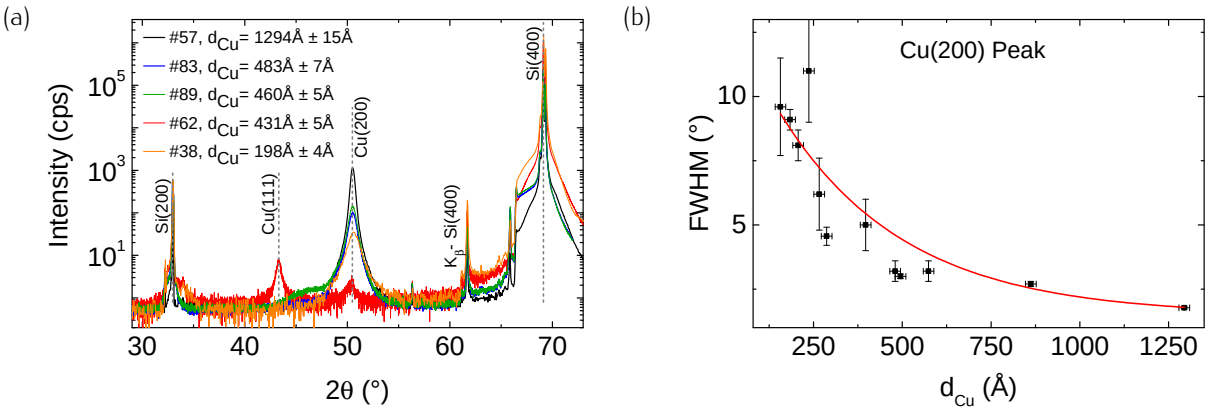

Fig. 3.17: *(a) Typical diffraction patterns obtained by θ-2θ-scans for Cu grown on Si(100). Sharp peaks correspond to the Si(100) substrate when measured with a Cu-K_α X-ray source. A Ni filter attenuates the K_β wavelength, which still generates Bragg peaks of the substrate as here for Si(400). If no Cu(111) Bragg peak is visible, epitaxial growth can be assumed. In contrast, sample #62 grew in a polycrystalline structure exhibiting both Cu peaks. (b) FWHM of rocking curves carried out at the 2θ value of the Cu(200) peak. The FWHM drops exponentially with increasing Cu thickness as indicated by the fit (red line) due to lattice relaxation.*

The etching time of 5% HF was expected to influence the epitaxy, but in a test series the etching times between 15 s and 3 min did not cause the appearance of the Cu(111) peak, with the exception of one sample that was etched for 2 min. No etching always resulted in the Cu(111) peak. In total, only 3 etched samples out of 37 showed the Cu(111) peak, one of them was sample #62. The other two cases cannot be explained and are suspected to be the result of an error in handling.

The small peak of #89 between both Cu peaks belongs to Fe and is discussed below. The Cu(200) peak position of the thinnest sample $2\theta = 50.63°$ is at a larger angle than the peak positions of the other three epitaxial samples of $2\theta = 50.52°$, which indicates strain. The calculation of the lattice constant parallel to the surface normal from the peak position using the Bragg equation results in $a = 3.603\,\text{Å}$ for sample #38 and $a = 3.610\,\text{Å} \pm 0.001\,\text{Å}$ for the other samples. Both values are 0.1–0.3% smaller than the lattice constant of bulk Cu with $a = 3.615\,\text{Å}$. From the Bragg peak's full width at half maximum (FWHM) in the range of 0.37°–1.12° and the peak position θ, the crystallite length along the sample normal can be estimated, as here for example for sample #57 using the Scherrer formula [93]:

$$L = \frac{K \cdot \lambda}{FWHM[rad] \cdot cos(\theta)} = \frac{1 \cdot 1.541\,\text{Å}}{0.37° \pi/180° \cdot cos(25.26°)} = 264\,\text{Å} \tag{3.1}$$

where K is the Scherrer form factor, which is ≈ 1, and $\lambda = 1.5406\,\text{Å}$ the Cu Kα wavelength of the X-ray source. The crystallite size for samples #38 ($d_{Cu} = 198\,\text{Å}$), #89 ($d_{Cu} = 460\,\text{Å}$), and #83 ($d_{Cu} = 483\,\text{Å}$) can be calculated to be 87 Å, 143 Å, and 133 Å, respectively. Thus, the samples contain crystallites of about 20–45% of the layer thickness, with the smallest crystallites occuring in the thinnest Cu layer and the largest in the thickest Cu layer.

Another method of characterizing the quality of the Cu growth is to perform rocking scans (Figure 2.2) at the Bragg angle of Cu(200) at $2\theta = 50.49°$. The FWHM of those rocking curves are plotted as a function of Cu thickness in Figure 3.17b. The FWHM drops from 9.6° exponentially to 1.8° as indicated by the fit (red line), with increasing Cu thickness from 157 to 1294 Å, which can be explained by the relaxation of the crystal structure with increasing thickness. Similar observations have been made in [20].

Fe layer. As well as the two Cu peaks, some XRD patterns already show a small additional peak corresponding to Fe. The Fe peaks of different patterns can be arranged according to two different peak widths. One peak shape has a FWHM smaller than 2.6°, shown in Figure 3.18a, and the other shape has a FWHM larger than 3.0°, shown in Figure 3.18b. Additionally, the Fe peaks in both figures are compared to the patterns of sample #97 with a pure Cu layer (black curve) and of sample #53 with a thick Fe layer of 160 Å (dark cyan curve). The Cu(200) peak is more intense than the Fe peak, while no evidence for a Cu(111) peak exists, suggesting epitaxial growth. The Fe peaks of Figure 3.18a are well separated from the Cu(200) peak, while the Fe peaks of Figure 3.18b coalesce with the Cu(200) peak. Two samples were measured at the diffractometer D500 instead of at the D5000, as noted in the legend. Sample #89 was measured at both instruments (Figure 3.18b). The pattern measured at the D500 shows two clearly separated peaks due to a better angular resolution. Apparently, the peak centers are at larger 2θ values than the Fe peak centers shown in Figure 3.18a. The Fe peaks of series 2 and 3 appear for $d_{Fe} \gtrsim 17$ Å, consisting of more than 9 monolayers (ML), while neither sample with $d_{Fe} \leq 15$ Å of series 2 and 3 show the Fe peak. The XRD patterns of series 1 were measured too fast, exhibiting a bad signal to noise ratio, such that a proper statement about the occurrence of the Fe(110) peak cannot be made. Sample #38, which is similar to series 1, does not show the Fe peak despite a thickness of $d_{Fe} = 22$ Å. During its *in-situ* measurement at REFSANS, the pumps of the chamber were accidentally shut off after sputtering the third Fe layer. Consequently, the pressure increased to a value of the order of 1 mbar, which almost certainly led to an oxidized Fe layer. Based on the discussions in Section 3.1, one would expect the growth of fcc Fe(100) up to the 10th monolayer for TD and PLD films and up to 16th ML for sputtered films, followed by bcc growth. Here, all Fe peaks are closer to the bcc Fe(110) peak, which indicates bcc structure and is, together with the observed thickness range, in good agreement with the literature. However, we did not find any indication of an fcc Fe(200) peak in the shape of the Cu(200) peak — neither for the films shown in Figure 3.18 nor for the thinner Fe samples. In contrast, Clemens *et al.* [68] found the shoulder of the Cu(220) peak increased with increasing Fe thickness, indicating fcc growth.

These patterns were fitted by a double peak to determine the exact Fe peak positions, plotted as a function of Fe thickness d_{Fe} in Figure 3.18c for the patterns of Figure 3.18a (cyan symbols) and for Figure 3.18b (red symbols). The peaks with the smaller FWHM have a peak center of $45.45° \pm 0.32°$, closer to the Fe(110) bulk value (blue dotted horizontal line), with the peak position shifting towards the bulk value for increasing Fe thickness. This implies less strain. The peak position at $46.70° \pm 0.08°$ of the broader peaks does not shift with

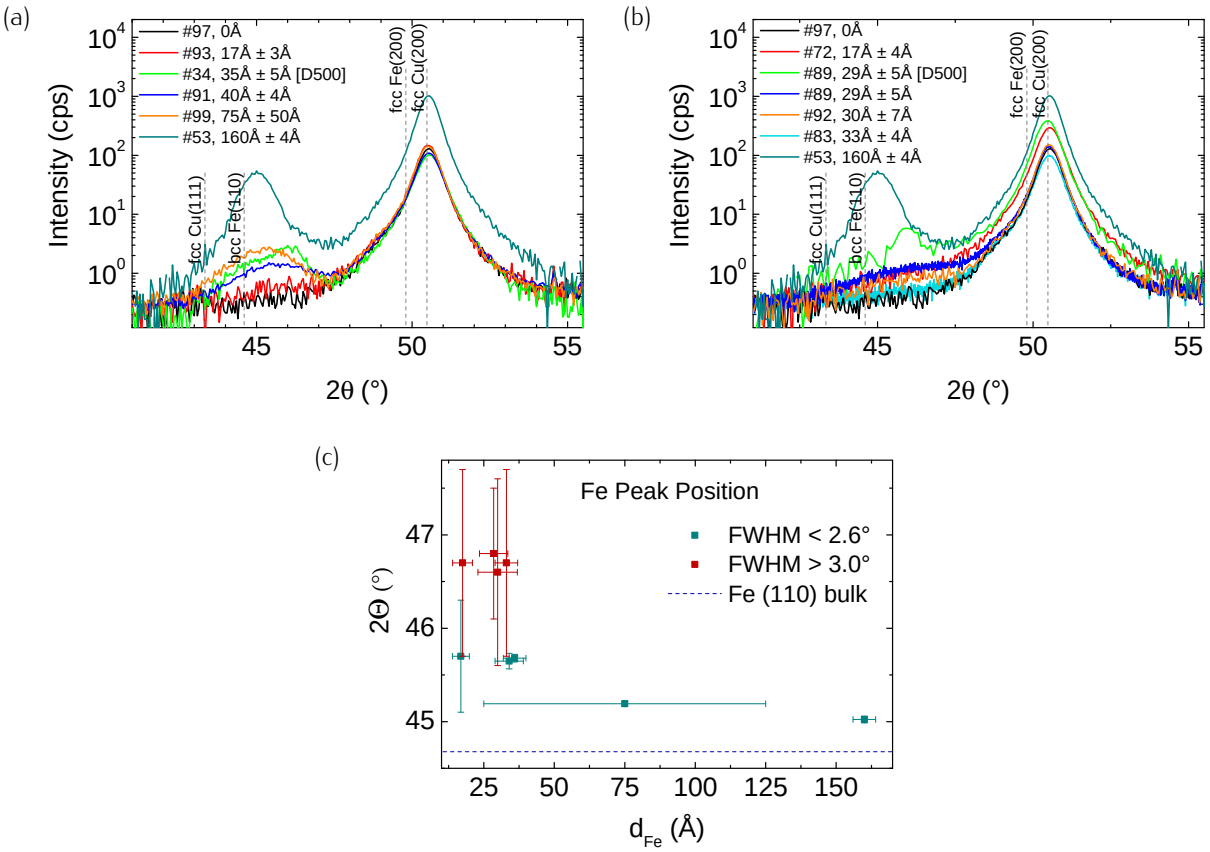

Fig. 3.18: *XRD patterns for samples with different Fe thickness (see legend) arranged by Fe peak width: (a) FWHM of Fe peak < 2.6°. (b) FWHM of Fe peak > 3.0°. Both figures also contain the patterns of #97 and #53 for comparison with no Fe layer and a very thick layer, respectively. All profiles exhibit an intense Cu(200) peak without the evidence of a Cu(111) peak. The Fe peaks from (a) are closer to the bcc Fe(110) peak than the Fe peaks from (b). Most of the XRD patterns were recorded using a D5000, but two samples were (additionally) measured at a D500 as labeled in the legend. The latter has better angular resolution, and one can even distinguish the Cu(200) and the Fe peak in (b). Figure (c) summarizes the Fe peak positions vs. Fe thickness extracted from fits of the patterns of (a) (cyan) and (b) (red), indicating two different growth modes existing in the same thickness range.*

thickness and occurs only in a small thickness range, possibly owing to too fewer data points. The large error bar of the sample with $d_{Fe} = 75\,\text{Å}$ is due to ambiguous fits.

It is apparent that both Fe peaks evolve in the same range of Fe thickness. Therefore, there are two different growth modes of bcc Fe(110) on Cu(100), with one growth mode being more strained than the other. From the mean peak position for both peak shapes using the Bragg equation, the lattice constant parallel to the surface normal can be calculated. This results in $a = 2.819\,\text{Å} \pm 0.019\,\text{Å}$ for the shapes with a FWHM $< 2.6°$ and in $a = 2.749\,\text{Å} \pm 0.005\,\text{Å}$ for the shapes with a FWHM $> 3°$. Compared to the bulk value of $a = 2.886\,\text{Å}$, the lattice

constant is reduced by 2.3% and 5.0%, respectively.

3.3.4 Off-surface XRD

Although we see strong indication for epitaxial growth in the out-of-plane configuration, where the scattering vector $\boldsymbol{Q}$ is parallel to the surface normal $\boldsymbol{n}$ and to the Cu<100>, we proved the epitaxy by performing so-called off-surface XRD measurements (Section 2.1.1) on sample #89 and #38 at a four-axis diffractometer. Here, the sample is aligned using the additional axis χ and φ such that $\boldsymbol{Q}$ is perpendicular to any sample plane instead of to the surface plane. For $\chi = 0°$, we measured in the out-of-plane configuration, while for $\chi \neq 0°$, we measured in the off-surface configuration. χ denotes the angle relative to the surface plane, while φ rotates around the surface normal (Figure 2.3). In the off-surface case, the axis of rotation of φ is not parallel to $\boldsymbol{Q}$. In cubic lattices, most of the planes exhibit a fourfold rotational symmetry with respect to the surface normal. Thus, φ can be used to align different equivalent planes.

Sample #89. Figure 3.19a compares the out-of-plane θ-2θ-scan ($\chi = 0°$) from Figure 3.17a with an off-surface θ-2θ-scan ($\chi = 54.74°$) for sample #89 measured with the D500 in the lower and upper panel, respectively. The latter was aligned such that $\boldsymbol{Q}$ is perpendicular to the Cu(111) planes, i.e. $\boldsymbol{Q}$ || Cu<111>. Consequently, the Cu(111) peak appears in the off-surface measurement, together with a Fe Bragg peak that could be interpreted as the Fe(110) peak. The residual peaks originate from the brass sample holder, which was replaced by a plexiglas holder immediately after this measurement to remove the disturbing brass peaks. The Fe(110) peaks of both scans appear at slightly different positions with $2\theta = 45.90° \pm 0.07°$ for $\chi = 0°$ and with $2\theta = 45.00° \pm 0.05°$ for $\chi = 54.74°$. The lattice constants can be calculated to be 2.794 Å ± 0.005 Å and 2.847 Å ± 0.003 Å, respectively, being reduced by 2.5% and 0.7% when compared to bulk bcc Fe. This result is higly questionable, since one would have expected from the Poisson ratio [94], that the lattice should be expanded in one direction when compressed in the other. Clemens *et al.* [68] also found a compression of the (200) and (110) off-surface lattice parameters of 2.80–2.86 Å for the Bain orientation, while the Pitsch orientation resulted in an expansion of the lattice. Further, according to the comparison of both measurements, the Fe(110) planes subtend an angle of $\chi \approx 55°$ with the surface plane instead of $\chi = 60°$, the expected value for a cubic lattice. Moreover, the Fe(110) peak corresponding to the Bain orientation should have been observed with $\chi = 45°$, since it would grow parallel to the Cu(100) surface.

To check this behavior, we performed χ-scans at the peak positions. These are plotted in Figure 3.19b for the Fe(110) peak that appeared in the out-of-plane measurement (lower panel) and for the Fe(110) peak that appeared in the off-surface measurement (upper panel) compared to χ-scan of the Cu(111) peak. The χ-scan of the Fe(110) peak corresponding to the out-of-plane measurement was measured at $2\theta = 45°$ by mistake and thus 0.9° from the peak center. However, the intensity was high enough, revealing a maximum at $\chi = 0° \pm 0.2°$, while

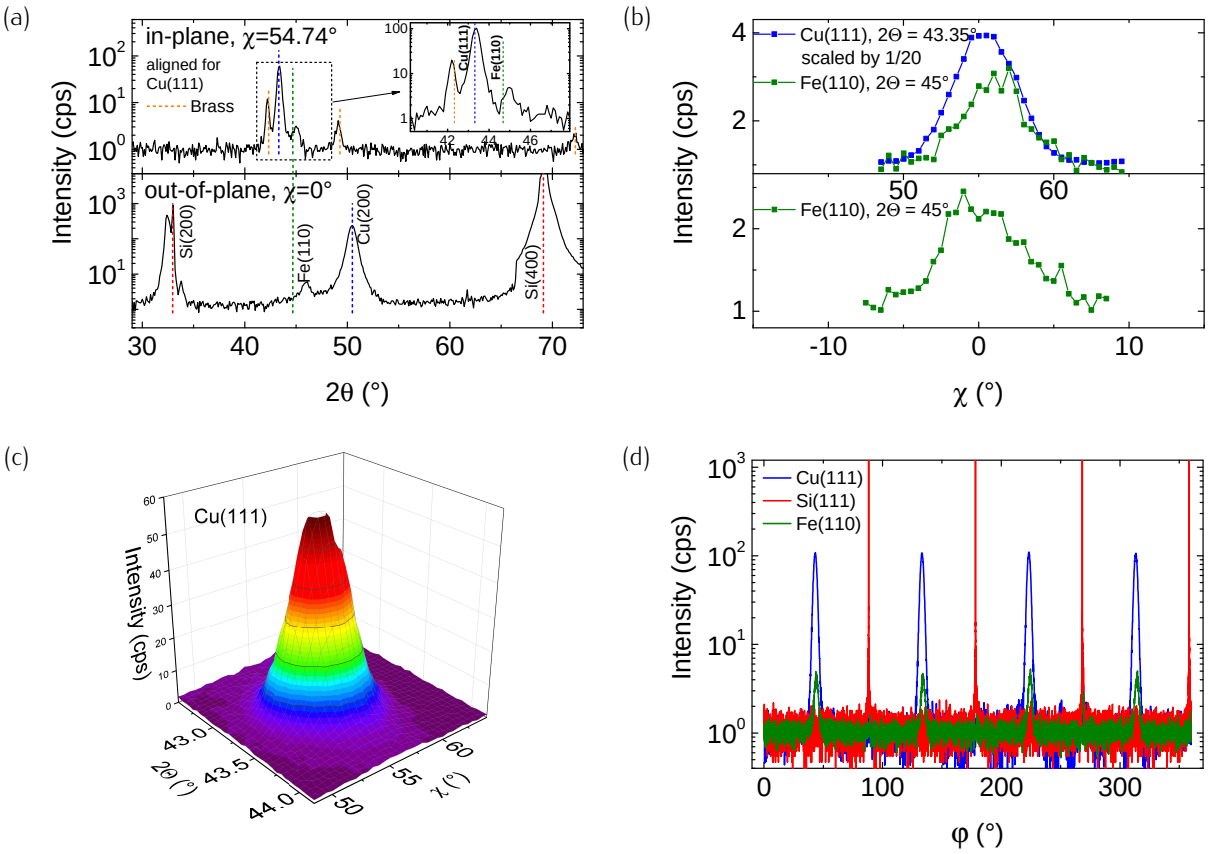

Fig. 3.19: *X-ray diffraction of sample #89 measured at the D500: (a) θ-2θ-scan with* $\boldsymbol{Q} \parallel \boldsymbol{n} \parallel$ *Si<400> (lower panel) and* $\boldsymbol{Q} \parallel$ *Cu<111> for φ = 45° (upper panel). (b) χ-scans of the Fe(110) peaks for (a) the out-of-plane peak (lower panel) and for the off-surface peak (upper panel), which is compared to the χ-scan of Cu(111). The latter peak was mapped for several χ and 2θ-values and is shown as 3D plot in (c). (d) φ-scans, i.e. a 360° rotation around the surface normal, when* $\boldsymbol{Q}$ *is perpendicular to Cu(111), Si(111), and Fe(110) but not perpendicular to the surface and hence not parallel to the axis of rotation. Every 90°, a plane is rotated into the Bragg condition.*

the off-surface (110) peak has a maximum at $\chi = 56.2° \pm 0.2°$. According to this determination, the Fe(110) planes subtend an angle of $56.2° \pm 0.4°$, which is still $\approx 4°$ smaller than expected for a cubic lattice. The corresponding angle in a tetragonal lattice can be calculated to 86° using a formula in [95] together with the measured lattice constants *a* and *c* of the off-surface and out-of-plane measurement. This is even farther from the measured value. Therefore, we still regard the Fe lattice as being cubic.

Note that the angle between (100) and (111) cubic planes is 54.7° and therefore close to the observed value of 56.2°. Since the (111) peaks are forbidden for a bcc lattice, this would imply the growth of fcc Fe(200) as surface plane, with the corresponding peak hidden in the Cu(200) peak. The peak appearing at $2\theta = 45°$ and $\chi = 56.2°$ could be attributed to the

fcc Fe(111) peak, which, for an unstrained structure, is expected to occur at $2\theta = 42.9°$. The strained lattice constant can be calculated with $2\theta = 45°$ to 3.4827 Å, which is 4% less than for unstrained fcc Fe. The out-of-plane Fe peak is likely the bcc Fe(110) peak, since it is expected that fcc Fe(200) grows cube on cube on Cu and not with a different lattice constant. This would suggest that both structures coexist, as was observed in [68] for sputtered films (Section 3.1.4)

A final interpretation of the off-surface data as strained fcc Fe or bcc Fe is difficult. Both corresponding lattice constants would be compressed perpendicular to the film, but by 4% and only 0.7%, respectively. Although this suggests a bcc structure, the bcc lattice would be compressed in plane and out of plane changing the Poisson ratio. Further, $\Delta\chi$ accords better to the fcc structure, being only 1.5° off, than to the bcc structure, being 5.2° off. In the following, I will refer to the peak as a bcc Fe(110) peak.

The Cu(111) peak has its maximum at $\chi = 55.3° \pm 0.05°$, which is the angle subtended by the Cu(200) and Cu(111) planes. This is a little in excess of the expected value of $\chi = 54.74°$. However, $\chi = 0°$ was determined by finding the maximum of the Si(400) peak, and no χ-scan was measured on the Cu(200) peak. By scanning χ and 2θ, the peak shape can be mapped as plotted in 3D in Figure 3.19c for the Cu(111) peak. The peak appears to be very symmetric in both angular directions.

Note that the Si(111) peak does not appear in the upper panel of Figure 3.19a, as the Cu grows at a 45° rotation to the Si substrate. To check this rotation, as well as the crystallinity of Fe and Cu, we performed φ-scans of the same sample (Figure 3.19d). In these scans, we aligned the sample to the corresponding θ, 2θ and χ values of a specific plane and rotated the sample around the surface normal by $\Delta\varphi = 360°$. As Cu and Si have a cubic lattice, the (111) planes possess fourfold rotational symmetry in respect to {100} directions, so one can expect a peak every 90° for a single crystal. Indeed, the 90° symmetry is observed in Figure 3.19d, with $\chi = 35.26°$ at $2\theta = 28.5°$ for Si(111), as well as with $\chi = 54.74°$ at $2\theta = 43.35°$ for Cu(111) and at $2\theta = 45.0°$ for Fe(110). The latter was rotated around the Fe surface normal <110>. There are no other peaks in between, thus we regard the Cu as monocrystalline. As expected, the Cu(111) peaks and the Si(111) peaks are separated by 45°. The φ-scan of Fe(110) also shows peaks only every 90°. This again suggests epitaxial growth.

Sample #38. Thomas Mairoser (Universität Augsburg) performed similar measurements on sample #38, which is suspected to have a pure Fe layer as well as an oxidized Fe layer. In the φ-scan of Figure 3.20a, this sample also shows Cu(111) peaks separated by 45° from the Si(111) peaks and by 90° relative to each other, indicating monocrystallinity.

Mairoser also recorded pole figures by scanning χ and φ, as shown in Figure 3.20b for $2\theta = 82.34°$ aligned for the bulk value of bcc Fe(221). As well as a peak at $\chi = 0°$, four peaks separated by $\Delta\varphi = 90°$ and at $\chi = 38.3° \pm 1.0°$ appear. This is far from the expected value of $\chi = 30°$ with the bcc Fe(110) as surface plane. Notably, the peaks exhibit

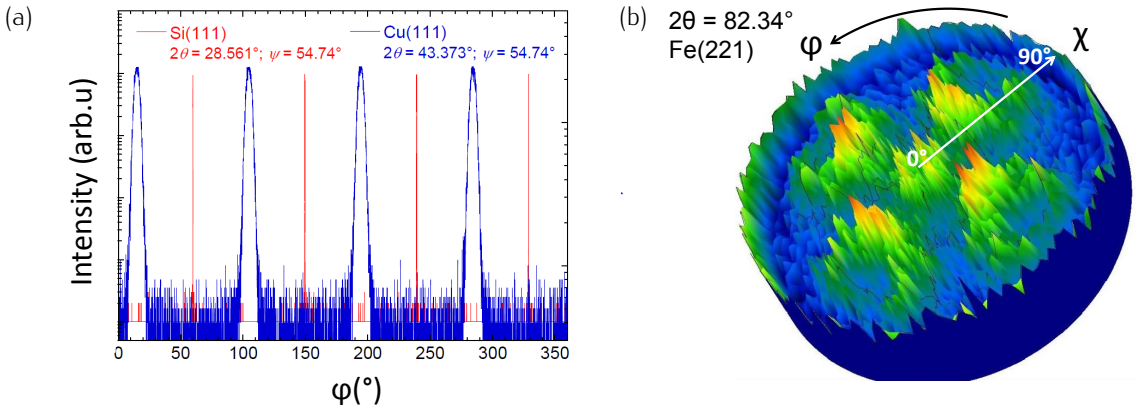

*Fig. 3.20: X-ray diffraction of sample #38 measured by Thomas Mairoser: (a) φ-scans, i.e. a 360° rotation around the surface normal, when **Q** is perpendicular to Cu(111) and Si(111), but not perpendicular to the surface. Thus, **Q** is not parallel to the axis of rotation. Every 90° the specific plane is rotated into the Bragg condition. (b) Pole figure aligned for bulk bcc Fe(221) with $2\theta = 82.34°$ recorded by scanning $0° < \chi < 90°$ and φ by 360°.*

symmetrically bent wings of less intensity with local maxima at $\chi = 61° \pm 3°$ separated by $\Delta\varphi \approx 19°$. This is reminiscent of the Pitsch orientation, with the two lateral peaks on each side of the bcc Fe(211) peak separated by $\Delta\varphi = 19.5°$ [55] (Section 3.1.2). However the χ-values of the main peaks and of the wings do not correspond to any expected bulk values. In addition, the fcc Fe peaks (311) and (220) separated from the Fe(211) peak by only $\Delta 2\theta = 6.6°$ and $\Delta 2\theta = 9°$, do not subtend similar χ angles with the fcc Fe(100) surface. The interpretation of the pole figure is limited, since it was not performed at the maxima 2θ-value but at the bulk value. The peaks may originate from the oxidized Fe layer. The peak at $\chi = 0°$ probably corresponds to the intensity of the flanks of the very intense Si(400) peak.

To investigate the appearance of the Fe(110) peak at $\chi \neq 0$ as shown for #89 in Figure 3.19a in the upper panel, a pole figure was recorded by Thomas Mairoser, shown in Figure 3.21a. Here, the sample was aligned to the bulk value of Fe(110) $2\theta = 44.68°$. Remember, this sample did not show a Fe peak in the out-of-plane diffraction pattern, as Fe oxidation probably resulted in a reduced thickness of pure Fe. However, this pole figure reveals four peaks separated by $\Delta\varphi = 90°$, which, with $\chi = 18.7° \pm 1.0°$, are very close to the out-of-plane direction. Additionally, four peaks appear with $\chi = 55.5°$, very close to $\chi = 56.2°$ observed in Figure 3.19a for sample #89. Here, the Fe(110) peaks are separated by $\Delta\chi \approx 37°$, far from the expected value of 60°, indicating the coexistence of two different structures. The peaks at $\chi = 18.7° \pm 1.0°$ would then correspond to fcc Fe(100) and the peaks at $\chi = 55.5°$ to the bcc Fe(110). However, in this case, assuming a correct alignment of the diffractometer, the fcc Fe(100) planes are not parallel to the surface. This is surprising, as we would expect parallel growth to Cu(100). If bcc Fe had grown in the Pitsch orientation, we would have observed side peaks similar to the (211) φ-scan. Again, we cannot exclude any contribution of the oxidized Fe layer. Moreover, as the scans were performed at the bulk 2θ-values, the

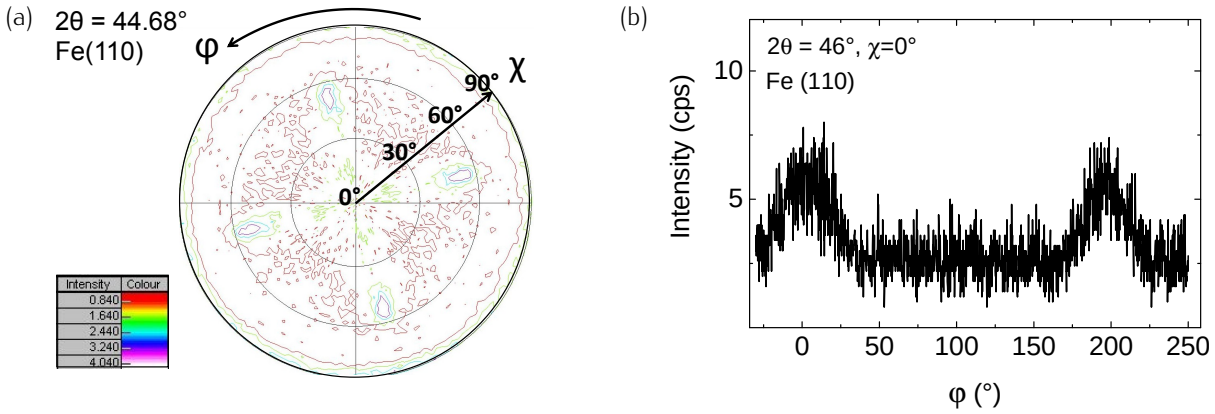

Fig. 3.21: *(a) Pole figure of Fe(110) of sample #38 with* $2\theta = 44.68°$ *recorded by scanning* $0° < \chi < 90°$ *and* φ *by* $360°$*. (b)* φ*-scans of Fe(110) of sample #89, i.e. again a* $360°$ *rotation around the surface normal, but here with* $\boldsymbol{Q}$ *parallel to the surface, where a constant peak intensity is expected. However, two peaks appear with* $\Delta\varphi = 196° \pm 3°$*.*

possibilities for a non ambiguous interpretation are limited.

Unfortunately, we did not record a similar pole figure for sample #89. However, we performed a φ-scan at $\chi = 0°$ for the out-of-plane Fe(110) peak of #89 (Figure 3.21b) and surprisingly found an oscillation of intensity. This means that the axis of φ-rotation was not exactly parallel to the surface normal, revealing an $196° \pm 3°$ asymmetry. As discussed above, those peaks could have the same origin as the peaks at $\chi = 18.7° \pm 1.0°$ of the Fe(110) φ-scan of sample #38 (Figure 3.21a). However, the peaks in the φ-scan of #89 are separated by $\Delta\varphi = 196° \pm 3°$ while the peaks in the φ-scan of #38 are separated by $\varphi = 90°$. This, together with the occurrence at different χ-values, indicates two different growth modes of Fe, if we assume that the oxidized Fe layer grew amorphously and does not contribute to the off-surface XRD peaks. Two growth modes have already been suggested from the pure out-of-plane XRD measurements. However, the growth modes identified by the off-surface and out-of-plane measurements cannot be correlated at this point. Note that mapping the reciprocal space by scanning the three angles 2θ, φ, and χ is very time-consuming. One pole figure, for example, took 57 h.

3.3.5 TEM

TEM images of the sample #38's cross-section were recorded by Fritz Philipp (Max Planck Institute for Intelligent Systems, Center for Electron Microscopy, Stuttgart). To apply this method, the sample has to be thinned to allow transparency for electrons. First, the sample surface was glued to a substrate to protect the surface during the preparation process. Then, the sample was sawed to obtain a small piece, which was mechanically thinned by grinding and subsequently milled by a FIB. An overview image at the lowest magnification can be

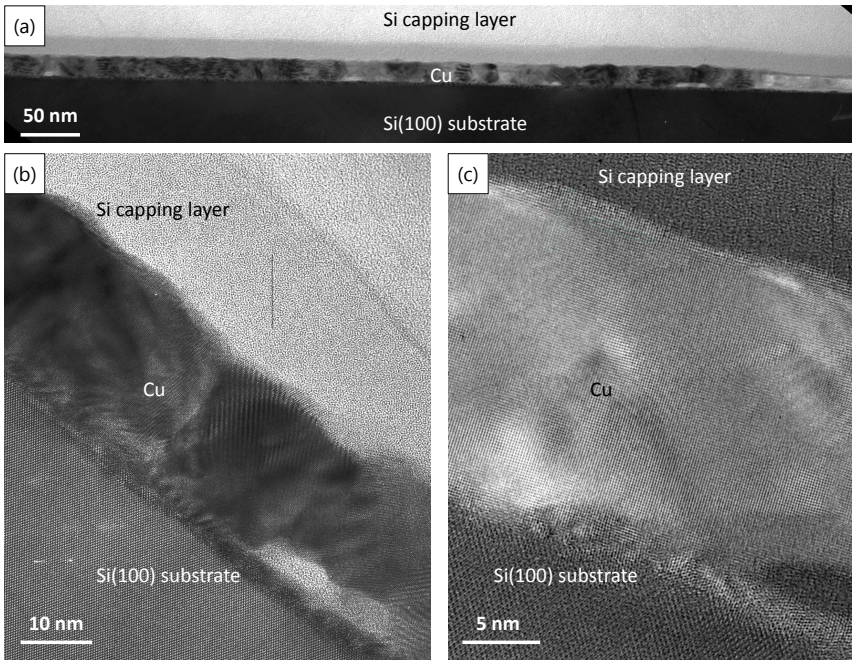

Fig. 3.22: *TEM images taken by Fritz Phillipp (MPI Stuttgart) of a cross-section of sample #38 with an overview image in (a) and recorded at higher magnifications in (b) and (c). The Fe layer cannot be distinguished from the Cu layer or the Si capping.*

seen in Figure 3.22a showing the sample cross-section, with the Si(100) as substrate (black), the Cu layer (textured layer) and the Si capping layer (dark gray). The Cu layer has many defects and appears to be almost polycrystalline, with a grain size of about the Cu thickness. However, the Cu(200) planes of each grain are always parallel to the Si(100) surface, while Si<110> || Cu<100> holds for the in-plane direction. The latter relation was also observed e.g. in [74] and is also in good agreement with our XRD φ-scan showing Cu growing at 45° rotation to the Si substrate. To observe the Fe or FeO layer, or a bilayer consisting of both materials with a total thickness of 22 Å ± 4 Å, the magnification was increased, as shown in Figures 3.22b and c. Different shades of gray within one layer are due to different sample thicknesses resulting from sample preparation. The thicknesses of Cu and Si fit very well to the thicknesses determined by XRR of $d_{Cu} = 198\,\text{Å} \pm 4\,\text{Å}$ and $d_{Si} = 215\,\text{Å} \pm 13\,\text{Å}$. In addition, the Cu roughness fit to the roughness determined by XRR of $\sigma_{Cu} = 10\,\text{Å} \pm 3\,\text{Å}$ corresponding to 5.5 ML Cu. However, no additional structure between the Cu layer and the Si capping is visible. For bcc Fe, Fritz Phillipp expected a strongly distorted non-quadratic unit cell containing dislocations. Instead, he found a pure projection of an fcc lattice along <100> with a quadratic unit cell up to the very last crystal plane indicating the growth of fcc Fe. However, XRD measurements (Section 3.3.4) cannot be interpreted as being ambiguous. They are more likely to indicate bcc Fe or at least a coexistence of fcc and bcc.

3.3.6 XANES

X-ray absorption near edge structure (XANES) spectroscopy was performed and fitted by Jaru Jutimoosik and Rattikorn Yimnirun (Suranaree University of Technology, Nakhon Ratchasima, Thailand) at the Synchrotron Light Research Institute (SLRI) in Thailand on Cu/Fe samples of series 1. The X-ray energy was scanned near the Fe K-edge energy from 7.1 keV to 7.2 keV. When the energy is high enough, the photon can be absorbed into the Fe K-shell followed by the emission of a photoelectron, which results in the strong increase of the X-ray absorbance at a critical energy, i.e. the K-edge (Figure 3.23). Since the X-ray energy in a XANES measurement is only some tens of eV higher than the K-level energy, the photoelectrons are slow enough to perform multiple scattering with the neighbor atoms. Multiple scattering resonances appear as peaks in the XANES spectrum. These are therefore a fingerprint of the local environment of the atom. For this reason, the XANES spectra of bcc and fcc Fe are different, as shown in the lower two calculated curves of Figure 3.23. The bcc Fe spectrum has one sharp peak directly after the K-edge at 7131 eV. Around that energy, the Fe fcc spectrum has a double peak and an additional peak at 7159 eV. The spectrum of the bcc Fe foil has less pronounced peaks, but still shows the characteristic peak at 7131 eV. Both values are marked via a vertical dotted line for comparison with other spectra. The spectra of sample #42–45 and of #38 are fitted using a composition of both the fcc and bcc spectra together with the spectra from FeO, as the Fe layer of #38 is suspected to be oxidized. The fits are drawn as thick solid lines.

Indeed, sample #38 looks distinctly different from the other samples, but similar to the spectrum of FeO. Both spectra have an even more pronounced and broader peak at 7131 eV than the bcc Fe spectrum, followed by a second smaller

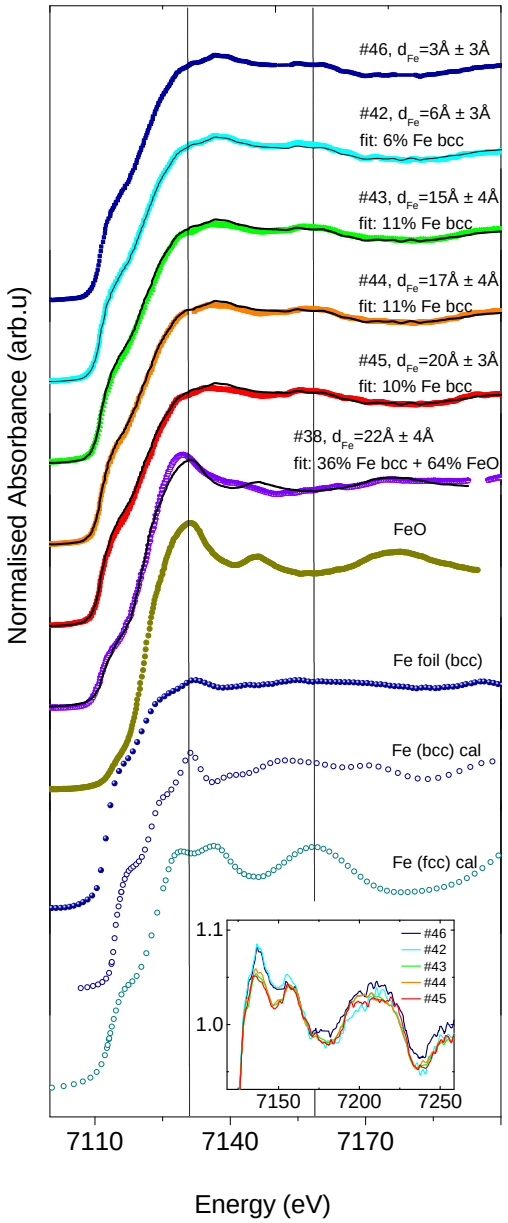

Fig. 3.23: XANES spectra measured and fitted by J. Jutimoosik and R. Yimnirun (Suranaree University of Technology, Nakhon Ratchasima, Thailand) of sample series 1 and compared to FeO, fcc Fe, and bcc Fe. A zoom of the spectra of series 1 is plotted for a direct comparison in the inset.

peak around 7143–7146 eV and another very broad peak at 7174–7177 eV. This sample was fitted to contain 64% of FeO and 36% of bcc Fe. As it can be seen from the inset, the spectra of the two thinnest samples #46 and #42 with d_{Fe} = 3 Å and 6 Å are very similar and are different from the spectra of samples #43–45 with d_{Fe} = 15–20 Å, indicating a structural change at a thickness between d_{Fe} = 6–15 Å. The amount of bcc Fe was fitted for sample #42 to be 6%, while the samples #43–45 were fitted to be 10–11%. The residual 94% of sample #42 was fitted to be fcc Fe, while the residual 89–90% of samples #43–45 was either fitted to be fcc Fe or a mixture of 5–7% FeO and 83–85% fcc Fe.

Both assumptions reveal similar good results. However, we do not expect the formation of FeO for samples #43–45 of series 1. The high amount of fcc Fe is also in contradiction with the clear bcc Fe structure observed in the out-of-plane XRD measurements of sample series 2 and 3. Unfortunately, due to the bad signal to noise ratio of the XRD measurements of series 1, which are not presented in this thesis, we are not able to compare the XRD patterns directly with the XANES results. It would be interesting to repeat those measurements. Since, the calculated spectrum of bcc Fe differs strongly from the measured spectrum of the bcc foil, we assume that the calculated fcc spetrum also differs from the measured fcc spectrum. Further, the spectra of a stressed film may probably deviate from the spectra of a relaxed fcc and bcc structure used for fitting. In contrast, the interpretation of XANES measurements of sputtered polycrystalline Fe/Cu multilayers found in [69] are very clear, since the spectra reproduce the Cu foil (fcc) and Fe foil (bcc) spectra very well. Therefore, our results of the fits should be handled with care. Nevertheless, this XANES measurement revealed a clear structural change between d_{Fe} = 6–15 Å, which is visible without fitting, and proved the oxidation of sample #38.

3.3.7 Summary

In this section, I showed that we can grow epitaxial Cu and Fe layers on Si(100) substrates. The Si(100) substrates were etched with 4–5% HF for 60 s to remove the SiO_2 layer and passivate the surface with covalently bound H atoms. This ensured stability for at least for several minutes (Section 3.3.1). Cu(100) was sputtered as a seed layer, followed by Fe, and by Si as a protective capping layer. For this purpose, the sputtering chamber (Section 3.2.1) was used, which was specifically designed to perform *in-situ* neutron reflectometry. We sputtered three sample series, each consisting of samples with different Fe thicknesses, for *ex-situ* characterization. The third series was sputtered after upgrade 2 (Section 3.2.1). This upgrade comprised the improvement of the base pressure and a new sample position, resulting in an increased sputtering rate by a factor 1.3–2.0. Accompanying upgrade 2 was the decision to sputter with a fully open valve position. XRR measurements revealed rates of 0.76 Å/s or 0.99 Å/s for the first two sample series and 1.27 Å/s for the third series (Section 3.3.2).

XRD measurements showed that Cu(100) and Fe grew epitaxially on the Si(100) substrate (Section 3.3.4). The lattice structure of Cu relaxed from d_{Cu} = 157 Å to d_{Cu} = 1294 Å

exponentially, which was evident in the reduction of the FWHM of the rocking curves of the Cu(200) peak from $\Delta\theta = 10°$ to $\Delta\theta = 2°$ (Section 3.3.3). The size of the Cu crystallites of $d_{Cu} = 198–483\,\text{Å}$ was determined to be 20–45% of the Cu thickness.

We observed the growth of bcc Fe(110) parallel to the surface for films with $d_{Fe} \geq 17\,\text{Å}$ (Section 3.3.3), which is in excellent agreement to Clemens *et al.* [68] (Section 3.1.4). The corresponding Fe peak exhibited either a FWHM$< 2.6°$ or FWHM$> 3.0°$, with a lattice constant of (2.819 ± 0.019)Å enlarged by 2.3% and (2.749 ± 0.005)Å enlarged by 5.0%, respectively. Sample #89 with $d_{Fe} = 29\,\text{Å} \pm 4\,\text{Å}$ was investigated in more detail by performing off-surface diffraction scans (Section 3.3.4). Here, we found a peak of epitaxially grown Fe, which can be assigned to either the bcc Fe(110) or the fcc Fe(111) plane. The plane subtends an angle with the surface plane of $\Delta\chi = 56.2°$. This angle is very close to 54.7°, which is the expected angle for a (111) plane with a (100) surface, indicating fcc, compared to 60° for a (110) plane with the (110) surface. However, we derived from the 2θ-value that the fcc lattice constant would be reduced by 4°, while the bcc lattice constant would be reduced by only 0.7°. Since fcc Fe is expected to grow cube on cube on Cu with a (100) surface (Figure 3.10), it is hard to measure the Fe peak in the out-of-plane direction where it coincides with the Cu peak. If the off-surface Fe peak really corresponds to the fcc structure, than both structures coexist, as the bcc Fe(110) peak was observed to be out of plane. This would be in very good agreement with Clemens *et al.* [68] (Section 3.1.4).

Although no Fe peak was visible in the out-of-plane scan of sample #38 ($d_{Fe} = 22\,\text{Å} \pm 4\,\text{Å}$), an off-surface Fe peak was found at very similar χ and 2θ value as for sample #89. The missing bcc Fe(110) out-of-plane peak could be explained by an FeO layer reducing the effective Fe thickness, which probably formed during an accidental shut down of the pumps. Pole figures revealed another peak at $\chi = 18.7°$, which could be attributed to the bcc Fe(110) growing tilted and not parallel to the surface. A contribution of the oxidized Fe layer cannot be excluded. The interpretation of the pole figure of Fe(211) is even more complicated. There are hints at an Fe Pitsch structure (Section 3.1.2), but the χ-values of the peaks cannot be attributed to specific planes. However, both pole figures were recorded at the 2θ values of bulk bcc Fe, which limits the potential of correct interpretation.

In contrast, TEM images of the very same sample show a pure fcc structure up to the amorphous Si capping layer, where the Fe structure cannot be distinguished from the Cu or the Si layer (Section 3.3.5). Fits of XANES spectra to this sample reveal that, in contrast to the TEM result, the Fe layer is oxidized by 64%, while 36% is bcc (Section 3.3.6). However, as the spectrum of the FeO seems to dominate the fit and the spectra of fcc and bcc are more similar, it is conceivable that a larger amount of the fcc phase could give an equally good fit result.

The other samples of sample series 1 investigated by XANES appeared to have 6% bcc for $d_{Fe} = 3\,\text{Å}$ and $d_{Fe} = 6\,\text{Å}$ and for $d_{Fe} \geq 15\,\text{Å}$ 10–11% bcc. The residual 94% of the 6 Å Fe layer was fitted to be fcc Fe, while the residual 89–90% of layers with $d_{Fe} \geq 15\,\text{Å}$ was either fitted to be fcc Fe or a mixture of 5–7% FeO and 83–85% fcc Fe.

From the XANES results, one may more likely interpret the XRD results of the off-surface Fe peaks of sample #89 as fcc peaks. However, note that this sample was sputtered after upgrade 2, which may have altered the growth conditions. Also the XANES fits may not be very reliable. Independently of the fits, the spectra clearly changed between 6 and 15 Å, featuring a structural change in this regime. Although, here, the bcc portion increased only from 6 to 10%, remaining constant until $d_{Fe} = 22\,\text{Å} \pm 4\,\text{Å}$, the structural trend is in agreement with the out-of-plane XRD measurement of sample series 2 and 3: the bcc phase was evident for $d_{Fe} \geq 17\,\text{Å}$.

3.4 Magnetic Characterization

So far, we have investigated the structural properties of sputtered Fe/Cu thin films. From Section 3.1, we know that those properties correlate strongly with the magnetic properties. With the aim of performing *in-situ* experiments using PNR to monitor the structural and magnetic properties simultaneously and during growth, we first performed *ex-situ* magnetization measurements to gather an idea of the correlation of magnetism and structure. This will serve as a starting point for the understanding of the magnetic characterization performed by PNR presented in Section 3.5.

I will present the SQUID measurements of sample series 1 in Section 3.4.1 and the XMCD measurements of sample series 3 in Section 3.4.2. These will then be summarized in Section 3.4.3 and compared with the polarized neutron-scattering experiments in Section 3.5.5 at the end of this chapter.

3.4.1 SQUID

Some magnetization measurements of sample series 1 performed by Thomas Mairoser (Universität Augsburg) using a SQUID are presented in Figure 3.24. All measurements performed on this series can be found in [77]. The substrate, the sputtered layers and the sample holder contribute to a diamagnetic signal, which needs to be subtracted to reveal the ferromagnetic signal. The magnetic signal was therefore subtracted by a background measured for sample #32, which consisted of no Fe layer, but of a Cu layer and a Si capping layer.

Figures 3.24a and 3.24c show the hysteresis curves at 10 K for the magnetic field aligned out of plane and in plane, respectively. Despite background subtraction most of the curves still had an additional diamagnetic slope, which sometimes appeared to be different in different field regions. An additional diamagnetic signal can occur as a result of to a small sample misalignment or a deviation of the substrate signal from the reference sample. To subtract this additional slope, one has to identify a clear hysteresis loop in the data to distinguish the diamagnetic from the magnetic signal. The curves of Figure 3.24a are subtracted by

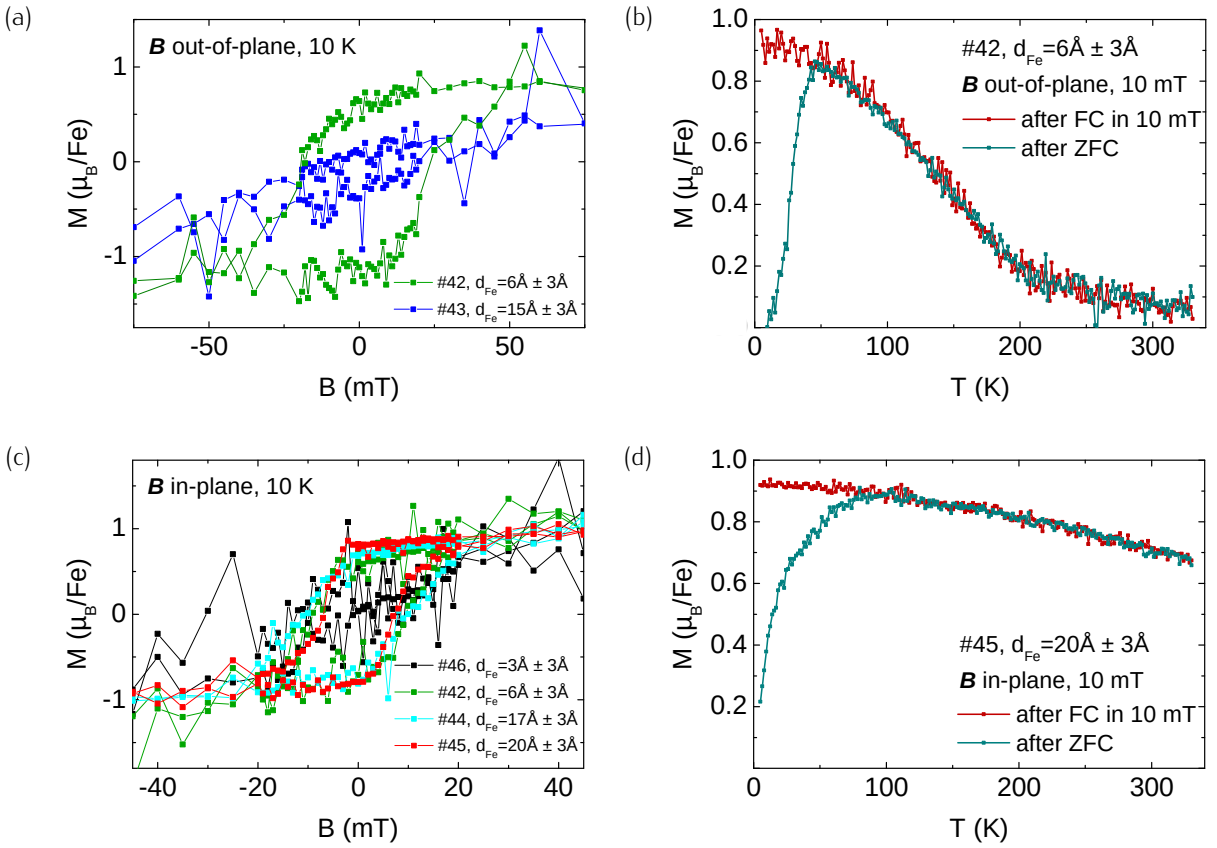

Fig. 3.24: *Magnetization of sample series 1 measured by Thomas Mairoser (Universität Augsburg) vs. magnetic field $\boldsymbol{B}$ at 10 K (left) and vs. temperature at 10 mT after FC and ZFC (right). Measurement of (a) and (b) are performed with the magnetic field aligned out of plane, while the curves of (c) and (d) are measured in an in-plane field. (adopted from [77])*

an additional diamagnetic signal, such that the saturation magnetization remains constant directly after closure of the hysteresis loop and at least for some tens of mT. The saturation coincides with the measurement for an in-plane field, indicating correct data treatment. The saturation magnetization can be estimated to be $0.9 \pm 0.1 \mu_B$/Fe for all curves. This is much lower than the bulk value of bcc Fe of $2.2 \mu_B$/Fe, which may be due to island growth or a mixture of fcc and bcc structures, as discussed in Section 3.1.

The thinnest Fe layer of sample #46 is either non-magnetic, showing just an additional diamagnetic background, or superparamagnetic, showing a remagnetization process of independent domains, i.e. islands. The next thinnest layer of sample #42, with $d_{Fe} = 6$ Å, already has a clear hysteresis loop for both field configurations. Here, the in-plane hysteresis has a much smaller coercive field of $H_c = 9.2\,\text{mT} \pm 0.3\,\text{mT}$, indicating an easy plane compared to the out-of-plane hysteresis with $H_c = 19\,\text{mT} \pm 2\,\text{mT}$, indicating the hard axis. Sample #43 with $d_{Fe} = 15$ Å shows a similar coercive field in an out-of-plane field but has a much larger saturation field of $H_s \approx 100$ mT (not shown), compared to #42 with $H_s = 50\,mT$. The

hysteresis of samples #44 and #45 in an in-plane field is very similar to the hysteresis of #42, with a saturation magnetization of (0.8±0.1)μ_B/Fe at $H_s = 20\,\mathrm{mT} \pm 2\,\mathrm{mT}$. Marco Halder conducted a similar measurement of a very thick amorphous Fe layer of 640 Å at the VSM. Here, we determined $H_c = 5.9\,\mathrm{mT}$ and $H_s = 7.2\,\mathrm{mT}$. Both values are even smaller than the values of sample series 1 indicating that the thicker the Fe layer, the more easily Fe can be magnetized along an in-plane direction. This can be also seen in Figure 3.24c, where the thickest Fe layer (#45) has the smallest coercive fields.

The missing data of samples #44 and #45 in an out-of-plane field and #43 in the in-plane field did not show a clear ferromagnetic signal. These Fe films cannot be magnetized along the corresponding direction or have a superparamagnetic magnetization curve with no or very little hysteresis [96] that is hard to distinguish from any diamagnetic contribution. Another explanation may be the growth of non-magnetic fcc Fe or a sample misalignment during the measurement.

The magnetization measurements as a function of temperature are compared after zero-field cooling (ZFC) and field cooling (FC) for the 6 Å film in 10 mT aligned out of plane (Figure 3.24b) and for the 20 Å film in 10 mT aligned in plane (Figure 3.24d). The figures show the superparamagnetic blocking temperature T_B, which is defined as the temperature of the first coincidence of both curves, with $T_B = 46 \pm 2\,\mathrm{K}$ for #42 in an out-of-plane field and $T_B = 95 \pm 4\,\mathrm{K}$ for #45 in an in-plane field. The occurrence of $T_B \neq 0$ is evidence of superparamagnetism, indicating that both films are discontinuous, probably growing as islands [77]. For $T < T_B$, the net magnetization after ZFC is much smaller than after FC. This indicates that the domains associated with the islands are not correlated: After ZFC, the magnetization of the domains was frozen randomly in the zero field, with the thermal energy too low to align all the spins parallel to the field [97]. By increasing the temperature, the thermal fluctuations increase, allowing the spins to align along the field, resulting in the increase of magnetization. T_c can be estimated to be $> 330\,\mathrm{K}$ for sample #45 and to $230\,\mathrm{K} \pm 15\,\mathrm{K}$ for sample #42 [77], which is the only sample with the evidence for a T_c smaller than room temperature.

Thomas Mairoser also investigated the *in-situ*-measured samples #38 and #62, but did not find a magnetic signal, although PNR measurements of #62 definitely show a ferromagnetic signal (Section 3.5.2). The PNR measurements of #38 also show a ferromagnetic signal based on first data interpretations performed by Wolfgang Kreuzpaintner.

3.4.2 XMCD

X-ray magnetic circular dichroism (XMCD) measurements on samples from series 3 were performed by Amitesh Paul at the synchrotron BESSY in Berlin. Here, one probes the absorption of X-rays with energies around the Fe L-edge for left circular (LCP) and right circular polarization (RCP) by measuring the total photoelectron yield. The absorption of both polarizations depends on the direction of the magnetization. Consequently, the difference in

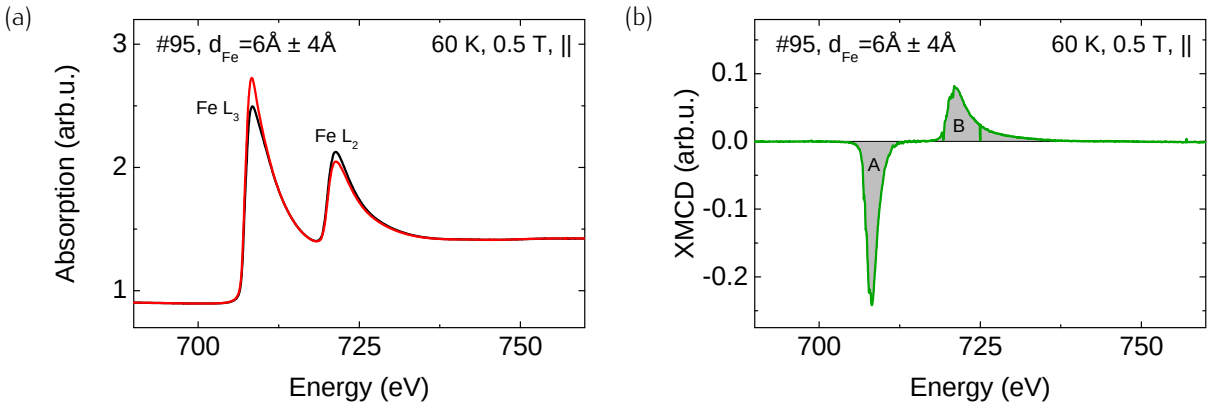

Fig. 3.25: *(a) Absorption spectra for LCP and RCP of X-rays at the Fe L-edges as a function of X-ray energy measured for sample #95 at 60 K in a 0.5 T in-plane field. The spectra exhibits high absorption at the energy of the Fe L_3 and Fe L_2 edge. (b) Difference of the spectra shown in (a). The integrated areas (gray) in the difference spectra are indicated as A and B at the Fe L_3 edge and Fe L_2 edge, respectively.*

absorption between LCP photons and RCP photons reveals the magnetic signal.

Figure 3.25a shows two typical absorption spectra as a function of photon energy. The first and second peaks are the Fe L_3- and L_2-edges for sample #95 at 0.5 T and 60 K. The absorption spectra of LCP and RCP are distinctly different. The difference of both spectra, is plotted in Figure 3.25b. The ratio of orbital and spin magnetic moment can be calculated by [98]

$$\frac{m_l}{m_s} = \frac{2}{3}\frac{A+B}{A-2B} \quad , \tag{3.2}$$

where A and B are the areas of the difference spectra, i.e. the XMCD signal, as shown in Figure 3.25b. This quantity is easiest to determine from XMCD, since it is independent of the degree of polarization and of the number of d-holes in the material [98]. In contrast, these parameters are necessary to determine m_l and m_s, directly.

However, since the error bars are huge, resulting in a negative m_l/m_s for sample #96, and we are not that interested in the m_l/m_s value anyway, it is sufficient to determine the areas A and B as a evidence for ferromagnetism. Figure 3.26 shows the absolute values of the areas A and B for sample #96, #95 and #92 with Fe thickness of 3 Å ± 3 Å, 6 Å ± 4 Å and 30 Å ± 7 Å. Note, the area A is positive and the area B is negative. A (open symbols) and B (filled symbols) are plotted as a function of temperature for an in-plane and an out-of-plane field of 0.5 T. Both areas are non-zero at low temperature for all three samples for the in-plane field as well as for the out-of-plane field, which is evidence for a magnetization in both directions. The areas decrease towards zero at 300 K for the two thinnest Fe layers of 3 and 6 Å, indicating $T_c <$ RT. In contrast, sample #92 with a Fe thickness of 30 Å shows almost constant areas as a function of temperature. This sample has therefore a $T_c >$ RT.

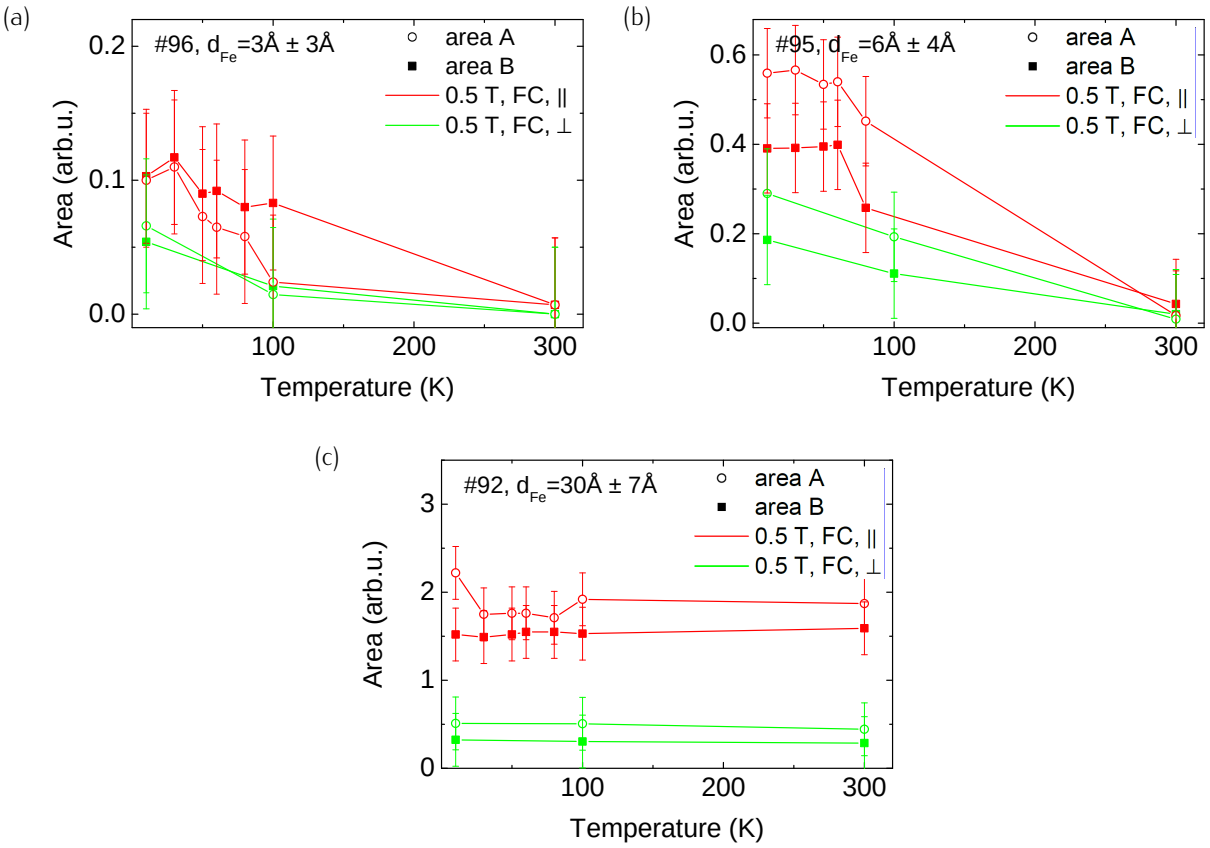

Fig. 3.26: *Area A and B of the difference spectra (shown in Figure 3.25b) as a function of temperature with an in-plane and out-of-plane field of 0.5 T for three samples of series 3: (a) #96, (b) #95, and (c) #92.*

A T_c smaller RT has been determined for a 6 Å sample by SQUID measurements of sample series 1, too, and a 20 Å sample exhibited a T_c larger than RT.

3.4.3 Summary

From the SQUID measurements of sample series 1 presented in Section 3.4.1, we found a region ranging from at least 6 to 15 Å, where the Fe layer could be magnetized in plane as well as out of plane. The latter was the hard axis. Therefore, this region is reminiscent of the intermediate phase for the PLD-grown films of between 5 and 7 ML (Section 3.1.4).

The in-plane hysteresis loops for Fe layers with 6–20 Å were very similar, with a saturation magnetization of $(0.8 \pm 0.1)\mu_B$/Fe for $H > 20$ mT. Compared to the bulk bcc Fe value of $2.2\mu_B$/Fe, the observed magnetization was reduced by almost a factor of 3, which indicates the existence of a large portion of fcc Fe as was suggested from XANES (Section 3.3.6) performed on the same sample series. From these data, we also determined a structural

change between 6 Å and 15 Å. The hysteresis loops of both samples were also different in an out-of-plane field: the thinner Fe layer was much harder to magnetize in this direction than the thicker Fe layer. Sample series 2 and 3 may have different structural and magnetic properties. From the very pronounced out-of-plane bcc Fe peak observed in XRD (Section 3.3.3), we would have expected a magnetic moment similar to that of bulk.

Magnetization measurements as a function of temperature compared after FC and ZFC revealed a blocking temperature of 45–100 K for a 6 and a 20 Å Fe film, which is a fingerprint of superparamagnetism, indicating the films to be discontinuous. From the measurements, we determined $T_c \approx 230\,\mathrm{K} < \mathrm{RT}$ for the 6 Å film. This was confirmed by XMCD measurements in Section 3.4.2, where a 3 and 6 Å Fe film exhibited $T_c < \mathrm{RT}$. In contrast, a 20 and a 30 Å Fe film had a T_c larger than RT, which was determined by SQUID and XMCD, respectively.

3.5 *In-situ* Polarized Neutron Reflectometry

As discussed in Section 3.1, the evolution of the magnetic and structural properties of Fe deposited on Cu(100) is very complex and is a function of thickness and growth conditions. It is therefore of tremendous advantage to monitor these properties directly during growth, since then several measurements at different thicknesses can be performed on just one sample with no need for the very time-consuming preparation of several samples with different thicknesses. More importantly, each change in property can be directly attributed to the newly added Fe layer ruling out the influence of, e.g. varying properties of substrate or seed layer from sample to sample, surface oxidation or pollution. Furthermore, every Fe layer can be sputtered at the very same sputtering conditions, i.e. room temperature, base pressure, or Ar pressure. This was not always feasible for the growth of the sample series introduced in Section 3.3.1 used for *ex-situ* characterizations, thus, excluding a unique interpretation of the data. Therefore, we performed *in-situ* PNR measurements using our mobile sputtering chamber, which was installed at the neutron beamlines. The basics of PNR were introduced in Section 2.2.2. More special techniques, including the sputtering chamber and the Selene setup realized at the Amor beamline, are described in Section 3.2.

In this section, I will summarize the *in-situ* experiments at REFSANS (FRM2, Garching, Germany) and at Amor (PSI, Villigen, Switzerland). I will present the setup of the beamline REFSANS in Section 3.5.1 followed by the results of the two samples #38 and #62 measured *in-situ* at REFSANS in Section 3.5.2. The setup of the beamline Amor is described in Section 3.5.3. In Section 3.5.4, the results of the two samples #83 and #89 measured *in-situ* at Amor will be discussed. In the final section (Section 3.5.5), the results are summarized and compared to the results of Section 3.3 as well as to literature.

3.5.1 Setup and Data Acquisition at REFSANS

To perform polarized neutron reflectometry on Fe thin films during growth, we installed the sputtering chamber at the sample position of the horizontal reflectometer REFSANS at FRM2 in February 2012 and August 2012. Sample #38 and #62 were grown during the first and second beamtime, respectively. In the following section, I will present the setup used at REFSANS and introduce the sputtering and data acquisition process.

Setup. The neutrons are transported from the moderator to the instrument via the neutron guide NL 2b (Figure 3.27). REFSANS is operated in the TOF mode. Inside the neutron guide, the wavelength band of typically 2–14 Å and the wavelength resolution (1% for sample #62 and 5% for sample #38) is selected by the number of revolutions per second and the position of the master (MC) and slave chopper (SC). The neutrons leave the evacuated neutron guide, pass the polarizer and the spin flipper. In the first beamtime we used a ^{3}He cell as a polarizer, the polarization of which can be flipped. In the second beamtime, we used a polarizing supermirror as polarizer in combination with an RF spin flipper. The polarized neutrons enter the chamber through the entrance window, which is additionally shielded with a Cd foil to define the beam laterally. The divergence of the beam is confined vertically by the slits B1 inside the neutron guide and B2 at the end of the neutron guide, as well as by the internal slits of the sputtering chamber B3 directly in front of the sample. Additionally, B2, the Cd foil, B3 and B4 was used to reduce the background. The total path from the polarizer to the sample is supported by magnetic guide fields to prevent depolarization of the neutrons, which are realized by external as well as internal iron yokes. The sample itself was

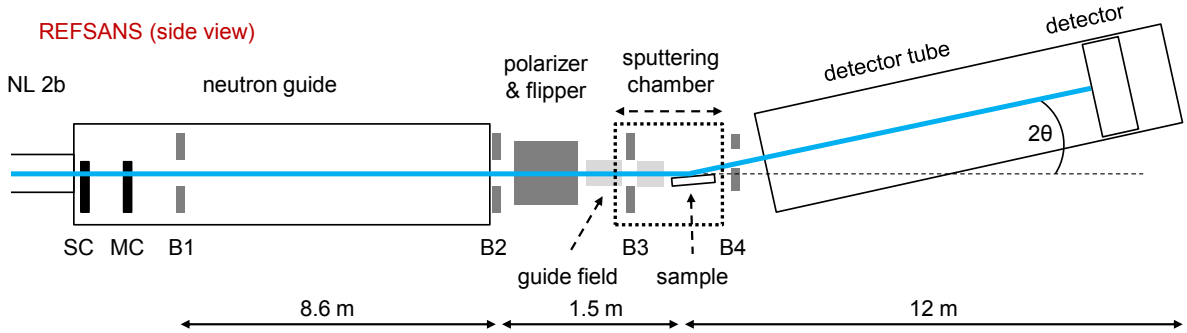

Fig. 3.27: Diagram of the setup at REFSANS as a side view. From the NL 2b neutron guide, the neutron beam passes the slave (SC) and the master chopper (MC). Afterwards the neutrons pass through the slits B1 and B2, the polarizer, and the flipper to enter the chamber. The neutron beam is defined by the internal slits B3 and is reflected from the sample. Yokes provide the polarization from the polarizer to the sample. The neutron beam exits the chamber again, passes the slit B4 and is detected by the detector. The neutron guide and the detector vessel are evacuated to reduce diffuse scattering. θ is determined by the sample tilt, while 2θ is determined by lifting the total detector vessel.

magnetized by applying a current of 12–22 A to the Helmholtz coils, giving rise to a magnetic field of 29 mT. After the beam is reflected by the sample, it exits the chamber through the exit window. The external slits B4, moving vertically and mounted on the chamber frame directly after the exit window, can block the direct beam. The neutrons enter the evacuated detector vessel and fly to the 2D (500 x 500) mm^2 multiwire ^{3}He detector [99], which can be positioned at between 2 and 12 m to change the angular and the wavelength resolution. The angle of incidence θ is controlled by the sample table of the sputtering chamber, while 2θ can be changed by lifting the whole detector vessel.

Figure 3.28 shows photos of the beamline with the sputtering chamber installed. The lefthand photo looks towards the neutron source. The neutron beam exists the green wall on the left, is defined by the slit B2 and passes the He^3 polarizer before it enters the sputtering chamber (center). The neutron beam is reflected from the sample surface and exits the chamber again. The beam passes slit B4 and arrives at the detector vessel on the right. The righthand photo shows a view towards the detector. The polarizer is visible in the foreground, followed by the chamber and the detector vessel. The red crane in the back, can lift the total detector vessel to align 2θ. The gas rack is positioned close to the chamber.

Sputtering process. We performed similar measurements during two beamtimes, growing sample #38 and sample #62, respectively. The Cu(100)/Fe samples were prepared as discussed in Section 3.3.1 with the sputter procedure and conditions summarized in Table 3.2, where the Fe layer was sputtered in several steps. The thickness of each layer is controlled via the opening time of the sample shutter.

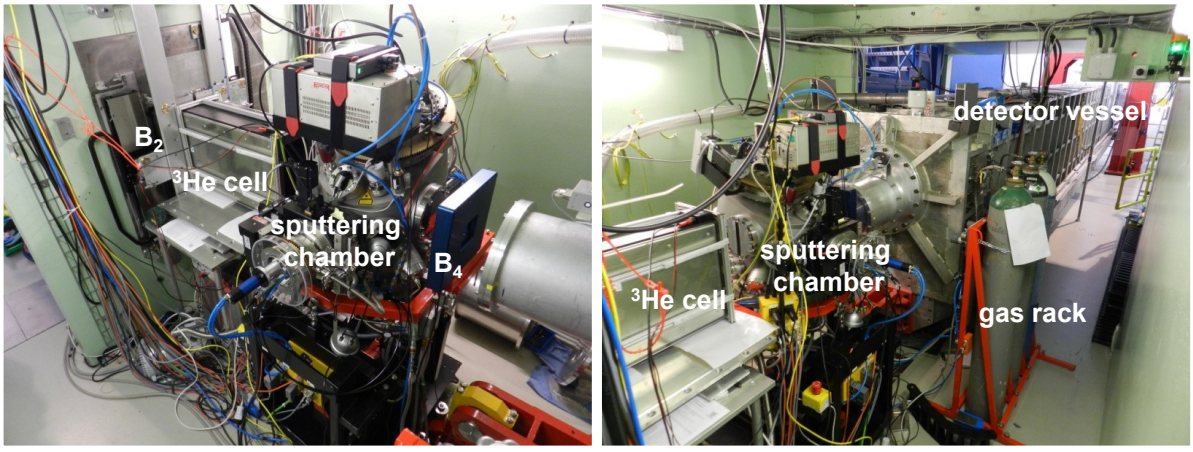

Fig. 3.28: *Photos of the sputtering chamber installed at REFSANS in February 2012. Left: view towards the neutron source, where neutrons exit the green wall, pass the slit B2 and the ^{3}He polarizer. They enter the sputtering chamber, are reflected by the sample surface, exit the chamber again, pass the external slit B4 and enter the detector vessel. Right: view along the detector vessel towards the detector. The gas rack is positioned next to the sputtering chamber.*

Sample #38			Sample #62		
angle	$time_{no\,pol}$	$time_{pol}$	angle	$time_{no\,pol}$	$time_{pol}$
0.125 °	7 min	0.5 h	0.35 °	0.5 h	0.5 h
0.25 °	13 min	1 h 7 min	0.80 °	1.5 h	2.5 h
0.60 °	1 h	5 h	2.20 °	2.5 h	5 h
1.40 °	9 h	20 h			
total time:	10 h 20 min	26 h 37 min		4.5 h	8 h

Table 3.5: *Summary of the angles of incidence used together with the measurement times per spin state for the non-polarized and polarized reflectivity curves for sample #38 in February 2012 and for sample #62 in August 2012. The total time denotes the measurement time per spin state and layer.*

Although the wavelength resolution was with 5% five times lower, the reflectivity curve of sample #38 had to be measured for 2.3 times as long as sample #62. This was due to higher diffuse background as well as greater substrate roughness. In contrast, for sample #62 we used the new sample table (Section 3.2.1), which was expected to produce less diffuse scattering as well as a new Si substrate from a different company, which proved to have much less roughness (Section 3.3.1). Further, we sputtered Cu at a lower Ar pressure, which reduced the Cu roughness by a factor of 2.5 compared to sample #38 (Table 3.4).

Data Acquisition. Owing to the broad wavelength distribution, a broad Q_z-range is simultaneously recorded for one angle of incidence. However, to obtain a wide Q_z-range up to 0.12 Å^{-1}, we measured the reflectivity at three to four incident angles. The slit openings were optimized for each angle to limit the exposure to the sample area reducing diffuse scattering. The angles used and their corresponding measurement times are summarized in Table 3.5. The measurements for each angular setting were normalized by a subsequent measurement of the direct beam, which was performed for sample #38 with the detector at $2\theta = 0°$, and for sample #62 for the same angles as the measurement itself. Figure 3.29a shows the spectrum versus wavelength of a measurement of sample #62 at $\theta = 1.4°$ compared to the spectrum of the direct beam. The spectrum of the measurement was divided by the spectrum of the direct beam for normalization, as shown in 3.29b. The small dip in the direct beam spectrum at $\lambda = 4$ Å is a result of Bragg scattering of the neutrons by the aluminum entrance window of the detector [77]. The wavelength of the detected neutrons was determined by their time of flight from the chopper to the detector. The plotted spectra are already ballistically corrected for the effect of gravity on the neutron's flight path [77]. The reflectivity curve was obtained by converting λ into Q_z, using Bragg's law $Q_z = 4\pi/\lambda \cdot sin(\theta)$. The different parts of each angle θ were combined into one reflectivity curve using different scaling factors to ensure that the overlapping regions coincide. The combined reflectivity curve was then normalized to the intensity of the total reflection. The reflectivity curves, polarized or unpolarized, were fitted using Parratt32 [17] or SimulReflec [19]. More details about PNR can be found in Section 2.2.2.

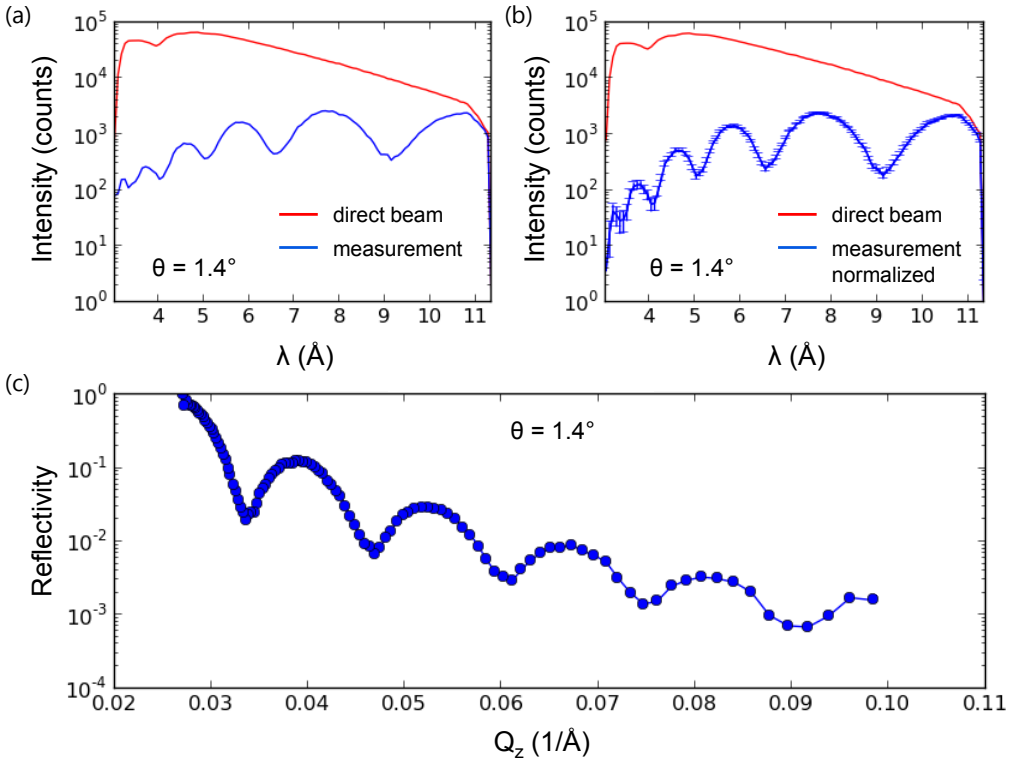

Fig. 3.29: *Reflectivity measurement for an angle of incidence $\theta = 1.4°$ of sample #62 after Cu deposition. (a) Spectrum of the direct beam compared to the spectrum of the reflectivity of the sample as a function of wavelength. The latter is normalized by the spectrum of the direct beam in (b). (c) The reflectivity curve is obtained by converting $R(\lambda)$ into $R(Q_z)$. At $\theta = 1.4°$ only a part of the reflectivity curve is measured.*

3.5.2 Results from REFSANS

So far, I introduced the setup at REFSANS and the data acquisition process in the previous chapter, I will now present the results of sample #38 and #62 measured *in-situ* during growth. We carried out polarized and unpolarized measurements before Fe deposition and after each deposition step of Fe. Here, I will present and compare the unpolarized as well as the polarized reflectometry data of both sample. These are compared to post growth X-ray data.

Unpolarized Measurement. The unpolarized reflectivity curves as a function of Q_z recorded after each step of sputtering of 2–5 s are plotted with offsets for sample #38 in Figure 3.30a and for sample #62 in Figure 3.30b. As expected, the increasing layer thickness results in a narrowing of the Kiessig fringes. Since a high amount of Kiessig fringes makes fitting easier, we increased the Cu thickness for sample #62, which can be seen in the closer Kiessig fringes of sample #62 with $d_{Cu} = 431\,\text{Å} \pm 5\,\text{Å}$ compared to $d_{Cu} = 198\,\text{Å} \pm 4\,\text{Å}$ of sample #38.

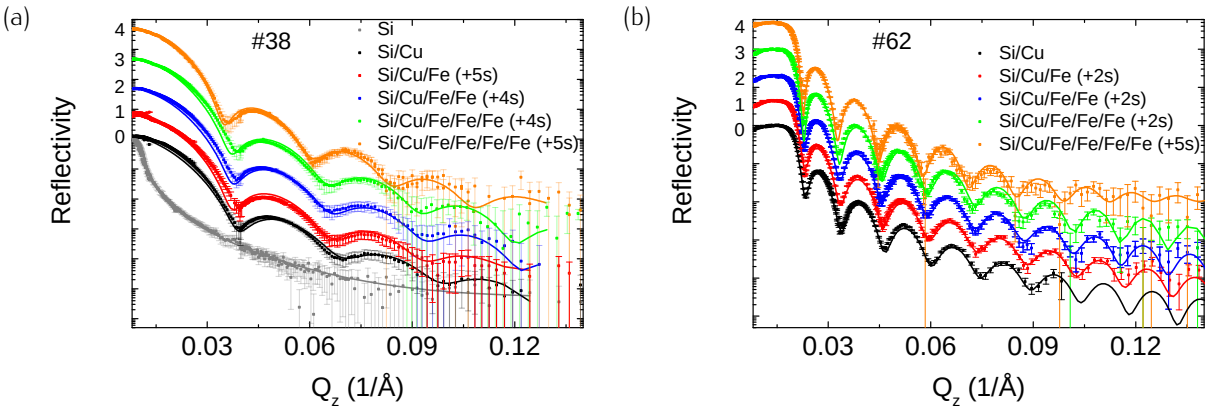

Fig. 3.30: *Unpolarized neutron reflectivity measurements recorded in situ during growth at REFSANS at FRM2 (a) for sample #38 and (b) for sample #62. Fits are represented by solid lines and data by symbols. The Fe thickness increases from bottom to top sputtered in steps of 2–5 s sputtering time (see legend), corresponding to 2.5–7.5 Å per step.*

This, together with the huge influence of the reduced substrate and Cu roughness of sample #62, can be also seen in Figure 3.31a, which compares the XRR curves of both samples measured *ex-situ* after the reflectivity measurements at REFSANS. Note that after the last neutron measurement, both samples were coated with a protective Si layer before they were removed from the sputtering chamber. Here, the reflectivity of sample #38 drops much faster than that of sample #62. The very pronounced long oscillation with two maxima visible in the reflectivity of sample #62 corresponds to the Si layer, which is four times thinner than that of sample #38.

Note that sample #62 was proved to consist of polycrystalline Cu: the etched substrate was put inside the evacuated chamber several days before we were able start the Cu deposition. We therefore expect the Fe to be polycrystalline, too. Although XRD measurements proved that the Cu and the Fe of sample #38 grew epitaxially (Section 3.3.4), XANES measurements revealed at least one oxidized Fe layer (Section 3.3.6), which is expected to influence the magnetic properties as well. The oxidization occurred, because the pumps to evacuate the chamber were accidentally shut off after the deposition of the third Fe layer, which then was exposed to a base pressure of 1 mbar.

The reflectivity curves were analyzed by fitting all neutron data as well as the XRR data. The fits (lines) are plotted together with the data (symbols) in Figure 3.30 and 3.31a. The neutron data of sample #38 have the worst fits, with huge deviations from the data points. We suspect that data processing, including some corrections, was not done properly and needs to be reconsidered. However, the data processing is very extensive and, as discussed later, the analysis of the corresponding polarized data is even more challenging due to the use of the ^{3}He polarizer. The data treatment of the polarized data was, therefore, not completed and cannot be compared to the unpolarized data anyway. The data and the analysis of sample #62 are of better quality and provide a good study at least of polycrystalline Fe. On these

grounds, the repetition of the data treatment of sample #38 is of less importance.

An exact determination of the thickness of the ultrathin Fe layers is very challenging owing to the very similar scattering length density (SLD) values of Fe and Cu, possible interdiffusion or intermixing at the interfaces and the formation of discontinuous layers. The results for both samples are plotted in Figure 3.31b (filled squares) as a function of sputtering time to determine and compare the sputtering rates. Error bars are estimated from the results obtained by different but almost equally good fits. The thickness was fitted by linear slopes $d_{Fe}(t) = R_{Fe} \cdot t + d_{Fe}(0)$ (lines) and resulted in:

#38: $d_{Fe} = (0.72 \pm 0.10)\text{Å}/s \cdot t + (3.2 \pm 1.2)\text{Å}$
#62: $d_{Fe} = (1.47 \pm 0.20)\text{Å}/s \cdot t + (3.2 \pm 1.0)\text{Å}$

Surprisingly, the Fe rate R_{Fe} of sample #62 is twice as high as that of sample #38, whereas $d_{Fe}(0)$ is the same. Polycrystalline Fe is expected to grow with many defects. These might have led to an increase in thickness per sputtering step, which appears as increased rate. The Fe rate determined from XRR data of series 1 together with sample #38 (Section 3.3.2) is (0.99 ± 0.122)Å, slightly larger than determined from the *in-situ* neutron reflectometry (NR) measurements of sample #38. The thicknesses determined by XRR from the fits of Figure 3.31a are indicated as open squares, which are both larger than the value determined from the *in-situ* NR. This can also be seen from the SLD profiles as a function of sample depth z based on the XRR and NR fits, which are compared in Figure 3.31c for sample #38 and in Figure 3.31d for sample #62. The SLD profiles obtained by NR correspond to the fit of the data after the very last Fe deposition. After the deposition of the protective Si capping layer, no further neutron data was collected. For this reason, the SLD profiles differ for X-ray and neutrons at the sample depth of the last Fe layer. Note that the SLD is one order of magnitude smaller for neutrons than for X-rays. Despite small differences of the SLD at the interface of sample #62 and the appearance of a thicker Fe layer when measured with X-rays, the profiles obtained by both measurement methods are in good agreement. The small deviations could be due to the different sensitivity for example of the SiO_2 layer, the neutron SLD of which can be better distinguished from the neutron Si SLD. The difference in Fe thickness may arise due to the Si capping, as at its interface intermixing may occur. This intermixing layer can probably not be distinguished from the Fe layer. Rather it appears together with the pure Fe layer as a thicker Fe layer.

Polarized Measurements. After every unpolarized measurement shown in Figure 3.30, we also recorded polarized neutron reflectivity (PNR) data. Since the polarization and the transmission of the ^{3}He cell is a function of time, the analysis of the polarized data of sample #38 was complicated. As a results, and together with additional problems of data treatment, the data analysis by Wolfgang Kreuzpaintner could not be completed. Therefore, I am only presenting PNR of sample #62 measured during the second beamtime using a polarizing supermirror.

Towards the end of the beamtime, the cooling water of the beamline became warmer than

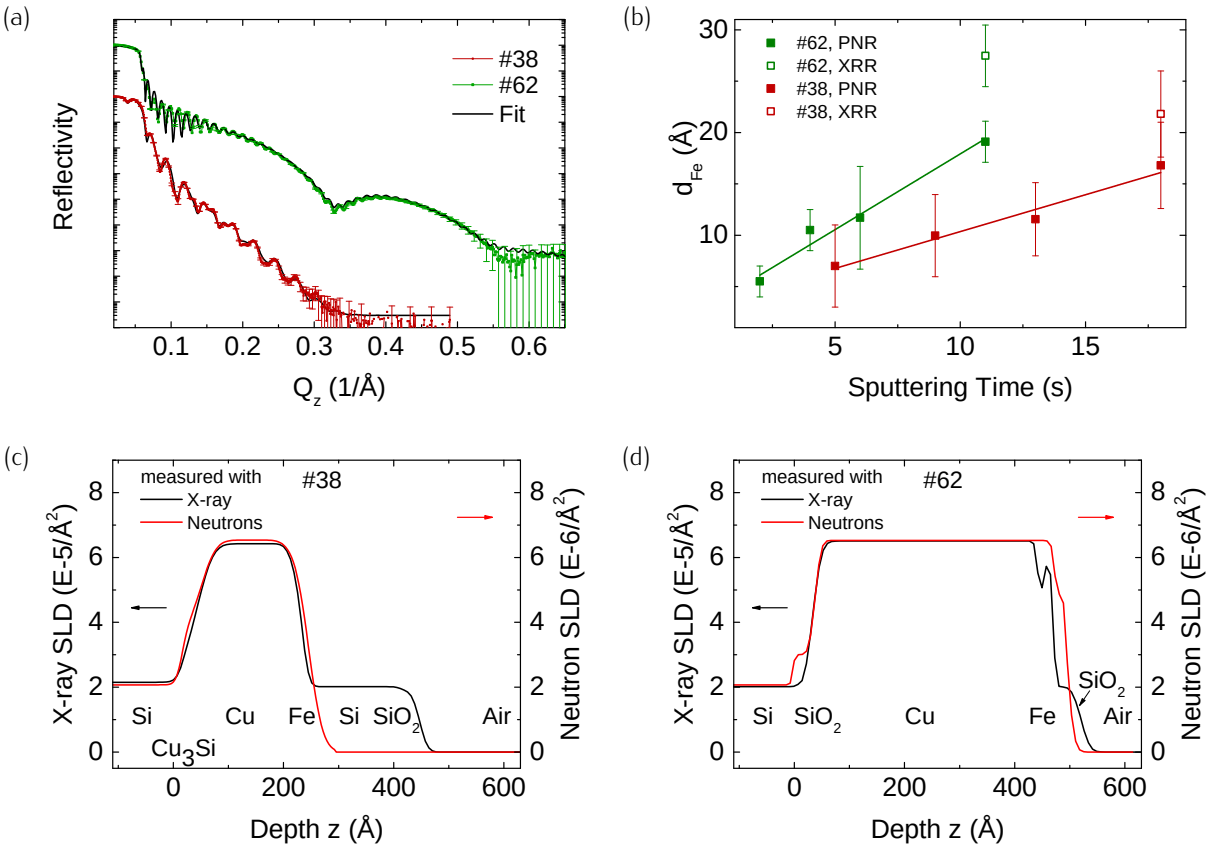

Fig. 3.31: *(a) XRR data of sample #38 and #62 as a function of Q_z together with fits (black lines). (b) Fe thickness versus sputtering time determined from the fits to neutron reflectivity from Figure 3.30 (filled squares), which are fitted by a linear slope (solid line) and compared to the thickness determined from XRR fits from (a) (open squares). The SLD profiles based on those fits are plotted as a function of sample depth z in (c) for sample #38 and in (d) for sample #62. The SLD profile measured with neutrons corresponds to data recorded after the last Fe deposition. The Fe layer appears thicker for X-rays, which may be due to the additional Si capping layer, which was sputtered after neutron reflectometry was performed and may form an intermixing layer.*

usual. This resulted in an increase in temperature of the water-cooled Helmholtz coils, which cut out at 125°C to prevent outgassing of the casting compound. The coils did indeed cut out during the spin-down measurement of the third Fe layer at the very last angle, affecting only $Q_z > 0.1\,\text{Å}^{-1}$. However, because of the high remanence values observed in similar samples (Section 3.4.1), the sample should not have lost much of its magnetization. For the measurement of the fourth Fe layer, we had to reduce the current from 22 A $\widehat{=}$ 29 mT to 12 A $\widehat{=}$ 16 mT to ensure a moderate temperature. From SQUID measurements with an in-plane magnetic field presented in Figure 3.24c, we know that the applied magnetic field was at least larger than the coercive field and only 4 mT smaller than the saturation field. Therefore,

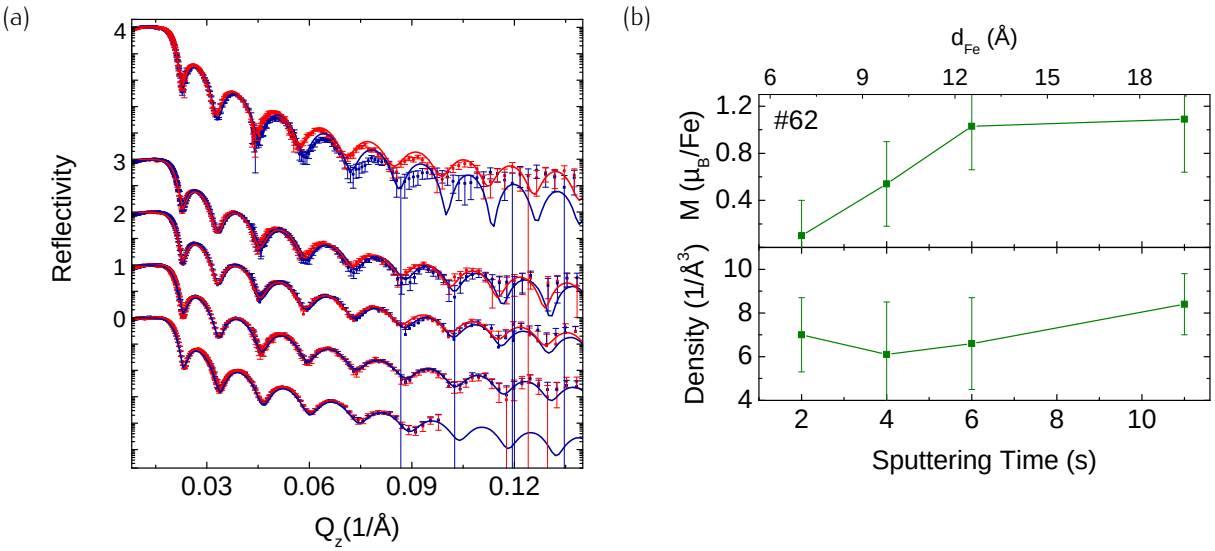

Fig. 3.32: *(a) PNR data of sample #62 recorded during growth at REFSANS (FRM2) with the Fe thickness increasing from bottom to top in steps of 2 s (layers 1–3) or 5 s (layer 4) sputtering time, which resulted in a Fe thickness from* 5.5 Å ± 1.5 Å *to* 19.1 Å ± 2 Å. *R+ data is indicated in red, R- data is indicated as blue symbols. The spin splitting increases with increasing Fe thickness. (b) Magnetic moment (upper panel) and Fe density (lower panel) as a function of sputtering time and Fe thickness based on the fits plotted in (a).*

we do not expect a strong influence on the magnetization, but it cannot be excluded.

A sequence of PNR data of sample #62 is shown in Figure 3.32a with the Fe thickness increasing from bottom to top in steps of 2 s (layers 1–3) or 5 s (layer 4) sputtering time, which resulted in an Fe thickness of 5.5 Å ± 1.5 Å to 19.1 Å ± 2 Å. R+ data is indicated in red and R- data in blue. The spin splitting increases with increasing Fe thickness. For a quantitative study, the PNR curves were fitted (lines) using SimulReflec [19]. The fit parameters magnetic moment and Fe density are plotted in Figure 3.32b as a function of sputtering time (lower axis) and Fe thickness (upper axis). Error bars are obtained from different models, for which during fitting, one parameter was always kept constant at extreme values that still provided reasonable fits. The magnetic moment (upper panel) rises with Fe thickness up to 11.7 Å and remains constant until 19.1 Å at a magnetization of $\approx 1.1\,\mu_B$/Fe, smaller than the bulk value of $2.2\,\mu_B$/Fe. This may also be caused by the reduced external magnetic field of the last data set. However, the saturation magnetization was determined to $(0.8 \pm 0.1)\mu_B$/Fe using a SQUID (Section 3.4.1) of similar samples up to $d_{Fe} = 20$ Å. This is, within error bars, in agreement to the magnetic moment determined here.

There may be several reasons for the small magnetization of the first two Fe layers. Firstly, we may not have reached the saturated state: this may be due to an in-plane direction of the hard axis or to a strong island growth resulting in superparamagnetism. However, by measuring a 6 Å Fe layer using a SQUID, we observed a hysteresis, with the easy axis lying in plane and a saturation field smaller than the applied magnetic field. Secondly, the

layers may have been too thin or had too many defects for a magnetic exchange. Thirdly, Fe may have grown as a mixture of bcc and non-magnetic fcc, reducing the net magnetization. Fourthly — and most likely — the Curie temperature was smaller than RT for thinner films, as it was measured by SQUID and XMCD for 3-6 Å Fe layers.

Since we know that the magnetic properties correlate strongly with the structural properties, studying the Fe density as a function of Fe thickness (lower panel) may provide further insight into the magnetic properties. Here, the density slightly drops from 5.5 to 10.5 Å and rises again, reaching the bulk value of 8.5 $Å^{-3}$. The tendency of increasing Fe density with thickness may be due to fewer defects and more filled layers as more Fe atoms are deposited. This would also explain the rise in magnetic moment. The outlier of the first Fe layer point could be due to a larger portion of fcc Fe, which has a larger density than bcc Fe and may also be responsible for the low magnetic moment of this layer. However, due to the RT measurement, these conclusions are very speculative. A more detailed discussion with a direct comparison of SQUID and PNR data will be presented in Section 3.5.5.

3.5.3 Setup and Data Acquisition at Amor Using Selene

As introduced in Section 3.2.2, a Selene setup can be utilized to reduce measurement time. This is especially important for *in-situ* growth studies, in which several and very thin layers have to be measured for a detailed analysis. The monitoring of the evolution of the properties should take place on a similar time scale as the growth. To help achieve this, we installed the sputtering system together with the Selene setup at the horizontal reflectometer Amor at the Paul Scherrer Insitute (PSI) in November 2013. Amor is operated in the TOF mode with a broad wavelength band of 4–14 Å. As a result, and given a divergence of 1.4° provided by the Selene setup, we used a high intensity neutron beam and recorded the reflectivity in a very wide Q_z-range at only one sample angle. By contrast, at REFSANS we used a collimated neutron beam, with neutrons of higher divergence simply blocked by the slits. The difference of both methods was illustrated in Figure 3.13. The corresponding section (Section 3.2.2) also provides a description of the basic concept of a Selene setup. In the following section, I will present the setup used at Amor and introduce the sputtering and data acquisition process.

Setup. A diagram of the beamline with the Selene setup including two Montel mirrors and the chamber installed is shown in Figure 3.33. After the beam exits the neutron guide, the wavelength band is selected by the choppers such that $\delta\lambda/\lambda = 5.6\%$. Afterwards, the beam is polarized by a polarizing supermirror bent like a logarithmic spiral to provide the same angle of incidence for the entire divergent beam on the polarizing coatings. The neutron polarization can be flipped by an RF spin flipper. The image that is focused on the sample is defined by the slit B1, which is adjusted to the limits of the accepting angles of the reflectors. The beam is then reflected from the first and second Montel mirror before entering the chamber through the neutron window. To allow full divergence, the internal slits of the sputtering chamber are not installed. Guide fields at the Selene reflectors and a yoke inside the chamber maintain

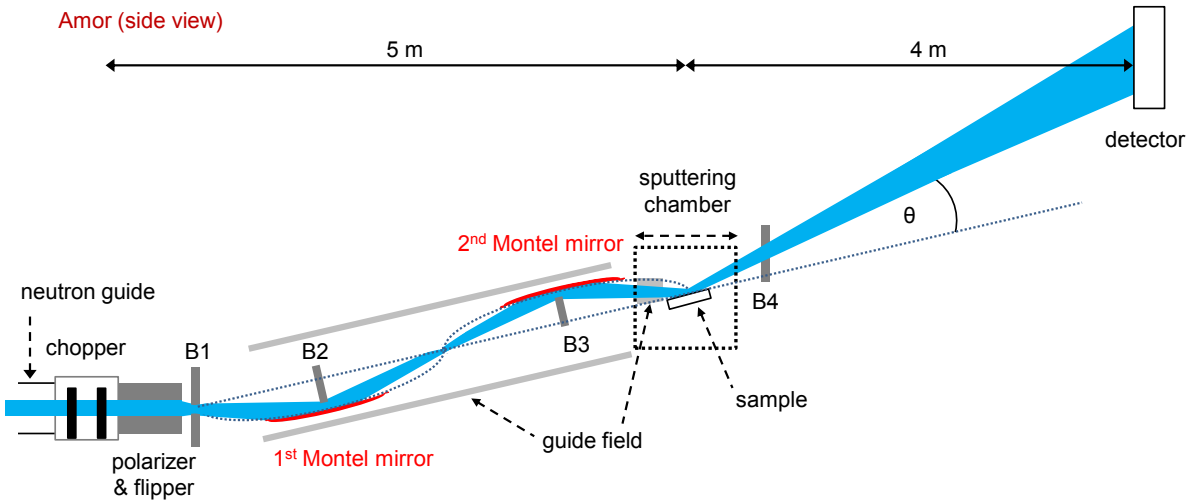

Fig. 3.33: *Schema of the Amor beamline with the Selene optics and the sputtering chamber installed. Neutrons from the neutron guide pass the choppers, the polarizer, and the flipper. The slit B1 defines the beam shape, which is imaged on the sample after being reflected from two elliptic reflectors, i.e. Montel mirrors. Guide fields at the Montel mirrors and inside the chamber maintain the neutrons's polarization up to the sample. The neutron beam is reflected from the sample, exits the chamber and hits the detector. The slits B2, B3, and B4 block not properly reflected neutrons and reduce diffuse background.*

the neutron polarization up to the sample. The chamber is positioned such that the sample is located in the focal point of the second Montel mirror, resulting in a neutron beam footprint of 2 mm^2. The beam is reflected from the sample surface, which is tilted to define the sample angle θ. Note that, due to the divergent beam, there is a wide range of angles of incidence for one θ. Therfore, we will refer to the angle θ as sample angle instead of angle of incidence. The reflected beam exits the chamber and enters the detector vessel (not depicted in Figure 3.33), which is flushed with Ar gas to reduce air scattering. The detector vessel and the ^{3}He detector can be lifted to adjust 2θ.

The beam displacement produced by the Selene setup is exaggerated in Figure 3.33. In reality, the Selene setup is almost horizontal. Note that the profile of the Montel mirror is L-shaped (Section 3.2.2), additionally focusing the beam also in a perpendicular direction to the paper plane, which causes the same beam displacement in the lateral direction. Unfortunately, the Amor beamline does not allow the detector or any other component to be displaced laterally. Thus, the beam width has to be reduced by 25% using slit B1, such that the total divergent beam after passing the Montel mirrors still hits the detector. A long-term strategy to achieve this additional degree of freedom, i.e. the lateral displacement of components, is being developed. There are also plans to replace the neutron guide by one with a larger divergence, which is expected to enhance the intensity by a factor of 4–5. Both measures will

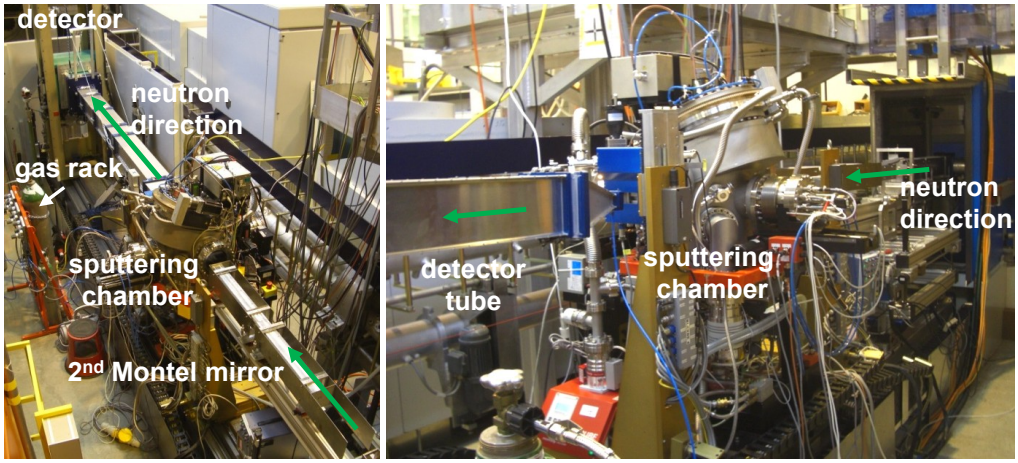

Fig. 3.34: Photos of the sputtering chamber installed at Amor in November 2013. Left: view towards the detector, where neutrons enter the second elliptical Montel mirror (bottom) and the sputtering chamber, where the beam is reflected from the sample surface, exits the chamber again and enters the detector vessel. The gas rack is positioned next to the sputtering chamber on the left. Right: view towards the neutron source.

increase the already high performance of the Amor beamline.

Sputtering process. During the beamtime, we sputtered sample #83 and sample #89. The Cu(100)/Fe samples were prepared as discussed in Section 3.3.1 with the sputter conditions summarized in Table 3.3. Further details about the sputtering chamber can be found in Section 3.11. In contrast to the REFSANS beamtime, this beamtime took place after the implementation of upgrade 2, which improved the base pressure and changed the sample position, leading to an increase in sputtering rate. Accompanied, we sputtered here with a fully open valve position.

For sample #83, the Helmholtz coils were installed. These had a small leakage or outgassed, resulting in a poor base pressure of $1 \cdot 10^{-6}$–$4 \cdot 10^{-6}$ mbar. Additional, we observed the coils glowing from time to time when the current was applied. This was accompanied by a further increase of base pressure up to 10^{-5} mbar. During the measurement, we applied a current of 19 or 20 A, corresponding to a magnetic field of 25 or 26 mT, sufficient to saturate the Fe layer. As the performance of the coils was poor, we removed them and replaced them with a

Sample #83		Sample #89	
angle	time_{pol}	angle	time_{pol}
1.1 °	50 min	2.3 °	15 min
2.6 °	2 h		

Table 3.6: Summary of the sample angles used at Amor together with the measurement times per spin state for samples #83 and #89.

permanent magnet of 60 mT. Thus, the second sample #89 had to be sputtered in a magnetic field. This is not expected to change the homogeneity of the Fe layers, since the Fe atoms coming from the target are not charged.

The sputtering rate should also not be influenced, since the Ar ions moving to the target will be deflected by this magnetic field on an arc, assuming single ionized Ar, with a radius of $\approx$ 27 cm — much larger than the plasma height of 3-6 cm. The ions will therefore still hit the target. However, the growth mode could change for Fe atoms depositing in a magnetic field, as reviewed by Enomoto [100]. This would generally have occurred if a magnetic field of several Tesla was applied or through simultaneous annealing of the sample. The dismounting of the coils improved the base pressure to $1.4 \cdot 10^{-7}$ mbar for the deposition of the first layer, continuously dropping to $3.2 \cdot 10^{-8}$ mbar for the deposition of the 15th layer 13 h later.

Data Acquisition. The nominal angles used for both samples and the measurement times per spin state are summarized in Table 3.6. For the first sample #83, we recorded the polarized data at two sample angles to cover a wide Q_z-range up to 0.13 Å^{-1}. Due to problems with the encoder of the sample rotation and to reduce the measurement time, we measured the second sample #89 at only one sample angle. The angle was optimized to cover the largest possible Q-range up to 0.09 Å^{-1}. In addition, we reduced the measurement time from 50 min to 15 min per spin state and layer.

The data processing to obtain the reflectivity curve is exemplified in the following. Figure 3.35a shows a typical color map of the reflected signal log I(λ, θ), here, of a measurement of sample #83 at $\theta = 1.1°$ after Cu deposition as a function of θ and λ. The triangle of high intensity at the bottom right corner represents the region of total reflection, while each diagonal stripe corresponds to one Kiessig fringe of the Cu. Figure 3.35b shows

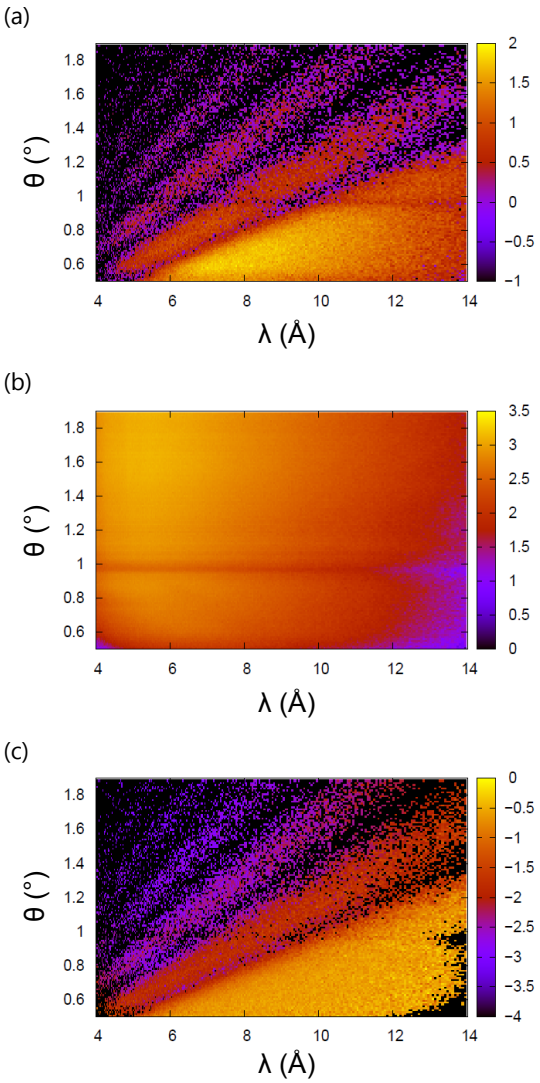

Fig. 3.35: *Intensity maps log I(λ, θ) measured at Amor of (a) sample #83 after Cu deposition and of (b) a supermirror with m = 5 used for normalization of the intensity map of (a) as plotted in (c). Supermirror with m = 5 used for normalization of the intensity map of (a) as plotted in (c).*

a similar intensity map of a measurement of a supermirror, with high intensity everywhere due to the large region of total reflection. In Figure 3.35c the data of (a) is normalized by a pixel-wise division of the measurement of the supermirror of (b). The horizontal stripe at $\approx 1°$ is produced by a misalignment of the elliptical Montel mirrors, where two guide segments adjoin and no neutrons are reflected. The wavelength of the detected neutrons was determined by their time of flight from chopper to detector. Each detector channel in x-direction can be converted into θ.

The reflectivity curve was obtained by converting each pixel of $I(\lambda, \theta)$ into $I(Q_z)$ using $Q_z = 4\pi/\lambda \cdot sin(\theta)$, where Q_z was integrated in Q_z steps such that $\delta Q_z/Q_z = 2\%$. For sample #83, which was measured at two sample angles, two different parts of the reflectivity curve at different Q_z-values have been recorded. Those were combined into one reflectivity curve using scaling factors to ensure that the overlapping regions coincide. The reflectivity curves were then normalized to the intensity of the total reflection and fitted using SimulReflec [19]. Further information about PNR can be found in (Section 2.2.2).

3.5.4 Results from Amor

Having introduced the Selene setup at AMOR and the data acquisition process in the previous chapter, I will now present the results of sample #83 and #89 measured *in-situ* during growth. We carried out polarized measurements before Fe deposition and after each deposition step of Fe. Here, I will compare the the polarized reflectometry data of both sample, which are additional compared to post growth X-ray data.

The PNR curves of samples #83 and #89 as a function of Q_z are shown in Figure 3.36. Each deposition step of Fe of 1.5 s sputtering time correspond to $\approx$ 1 ML with the Fe thickness increasing from bottom to top to 23 Å $\pm$ 5 Å and 26 Å $\pm$ 12 Å, respectively. The reflectivity R+ for spin up neutrons and R- for spin down neutrons, are indicated as red and blue symbols, and the fits as solid lines. For both samples, the Kiessig fringes get closer to each other and the difference in the R+ and R- signal increases for increasing Fe thickness. During the measurement of layer 9 of sample #89 (Figure 3.36b), the sample was suddenly misaligned for some reason and the measurement was useless. This was only observed after continuing the sputtering process. Thus this measurement could not be repeated. For the final layer, we decided to sputter three layers at once and only measured the 15th layer.

Each layer was fitted (lines in Figure 3.36) to determine the Fe thickness, magnetic moment, and Fe density. XRR measurements were performed *ex-situ* after the experiment. These are shown in Figure 3.37a for sample #83 and in Figure 3.37c for sample #89. The fits (black lines) are compared to the PNR fit of the last layer in Figure 3.37b and in Figure 3.37d for both samples. The corresponding SLD profiles are plotted as a function of sample depth z. This time, the samples were not coated with a Si capping layer after the neutron experiment.

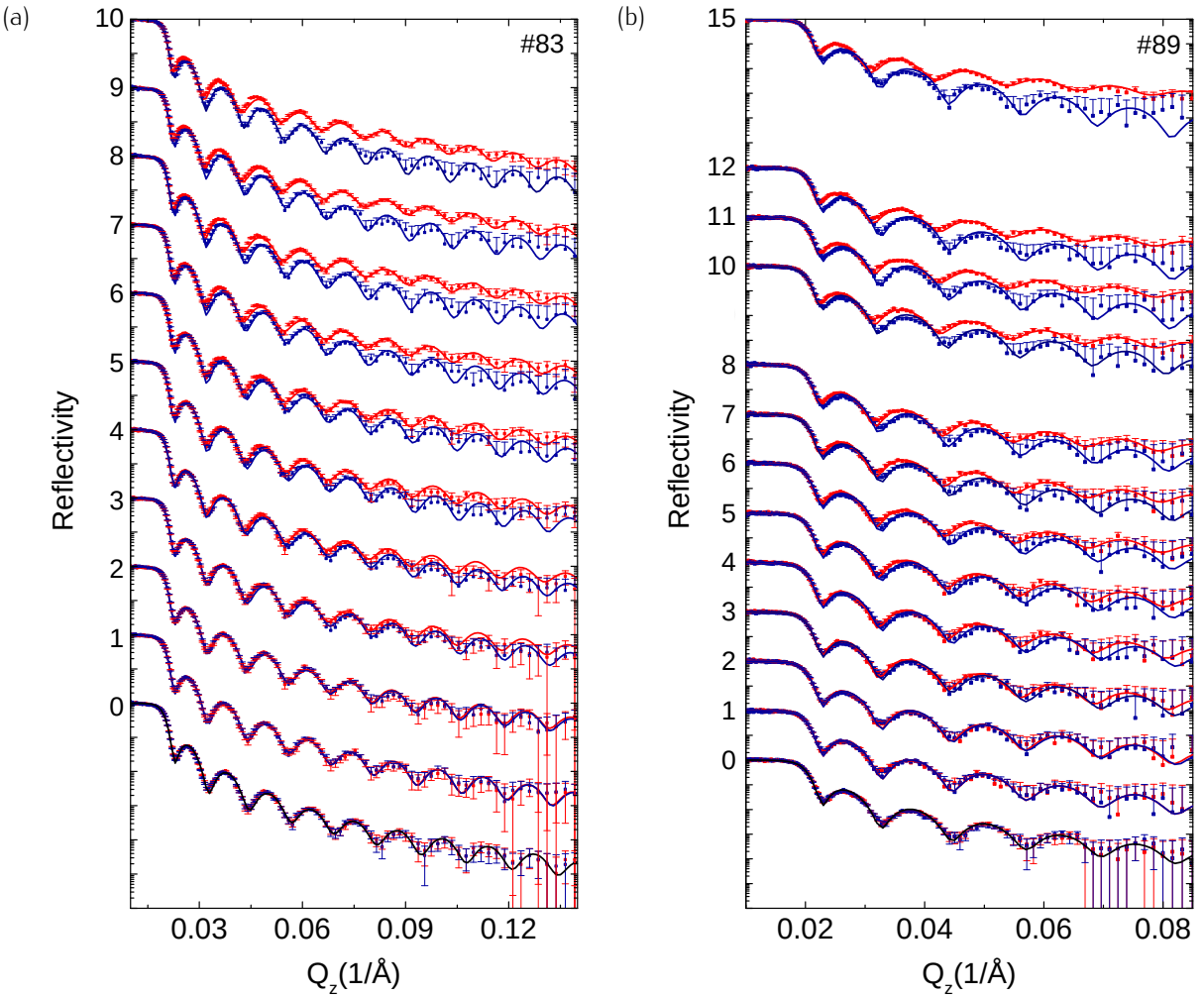

Fig. 3.36: *PNR data measured in situ at Amor (PSI) with the Fe thickness increasing from bottom to top in steps of 1.5 s sputtering time (a) for sample #83 and (b) for sample #89. R+ data is indicated in red, R- data is indicated as blue symbols, and fits are shown as solid lines. The spin splitting increases with increasing Fe thickness.*

Sample #83, however, has an additional 11th Fe layer that could not be measured by PNR owing to a shut-down of the neutron source. Thus, at z-values of the last Fe layer of sample #83 differ between the SLD profiles based on the neutron fits and the XRR fits. This aside, and apart from the fact that the neutron SLD is one order of magnitude smaller, the neutron profile reproduces the shape of the X-ray SLD for both samples very well. Since the neutron SLD of Fe is different to Cu, although the X-ray SLDs of both metals are very similar, then neutrons here are more sensitive.

The Fe thickness determined by the PNR fits of both samples (Figure 3.36) is plotted as a function of sputtering time in Figure 3.38a (filled symbols), fitted by a line with a linear slope (line) and compared to the thickness determined from XRR fits (open symbols). The results of

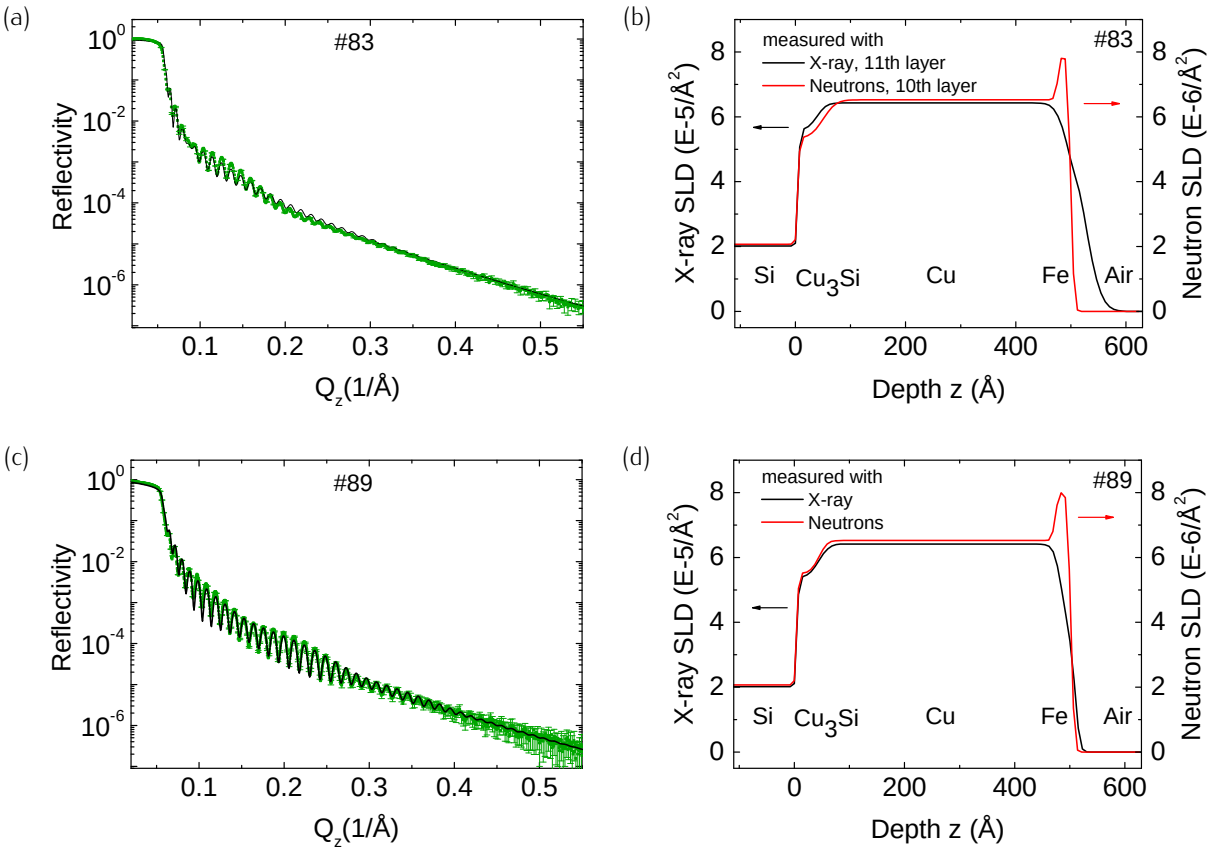

Fig. 3.37: XRR measured ex-situ as a function of Q_z together with a fit (black line) (a) of sample #83 and (c) of sample #89. (b) and (d) show SLD profiles based on the fit from (a) and (c), respectively, and on the neutron fit corresponding to data recorded after the deposition of the last Fe layer from Figure 3.36 as a function of sample depth z.

the two methods are in excellent agreement for sample #89, while the Fe thickness of sample #83 determined by XRR deviates from the extrapolation of the fit to the 11th Fe layer. Both XRR curves were fitted with FeO as a top layer. We calculated an effective Fe thickness by considering the composition and the reduced density of the oxide. The pure Fe layer was, however, fitted to 29 Å ± 4 Å, larger than the value of 24 Å expected from the PNR fit. The fit for the Fe thickness as a function of sputtering time yields:

#83: $d_{Fe} = (1.27 \pm 0.05)\text{Å}/s \cdot t + (3.3 \pm 0.3)\text{Å}$
#89: $d_{Fe} = (1.28 \pm 0.06)\text{Å}/s \cdot t - (0.5 \pm 0.1)\text{Å}$

The Fe sputtering rates of both samples are in very good agreement, while $d_{Fe}(0)$ are different, indicating a different initial growth. The growth could have been influenced by the poor base pressure during sputtering of sample #83 or by the permanent magnetic field during sputtering sample #89. The rates are only 0.3 Å/s smaller than the rates of series 3 estimated from XRR (Section 3.3.2). Since each Fe layer was sputtered for 1.5 s and XRD determined a distance of the bcc Fe(110) planes of 1.94 Å, we always sputtered the amount of 1 ML. The same fits

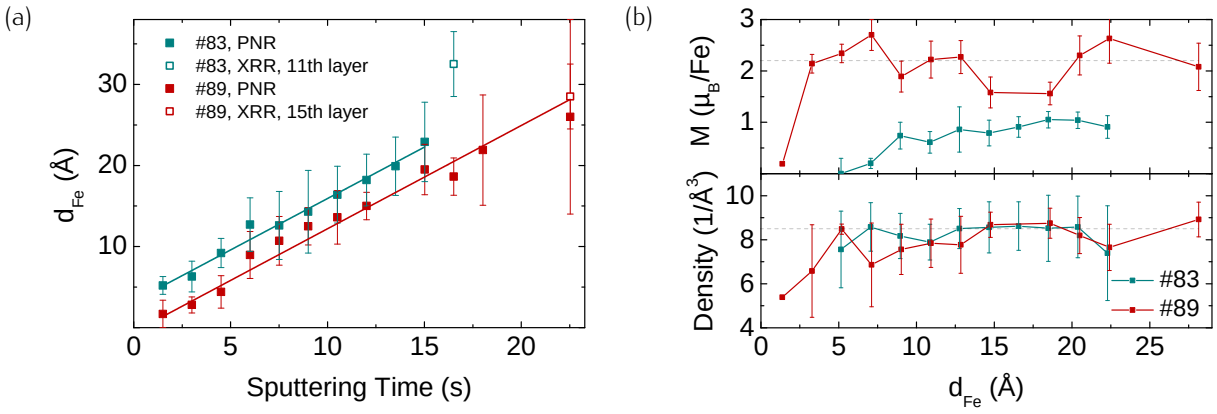

Fig. 3.38: *(a) Fe thickness of samples #83 and #89 versus sputtering time determined from PNR fits from Figure 3.36 (filled squares). These are fitted by a linear slope (solid line) and compared to the thickness determined from XRR fits from (c) and (a) (open squares). (b) Magnetic moment and Fe density of samples #83 and #89 extracted from PNR fits of Figure 3.36 as a function of Fe thickness calculated from the fit.*

also provided the magnetic moment and Fe density, which are summarized in Figure 3.38b in the upper and lower panel and plotted as a function of d_{Fe} calculated from the linear fits of Figure 3.38a. It is obvious, that the magnetic moment is much higher for sample #89, varying by 15–30% around the bulk value of $2.2\mu_B$/Fe (dashed horizontal line), than for sample #83. The latter reaches $(1.0 \pm 0.1)\mu_B$/Fe for $d_{Fe} \geq 13$ Å, showing a very similar behavior to sample #62 sputtered at REFSANS. In contrast, the magnetic moment of sample #89 rises much faster, with the bulk value already reached for the second ML. The Fe density (lower panel) of sample #89 increases, despite an outlier at 5 Å, to 15 Å, where it reaches the bulk value (dashed horizontal line). The density measured for sample #83 coincides with this curve within the error bars. This behavior is similar to the evolution of density for sample #62.

3.5.5 Summary and Discussion

This section aims to summarize the results of the *in-situ* PNR measurements. These are then compared with results obtained by the *ex-situ* characterizations of Section 3.3 and Section 3.4 as well as results quoted in the literature introduced in Section 3.1.

Four Fe/Cu(100) samples were grown during *in-situ* PNR experiments, the results of which improved from sample to sample. The first experiment (Section 3.5.2), during the growth of sample #38, can be regarded more or less as a test measurement: The ^{3}He-cell leads to a polarization and transmission that varies with time. Thus, the ^{3}He-cell polarizer complicated data interpretation. In addition, the diffuse background as well as the sample roughness required extremely high measurement times of 28 h per spin state and layer (Table 3.5). Furthermore, the Fe layer partially oxidized after an accidental shut-down of the pumps. The Fe layer grew epitaxially, in contrast to the second *in-situ*-measured sample #62, the

substrate of which reoxidized before deposition started. The measurement could be performed in a much shorter time of 8 h per spin state and layer using a supermirror as polarizer. Data treatment was straightforward, resulting in reflectivity curves up to $Q_z = 0.14\,\text{Å}^{-1}$. The latter improved due to upgrade 1 of the sputtering chamber (Section 3.11), which reduced diffuse scattering, and to a smoother Si substrate. Both samples were measured at REFSANS (FRM2), which is operated in the TOF-mode.

The next two samples were measured at Amor (PSI) (Section 3.5.4), where we used Montel mirrors in a Selene configuration (Section 3.2.2) to focus the beam on the sample and to additionally provide, besides a broad wavelength spectrum due to the TOF-mode, a divergent beam of $\Delta\theta = 1.4°$. This allowed us to measure with a high intensity beam recording a wide Q_z-range at only one angle. The first sample grown in this beamtime, sample #83, was sputtered with a poor base pressure, since the coils installed had a leakage or outgassed. After demounting the coils, the best sputtering and measurement process was performed for sample #89, with a very good base pressure down to $3 \cdot 10^{-8}$ mbar and extremely short measurement times. While we measured sample #83 at two different sample angles up to $Q_z = 0.14\,\text{Å}^{-1}$ and had testing measurement times of 2 h 50 min per spin state and layer, we decided to measure sample #89 at only one angle optimized for Q_z-values up to $0.09\,\text{Å}^{-1}$ (Table 3.6). We also reduced the measurement time from 50 min for the first angle used for sample #83 to 15 min, which still provided a high signal-to-noise ratio and clear spin splitting, which increased with layer thickness.

The measurement time of sample #83 was 3 times faster than the measurement time at REFSANS for sample #62 (Table 3.5), which had similar statistics and Q_z-range, although we illuminated only a $2\,\text{mm}^2$ sample area. Note that if we had measured at REFSANS with a wavelength resolution of 5.6% instead of 1%, we would have saved measurement time, too. However, if the potential of Amor in combination with Selene is fully exploited by realizing the measures mentioned above, the measurement time will be scaled down to only a few minutes.

The reflectivity curves measured at both instruments exhibited a drop of intensity of five orders of magnitude. The value of the drop is often referred to as dynamic range. If the diffuse background of an instrument is high, the dynamic range is reduced. However, for the measurement at Amor, the reflected signal was still larger than the diffuse background, indicating that the dynamic range is larger than five orders of magnitude.

For a quantitative study, all neutron reflectometry curves were fitted. From these fits we determined the Fe sputtering rate R_{Fe} of 0.72–1.47 Å/s. R_{Fe} of sample #62 was increased by a factor of 2 compared to sample #38. This could be attributed to a very poor polycrystalline growth with many defects appearing as thicker layer. The Fe rates for sample #83 and #89 were also increased here, as a result of upgrade 2 of the sputtering chamber (Section 3.11). While the rate for sample #38 is in good agreement with the rates determined by XRR of sample series 1, the rate determined by XRR of sample series 3 (Section 3.3.2) is 20% greater than the rate determined by PNR of samples #89 and #83. The same applies to the Fe thickness of the *in-situ*-measured samples: with the exception of sample #89, the

Fe layer was determined to be 30–45% thicker by XRR than by PNR. Since the contrast in SLD of Fe and Cu is larger for PNR, and as the *in-situ* measurements had to be fitted with fewer parameters for samples without an oxide layer, this method is more sensitve than XRR. However, the Q_z-range recorded by PNR is 2–4 times smaller, which reduces the reliability of the fit.

Figure 3.39 summarizes the magnetic moment determined by PNR for samples #62, #83 and #89 and compares the results to SUQID data of sample series 1 (Section 3.4.1). In order that our data can be better compared to the results from literature, the Fe thickness is converted into the number of monolayers (ML). However, we did not measure the number of ML directly by LEED as it was usually done in publications presented in Section 3.1. Instead we used the mean lattice constant determined from the bcc Fe(110) XRD peak for samples with $d_{Fe} > 17\,\text{Å}$ to calculate the number of ML with $1\,\text{ML} = 1.965\,\text{Å}$, which is of course only a rough estimate disregarding the evolution of the lattice constant with Fe thickness as it is expected. Furthermore, the thickness determination by XRR brings about an error of $1\,\text{Å} \leq \Delta d_{Fe} \geq 7\,\text{Å}$, which corresponds to 0.5–3.6 ML.

Sample #89 clearly shows a totally different behavior to that of samples #62 and #83 as well as to sample series 1, with a much higher magnetic moment very close to the bulk value (horizontal dashed line), but oscillating around that value. This is reminiscent of region II of the TD-grown films (Section 3.1), for which the magnetization oscillates owing to the

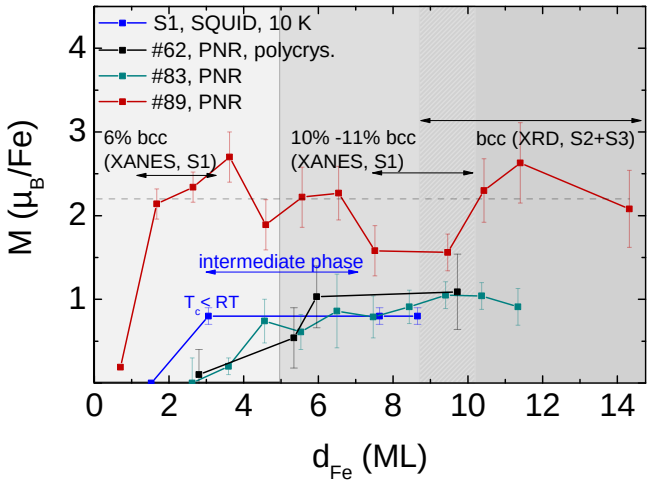

Fig. 3.39: *Comparison of the in-plane magnetic moment as a function of Fe-layer thickness of all in-situ PNR results and of SQUID data for sample series 1 (S1). The number of ML was calculated by the mean lattice constant determined by out-of-plane XRD for films with $d_{Fe} > 17\,\text{Å}$ and is therefore only a rough estimation. The intermediate regime denotes the area, in which an out-of-plane magnetic moment was also detected by the SQUID. Regions of different structures are indicated by the gray shaded areas. These are based on XANES results on sample series 1 (S1) and on XRD measurement of sample series 2 and 3 (S2+S3).*

interplay of the FM top layer and the odd or even number of AFM buried layers. However, there are too few data points to confirm such behavior for sample #89 and to distinguish it from noise. Moreover, the Neel temperature was measured to be smaller than RT for the TD-grown films [5, 36]. There was also no need to fit the data using a alternating magnetized or non-magnetic buried layers, as the model of FM layers fitted well. The magnetization of all curves rises with Fe thickness. Sample #89 already reached the magnetization of bulk at around 2 ML.

Although sample #62 grew polycrystalline and the magnetic field of the last Fe layer was weaker than the saturation magnetization, the evolution of the magnetization is very similar to sample #83. Both samples have a reduced magnetic moment at 2–6 ML. This is thought to originate from a large portion of fcc or from the volume of Fe islands being too small for magnetic exchange. The Fe layers of sample #83 may also be partially oxidized owing to the bad base pressure. An out-of-plane magnetization or a T_c smaller than RT may also explain the reduction. If we compare our results to the SQUID data of sample series 1 (S1), where we indeed observed that $T_c <$ RT for $d_{Fe} = 3$ ML, we can conclude that T_c being smaller than RT is probably the major contributory factor of the reduced magnetization for samples #62 and #83 around this thickness. This is also in agreement with XMCD data (Section 3.4.2).

The saturation magnetization measured by SQUID and PNR of 0.8–1.1μ_B/Fe coincides within error bars for samples S1, #62, and #83 and is much smaller than the bulk value or the value determined for sample #89. Although the samples #62 and #83 measured by PNR had drawbacks, i.e. polycrystalline growth and bad basis pressure, respectively, sample series 1 used for SQUID measurements were of good quality. Further, the results of the SQUID measurements are thought to be reliable and confirm the PNR data.

Although samples #83 and #89 both have an out-of-plane bcc Fe(110) XRD-peak (Figure 3.18b) with a FWHM $> 3°$, the intensity of the Fe peak is larger by a factor of 6.5 for sample #89 than for sample #83, despite an almost equal Fe thickness. This, together with the magnetization value of bcc Fe, indicates that sample #89 grew as a pure bcc layer. Note that an fcc portion in sample #89 could not be finally clarified by XRD (Section 3.3.4). The growth conditions of sample #89 differed to sample #83 in the improved base pressure and the permanent magnetic field of 60 mT. Both parameters could, in principle, be responsible for the different structural and magnetic properties. The good base pressure required to sputter at a very high argon flux of 25–26 sccm for sample #89 to stabilize the plasma, compared to 11 sccm for sample #83, shows that the base pressure p_0 has a strong impact on the plasma stability and therefore probably also on the growth conditions.

Most studies of the Fe/Cu(100) system were performed using MOKE, so not many absolute magnetization values were measured. An XMCD study on TD-grown films [101] determined the mean spin magnetic moment to 2.8μ_B in region I and to 0.8μ_B in region II, while the orbital magnetic moment was much smaller. The latter value is similar to the values determined by SQUID for S1 and PNR for samples #62 and #89, which indicates the formation of antiferromagnetic (AFM) fcc underlayers with a magnetic top layer as observed for region II

in TD-grown films and in region III for PLD-grown films. When measured above the Neel temperature $T_N \approx 200\,\mathrm{K}$ [5, 36] as it was in our case, the magnetization remains constant.

This would be in accordance with the XANES measurement (Section 3.3.6), the spectra of which were fitted with a very high amount of about 90% fcc Fe. Again, the PNR data could be fitted using a pure FM layer, instead of non-magnetic buried layers. The small portion of 6–11% bcc determined by XANES indicates nanomartensite, i.e. bcc Fe in the Pitsch orientation. Indications of the Pitsch orientation were found in off-surface XRD measurements of sample #38. The structural change between 3 ML and 8 ML, here indicated as differently shaded areas in Figure 3.39, does not appear in the magnetic signal of samples #62, #83, or S1. However, the position of the structural change reminds us of the transition from region I and region II for TD films, where the nanomartensitic phase changes to fcc. The intermediate phase, in which the Fe layer could be magnetized in the out-of-plane as well as in the in-plane direction is indicated by the blue arrow between 3 ML and 8 ML. A similar behavior was found for 5–7 ML films by PLD, while TD films could only be magnetized in one direction. Moreover, our XMCD measurements revealed an out-of-plane magnetization, besides for the 3 ML Fe layer, also for an 1.5 and 15 ML Fe layer. This measurement was performed at 500 mT, while the SQUID measurement was performed at only 10 mT. With the higher field, it is more probable to magnetize the thicker Fe layer perpendicular to the surface.

Overall, we can conclude that sputtered Fe/Cu(100) films show at least two different growth modes. One growth mode may be dominated by fcc Fe for the first 10 ML similar to TD- and PLD-grown films, which is hard to determine from XRD, but is evident in the XANES spectra. The reduced magnetization is in agreement with a possible fcc structure, for which the 6–11% bcc is responsible for the magnetization and may grow in the nanomartensitic phase, as discussed for TD films. The orientation of magnetization is less complex than for PLD-grown films, for which an in-plane magnetization always emerged. A transition to a pure bcc cannot be determined from our measurements. It may also be possible that both structures coexist.

We also grew one sample, in which bcc Fe seems to grow right from the beginning, already exhibiting the magnetization of bulk bcc Fe for $d_{Fe} > 1\,ML$. This can be regarded as the second growth mode. The exact origin of the different growth modes could not be clarified within the scope of the thesis. Note that the out-of-plane XRD peak of bcc Fe(110) is especially pronounced for sample series 3. These were grown without the permanent magnet, but with the improved base pressure. Thus, the latter my dominate the growth. However, the influence on the growth seems to be even more complex, since the out-of-plane bcc Fe peak of sample series 3 appeared with two different peak width, which implies a different evolution of strain.

3.6 Conclusion

In this chapter of my thesis, I demonstrated that our mobile sputtering system, together with the Selene setup, is a very powerful tool for monitoring the magnetic properties of thin films during growth. Using this method, we showed that the Fe/Cu(100) thin films can be grown with different properties. Here, the Fe grew either as bcc with the magnetization of bulk Fe of $2.2\mu_B$/Fe or with a large portion of fcc with a reduced magnetic moment of 0.8–$1.1\mu_B$/Fe. Both structures revealed an in-plane magnetization at RT for $d > 4$ ML. We found indications for the Pitsch orientation in XRD pole figures, indicating nanomartensitic structures, and a structural transition between 3 and 8 ML from XANES spectra. To verify the structural details, other *in-situ* methods, including STM or RHEED, need to be applied. Off-surface XRD measurement should also be extended.

During the last measurement at Amor combining the Selene optics with TOF, we were able to perform 13 measurements within 13 h during the growth of one sample. Here, it turned out that the sputtering process, i.e. driving guns and sample and controlling the sputter parameters, needed about the same time of 20–30 min as the measurement itself. We expect the measurement times to reduce to only a few minutes per spin state and layer in the near future, since some upgrades, i.e. a new neutron guide and the lateral displacement of components, are planned at the Amor beamline. However, one will then also have to reconsider the sputtering process to maintain a similar timescale.

Chapter 4

Structural and Magnetic Properties of MnSi(111) Thin Films

While the magnetic properties of bulk MnSi have been widely studied and are well known, controversy still surrounds discussions of the magnetic properties of MnSi thin films. Since the discovery of the first magnetic skyrmions in 2009 in MnSi [8, 102, 103], this material has been the most studied material of the B20 compounds. Skyrmions are named after the particle physicist Tony Skyrme, who proposed particle-like solutions in non-linear meson field theory [104]. This description also applies to magnetic skyrmions, which are chiral spin structures arranged as vortices with particle-like behavior. A typical hexagonal skyrmion lattice is illustrated in Figure 4.1a. This structure is repeated in parallel play to the hexagonal lattice, forming skyrmion tubes along the external magnetic field throughout the entire magnetic domain. The skyrmion lattice can be represented by three helices separated by 120°, pointing from one skyrmion to the next (Figure 4.1b).

Such skyrmion lattices have attracted great interest in the context of new applications. For instance, small-angle neutron scattering demonstrated that tiny electric currents generate spin transfer torques sufficient to induce a motion of the skyrmion lattice [9]. The current densities required are five magnitudes smaller than for conventional domain motion. Moreover, since skyrmions cannot be continuously transformed into a ferromagnetic state or a different magnetic structure without being destroyed, they are topologically protected and therefore provide stability [105]. Overall, skyrmions are stable structures which can be easily driven by tiny electric currents — properties which are predestined for magnetic storage media, provided they can be realized in thin films. Additionally, initial investigations of B20 systems with reduced dimensionality imply an extension of the skyrmion phase compared to bulk, as it seems to exist partially also in zero magnetic field (Section 4.1). Hence, thin films play a central role for future applications. It is therefore of great interest to explore the evolution of the magnetic structure in epitaxial MnSi thin films, which will be the aim of this chapter. The upcoming importance of skyrmions in thin films is reflected in the increasing number of

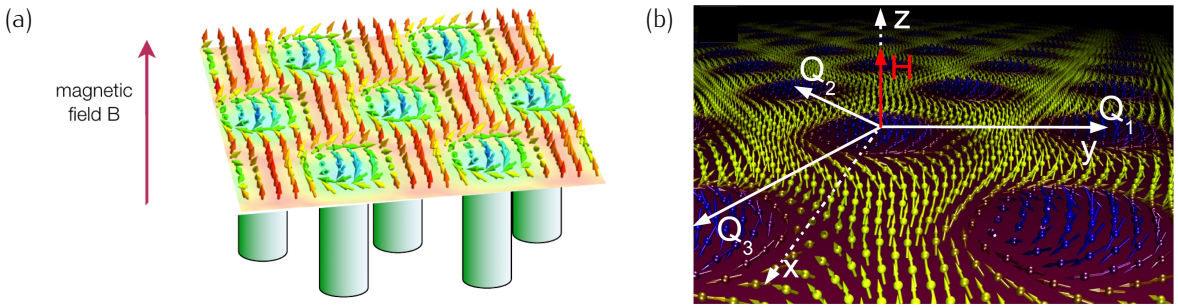

Fig. 4.1: *(a) Schema of a hexagonal skyrmion lattice forming skyrmion tubes along* $\boldsymbol{B}$ *as illustrated by Markus Garst (Source: [106]). (b) Triple helix structure of the skyrmion lattice indicated in real-space, with each helix being separated by* 120° *(Source: [107]).*

publications in the last two years concerning this topic.

We focused on in-plane magnetic field configuration using neutron scattering for magnetic characterization, especially grazing incidence small-angle scattering (GISANS) (Section 2.2.1). This is a powerful tool to directly investigate the wavevector of a magnetic structure, as it has already successfully been used for bulk MnSi [8]. So far, no one has used this technique on B20 thin films. In addition, we used off-specular reflectometry (OSR), a technique tailored for thin films (Section 2.2.3). This allowed us to measure the wavevector of a magnetic structure directly. Finally, we carried out polarized neutron reflectometry (PNR) as an indirect method (Section 2.2.2). Using this method, we achieved a study of a very sensitive magnetic depth profile, giving us additional information about the spin direction. From this combination of scattering techniques, we obtained a microscopic picture of the magnetic structure of epitaxial MnSi thin films. The investigations were supported by SQUID-VSM measurements by Shilei Zhang (University of Oxford).

In the first Section 4.1, I will give a literature overview, briefly introducing the properties of bulk MnSi and presenting the latest findings on skyrmions in reduced dimensionality. For this, I will focus on epitaxial MnSi(111) thin films. Section 4.2 introduces our MnSi(111) thin film samples grown by Thorsten Hesjedal (University of Oxford) and their structural characterization. In Section 4.3, the neutron-scattering experiments are described, including some overall considerations and the detailed setup of the used neutron beamlines, NREX and SANS1, at the neutron source Forschungsreaktor München II (FRM II), Heinz Maier-Leibnitz Zentrum (MLZ), Munich. Here, I also specify the data analysis procedure for each measurement technique used. The results measured in an in-plane magnetic field via neutron scattering are presented in Section 4.4 and discussed in Section 4.4.6, where I will also briefly discuss the configuration with an out-of-plane magnetic field. Finally, Section 4.5 summarizes our findings and draws a conclusion.

4.1 MnSi in Different Dimensions — a Literature Review

In the first two sections, I will briefly define the B20 material group (Section 4.1.1) and outline the well established phase diagram of bulk MnSi (Section 4.1.2). Afterwards, I will review the research conducted on the influence of reduced dimensionality on skyrmions (Section 4.1.3) realized as thin crystal plates, as epitaxial thin films and as nanowires. The final Section 4.1.4 focuses on the experimental results and on theoretical approaches for epitaxial MnSi(111) thin films.

4.1.1 B20 Crystal Structure

MnSi crystallizes in a non-centrosymmetric cubic B20 structure with space group $P2_13$ and a lattice constant of 4.56 Å [107]. Owing to the lack of inversion symmetry, the crystal structure can appear right- or left-handed. As described in the next section, this also results in an additional term in the free energy density — the Dzyaloshinskii-Moriya interaction. It gives rise to a complicated magnetic behavior, during which incommensurable helical structures, including skyrmions, emerge. Materials crystallizing in a B20 structure are therefore also called chiral helimagnets. They exhibit very similar magnetic phase diagrams. Representatives of this B20 structure are, in principle, monosilicides and monogermanides, i.e. MnSi, $Mn_{1-x}Fe_xSi$, $Mn_{1-x}Co_xSi$, FeGe, MnGe, and the insulator Cu_2OSeO_3 [108].

4.1.2 Magnetic Properties of Bulk MnSi

At first glance, MnSi is an itinerant ferromagnet. But its magnetic behavior has been discovered to be much more complex. All phases are summarized in a B-T phase diagram in Figure 4.2. When cooling bulk MnSi from room temperature in a zero magnetic field, a paramagnetic to helimagnetic transition occurs at $T_c = 29.5\,\mathrm{K}$ [8]. Here, the spins rotate in the plane perpendicular to the propagation direction of the helix. The helices are left-handed, with a length of $L_H = 18\,\mathrm{nm}$ [107]. Furthermore, applying a magnetic field of $B_{c1} = 0.1\,\mathrm{T}$ gives rise to a transition to the conical phase, where the wavevector $\boldsymbol{k_H}$ of the helices aligns along the field direction and the spins start to cant towards $\boldsymbol{B}$ until the ferromagnetic state is reached at high fields above 0.55 T. The critical field of this transition, i.e. B_{c2}, drops with increasing temperature. In the regime of the conical phase, the phase diagram includes the first example of a new form of magnetic order composed of topologically distinct spin solitons — the skyrmion lattice [8], which is illustrated in Figure 4.1a. The evolution of these magnetic properties is controlled by four different energy scales, which are described near T_c within the frame of Ginzburg-Landau theory [8, 109, 110] by the free energy density F:

$$F[\boldsymbol{M}] = \int d^3r[r_0\boldsymbol{M}^2 + J(\nabla\boldsymbol{M})^2 + U\boldsymbol{M}^4 + 2D\boldsymbol{M}\cdot(\nabla\times\boldsymbol{M}) - \boldsymbol{B}\cdot\boldsymbol{M} + h.O.], \quad (4.1)$$

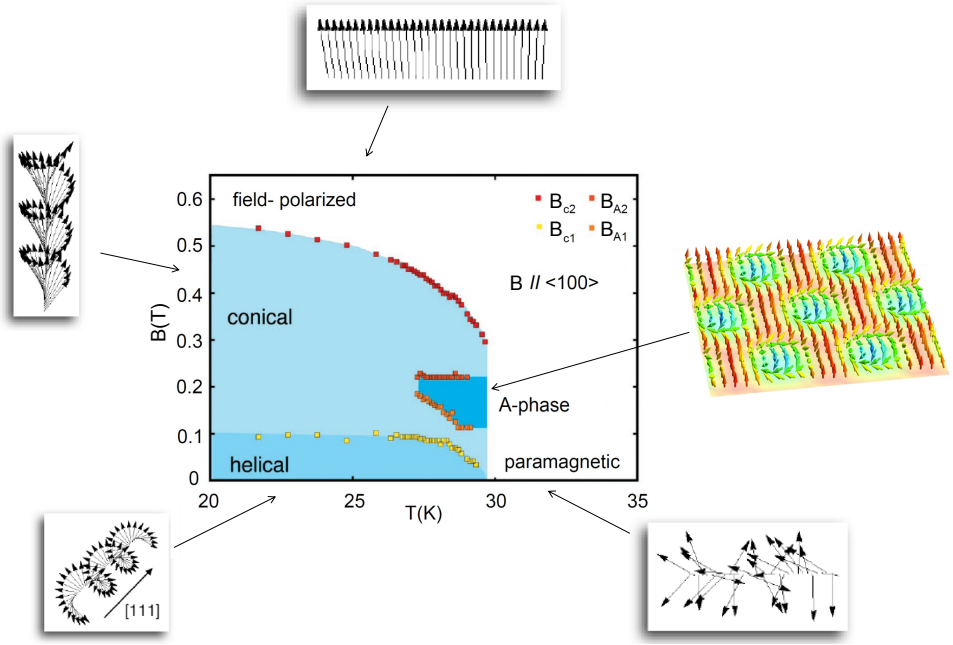

Fig. 4.2: *B-T phase diagram of bulk MnSi showing the magnetic phases. Below $T_c = 29.5\,K$ and at small magnetic fields, the spins align helically with $\boldsymbol{k_H} \,||\, <111>$. Above $B_{c1} \leq 0.1\,T$ the helices rotate to $\boldsymbol{k_H} \,||\, \boldsymbol{B}$, with the spins starting to tilt towards $\boldsymbol{B}$. Above B_{c2}, the ferromagnetic phase is reached. In a small pocket below T_c, the skyrmion phase, also called A-phase, is stabilized. (adapted from: [8, 106], illustrations by Markus Garst)*

where the second term represents the ferromagnetic exchange (FM), with J the stiffness. This term favors the spins to align in parallel. The fourth term accounts for the Dzyaloshinskii-Moriya (DM) interaction with the coupling constant D, which is due to spin-orbit-coupling and arises from the lack of inversion symmetry of the crystal. This term favors the spins to align perpendicular. Based on this ansatz, the minimization of the functional leads to the emergence of helical order [111]. The fifth term represents the Zeeman energy, which favors the spins aligning parallel to the magnetic field. Higher order terms are summarized in h.O..

The propagation vectors in the helical phase were determined to pin to the <111> direction. This pinning is caused by the h.O. term, which contributes to the free energy density and considers higher order spin-orbit coupling stemming from the crystal lattice [109, 111]. In the case of a cubic lattice, this results in the magnetocrystalline anisotropy

$$\Delta F^{(4)} = \lambda_1 \sum_q (\hat{q}_x^4 + \hat{q}_y^4 + \hat{q}_z^4)\,|\boldsymbol{m_q}|^2 + \lambda_2 \int M_x^4 + M_y^4 + M_z^4 \tag{4.2}$$

This term is small compared to the previous ones and a magnetic field of just 0.1 T destroys this pinning and rotates the propagation vector of the helices along the magnetic field.

This brief summary does not tackle with the complexity of the magnetic properties. Bulk MnSi has been studied for decades [112–114] and was the focus of even more interest after

the discovery of the skyrmion lattice in 2009 [8]. This has led to intense investigations in terms of, for example, the topological Hall effect (THE) [9, 115], the direct observation of the skyrmion lattice by magnetic force microscopy (MFM) [116], collective excitations of the different magnetic structures [117, 118], and investigations under uniaxial pressure [119, 120]. An overview of the immense quantity of results can be found in [105, 108, 121].

4.1.3 Skyrmions in Reduced Dimensionality

Key issues for the exploitation of the magnetism in epitaxial thin films are the role of surface and shape anisotropy, the effects of strain, and finite size effects. These mechanisms result in uniaxial anisotropy with either easy-plane or easy-axis character. And all these mechanisms may be strong enough to modify the magnetic structure radically. A first step towards the understanding of the magnetism of epitaxial thin films is the understanding of the magnetism in freestanding thin crystal plates, for which, at least, a contribution of epitaxial strain can be excluded.

Thin Crystal Plates. Thin plates obtained from B20 bulk single crystals form a system with low dimensionality in one direction. Thus, shape anisotropy based on the long ranged magnetic dipolar interaction or finite size effects may play an important role. Additionally, an increase of the ratio of surface to volume atoms can cause the surface anisotropy to dominate.

Tonomura *et al.* [122] investigated a thinned MnSi crystal with a thickness of 50 nm in an out-of-plane magnetic field using Lorentz TEM. As depicted in Figure 4.3a, the authors observed the propagation vector of the helices to lie in-plane (top), whereas the conical phase (bottom) is totally suppressed. This suppression may be caused by surface anisotropy or by strain induced from the thinning. Although $d_{MnSi} > L_H$, finite size effects can not be excluded. The Lorentz TEM images (Figure 4.3b) reveal the same helix length L_H as in bulk MnSi of 18 nm. The lefthand image was recorded in the helical phase at 0 T and the righthand image in the skyrmion phase at 0.18 T. Compared to bulk, they found a decrease of T_c by 7 K and a more extended skyrmion phase, which even persists below 10 K and up to T_c for a wide field range — from 0.18 to 0.4 T (middle panel of Figure 4.4a).

Lorentz TEM was also used to study two other B20 materials, i.e. $Fe_{0.5}Co_{0.5}Si$ [123] and FeGe [124], in the form of thin crystal plates in an out-of-plane magnetic field. An extended skyrmion lattice was found here too, as well as an in-plane helical state exhibiting the same helix wavelength as in bulk. While the sample of $Fe_{0.5}Co_{0.5}Si$ had a thickness of 90 nm, the sample of FeGe was wedge-shaped allowing a thickness-dependent investigation. The authors observed that, instead of the conical phase, the skyrmion lattice was increasingly favored with decreasing FeGe thickness from 75 to 15 nm. The suppression of the conical phase as depicted at the bottom of Figure 4.3a may be primarily because the helices cannot form one integer repetition along the film normal in the reduced layer thickness of $d_{MnSi} \leq L_H$ with the helix lengths $L_H = 70$ nm for FeGe and $L_H = 90$ nm for $Fe_{0.5}Co_{0.5}Si$. Although in

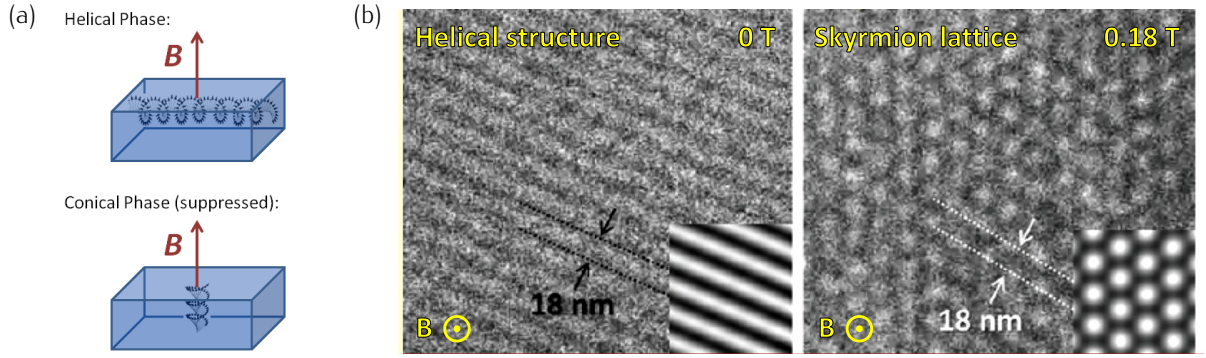

Fig. 4.3: (a) Schemes of the helical phase (top) and the suppressed conical phase (bottom) in a MnSi crystal plate observed in a vertical magnetic field using Lorentz TEM. (b) Corresponding Lorentz TEM images from the helical phase at 0 T and the skyrmion phase at 0.18 T. Insets are filtered images. (Source: [122])

those studies the helix periodicity was determined to be the same as in bulk, a reduction of the pitch from 62 to 50 nm was spotted in ca. 100 nm thick Cu_2OSeO_3 crystal plates [125]. This study also identified an extended skyrmion phase using Lorentz TEM for the direct observation in real space.

However, these systems do not experience uniaxial strain, as is the case for epitaxially grown thin films. Additionally, the surface anisotropy is modified by the adjacent material, e.g. the Si substrate, and not by air as for thin plates. Therefore, different magnetic behavior is expected than for bulk samples or thin plates, and those differences can be solely attributed to the additional anisotropies: strain or/and interface anisotropy.

Skyrmions in Thin Films. Several recent publications proved the existence of skyrmions in epitaxial thin films. One monolayer of Fe deposited on an Ir(111) surface revealed a skyrmion lattice, which was imaged by spin polarized STM (SP-STM) [126]. Romming *et al.* were able to create and destroy single skyrmions in a PdFe bilayer via a spin polarized STM (SP-STM) tip [127]. Another creation of single skyrmions was achieved by a pulsed laser beam irradiating on a 20 nm amorphous $Tb_{22}Fe_{69}Co_9$ film [128].

As already mentioned above, epitaxial thin films of B20 materials have also drawn considerable attention because of their magnetic properties. MnSi(111) thin films are the most studied B20 thin films for magnetic properties. This will be further discussed in Section 4.1.4.

In an out-of-plane magnetic field, Huang *et al.* [129] found an extended skyrmion phase compared to bulk by measuring the Hall resistivity of epitaxially grown FeGe(111) thin films with 18–300 nm thickness. The resistivity arising as a result of THE was deduced by subtracting a fit of the resistivity taking into account the normal and anomalous Hall effect. Using this method, Huang *et al.* found the skyrmion phase, associated with the high THE signal, to exist even in zero field, with B_{c2} being 10 times higher than bulk B_{c2}. The authors

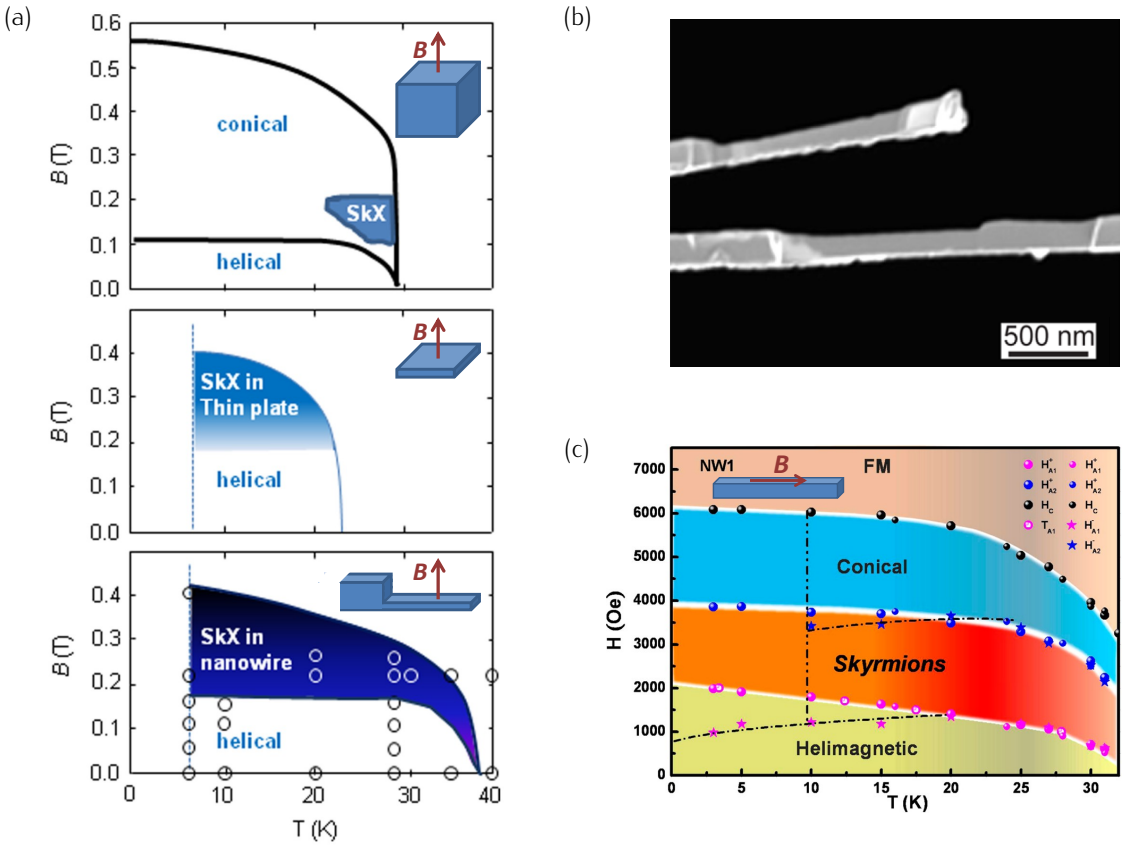

Fig. 4.4: *(a) Magnetic phase diagram of a MnSi crystal in different forms (from top to bottom): as bulk (3D), as a thin plate (2D), and as a single nanowire thinned to 50 nm (1D) as shown in (b) (adapted from [130]).* $\boldsymbol{B}$ *was applied perpendicular to the film or nanowire. (c) Phase diagram for MnSi nanowire with a width of 410 nm and* $\boldsymbol{B}$ *parallel to the nanowire axis (adapted from [131]). In all cases of low dimensionality, the skyrmion phase (Skx) is extended compared to bulk.*

determined T_c to be 271 K, thus 7 K smaller than in bulk.

Yokouchi *et al.* [132] also performed Hall measurements in a perpendicular magnetic field on $Mn_{1-x}Fe_xSi$ thin films with thicknesses 10 nm$\leq d \leq$ 20 nm and $0 \leq x \leq 0.04$. To distinguish the THE signal from the normal and anomalous Hall effect, they studied the signal at several small inclination angles of the sample relative to the magnetic field. At a critical angle, the skyrmion lattice vanishes, and with it the THE signal. Hence, the difference in signal can be attributed to the pure THE. Using this procedure, the authors established a B-T phase diagram of the skyrmion phase. It appeared to be wider than for bulk, increasing further for $d < 15$ nm, which is in the order of the helical period. Additionally, they observed T_c to be 5-25 K larger, depending on doping, than in bulk.

Porter *et al.* [133] carried out initial magnetoresistance and magnetometry measurements on epitaxial FeSi and $Fe_{0.5}Co_{0.5}Si$. The latter exhibits a T_c of 61 K. By applying an in-plane magnetic field, the same group recently used PNR to observe helices with a period of 9.3 nm

directed along the film normal in a 50 nm $Fe_{0.7}Co_{0.3}Si$ film [134]. Additionally, the authors performed Hall measurements with an out-of-plane field and detected a signal varying as a function of B and T. Strain in 50 nm $Fe_{1-x}Co_xSi$ epitaxial layers was examined in detail in [135]. The samples were determined to exhibit in-plane tensile strain, resulting in an out-of-plane compressive strain. The magnitude of the strain in both directions increased with increasing doping. T_c increased with doping up to $x = 0.4$ to 77 K and dropped again above 77 K. Similar behavior was observed for bulk, but in epitaxial films T_c was always larger than the bulk value.

Skyrmions in Nanowires. A further reduction of the dimensionality to quasi 1D can be achieved by growing nanowires. Single MnSi nanowires with a length of several μm were grown by chemical vapor deposition (CVD). They exhibited a rhombus as cross section with a width between 200 nm and 410 nm [130, 131]. Yu *et al.* [130] used a focused ion beam (FIB) to thin the nanowire and to produce a rectangular cross section with a thickness of only 50 nm. By applying a magnetic field perpendicular to the thinned surface, they observed an in-plane helical phase with the same pitch as in bulk as well as a skyrmion lattice using Lorentz TEM. The phases are depicted in the bottom phase diagram of Figure 4.4a. T_c, with a value of 35 K, is higher and the skyrmion phase is larger than for bulk (upper panel). Nevertheless, T_c also differs to that of a thinned crystal (middle panel). The insets illustrate the magnetic field orientation relative to the sample.

In contrast, Du *et al.* [131] did not change the cross section of their nanowire after growth and applied the magnetic field along the wire axis. Magnetoresistance (MR) measurements featured kinks similar to the MR measurements obtained from bulk indicated the skyrmion phase. By tracking those kinks in the resistance measured vs. B or T, the authors obtained the phase diagram of Figure 4.4c. T_c was determined to be 32 K, which is similar to the value obtained by Yu *et al.* The skyrmion phase is extended as well, down to 3 K, and the transition from helical to skyrmion phase is also similar to the results of Yu *et al.* But by contrast, they observed a conical phase above the skyrmion phase, which is not visible in the phase diagram of Yu *et al.* This may be due to the lack of data points measured by Lorenz TEM, the different applied field direction, the spatial confinement in the thinned nanowire, or additional strain arising from dislocations produced by the FIB.

Theoretical Studies Recently, theoretical studies on the formation of skyrmions in two dimensions have also been published. Manipulation of the skyrmion via a current was discussed in [136, 137], while other groups reported on the formation of skyrmions in a single nanodisk as a function of its radius [138] and on artificial skyrmions in an array of nanodisks stabilized in wide temperature and field ranges without the need for DM interaction [139].

4.1.4 Epitaxial MnSi(111) Thin Films

MnSi typically grows along its <111> direction on Si(111) substrates. To overcome the large lattice mismatch between MnSi with $a_{MnSi} = 4.561$ Å and Si with $a_{Si} = 5.431$ Å, MnSi

grows with a lattice rotation of 30° and its <110> parallel to Si <112> on the Si substrate [140–142]. This leads to tensile strain of $(a_{MnSi}cos(30°) - a_{Si})/a_{Si} = -3.2\%$ [141, 142]. Those MnSi(111) thin films are usually grown epitaxially by thermal deposition using either solid phase epitaxy (SPE) [140–144], where Mn or a Mn/Si multilayer is annealed to form MnSi or by molecular beam epitaxy (MBE) [10, 13, 145, 146], where Mn and Si are deposited simultaneously followed by annealing at 400°C. In the latter case, few monolayers of Mn have to be annealed on the Si substrate to form a MnSi seed layer prior to the co-deposition of Mn and Si.

Karhu *et al.* reported a reduction of roughness by a factor of two when using MBE instead of SPE [145]. Both methods result locally in the formation of $MnSi_{1.7}$ precipates with a diameter of up to a few hundred nm [140, 145]. Films with fractions of $MnSi_{1.7}$ up to 11% still show a similar T_c of 41.4–44.0 K [147]. Samples containing more than 20% show different in-plane and out-of-plane strain [147]. Karhu *et al.* investigated the strain of the samples grown by SPE [140] and by MBE [147] as a function of thickness using XRD for the determination of out-of-plane strain and using a TEM technique for the determination of in-plane strain. The MBE grown samples show a slightly higher in-plane strain between 0.5% and 1.2% and slightly higher absolute values of out-of-plane strain between -0.25% and -0.5%. A further important observation of the same group using TEM, was the finding of domains with right-handed and left-handed crystal structure [140, 145].

This group also investigated the magnetic properties. Due to surface anisotropy, strain, and shape anisotropy, a uniaxial magnetic anisotropy develops, with the out-of-plane axis either the hard or easy axis for the magnetization. Karhu *et al.* found higher saturation fields for a magnetic field applied out of plane compared to in plane [140, 147]. This indicates a hard axis, i.e. easy-plane anisotropy. Consequently, for a helical ground state, one would expect the k_H-vector to align out of plane. This would allow the spins to lie in plane following the easy-plane anisotropy of the magnetization. This was also supported by the same group when plotting the remanence normalized by the saturation magnetization as a function of MnSi thickness, which was measured after applying a high in-plane field of 5 T [145]. The curve shows oscillatory behavior with a remanence dropping to zero for certain thicknesses. This could be explained by helices propagating along the film normal and a fixed helix length, resulting in the cancellation of the total in-plane moments for an integer number of helices fitting into the film. If the thickness is not an integer multiple of the helix pitch, not all moments cancel out and contribute to the remanence. From this oscillatory behavior of the remanence as a function of thickness, the authors fitted the helix pitch to 13.9 nm. They describe this as being the ground state and independent of the MnSi thickness. Their fit is better for the MBE grown samples than for the SPE grown samples, probably owing to heterogeneities [145]. As a consequence, they performed subsequent investigations only on the MBE grown samples.

Given the uniaxial anisotropy, different magnetic properties for in-plane and out-of-plane magnetic fields are expected. For this reason, I will discuss both configurations separately.

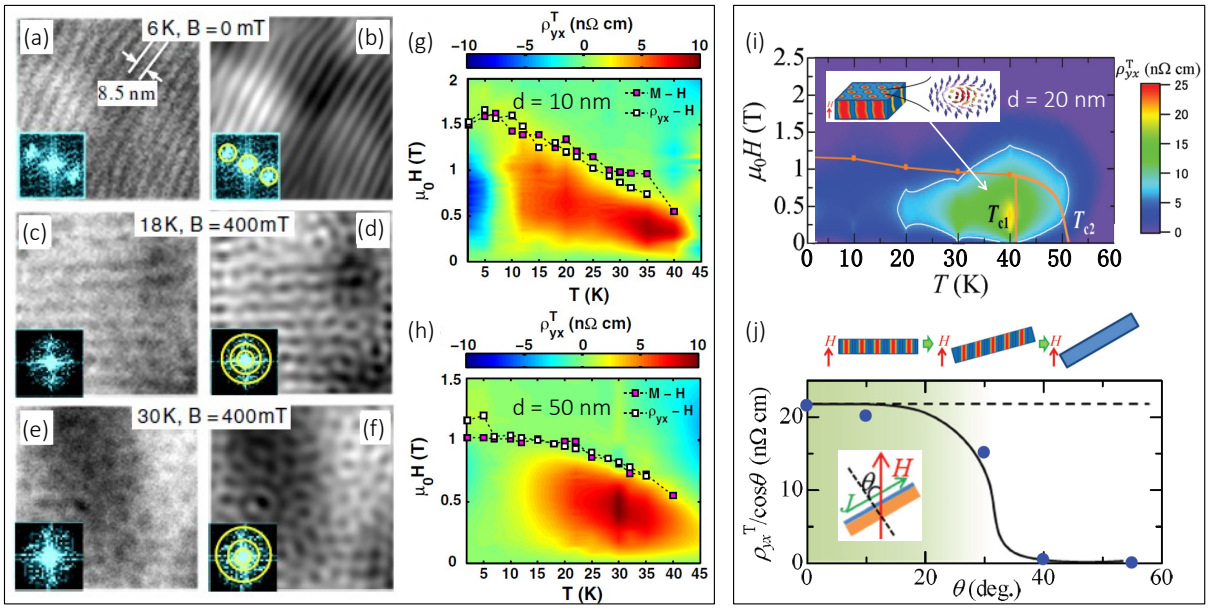

Fig. 4.5: $\boldsymbol{B}$ *out of plane: (a)–(f) Lorentz TEM images of a 10 nm epitaxial MnSi film at 0 T and at 400 mT. The lefthand column shows the raw data, and the right column shows the filtered images. The insets depict the fast Fourier transforms of the real-space images. The Hall-effect signal is plotted as a color map in a B-T-diagram for a 10 nm sample (g) and for a 50 nm sample (h) (Source: [13]). (i) Topological Hall effect (THE) signal extracted from the Hall signal and plotted as color map in a B-T-diagram for a 20 nm MnSi sample. A high THE signal gives rise to a skyrmion lattice, as depicted in the inset. The phase diagram is in good agreement with (g) and (h). The extraction of THE signal was performed by studying the Hall effect signal as the sample was tilted relative to* $\boldsymbol{B}$*, as depicted in (j). Here, the skyrmion lattice vanishes for an sufficiently large angle. The difference in the Hall effect signal reveals the THE signal, which drops as a function of tilt angle (Source: [132]).*

T_c, however, was observed to be independent of the magnetic field direction and of the MnSi thickness. It was determined to be 45 K in [13] and to be 41.6–44 K in [10].

$\boldsymbol{B}$ out of plane. Li *et al.* [13] identified a skyrmion lattice at 400 mT for 18 K and 30 K and a helical phase in zero field at 6 K with k_H in plane and a pitch of 8.5 nm using Lorentz TEM (Figure 4.5a–f). This group was the first and, so far, the only group to observe the skyrmions in epitaxial B20 films in real space. To form a phase diagram, they measured the Hall effect and plotted its signal as function of B and T for a 10 nm (Figure 4.5g) and 50 nm (Figure 4.5h) MnSi film. A high Hall resistivity, probably due to an additional THE signal, covers a wide region of the phase diagram from 10 to 40 K, indicated in red. Comparison to the Lorentz TEM images identified this region as the skyrmion phase.

This in good agreement with the phase diagram of a 20 nm MnSi film observed by Yokouchi *et al.* [132] of the same group and shown in Figure 4.5i, with the pure THE signal illustrated

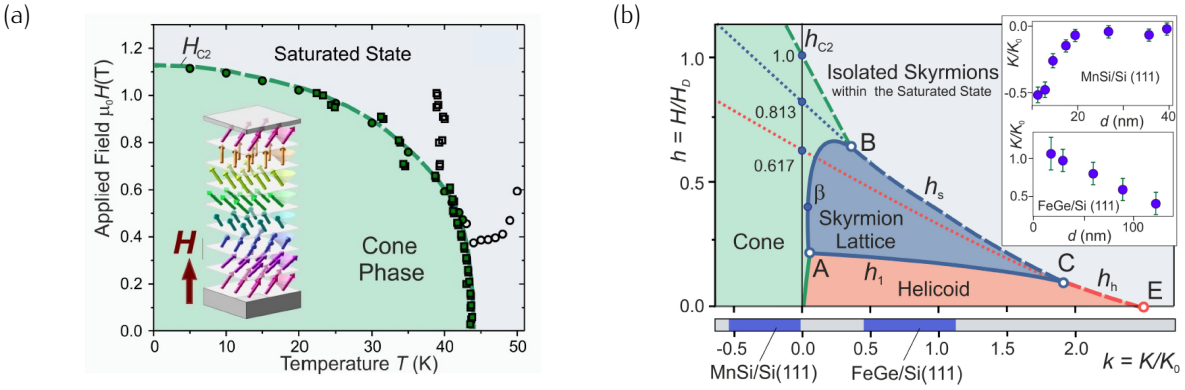

Fig. 4.6: ***B*** *out of plane: (a) B-T phase diagram for MnSi, independent of thickness, as proposed by Wilson et al. (b) Corresponding theoretical B-K_u phase diagram generalized for all B20 systems as a function of the uniaxial anisotropy K_u. H_D = 0.77 T±0.05 T [11] is the critical field of the transition to the ferromagnetic state for K_u = 0 and K_0 the effective anisotropy. Due to the negative K_u of MnSi, only the conical phase can establish additional to the paramagnetic or ferromagnetic state. Since FeGe has a positive K_u, a helical phase, a skyrmion phase and isolated skyrmions can also occur in this material. (Source: [12])*

as color plot. For high THE signal, the expected skyrmion structure is shown in the inset. To distinguish the pure THE signal from the normal and anomalous Hall effect, the authors measured the signal while tilting the sample relative to the magnetic field. They found that the skyrmion lattice vanishes for a sufficiently large angle, as schematically depicted in Figure 4.5j. The difference in the Hall signal before and after the vanishing of the skyrmion lattice can be attributed to the THE signal. The THE signal drops as a function of tilt angle θ.

By contrast, Wilson *et al.* [12] predicted a pure conical phase with a helical length of 13.9 nm and therefore the absence of the skyrmion phase as depicted in Figure 4.6a. This was determined by the oscillation of the remanence in [145], as discussed above. They calculated the solutions for the magnetic structure by minimizing the energy functional for an out-of-plane magnetic field consisting of the FM, DM, and Zeeman terms as well as the uniaxial and magnetocrystalline anisotropy. This ansatz does not include shape anisotropy. The exchange stiffness constant J of the FM term and the coupling constant D of the DM term were determined by their ground state helix length of 13.9 nm. Possible solutions of the free energy density were an in-plane helicoid, an out-of-plane cone, an in-plane skyrmion lattice and isolated in-plane skyrmions.

Using a different ansatz without the cubic anisotropy, but including the shape anisotropy, the same group obtained only one possible solution for the out-of-plane field, that is the out-of-plane cone phase, as was published in an earlier paper [147]. The occurrence of all solutions was a function of the uniaxial anisotropy K_u. This is illustrated in the H-K_u phase diagram in Figure 4.6b. Owing to the easy-plane anisotropy, which is defined in this paper by a negative K_u, it is not possible to reach the skyrmion phase, but only the cone phase. In contrast, FeGe possesses a hard axis anisotropy, i.e. a positive K_u, and a skyrmion lattice

is expected according to this phase diagram. Indeed, a skyrmion lattice was observed in the Hall signal in [129] as mentioned above (Section 4.1.3). Wilson *et al.* supported their theory by magnetization measurements. They argued from the lack of peaks in dM/dH as a function of H and of T that no first-order transitions occur. In addition, they did not find a hysteresis in the magnetoresistance, which was typical for the skyrmion phase in bulk. In a previous paper published by the same group, the authors had already stated the existence of the cone phase with helices propagating along the sample normal [145]. They drew that conclusion from polarized neutron reflectometry (PNR) measurements with an out-of-plane field of 0.2 T and 0.6 T. They observed a peak in both spin-flip channels at $2\pi/13.9$ nm corresponding to the wavevector of the conical phase with a cone angle of $\leq 54°$. However, the signal was very weak, and they only presented two measurements that exhibit this feature. Some collaborators, i.e. Monchesky *et al.*, comment on Li *et al.*'s Lorentz TEM images, stating the results to be artifacts from the microscope [148] and demonstrate how to obtain similar images through misuse of the technique. Li *et al.* reject the reproach in [149].

The saturation magnetic field at 5 K drops from 1.4 to 1.0 T for increasing MnSi thickness from 10 to 40 nm. This in good agreement to Li *et al.*, who obtained similar values for the 10 nm and 50 nm films (Figure 4.5).

The contradiction between the publications of Li *et al.* and Yokouchi *et al.* on the one side and Wilson *et al.* on the other concerning the magnetic structure of MnSi thin films in an out-of-plane field cannot be solved within the scope of this thesis, as experiments using this field configuration did not show any magnetic signal (Appendix). However, I will discuss those measurements, compare our results to those publications, and draw some conclusions at the end of this thesis (Section 4.4.6).

$\boldsymbol{B}$ in plane. Karhu *et al.* published calculations minimizing the energy functional as described above, this time including shape anisotropy but no cubic anisotropy. This leads to three solutions for an in-plane field: an in-plane helicoid, a distorted cone lying in-plane and a distorted skyrmion lattice with the three k_H-vectors lying perpendicular to the plane [147]. The solutions are again a function of uniaxial anisotropy. Each phase has to be entered by increasing the field to the ferromagnetic state for a wide range of uniaxial anisotropies. The corresponding H-K phase diagram is plotted in Figure 4.7a. This time the easy-plane anisotropy is defined as positive K, in contrast to the negative K in Wilson *et al.*'s paper discussed above [12].

However, the data measured by polarized neutron reflectometry (PNR), presented by Karhu *et al.* in the very same paper [147], does not confirm their theoretical results. Figure 4.8a illustrates a typical PNR setup with an in-plane field. As described in Section 2.2.2, the spin channels of the reflectivity R++ and R-- are sensitive to the magnetization component parallel to the spin polarization, here M_x, while R+- and R-+ are sensitive to M_y. In the case of equally distributed right- and left-handed helices, the magnetization profiles form a sinusoidal shape (Figure 4.8c) in $M_x(z)$, while the M_y component is canceled out. Figure 4.8b

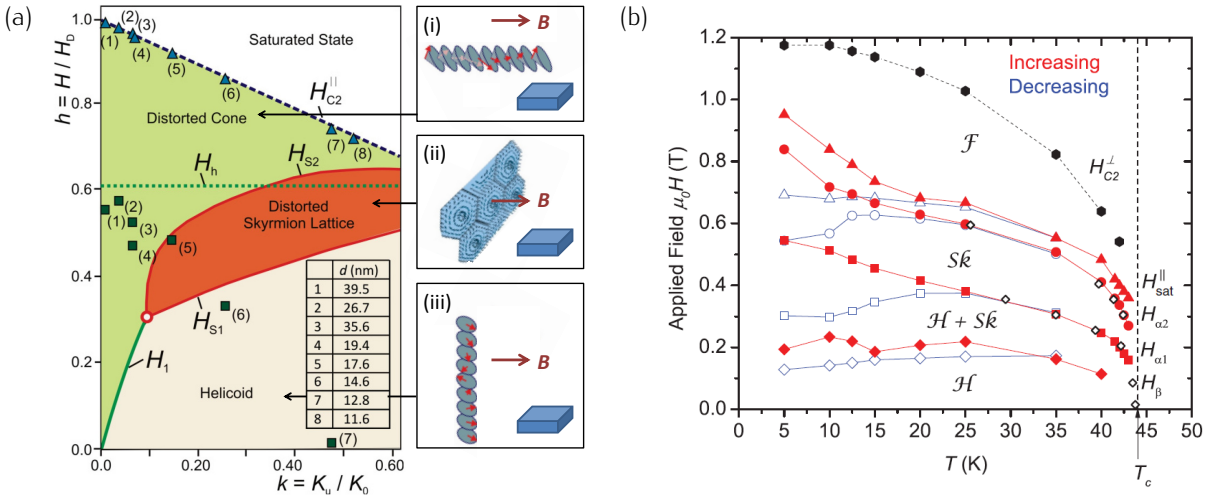

Fig. 4.7: ***B*** *in plane: (a) Theoretical H-K_u phase diagram generalized for all thicknesses as a function of the uniaxial anisotropy K_u. H_D = 0.77 T±0.05 T [11] is the critical field of the transition to the ferromagnetic state for K = 0 referring to bulk (Source: [147]) and K_0 the "effective stiffness". The spins possibly arrange as distorted cones lying in the sample plane (i), as distorted sykrmions with the three k_H-vectors perpendicular to the plane (ii) or as helices propagating out-of-plane (iii) (adapted from [147]). (b) B-T phase diagram of a 26.7 nm MnSi film, obtained from peaks in the static susceptibility for increasing and decreasing magnetic fields, consists of a helical phase, a skyrmion phase and a mixture thereof and is therefore distinctly different from the prediction of (a) (Source: [10]).*

shows the PNR data of a 26.7 nm MnSi sample measured by Karhu *et al.* [147]. R+- and R-+ do not show a signal, which confirms the equal distribution of right- and left-handed helices. By fitting the reflectivities R++ and R--, they found a helical phase at 6 K and 1 mT (top panel), which appears as a sinusoidal magnetic depth profile as shown in the right column. As the magnetic field is increased (from top to bottom panel of the right column), more and more spins align parallel to it and the profile deviates from a clear sinusoidal shape by developing plateaus and forming a soliton-like shape. The oscillatory behavior along the film normal still shows the nature of a helix propagating perpendicular to the surface. At a field of 0.8 T (bottom panel) the magnetic moment remains constant through the film depth, associated to the ferromagnetic state or, as they write, to an in-plane conical phase. However, for that sample — due to its specific uniaxial anisotropy — their theory predicted an in-plane conical phase for fields much smaller than 0.8 T, as can be seen from Figure 4.7a, in which the 26.7 nm sample is labeled with the number (2). This publication itself is therefore inconsistent. Note that the value of the uniaxial anisotropy K_u of each sample was calculated via the saturation fields for out-of-plane and in-plane magnetic fields as well as for their ground-state helix pitch of 13.9 nm. This means that their entire theory is based on this experimental value, which in turn determines A, D and K_u.

Wilson *et al.* of the same group then published a phase diagram (Figure 4.7b), which exhibits a helical phase, a mixed phase consisting of helices and skyrmions and a pure skyrmion phase.

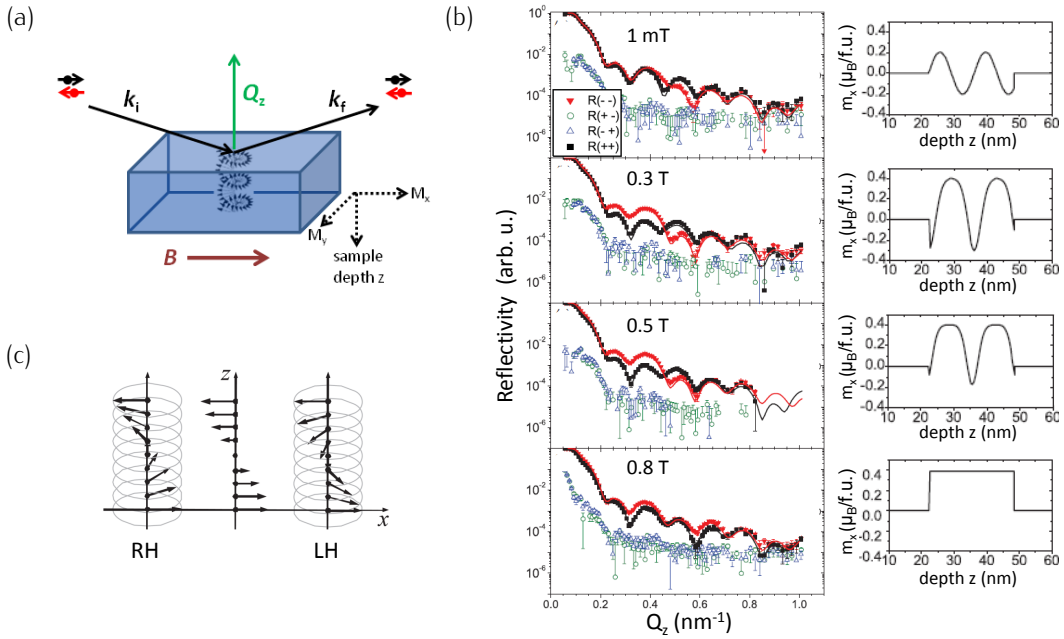

Fig. 4.8: *(a) Schema of PNR in an in-plane magnetic field resulting in helices directed along the surface normal. $R^{++}(Q_z)$ and $R^{--}(Q_z)$ are sensitive to the magnetization component $M_x(z)$, while $R^{+-}(Q_z)$ and $R^{-+}(Q_z)$ are sensitive to $M_y(z)$. (c) Left-handed (LH) and right-handed (RH) helices contribute to $M_x(z)$. If helices of both chiralities are equally distributed, the M_y component canceled out (Source: [150]). (b) Reflectivity data (symbols) of a 26.7 nm MnSi thin film as function of Q_z measured for all four spin channels at 6 K and in an in-plane magnetic field ranging from 1 mT (top) to 0.8 T (bottom). The figures of the right column show the depth profiles, i.e. magnetic moment in x-direction as function of z, corresponding to the fits (lines) of the reflectivties. As the magnetic field increases, the profiles deviate from a pure sinusoidal shape, with an increasing number of spins aligned parallel to the magnetic field. (Source: [147]).*

The phase transitions were determined by magnetometry measurements [10] tracking peaks in dM/dH vs. H, while the identification of the phases was only based on theory. Although this theory was adapted from the previous paper, they did not comment on the contradiction between their experimental results and the theoretical phase diagram of the previous paper illustrated in Figure 4.7a, where the distorted conical phase was predicted.

In their recent paper, Wilson *et al.* [11] applied a new approach for an in-plane field, minimizing the energy functional consisting only of the FM, DM, and the Zeeman term, which is reduced for helicoids propagating along the film normal with $\boldsymbol{m} = \boldsymbol{M}/M_s$ being the unit vector of the magnetization and $\boldsymbol{m} = (sin\theta, cos\theta, 0)$:

$$\omega(\theta) = J\left(\frac{d\theta}{dz}\right)^2 - D\frac{d\theta}{dz} - H\,M_s\,cos\,\theta, \tag{4.3}$$

where J is again the exchange stiffness and D the DM coupling constant, which are related by

$J/D = 2\pi/13.9\,\text{nm}$. The authors calculated the solutions by minimizing this energy density in a layer of finite thickness with free boundary conditions. They argue that owing to the Zeeman energy, the moments in the center of the film have to be aligned parallel or antiparallel to the magnetic field, and they use this as a condition for the solutions. The solutions for a 29.7 nm MnSi film result in helices as depicted in Figure 4.9a. The pitch of the helix switches as a function of magnetic field. The authors calculated the critical fields for a sample with a thickness of 29.8 nm in [11]. Here, the helix performs 2.0 turns for magnetic fields up to 0.22 T, 1.5 turns up to 0.46 T and above this value only 0.5 turns. The fewer the turns, the more the spins can align parallel or antiparallel to the field, which is energetically favored. Moreover, the increasing alignment leads to a deviation from a simple helix with evenly rotating spins. This behavior is reminiscent of the situation discovered in [151], where TEM images of a 70 nm thick $Cr_{1/3}NbS_2$ crystal indicate in-plane helices as ground state. By applying a magnetic field perpendicular to the helix propagation, the magnetic structure changes continuously, forming a chiral soliton lattice whose pitch increases continuously with increasing field. Such behavior can be well described by a one-dimensional chiral sine-Gordon model, with soliton solutions [151]. In contrast, in the case of a helix propagating perpendicular to the film, the evolution with field occurs not in a continuous, but rather in an abrupt manner as soon as the boundary conditions are fulfilled.

Wilson *et al.* supported their theory by PNR measurements, where they did not fit the magnetic profiles, but directly used the 2D projection of their solutions plotted in Figure 4.9b. These fit perfectly the spin asymmetries (SA), with $SA = (R{+}{+}{-}R{-})/(R{+}{+}{+}R{-})$ (Section 2.2.2). The SA at 32 mT only does not follow the calculated magnetic structure. Therefore,

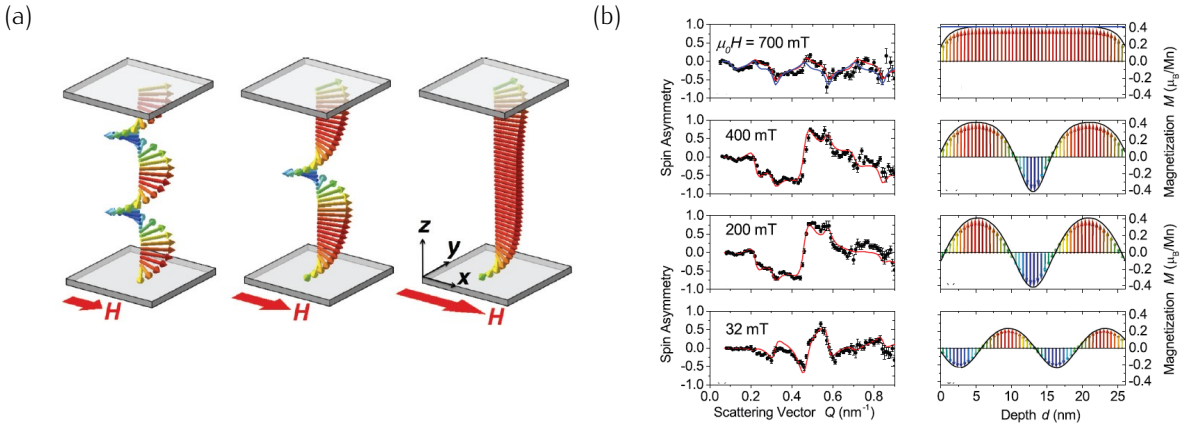

Fig. 4.9: ***B*** *in plane: (a) Solutions for a magnetic helix in a 29.7 nm MnSi film, where the helix length reduces with increasing magnetic field (from left to right), providing more spins aligned parallel to the field. (b) Spin asymmetries of PNR data recorded at 5 K for a 26.7 nm MnSi film shown in the left column. Fits are indicated as red lines and are based on the magnetic depth profiles shown in the right column, which are (besides a phase shift in the bottom panel) the 2D projections of (a). (Source: [11])*

they had to fit the magnetic depth profile to a helix with almost two integer repetitions as expected, but with a phase shift in comparison to their calculated solution. The magnetic fits are considerably different to the fits published in the earlier publication discussed above [147], although the data was recorded at the same temperature and similar fields.

The saturation magnetic field at 5 K was found to increase from 0.5 to 0.85 T for increasing MnSi thickness from 10 to 20 nm, where it remains constant within ±0.1 T for thicknesses up to 40 nm [147].

They also investigated also the dependence of the helix periodicity as a function of MnSi thickness, which was only published in an earlier version of their paper [152]. Here, they showed the helix length switching at critical thicknesses for a constant magnetic field. Nevertheless, there has to be a reason for the removal of this topic in the final publication.

Although they focused on the helical phase in both versions of the paper discussed above [11, 152], they referred to the existence of a skyrmion lattice shown in their previous paper [10] and seem to still regard this as true. The contradiction to the previous paper as well as the indirect measurement methods make clear the importance of conducting microscopic investigations on MnSi thin films using neutron scattering. Using this technique, we will solve this contradiction and clarify the magnetic properties of MnSi. In this chapter, I will discuss how we measured the magnetic wavevector of the helices directly. The helices are indeed aligned along the surface normal. I will also show that the phase diagram is dominated by the helical phase — divided, however, into subphases with different helix lengths.

4.1.5 Summary

This section aims to summarize and provide a basis for finding a consistent picture of the mechanisms responsible for the magnetic behaviors observed in different forms of B20 crystals.

Thin freestanding plates of MnSi [122], FeGe [124], $Fe_{0.5}Co_{0.5}Si$ [123], and CuO_2SnO_3 [125] in the thickness range of 15–100 nm reveal an in-plane helical ground state with, except for CuO_2SnO_3, the periodicity of bulk as well as an extended skyrmion phase under a magnetic field parallel to the film normal $\boldsymbol{n}$. The conical phase is expected to be suppressed, either because the helix wavevector $\boldsymbol{k_H}$ cannot align along the confinement $\boldsymbol{n}$, which is often referred to as finite size effect, or because surface anisotropy dominates. Shape anisotropy usually aligns the spins in plane: this would favor the helices to propagate along the film normal. Both mechanisms are depicted in Figure 4.10. For B20 plates, shape anisotropy seems to play a minor role. Because thin epitaxial films have a very similar shape, I regard this energy contribution to be rather small compared to other effects.

It has been suggested [13] that strain is responsible for an increased T_c, which is in good agreement to the increase of T_c in epitaxial $Fe_{1-x}Co_xSi$ films by 25–30 K [135] and in epitaxial $Mn_{1-x}Fe_xSi$ films by 5–25 K (Section 4.1.4), both exhibiting in-plane tensile strain. In contrast,

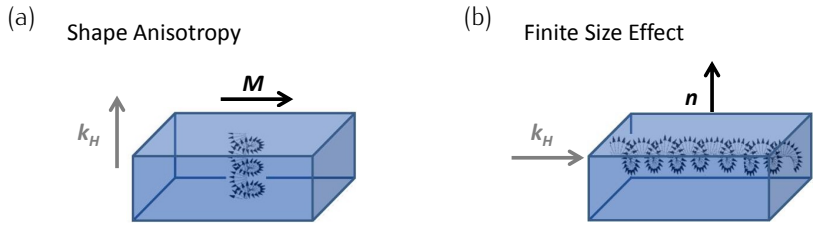

Fig. 4.10: *(a) Shape anisotropy aims to reduce stray fields by aligning $\boldsymbol{M} \perp \boldsymbol{n}$ and preferentially along the longest sample edge. This favors the helix aligning out of plane. (b) The finite size effect may cause the helices to align along a long sample edge instead of along the strong confinement along $\boldsymbol{n}$, forming a sufficient number of integer helix turns.*

T_c of an epitaxial FeGe film is reduced by 7 K compared to bulk and was also determined to exhibit in-plane tensile strain [129]. However, the different kind of in-plane strain, i.e. tensile or compressive, could be responsible for an increase or decrease of T_c in nanowires. The strain in CVD-grown MnSi nanowires was not examined, but T_c was found to be slightly increased. The strain induced by the growth should be very low, since the lattice in the nanowire should be relaxed after some μm of growth. Or, it may be induced by the FIB. T_c is definitely increased by 7 K for the freestanding MnSi plate, while the value has not been determined for FeGe and $Fe_{0.5}Co_{0.5}Si$ plates. This change of T_c in MnSi plates could indeed be induced by compressive strain due to mechanical thinning. Of course, other contributory factors cannot be excluded.

The thinned MnSi nanowire examined in [130] has a similar thickness to the plates but with a width reduced to 200 nm. Whether this reduction of width is sufficient to introduce an additional relevant confinement is questionable. As well as T_c, the magnetic phase diagram is also similar to the MnSi plate, exhibiting an in-plane helix with the bulk pitch. Even here, the shape anisotropy is not strong enough to align the spins along the wire.

A very similar phase diagram, but with an additional conical phase above the skyrmion phase was observed for the thick nanowire with a width and thickness of 410 nm [131]. In contrast to the other nanowire study, the magnetic field was applied along the wire. This should favor the spins to align in plane, which would suppress the conical phase. Note that this phase diagram was determined by tracking features in the static susceptibility and not by a real-space imaging method. On the other hand, the other nanowire study could have missed the conical phase due to too less data points at high fields.

In epitaxial thin films, in contrast to nanowires or plates, the helix pitch differs from the pitch in bulk, as was discovered for MnSi with 8.5 nm [13] or 13.9 nm [145] and for $Fe_{0.7}Co_0.3Si$ with 9.3 nm [134].

All magnetic structures observed in B20 thin films are summarized in Figure 4.11. The corresponding publications are listed in Table 4.1.

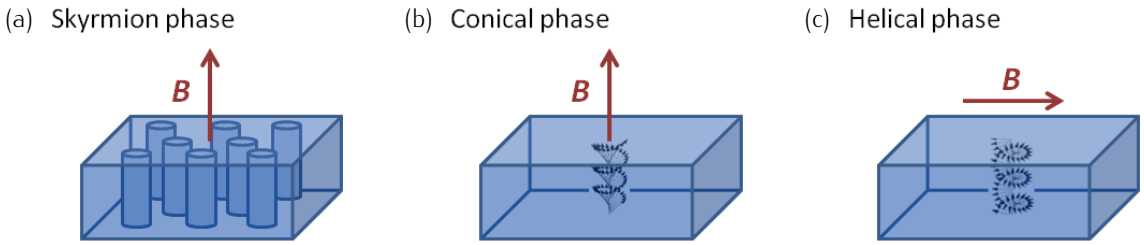

Fig. 4.11: *Summary of all magnetic structures observed for B20 epitaxial thin films: (a) the skyrmion phase and (b) the conical phase were predicted for the magnetic field aligned parallel to the surface normal. (c) The helical phase was observed in an in-plane magnetic field. Corresponding material systems and publications are summarized in Table 4.1.*

$\boldsymbol{B}$ out of plane

Structure	Material	In-plane Strain	T_c	Magn. Anisotr.	Method	Ref
skyrmion phase	MnSi	tensile	>		THE, TEM	[13]
	$Mn_{1-x}Fe_xSi$	tensile	>		THE	[132]
	$Fe_{0.7}Co_{0.3}Si$	tensile	>	easy plane	THE	[134]
	FeGe	tensile	<	easy axis	THE	[129]
conical phase	MnSi	tensile	>	easy plane	PNR Magnetometry Magnetoresist. Calculations	[145] [12]

$\boldsymbol{B}$ in plane

Structure	Material	Strain	T_c	Magn. Anisotr.	Method	Ref
helical phase	MnSi	tensile	>	easy plane	PNR Magnetometry Magnetoresist. Calculations	[147], [11]
	$Fe_{0.7}Co_{0.3}Si$	tensile	>	easy plane	PNR	[134]

Table 4.1: *Summary of studies about the magnetic structure of B20 thin films for out-of-plane (top) and in-plane (bottom) magnetic fields. The observed magnetic structures (1st column) correspond to the structures shown in Figure 4.11. T_c is indicated relative to the bulk value in the 4th column.*

By applying a magnetic field along the surface normal $\boldsymbol{n}$ (upper table), Hall-effect measurements revealed an extension of the skyrmion phase for epitaxial MnSi [13], $Mn_{1-x}Fe_xSi$ [132], $Fe_{0.7}Co_{0.3}Si$ [134] and FeGe [129] — similar to the observation in plates. This is in contrast to calculations, magnetometry, and magnetoresistance measurements of epitaxial MnSi in [12]. This difference may arise as a result of the different measurement method or the different structural properties of the samples, e.g. strain. By applying a magnetic field in plane (lower

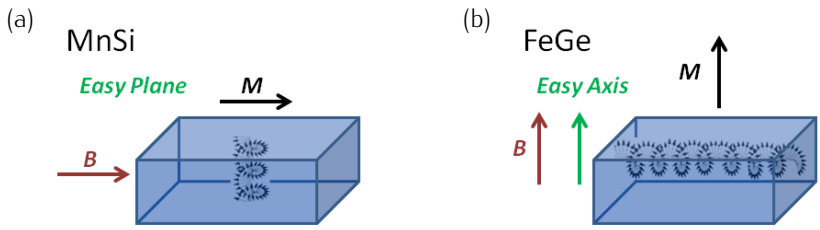

Fig. 4.12: *(a) The Zeeman energy and the easy-plane anisotropy in MnSi favor* $\boldsymbol{k_H} \,||\, \boldsymbol{n}$ *for an in-plane field. (b) The Zeeman energy and the easy-axis anisotropy in FeGe favor* $\boldsymbol{k_H} \perp \boldsymbol{n}$ *for a vertical field.*

table), the helices align out of plane for MnSi [11] and for $Fe_{0.7}Co_{0.3}Si$ [134].

The case seems to be clear for FeGe in an out-of-plane field (Figure 4.12b) and for MnSi or $Fe_{0.7}Co_{0.3}Si$ in an in-plane field (Figure 4.12a): The magnetic field is aligned parallel to the easy axis and to the easy plane, respectively. For FeGe, this should result in an in-plane helix, while for MnSi and $Fe_{0.7}Co_{0.3}Si$ the helix aligns out of plane, as postulated by Wilson *et al.* [11] and as will be demonstrated in this thesis. Here, the interplay of uniaxial anisotropy and Zeeman energy is strong enough to overcome the finite size effect, and the helices can also be aligned within a confinement.

Note that $\boldsymbol{k_H}$ in FeGe has not been measured yet. However, the calculated phase diagram for an out-of-plane field of Wilson *et al.* [12] predicts the skyrmion phase alongside the helical phase shown in Figure 4.12b. Indeed, the latter was observed in the THE signal by Huang *et al.* [129]. However, for all three materials [129, 135, 147], the type of uniaxial magnetic anisotropy was calculated using a formula in [147]. The formula is based on the ground-state helix length. It is not clear which value was used for FeGe as the helix length was not measured. Furthermore, although the coercive fields of all three materials are larger for an out-of-plane field than for an in-plane field, they end up with a different magnetic anisotropy direction. This maybe due to magnetization curves, which were not corrected for demagnetization effects.

What happens when the magnetic field is not parallel to the easy axis or easy plane, as is the case for MnSi under an out-of-plane field? Which energy term dominates: Zeeman energy or uniaxial anisotropy? Is there close competition and does this explain the contradiction between results for MnSi thin films of Wilson *et al.* [12] and Li *et al.* [13]? Although these questions cannot be answered within the scope of this thesis, we will address them again at the end (Section 4.4.6) and consider our measurements, which did not show any magnetic signal.

Sample	d_{MnSi}	Size	Instrument	Method	Comment
SI121	(553 ± 10) Å	(19x23) mm^2	NREX SANS1	PNR, OSR GISANS	Cu capping
SI048	(495 ± 10) Å	(10x12) mm^2	NREX	PNR	no capping
SI008	(390 ± 10) Å	(19x23) mm^2	SANS1	GISANS	no capping

Table 4.2: *Samples used for neutron experiments*

4.2 Sample Growth and Quality

The MnSi thin film samples investigated in this thesis were grown by Thorsten Hesjedal (University of Oxford) using MBE. As a first step, the Si(111) substrate was annealed at 990°C for one hour to remove the SiO_2 layer. Afterwards, a nominal 20 Å Mn layer deposited on the Si substrate was annealed at 400°C for one hour to form a MnSi seed layer. Then a nominally 500 Å-thick MnSi film was deposited by co-deposition of Si and Mn, which was in turn annealed at 400°C for one hour. While Mn was evaporated from an effusion cell, Si was evaporated by an e-beam. The samples used for neutron scattering are summarized in Table 4.2. An additional Cu layer was grown on top of sample SI121, with the purpose of enhancing neutron scattering within the MnSi layer in subsequent experiments performed in this thesis.

Figure 4.13a shows XRD patterns of a θ-2θ scan with the Q-vector perpendicular to the surface (Section 2.1.1). As well as the very sharp Si-substrate peaks, the MnSi(111) and the MnSi(222) peak are observed. This is a strong hint that the samples were grown epitaxially,

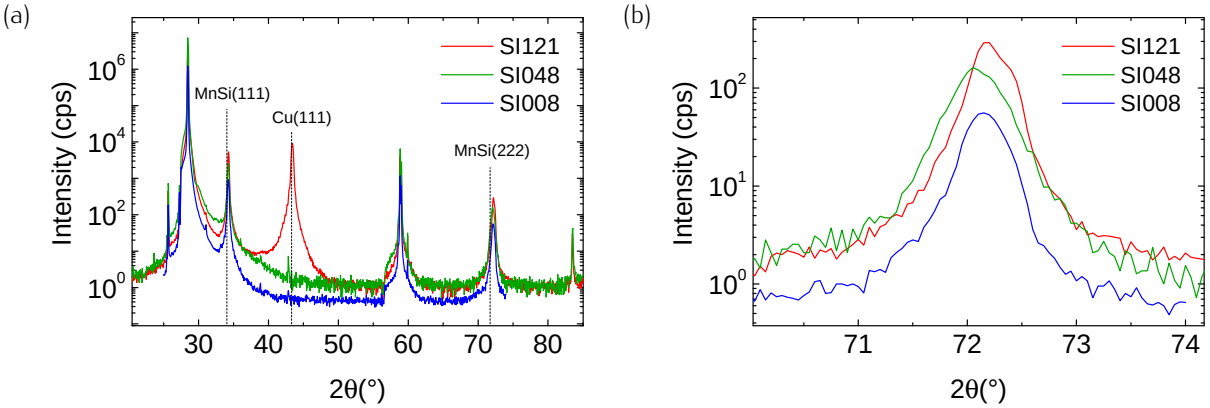

Fig. 4.13: *(a) Diffraction pattern of all the MnSi samples investigated, revealing peaks of the parallel planes MnSi(111) and MnSi(222). All unlabeled peaks correspond to the Si(111) substrate, indicating epitaxial growth of MnSi(111). The Cu(111) peak occurs as a result of the capping of sample SI121. (b) Enlarged view of the MnSi(222) peaks, the center of which deviates only within a range of* 0.11°.

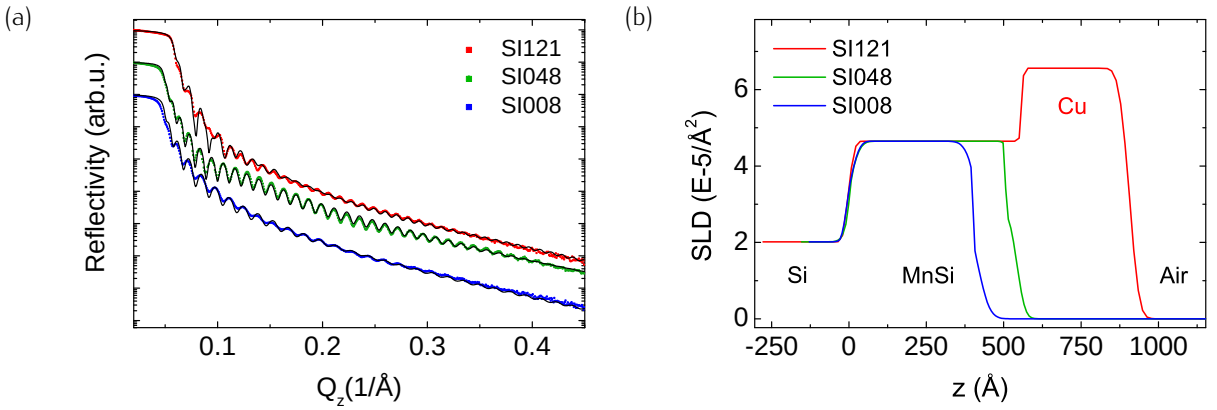

Fig. 4.14: *(a) Reflectometry curves of all the MnSi samples investigated. The black curves are fits. (b) SLD profiles resulting from the fits as a function of the sample depth z with the surface of the substrate at z = 0. From the fit, we obtained the MnSi thicknesses of* 390 Å *(SI008),* 495 Å *(SI048), and* 553 Å *(SI121).*

because in a polycrystalline sample the (102) peak and the (112) peak would be five times and three times more intense than the (111) peak, respectively. The MnSi(222) peaks of the three samples are in the range of $2\theta = 72.06°$–$72.17°$ (Figure 4.13b). In comparison to the expected value of bulk MnSi of $2\Theta = 71.7°$, there is a reduction of the (222) plane distance of less than 1%. From the FWHM in the range of 0.37–0.45° and the peak position θ, the crystallite length along the sample normal for sample SI121, for instance, can be estimated using the Scherrer formula [93]:

$$L = \frac{K \cdot \lambda}{FWHM[rad] \cdot cos(\theta)} = \frac{1 \cdot 1.541\,\text{Å}}{0.37\pi/180 \cdot cos(36.09°)} = 295\,\text{Å}, \tag{4.4}$$

where K is the Scherrer form factor, which is ≈ 1, and λ the Cu Kα wavelength of the X-ray source. The crystallite size for samples SI008 and SI048 can be calculated to be 264 Å and 243 Å, respectively. Thus, the samples contain crystallites with a size of about 50–70% of the layer thickness.

To check the interface quality and layer thicknesses, we carried out XRR measurements (Section 2.1.2). Figure 4.14a shows the reflectivity as a function of Q_z for all three samples. The data were fitted using Parratt32 1.6 [17]. The SLD profile resulting from the fits (black lines in Figure 4.14a) is plotted in Figure 4.14b as a function of sample depth z, where the Si/MnSi interface is at $z = 0$ and the surface at $z \gg 0$. The Si/MnSi interface roughness is between 22 Å and 30 Å.

Recent electron backscattering diffraction (EBSD), carried out by Susannah Speller (Department of Materials, University of Oxford), revealed equally distributed right- and left-handed domains in nominal 300 Å and 500 Å samples. Hence, the samples exhibit similar qualities as the samples used by Karhu, Wilson *et al.* [10–12, 145, 147].

Finally, our samples were investigated by torque magnetometry by Matthias Brasse. The

magnetic anisotropy was determined as easy plane with an uniaxial anisotropy constant of $1.2\,kJm^{-3}$ for a nominal 30 nm film and of $7.9\,kJm^{-3}$ for a nominal 10 nm film [153]. While the first value is in good agreement with the value determined by Karhu *et al.* [147], the second is 4 times smaller.

4.3 Neutron-scattering Experiments

We performed neutron-scattering experiments with in-plane and out-of-plane magnetic fields. Here, we will report only on neutron experiments conducted with an in-plane magnetic field, since out-of-plane experiments did not show a magnetic signal. However, the latter are presented in the Appendix and briefly discussed in Section 4.4.6. At FRM II, we applied grazing incidence small-angle neutron-scattering (GISANS) measurements to MnSi(111) thin films at the instrument SANS1 as well as polarized neutron reflectometry (PNR) and off-specular reflectivity (OSR) measurements at the instrument NREX. All these methods were already introduced in Section 2.2. Both instruments have a 2D detector, allowing Q_y and Q_z to be measured directly. We only observed magnetic signals along Q_z and not along Q_y, which allowed us to perform off-specular reflectivity measurements at NREX to obtain Q_x-Q_z-maps. The setup used at SANS1, as well as the data analysis for GISANS, are presented in the first Section 4.3.1. Afterwards, I will discuss some preliminary considerations important for the measurement techniques themselves (Section 4.3.2). In Section 4.3.3, I will present the setup of NREX and discuss the data analysis for OSR and PNR.

4.3.1 Setup and Data Acquisition at SANS1

Setup. At SANS1 (FRM II) we performed GISANS measurements (Section 2.2.1) at a wavelength of 5.5 Å with $\delta\lambda/\lambda = 10\%$ and using the setup shown in Figure 4.15. The sample normal was the MnSi <111> direction. The magnetic field $\boldsymbol{B}$ was fixed parallel to the sample plane. The sample was aligned parallel to either the MnSi <112> edge or the MnSi <110> edge. For $\omega = 0$, the incident beam was aligned with $\boldsymbol{k_i} \perp$ <111> and $\boldsymbol{k_i} \parallel \boldsymbol{B}$. The sample, together with the magnet, could be tilted with respect to the sample horizon to change the angle of incidence (angle ω) and rotated around the sample normal (angle χ). Both degrees of freedom were used to run so-called rocking scans to find the maximum of a Bragg peak, corresponding to a magnetic structure, which fulfills the Bragg condition. The resulting curve, i.e. the intensity of Bragg peak vs. rocking angle, is called the rocking curve. Its FWHM depends on the instrument resolution as well as on the magnetic structure itself. When the sample is inclined with $\omega \neq 0$, the reflected spot also occurrs on the detector, with $\boldsymbol{k_f}$ forming an angle relative to $\boldsymbol{k_i}$ of 2ω. For periodic magnetic structures, i.e. helices, along the <111> direction, two Bragg spots evolve along Q_z at the detector. These are symmetrical around the direct beam spot. The lower spot is weaker, owing to the attenuation of the signal transmitted

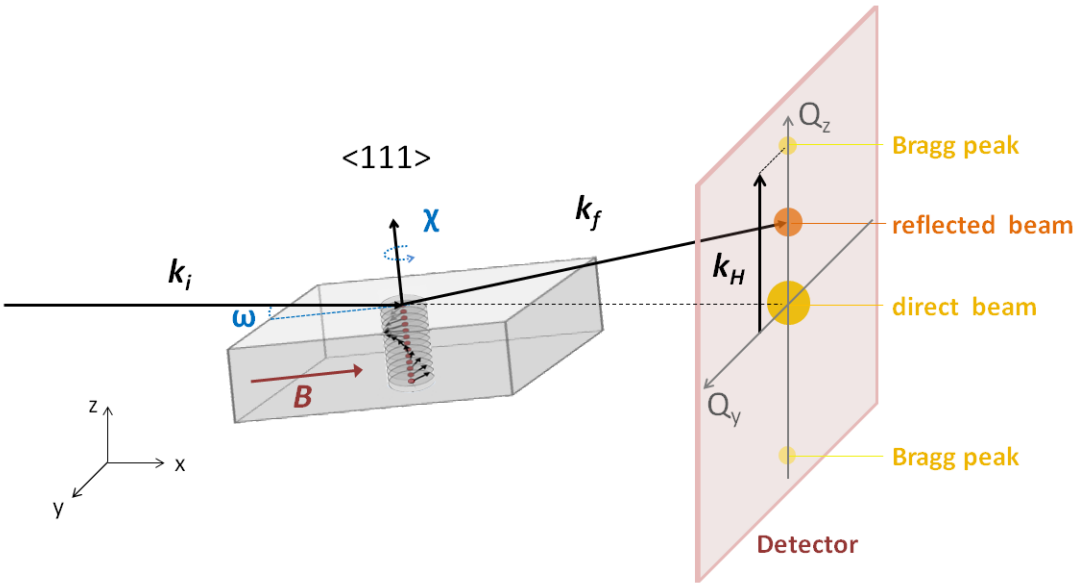

Fig. 4.15: *Setup used at SANS1 (FRM II). For $\omega = 0$, the sample normal <111> of the MnSi thin film is aligned with $\boldsymbol{k_i} \perp$ <111> and $\boldsymbol{B} \perp$ <111>. The sample and the magnet were fixed to each other and were either aligned with $\boldsymbol{B}$ || <112> or $\boldsymbol{B}$ || <110>. The reflected spot occurs for $\omega \neq 0$. The magnetic structure, i.e. a helix propagating along <111>, gives rise to magnetic Bragg spots along Q_z. The sample can be rocked using the angles ω or χ. On the detector, two Bragg spots occur in both directions of <111> with the lower spot being weaker due to the transmission through the sample. The strongest spot is that of the direct beam, while the reflected is much weaker. The wavevector of the helix is referred to as $\boldsymbol{k_H}$, the value and direction of which can be read off the detector position of the Bragg spot relatively to the position of the direct spot.*

through the sample. The strongest spot belongs to the direct beam, while the reflected beam is much weaker. From the position of the magnetic Bragg spot relative to the position of the direct spot, the helix wavevector $\boldsymbol{k_H}$ can be determined. Here, for $\boldsymbol{k_H}$ || <111>, ω is the relevant rocking angle to reach the maximum intensity of the Bragg peak at the detector.

The detector can be positioned along the detector tube, but it cannot be tilted. The beam size is determined by a pinhole in front of the sample, allowing the same resolution in Q_z and Q_y. The beamline can be used with the sample aligned horizontally or vertically, which only changes the instrument angle we use to define the angle of incidence. We measured at constant angles of incidence between 0.57 and 0.66°. The reason for that is discussed in the next section. All incident angles, together with the corresponding Q_z-values of the reflected spot, are summarized in Table 4.3.

Data Acquisition. To prevent missing a magnetic Bragg peak with a non-zero Q_y, we conducted rocking scans around the surface normal, i.e. χ in horizontal geometry, in a wide

Geometry	Sample	k_i,B	Incident angle	$Q_{z,Reflex}$
horizontal	SI121	<112>	$\chi = 0.652°$	0.0263 Å^{-1}
vertical	SI121	<110>	$\omega = 0.657°$	0.0258 Å^{-1}
vertical	SI008	<110>	$\omega = 0.569°$	0.0227 Å^{-1}

Table 4.3: *Sample geometries at SANS1*

range, with $4° \leq \Delta\chi \leq 8°$, for each measurement. However we did not find a magnetic Bragg peak and we summed up all the images of the rocking scan. For the sake of convenience, I will, independently of the sample geometry, refer to the incident angle as ω and describe the rotation around the surface normal with χ.

Each detector image was recorded after field cooling (FC) from 60 K and was subtracted by a background measurement performed in the same way at 60 K. Finally, the data was normalized to the counts measured at the monitor, which is located in front of the sample and continuously absorbs a portion of neutrons to measure the current neutron flux. This normalization, therefore, takes into account intensity fluctuations. For each set of measurements, the direct beam was also measured without the beam stop and sample. Grasp V6.72 [154] was used for data analysis. The center of the direct beam at the detector was fitted and then set as the zero point of Q_y and Q_z. All Q_y and Q_z values were calculated via the detector's y and z channel relative to the zero channel. The detector image was then smoothed by the option "Gauss 2pxl FWHM" or "Gauss 3pxl FWHM". For a detailed study, intensity profiles along Q_z will be compared for different temperatures and fields. The error bars of the averaged intensities were calculated by Grasp.

4.3.2 Preliminary Considerations

As we performed GISANS measurements with a non-zero incident angle, the reflected spot was observed on the detector. In this section, I will show where the reflected spot and the Bragg spot occurred on the detector and how we could distinguish between them. This description will also explain our motivatation for the usage of off-specular reflectivity (OSR) at NREX, which will be introduced in the next section, 4.3.3.

GISANS, Reflectivity, or Both? Figure 4.16a shows a typical detector image at SANS1 for $\omega = 0.4°$ with the bright reflected beam along <111> and the rectangular beam stop lowering the intensity of the direct spot in the detector center. By scanning ω, the reflected spot moved along the z-direction. By integrating the intensity in the red box sketched in Figure 4.16a for each ω, one obtains the reflectivity curve shown in Figure 4.16b, i.e. the integrated intensity as a function of ω. At 0°, the reflected intensity is absorbed by the beam stop. By increasing the angle, the reflected spot passes the beam stop, where total reflection still occurs, as indicated by the high-intensity plateau. Above the critical angle of

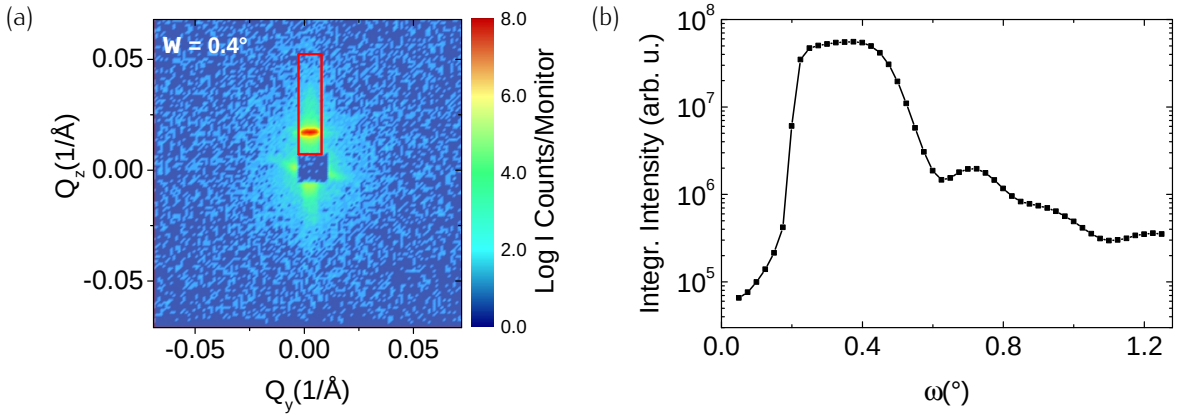

Fig. 4.16: *SI121 measured at 27 K, 0.5 T: (a) Detector image at SANS1 with reflected beam for $\omega = 0.4°$. The dark rectangle in the center is due to the beam stop. (b) The integrated intensity of the red box in (a) as a function of ω reveals the reflectivity curve.*

the sample, the intensity drops steeply as expected and exhibits Kiessig fringes. Since we integrated the intensity not only of the reflected spot, but of the region within the entire red box, the contribution of the off-specular intensity in this curve is high. However, a typical reflectivity curve is still observable. This proves the alignment and the correct understanding of the spot. Figure 4.16a does not reveal any magnetic Bragg peaks, due to the fact that it is much weaker than the reflected beam. To see it, the background has to be subtracted first.

Bragg Condition. Figure 4.17a shows a detector image of the reflected beam measured at SANS1 for $\omega = 0.85°$, 27 K, and 0.5 T. To find a magnetic Bragg peak, we rocked ω and χ to

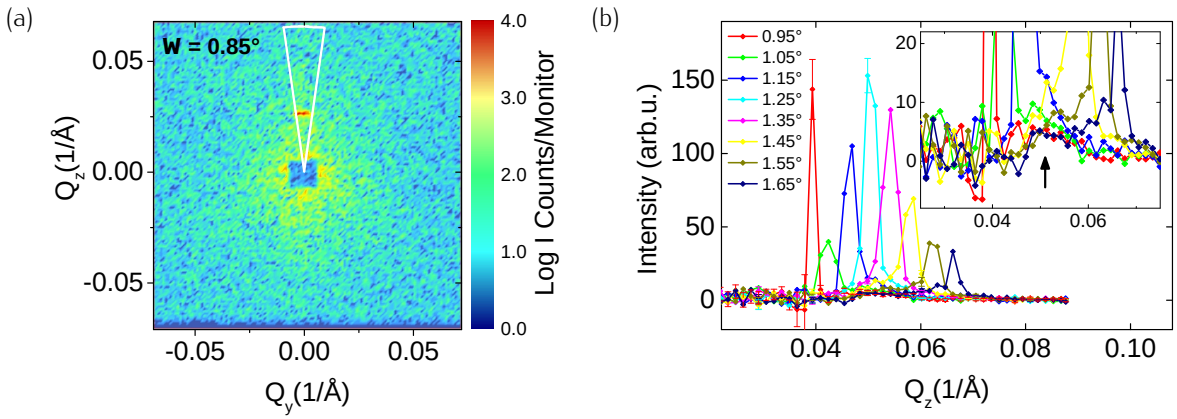

Fig. 4.17: *SI121 measured at 27 K, 0.4 T at SANS1: (a) Detector image for the incident angle $\omega = 0.85°$ showing the reflected beam with high intensity. The dark rectangle in the center is due to the beam stop. (b) Along Q_y integrated intensity of the white sector in (a) as a function of Q_z for $0.95° \leq \omega \leq 1.65°$. Owing to the background subtraction, spikes remain at the position of the reflected beam, which superimpose the magnetic Bragg peak (black arrow) as shown in the inset.*

fulfill the Bragg condition and succeeded in finding a magnetic Bragg peak along <111>. In this direction, only the ω scan was necessary to find the maximum of the rocking curve. We subtracted the background image, which was measured at 60 K above the Curie temperature, and integrated the intensity along Q_y within the white sector indicated in the figure. The resulting intensity profiles are plotted in Figure 4.17b for several ω. The sharp spikes in intensity are due to small intensity differences of the specular spot at 27 K and 60 K, indicating small changes of sample position or sample bending. As shown in the inset, the underlying intensity reveals the magnetic Bragg peak. The figure shows the maximum of the magnetic Bragg peak at $Q_z \approx 0.05\,\text{Å}^{-1}$ (arrow in Figure 4.17b), which is reached for $\omega_{Bragg} = 1°$–$1.5°$ when the reflected beam moves across it. Indeed, the reflection coincides exactly with the Bragg peak. This is always the case for a k-vector of a magnetic structure parallel to the sample normal, since the Q-vector of the specular reflection is also parallel to the sample normal (Figure 4.18). Assuming $\boldsymbol{k_H}$ is exactly perpendicular to $\boldsymbol{k_i}$ with $k_H = 0.05\,\text{Å}^{-1}$, one would have to rock to $\omega = 1.25°$ to fulfill the Bragg condition.

Owing to the bad signal-to-noise ratio and the high spikes formed after background subtraction of the ω scan shown in Figure 4.17b, an extraction of the rocking curve was not possible and thus remains unknown. To observe a clear magnetic signal, we must not measure at the exact Bragg condition, i.e. the maximum of the rocking curve, but elsewhere at the rocking curve. Only then, the specular spike does not conceal the magnetic Bragg peak. Fortunately, we found that the intensity of the Bragg peak was still high enough even far from the Bragg condition when measured at SANS1, as can been seen for sample SI008 and SI121 in Figure 4.19. Here, we measured for longer than in the scan of Figure 4.17b. Again, the background image was subtracted and the intensity integrated along Q_y within a sector. In Figure 4.19a the magnetic Bragg peak is observable even within $\Delta\omega = 0.55°$. In Figure 4.19b, the inci-

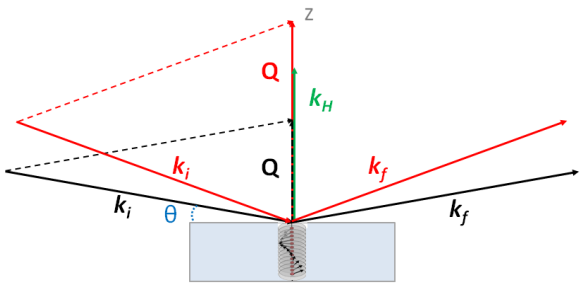

Fig. 4.18: *The scattering vector is defined by $\boldsymbol{Q} = \boldsymbol{k_i} - \boldsymbol{k_f}$. For reflectivity measurements, the incident angle is $\theta_i = \theta_f = \theta$ resulting in a scattering vector with a pure Q_z component. By scanning θ the modulus of $\boldsymbol{Q}$ changes as shown for a small θ (black scattering triangle) compared to a larger θ (red scattering triangle). Since the wavevector of the helix $\boldsymbol{k_H}$ (green) is also directed along z, the specular reflection will coincide with the Bragg peak when measured at the Bragg angle.*

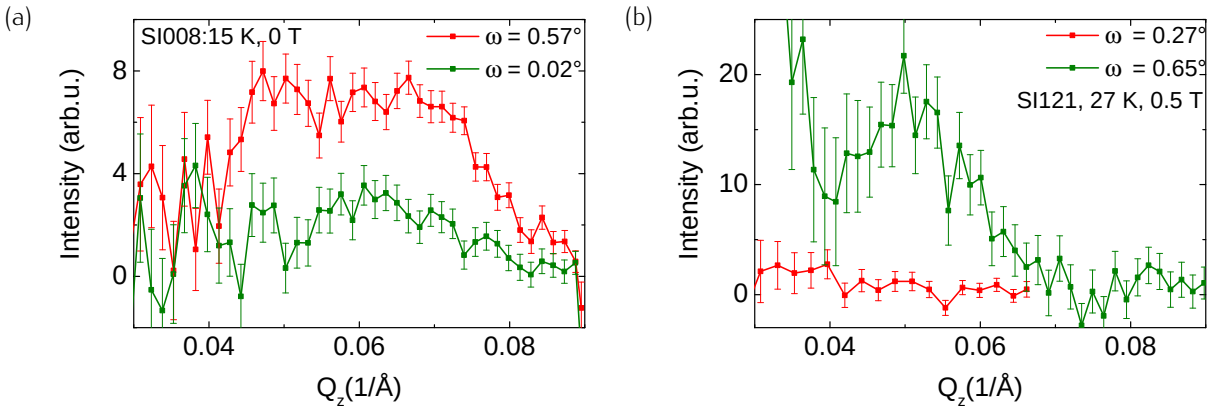

Fig. 4.19: *Along Q_y integrated intensity in the white sector as shown in Figure 4.16a showing the intensity profile of the magnetic Bragg peak as function of Q_z for two different incident angles ω measured at SANS1 on (a) sample SI008 and (b) sample SI121, respectively. The spike of the reflected beam occurs at $Q_z < 0.03\,\text{Å}^{-1}$, when not measured at the exact Bragg condition. The Bragg peak is still visible in (a) within $\Delta\omega = 0.55°$, while in (b) it has vanished for $\omega = 0.27°$.*

dence angle $\omega = 0.65°$ results in the appearance of the reflected spot at low Q_z. This is still separated by $\Delta Q_z = 0.024\,\text{Å}^{-1}$ from the Bragg peak. At $\omega = 0.27°$, no Bragg peak was observed.

In summary, the specular beam hides the Bragg peak when measured directly at the Bragg condition. Moreover, the rocking curve is quite broad, which is mainly due to the coarse resolution of $\delta\lambda/\lambda = 10\%$ at SANS1. An additional major contribution from the magnetic structure itself cannot be excluded at this point. However, this enables us to measure at constant angles of incidence which are smaller than the Bragg angle (Table 4.3), such that the reflected spot is separated from the Bragg peak.

4.3.3 Setup and Data Acquisition at NREX

Setup. The monochromatic instrument NREX (FRM II) is a beamline dedicated to reflectometry using a neutron beam with a fixed wavelength of $\lambda = 4.31\,\text{Å}$. Although the sample-detector distance is much smaller than at SANS1, the Q_z resolution was higher owing to a very good wavelength resolution of 2%. In contrast, the resolution in Q_y was quite coarse: in order to illuminate the total sample, the horizontal slits are usually widely open. Since we did not investigate Q_y values in PNR or off-specular reflectometry (OSR), the resolution in this direction was not relevant. The sample geometry, as shown in Figure 4.20a, was very similar to the setup used at SANS1. Again, we applied the magnetic field in plane, i.e. $\boldsymbol{B} \perp$ <111>. For reflectometry, the incident angle is typically referred to as θ. The sample together with the magnet can be tilted to align θ. Additional, the detector can be tilted by 2θ to realize θ-

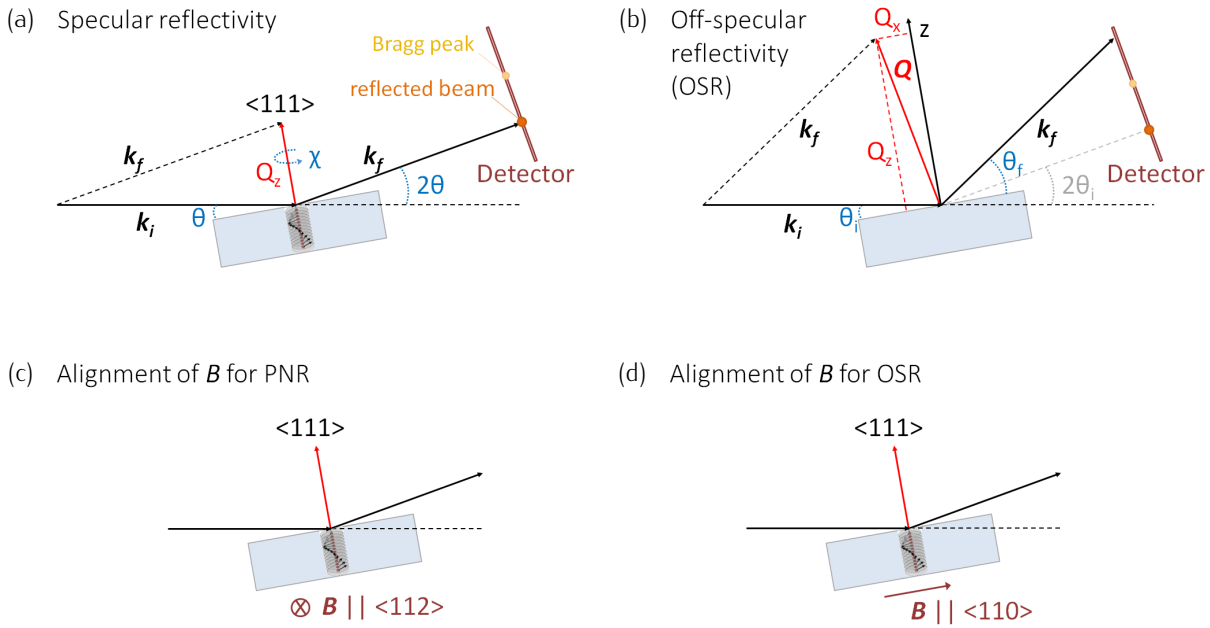

Fig. 4.20: *Setup used at NREX (FRM II) as side view. (a) For $\theta = 0$, the sample normal <111> of the MnSi thin film is aligned with $\boldsymbol{k_i} \perp$ <111>. The reflected spot occurs for $\theta \neq 0$. The magnetic structure, i.e. a helix propagating along <111>, gives rise to a magnetic Bragg peak along Q_z. The detector can be tilted to perform θ-2θ-scans moving the reflected spot across the Bragg peak. The scattering vector can be described by $\boldsymbol{Q} = \boldsymbol{k_i} - \boldsymbol{k_f}$. The specular reflectivity only considers data with $\theta_i = \theta_f = \theta$ resulting in a scattering vector with a pure Q_z component, while (b) also considers the off-specular reflectivity with $\theta_i \neq \theta_f$ for data analysis using the same setup and same scan-type as in (a). Here, one is sensitive also to the Q_x component of the wavevector of the magnetic structure. The in-plane magnetic field is aligned for $\theta = 0$ (c) with $\boldsymbol{B} \perp \boldsymbol{k_i}$ and $\boldsymbol{B}$ || <112> for PNR and (d) with $\boldsymbol{B} \parallel \boldsymbol{k_i}$ || <110> for OSR.*

2θ scans. For $\theta = 0$, the surface normal was again aligned with $\boldsymbol{k_i} \perp$ <111>. This resulted in the evolution of helices with the wavevector $\boldsymbol{k_H}$ || <111> with a Bragg peak along Q_z. However, OSR accounts for slightly tilted helices and measures the additional Q_x component. Then, Q_x-Q_z maps reveal the Bragg sheets (Section 2.2.3) of $\boldsymbol{k_H}$ in the off-specular regime, i.e. for angles $\theta_f \neq 2\theta_i$. The setup is plotted in Figure 4.20b for one specific off-specular $\boldsymbol{k_f}$. The in-plane magnetic field was aligned for $\theta = 0$ with $\boldsymbol{B} \perp \boldsymbol{k_i}$ and $\boldsymbol{B}$ || <112> for PNR (Figure 4.20c), while it was aligned with $\boldsymbol{B} \parallel \boldsymbol{k_i}$ || <110> for OSR (Figure 4.20d).

PNR. Polarized neutron reflectometry (Section 2.2.2) was applied to measure magnetic moments in plane and as a function of sample depth. For this purpose, one has to use a polarizer. We performed θ-2θ scans to record the specular reflectivity, using an analyzer for all four spin channels (R++, R--, R+-, R-+) and no analyzer for two spin channels (R+, R-). The latter two measures only the component of the magnetization parallel to the magnetic field. The PNR data was recorded after zero-field cooling (ZFC) from above T_c, i.e. 55 K, to 10 K, followed by zero-field heating (ZFH) to the desired temperature. Subse-

quently, all fields chosen at this temperature were applied in ascending order. From here, measurements at higher temperatures were performed, followed by ZFH, whereas lower temperatures were applied after heating up to 55 K and by subsequent ZFC. For data analysis, we calculated the spin asymmetry, which can be written as: $SA = (R^{-} - R^{+})/(R^{-} + R^{+})$ or $SA = (R^{--} - R^{++})/(R^{--} + R^{++})$ (Equation 2.4). This, together with the reflectivity, was fitted using the program SimulReflec [19].

Off-specular Reflectivity. In a test measurement, we demonstrated successfully that we can accomplish SANS at NREX for a bulk MnSi sample, for which the phase diagram is well known. From that, we assumed that it could also be possible at NREX to see the same magnetic SANS peaks under grazing incidence in a thin sample. As discussed above (Section 4.3.2), GISANS could not be measured at the maximum intensity of the Bragg peak. At NREX the Q_z resolution is much better than at SANS1, which reduces the width of the rocking curve. Therefore, we could not directly observe the magnetic Bragg peaks in the GISANS image by measuring below the Bragg angle. As we did not find Bragg peaks along Q_y at SANS1, we decided instead to measure the off-specular reflectivity by running θ-2θ scans. From these we obtained Q_x-Q_z intensity maps which allowed us to observe the corresponding Bragg sheets of the specular Bragg peak in the off-specular regime (Section 2.2.3). A Q_x-Q_z scattering map can be deduced from a θ-2θ scan by integrating along the y-Channels and calculating Q_x and Q_z from Figure 4.20b using Equations 2.5 and 2.6

$$Q_x = \frac{2\pi}{\lambda}\left(cos(\theta_f) - cos(\theta_i)\right)$$
$$Q_z = \frac{2\pi}{\lambda}\left(sin(\theta_f) + sin(\theta_i)\right),$$

with $\theta_i\,(= \theta)$ and θ_f being the initial and final angle as depicted in Figure 4.20b. As for the SANS1 data, all intensity maps were again measured after FC from 60 K, normalized to the counts at the monitor and subtracted by background data, measured at 60 K and also normalized to the counts at the monitor. In the following data analysis, we excluded the spikes at the position of the specular beam — again resulting from background subtraction (Section 4.3.2) — by considering only data points with Q_x values lower than Q_x of the specular beam, i.e. $Q_x < -3 \cdot 10^{-6}\,\text{Å}^{-1}$. To obtain intensity profiles along Q_z, the Q_x-Q_z intensity data set $I(Q_x, Q_z)$ was arranged by increasing Q_z values reducing the data set to $I(Q_z)$. This resulted in a very high data density and the intensities of every 100 adjacent Q_z values were summed up. Using this method, we lost information about Q_x. However, generating $I(Q_x)$ profiles by using data points in the region of one Bragg sheet gives us the rocking curve superimposed by the spikes at the position of the specular beam. Extracting the pure rocking curve is, one more, not possible, so this profile does not provide any additional information. The corresponding error of the intensity was estimated by scaling the intensity by the mean monitor counts to obtain the intensity with absolute values of the signal I_{Signal} and background I_{BG}. The total error after background subtraction was $\Delta I(Q_x, Q_z) = \sqrt{I_{Signal}(Q_x, Q_z)/(\Delta t)^2 + I_{BG}(Q_x, Q_z)/(\Delta t)^2}$. The error of the intensity after summing up 100 adjacent points reduced then to $\Delta I'(Q_z) = \sqrt{\sum_{i=1}^{100}\left(\Delta I(Q_{z,i})\right)^2}$. Afterwards the error was again

scaled down by the mean monitor counts.

4.4 Results

Having introduced the setup and measurement techniques in the previous chapter, I will now present the results obtained for MnSi thin films when measured in an in-plane magnetic field. In the beginning, I will report on data performed on sample SI121, for which all measurement techniques were applied: grazing incidence small-angle neutron scattering (GISANS), off-specular reflectivity (OSR), and polarized neutron reflectometry (PNR) — all with the purpose of identifying the magnetic phases of the MnSi thin film as a function of magnetic field and temperature. Since the k-vectors of a magnetic structure can be measured directly by GISANS and OSR, this data is presented and discussed in the first section, 4.4.1. Afterwards, I will investigate the influences on the results, i.e. the effect of the in-plane magnetic field direction, the cooling history, and the used instrument (Section 4.4.2). Using those results, I will discuss the data in more detail and extract a first phase diagram (Section 4.4.3). Next, the results of PNR are presented and the phase diagram updated (Section 4.4.4). The results of GISANS and off-specular reflectivity will serve as a model for fitting the PNR data, where one can only measure the k-values indirectly. In Section 4.4.5, the results are compared to data recorded on samples SI008 and SI048. Finally, in Section 4.4.6, I will summarize the presented results and discuss their implications, together with the results of unsuccessful measurements performed in an out-of-plane field and presented in the Appendix.

4.4.1 Direct Phase Determination using GISANS and OSR

A direct investigation of the wavevector of a periodic magnetic structure is possible using GISANS and OSR, which enable the observation of the corresponding magnetic Bragg peak and the magnetic Bragg sheet in reciprocal space, respectively. In this section, I will describe those results qualitatively. As described in Section 4.3.1 and 4.3.3, the magnetic field was aligned in plane and for $\omega = 0$ or $\theta = 0$ parallel to $\boldsymbol{k_i}$.

GISANS. Figure 4.21 shows some exemplary detector images of sample SI121 with $d_{MnSi} = 553\,\text{Å}$, recorded at SANS1 (Section 4.3.1) at 15 K and subtracted by the background image. The detector channels have been converted to Q-values and the scattered intensity is encoded in color. In the center of the detector images, a rectangle of low intensity occurs, which is surrounded by high intensity: this is the direct beam shadowed by the beam stop. Slightly above this, there is a smaller spot of high intensity indicated by the yellow arrow. This is the spike at the position of the specular spot resulting from background subtraction. At 0 T (Figure 4.21a), two magnetic Bragg spots are located symmetrically around the direct beam. The lower one has less intensity (Bragg peak A'), as it is attenuated, owing to the transmission through the sample, whereas the upper one was recorded on the reflecting side of the sample

(Bragg peak A). Both Bragg spots are elongated along Q_z. Applying an in-plane magnetic field along <110> of 0.4 T results in the detector image of Figure 4.21b. The intensity of each spot drops and splits into two Bragg spots: A and B, and A' and B'. An increase of the field to 0.55 T (Figure 4.21c) leaves only the spot B and B', while at 0.8 T (Figure 4.21d) the Bragg spots have vanished.

Since the coordinates of the maximum intensity of the Bragg spots are at zero Q_y and non-zero Q_z, the first three detector images (Figure 4.21a-c) reveal periodic magnetic structures along the surface normal, i.e. the <111> direction, which can be interpreted by two phases. Phase 1 exhibits the magnetic Bragg peak A and A' (Figure 4.21a) and phase 2 exhibiting the magnetic Bragg peak B and B' (Figure 4.21c). As we will show later on (Section 4.4.3),

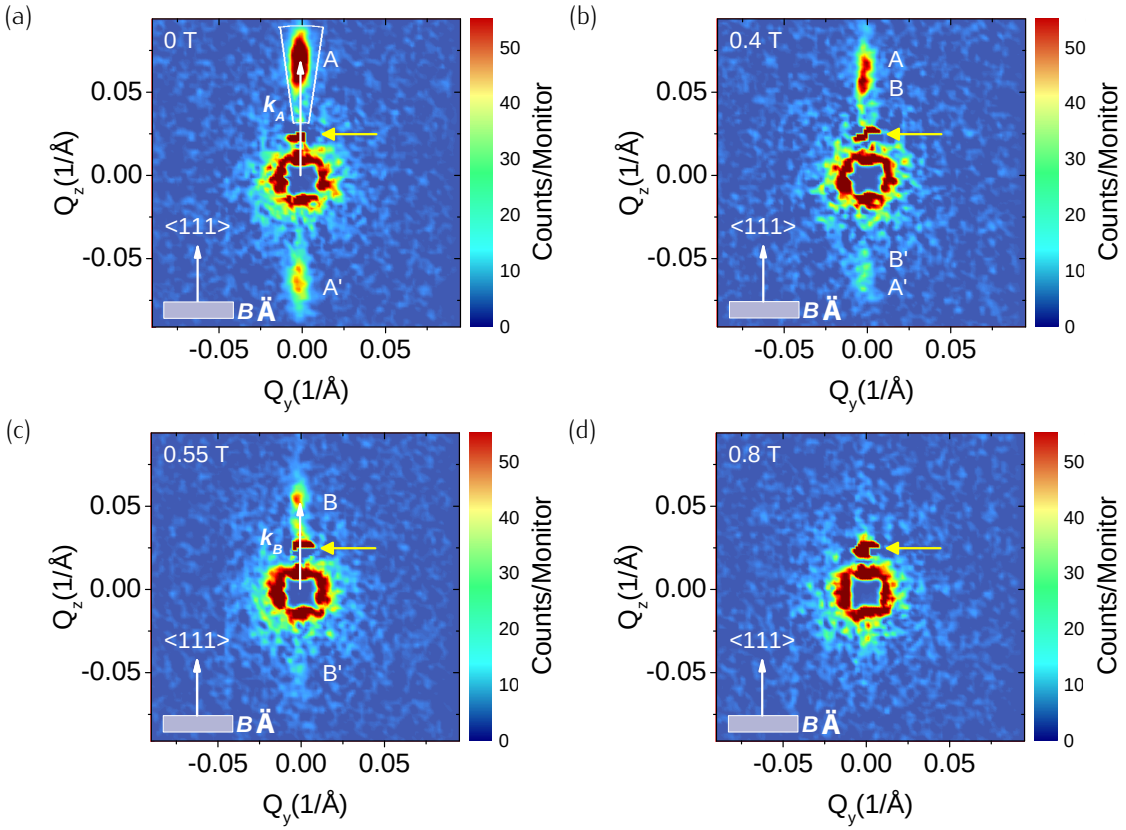

Fig. 4.21: GISANS at SANS1: Detector images of sample SI121 (d_{MnSi} = 553 Å) as intensity color maps in counts per monitor vs. Q_z and Q_y at 15 K and (a) 0 T exhibiting peak A (phase 1), (b) 0.4 T exhibiting a double peak (intermediate phase), (c) 0.55 T exhibiting peak B (phase 2) and (d) 0.8 T showing no magnetic signal. The dark rectangle in the center is due to the beam stop shadowing the direct beam. The yellow arrow indicates the position of the reflected beam. Peaks A and B evolve above the reflected side of the sample, while peaks A' and B' are attenuated due to the transmission through the sample. The insets show the sample geometry with <111> $\| \boldsymbol{k_A} \| \boldsymbol{k_B}$ and for $\omega = 0$ $\boldsymbol{B} \| \boldsymbol{k_i}$.

the state in Figure 4.21b belongs to an intermediate phase consisting of phases 1 and 2. In reciprocal space, the positions of the Bragg peaks can be represented by the wavevectors $\boldsymbol{k_A}$ and $\boldsymbol{k'_A}$ of phase 1 and $\boldsymbol{k_B}$ and $\boldsymbol{k'_B}$ of phase 2, with $k_A = k'_A$, $k_B = k'_B$, $k_A > k_B$. In real space, the corresponding magnetic structure can be described as helices propagating along <111> with the helix length $L_A < L_B$. The phase corresponding to Figure 4.21d does not reveal any Bragg spots, which is due either to a field polarized phase, a paramagnetic phase, a k-vector exceeding the accessible Q-range, or to the method not being sufficiently sensitive.

Off-specular Reflectivity. Q_x-Q_z scattering maps, obtained as described in Section 4.3.3 on the same sample but at NREX at 15 K, are shown in Figure 4.22. In contrast to the GISANS measurement of SANS1, the signal is measured only above the horizon and is integrated along Q_y. Further, the Bragg peak at $Q_x = 0$ is not visible, because it is superimposed by the spikes of the specular intensities (dark blue and dark red vertical stripes). Figure 4.22a shows a scattering map recorded at 30 mT, exhibiting one magnetic Bragg sheet corresponding to peak A (black arrow) in the off-specular regime. It appears as a horizontal high-intensity stripe at constant Q_z. This phase corresponds to phase 1 as determined by GISANS. The scattering map of Figure 4.22b exhibits two Bragg sheets corresponding to peaks A and B in the off-specular regime (two horizontal stripes indicated by arrows) and was therefore recorded in the intermediate phase. In this setup geometry, 0.24 T was the maximal reachable field, and thus phase 2 was not accessible. In the next sections, the data is discussed in more detail and more quantitatively using intensity profiles along Q_z.

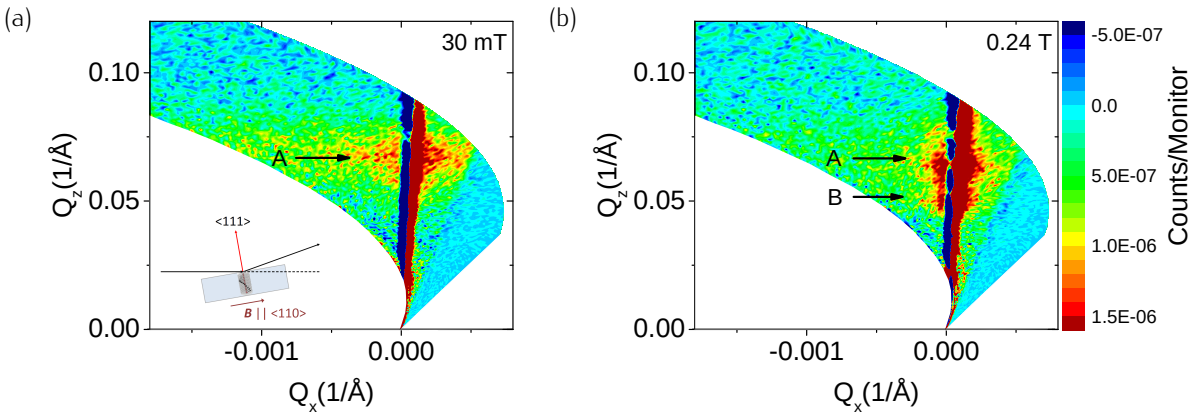

Fig. 4.22: Off-specular reflectivity at NREX: Scattering map of sample SI121 ($d_{MnSi} = 553$ Å) in counts per monitor vs. Q_x and Q_z measured at 15 K. The vertical stripes at $Q_x = 0$ correspond to the specular reflection. The magnetic Bragg sheets (horizontal stripes of high intensity) can be observed at constant Q_z in the off-specular regime and show (a) peak A of phase 1 at 30 mT and (b) the double peak of the intermediate phase at 0.24 T. The setup is plotted as inset, which is equivalent to the setup used at SANS1. The results are in good agreement with data recorded by GISANS at SANS1 (Figure 4.21).

4.4.2 Influence of Measurement Conditions

In this section, I will confirm the stability and reproducibility of the results in terms of influences of the in-plane magnetic field direction, the cooling history, and the instrument used. I will therefore compare the intensity profiles of sample SI121 ($d_{MnSi} = 553$ Å) of the magnetic Bragg peak versus Q_z for different measurement conditions. I will only discuss the Bragg peaks above the sample horizon, i.e. peak A and peak B (Figure 4.21), as they are much more intense than peak A' and peak B' measured in transmission. The intensity profiles were obtained as described in Section 4.3.3 and 4.3.1.

In-plane Magnetic Field Direction. All GISANS data measured at SANS1 were recorded with an in-plane field. For $\omega = 0$, the incident beam was aligned with $\boldsymbol{k_i} \parallel \boldsymbol{B}$, as depicted in Figure 4.15, and the sample was oriented with either $\boldsymbol{k_i} \parallel$ <110> or $\boldsymbol{k_i} \parallel$ <112>. Figure 4.23 compares the intensity profiles of the Bragg peak A of phase 1 versus Q_z at 0.05 T for

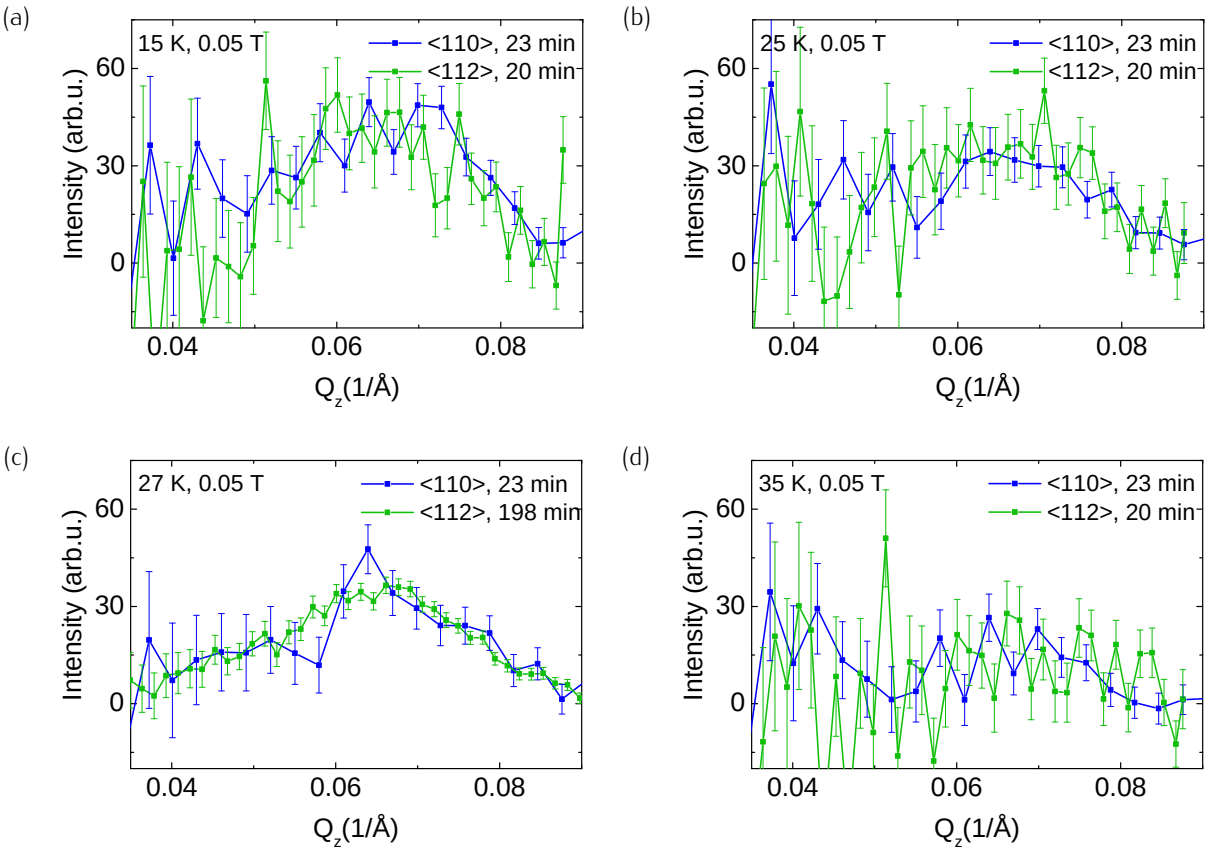

Fig. 4.23: Intensity of Bragg peaks of sample SI121 ($d_{MnSi} = 553$ Å) vs. Q_z recorded at SANS1 for $\boldsymbol{B} \parallel$ <110> and $\boldsymbol{B} \parallel$ <112> using different measurement times (see label). Data was measured in phase 1 at 0.05 T and (a) 15 K, (b) 25 K, (c) 27 K, and (d) 35 K. The comparison shows that the profiles are the same for different in-plane field directions.

both directions. For all four temperatures from 15 K (Figure 4.23a) to 35 K (Figure 4.23d) the profiles are in good agreement. Different statistics are due to different measurement times. I conclude that there is no indication for a magnetic in-plane uniaxial anisotropy.

Cooling History. We checked the stability of the phase 2 at SANS1 by comparing the profile of peak B after ZFC and FC (Figure 4.24a) as well as after FC in a low field of 0.4 T and in a very high field of 5 T (Figure 4.24b). The intensity of the profile recorded after ZFC is only less than 20% higher than that of the profile recorded after FC, both measured at 15 K and 0.05 T. The profiles at 27 K and 0.4 T — both recorded after FC but at different field values — are exactly the same.

Instrument. Finally, we prove that the profiles are reproducible, even when using different instruments. Figure 4.25 compares the profiles of the magnetic Bragg peaks at 15 K (Figure 4.25a–b) and 27 K (Figure 4.25c–d) measured in a small field typical for phase 1 (Figure 4.25a–c) and in a middle field typical for the intermediate phase (Figure 4.25b–d). All NREX intensities are scaled by one and the same factor to fit to the SANS1 data, so that the relative intensity is comparable. In Figure 4.25a the profile of peak A recorded at SANS1 is less than 20% higher than the profile from NREX. This could be due to a small drop in the intensity by applying a field of 30 mT, which was the permanent magnetic field at the sample without applying current to the coil. The maximum intensities for all other graphs (Figure 4.25b–d) coincide for both instruments using the same scaling factor. The double peak of the intermediate phase (Figure 4.25b and d) is more pronounced for the NREX data. Especially for the peak at a lower Q_z value, i.e. peak B, measured at 15 K and 0.24 T (Figure 4.25b), the intensity recorded by NREX is much higher than for the SANS1 profile. We expect the incoming amplitude associated with the reflectivity, which decreases with Q_z, to be

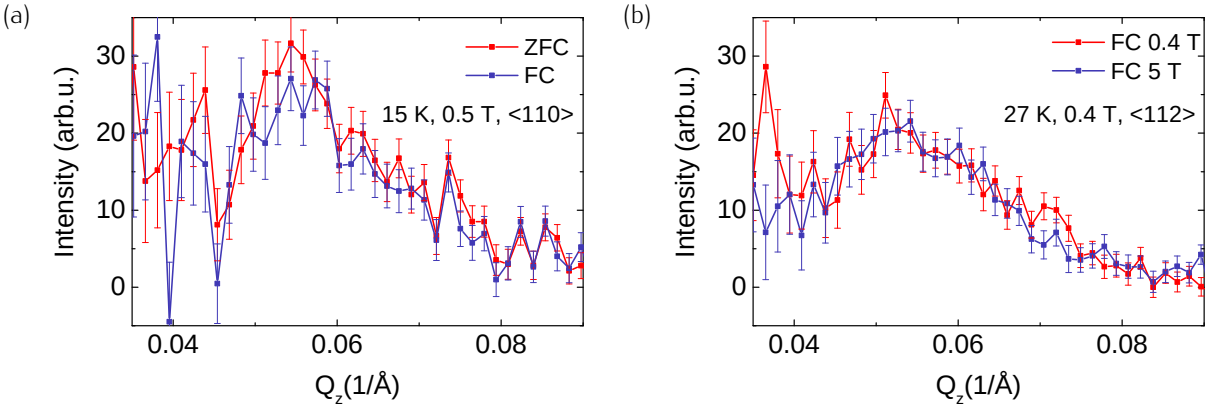

Fig. 4.24: Intensity of Bragg peaks of sample SI121 (d_{MnSi} = 553 Å) vs. Q_z recorded at SANS1 in phase 2. (a) Comparison of profiles recorded after ZFC and FC at 15 K and 0.5 T with $\boldsymbol{B}$ || <110>. (b) The comparison of profiles obtained after FC in 0.4 T and 5 T, measured at 27 K and 0.4 T with $\boldsymbol{B}$ || <112> shows that the profiles for different cooling histories are the same.

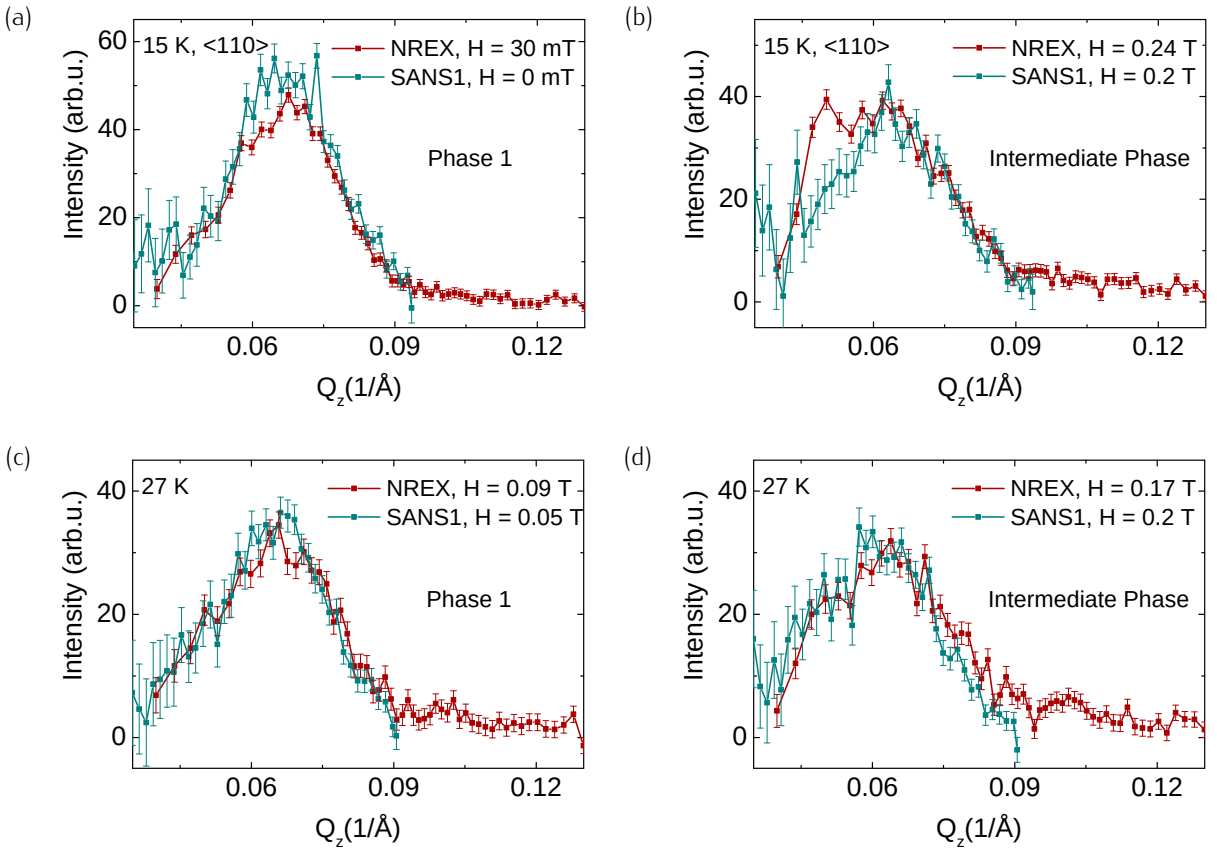

Fig. 4.25: *Intensity of Bragg peaks of sample SI121 (d_{MnSi} = 553 Å) vs. Q_z recorded at SANS1 and NREX: (a) and (b) at 15 K and (c) and (d) at 27 K. (a) and (c) correspond to phase 1, while (b) and (d) correspond to the intermediate phase. Every NREX profile was scaled by the same factor to fit to the SANS1 data.*

responsible for this. In contrast, for GISANS, we measured at a constant angle of incidence providing a constant incoming amplitude. Nevertheless, the characteristic features to identify the phases are the same for all data recorded by both instruments, and even the shape is exactly the same for three out of four data sets.

We were therefore able to show that our data is reproducible, at least for data acquired away from phase transitions.

4.4.3 Properties of Phases

So far, I have introduced the phases and showed their stability and reproducibility for sample SI121 (d_{MnSi} = 553 Å). In this section, I will discuss the features of the phases in detail and determine the phase boundaries of the same sample. As discussed above, it is possible to directly compare the results recorded with the in-plane field directions $\boldsymbol{B}$ || <110> and

$\boldsymbol{B}$ || <112> and to compare data obtained from SANS1 and NREX. I will therefore use all the data to give a detailed analysis of the phases and to localize the phase transitions. Once again, intensity profiles are generated from the magnetic Bragg peak emerging on the side of the reflecting surface as a function of Q_z. All measurements are recorded after FC from 60 K.

Figure 4.26a provides an overview of the magnetic Bragg peak profiles in each phase. For the purpose of clarity, error bars are only added in Figure 4.26a. In phase 1, peak A dominates at $k_A = 0.067\,\text{Å}^{-1} \pm 0.002\,\text{Å}^{-1}$, while peak B, at $k_B = 0.052\,\text{Å}^{-1} \pm 0.002\,\text{Å}^{-1}$, is very small. In the intermediate phase, peak B clearly contributes to the total shape and a double peak evolves, forming a mixture of phases 1 and 2. In phase 2, only peak B remains. This figure also compares the profiles to no magnetic signal. It cannot yet be determined what type of phase this is. The magnetic Bragg peaks A and B correspond to helices directed along the surface normal with a helix length $L_A = 94\,\text{Å} \pm 3\,\text{Å}$ in phase 1 and $L_B = 121\,\text{Å} \pm 5\,\text{Å}$ in phase 2. Consequently, the helix length increases as the magnetic field increases. Although the intermediate phase represents a continuous phase transition from phase 1 to phase 2, we define artificial boundaries for this intermediate phase (IP) by creating reasonable criteria. In the following, we will refer to the transitions to and from the intermediate phase as "phase transitions", although there is no thermodynamic transition. All profiles were fitted by a Gaussian, plotted as a thick line. From the single peak fitting of peak A at 0 T and 15 K and of peak B at 0.5 T and 27 K, we fixed the shape, the baseline and roughly the limits for the peak centers and the FWHM for the double peak fitting. All characteristic features of the profiles discussed in this section were determined from the fits. In the following section, I will discuss the properties of the phases in detail, referring to the amplitude, the peak position, the FWHM, and the integrated intensity. The results are then summarized in a phase diagram.

Amplitude. Figure 4.26b shows all profiles corresponding to phase 1, which establishes for magnetic fields with $0\,\text{T} \leq B \leq 0.1\,\text{T}$. By increasing the magnetic field or temperature, the intensity of peak A, i.e. $I_A^{max} = I(k_A)$, undergoes a very marked decrease of >20% compared to the highest peak intensity $I_A^{max} = 51$ recorded at 0 T and 15 K. The intensity of peak B, i.e. $I_B^{max} = I(k_B)$, is lass than 40% of the intensity of peak A and vanishes in the slope of peak A. The intermediate phase shows a more complicated behavior, which can be seen from Figure 4.26c. I therefore divided this phase into three regimes, a–c. All shapes possess the clear double peak for magnetic fields between 0.17 T and 0.4 T, but the relative and absolute intensities of peaks A and B are different. In all regimes, the intensity of peak A has droped to I_A^{max}<36, while the intensity of peak B is $I_B^{max} \geq 14$.

In regime a (Figure 4.26d), $I_A^{max} \geq 30$ is as high as in phase 1, while peak B has increased to $40\% \cdot I_A^{max} < I_B^{max} < 60\% \cdot I_A^{max}$. Only the measurement at 15 K and 0.2 T does not show such an intense peak B. The reason for this is not known. The high intensity at peak A is probably an outlier and the profile corresponds to regime b.

In regime b (Figure 4.26e), the overall intensity has dropped by about 20% compared to regime a ($I_A^{max} < 26$) and the peak B increased to $60\% \cdot I_A^{max} \leq I_B^{max} < I_A^{max}$. In regime c (Figure 4.26f), it is the other way round, with $80\% \cdot I_B^{max} \leq I_A^{max} < I_B^{max}$ resulting in peak A being less intense.

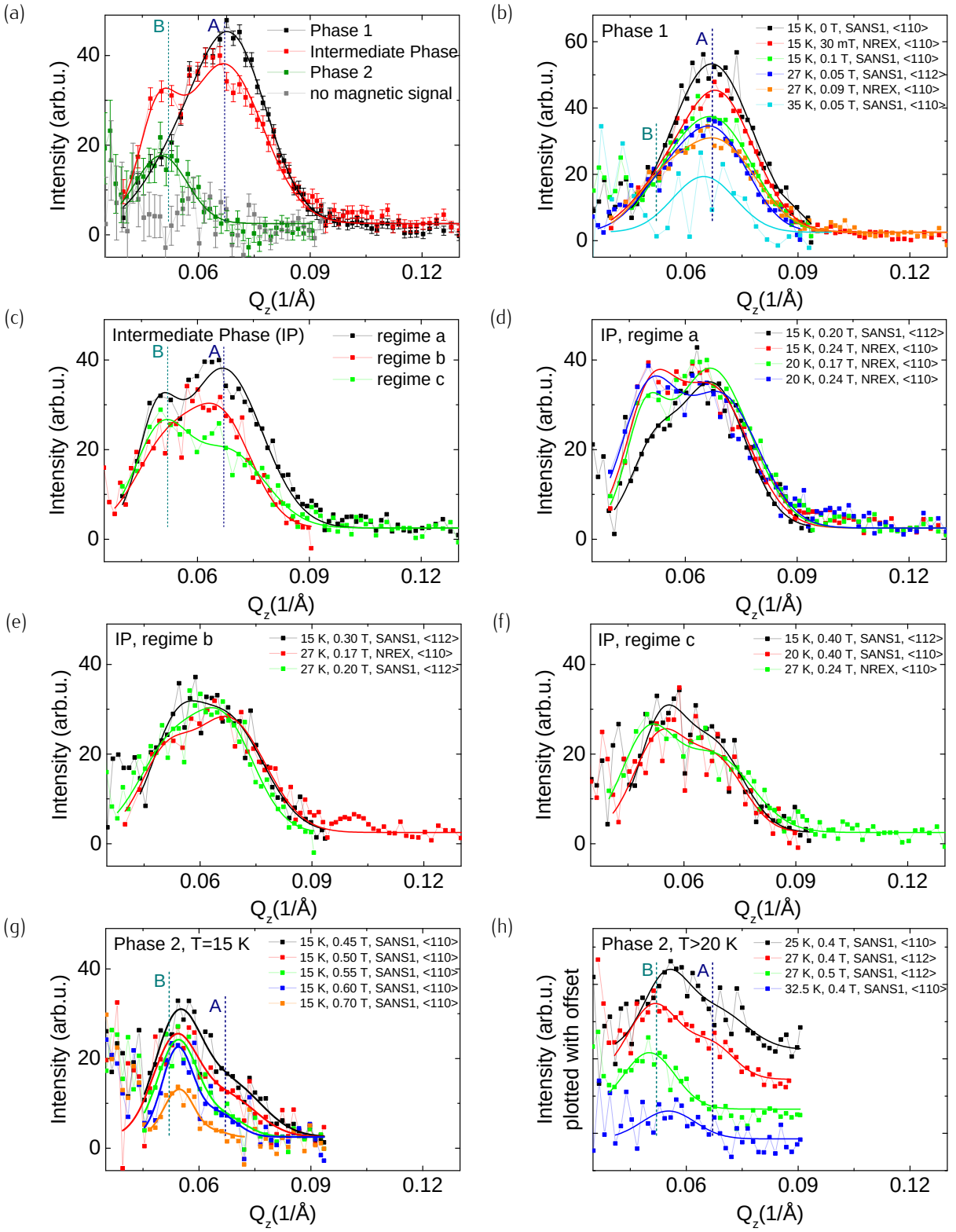

Fig. 4.26: All magnetic peak profiles of sample SI121 (d_{MnSi} = 553 Å) measured at SANS1 or at NREX at temperatures between 15–35 K and $\boldsymbol{B}$ || <110> or <112> (see legend). (a) Overview of the different shapes of all phases. In (b)–(h) the profiles are arranged by shape and phase. Thick lines represent Gaussian fits.

In phase 2 (Figure 4.26g, 4.26h), the intensity of peak A drops further to $I_A^{max} \leq 50\% \cdot I_B^{max}$.

The evolution of the maximum intensity of peaks A and B is summarized in Figure 4.27a for 15 K (upper panel) and 27 K (lower panel). At zero field (phase 1), I_A^{max} is higher than 40 and drops steeply with increasing field, while the intensity at the peak position B is ≈ 9. Phase 1 can be determined by $I_B^{max} \leq 40\% \cdot I_A^{max}$. As soon as I_B^{max} starts rising to ≥ 14, we determine the magnetic structure to enter the intermediate phase with $40\% \cdot I_A^{max} < I_B^{max} < 60\% \cdot I_A^{max}$ as

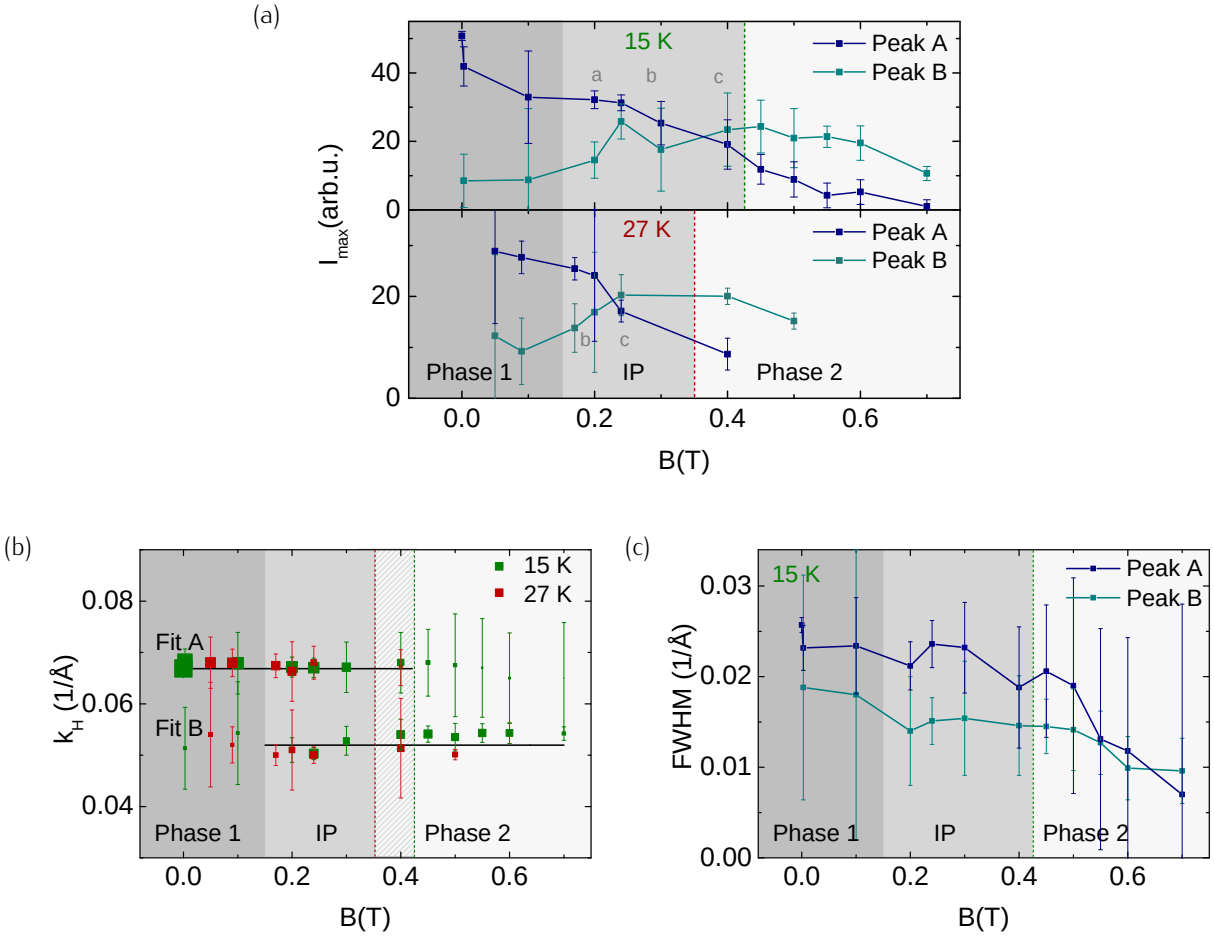

Fig. 4.27: Results of Gaussian fits: (a) The maximum intensity of peaks A and B as a function of magnetic field $\boldsymbol{B}$ for 15 K (upper panel) and 27 K (lower panel) shows that the intensity of peak A drops, while the intensity of peak B rises. (b) Modulus of the magnetic wavevector $\boldsymbol{k_H}$, i.e. peak position, along Q_z vs. the magnetic field $\boldsymbol{B}$ for 15 K and 27 K. The size of the symbols is scaled with the peak amplitude. Black lines A and B are horizontal fits of peak position k_A and k_B. (c) FWHM as a function of magnetic field $\boldsymbol{B}$ of peaks A and B drops, with peak A being broader than peak B. In all images, phases 1 to 2 are highlighted in gray. Dotted vertical lines depict the transition from the intermediate phase (IP) to phase 2 for 15 K (green) and for 27 K (red).

described above. The crossover of the intensity curves of peaks A and B, corresponds to the transition from regime b to c. Afterwards, both peaks drop, with peak A dropping quickly to $I_A^{max} \leq 50\% \cdot I_B^{max}$, which we determine as the transition to phase 2 occuring at higher fields for 15 K (dotted green line) than for 27 K (dotted red line).

For the sake of completeness, I also want to mention an additional small peak around $Q_z = 0.10\,\text{Å}^{-1}$ for the NREX data. This Q-range was accessible for the OSR measurement but not for the GISANS measurements at SANS1. This peak is most pronounced in phase 2 at 20 K for 0.24 T and at 27 K for 0.17 T and vanishes at 15 K for 30 mT and at 27 K for 0.24 T. Since it has only 20% of the intensity of peak A and it does not show similar systematic behavior to peak A and peak B, I have not taken it into account for further descriptions.

Peak Position. Another important feature to evaluate as a function of magnetic field is the center of peaks A and B, i.e. the wavevector $\boldsymbol{k_H}$ of the magnetic structure. This is depicted in Figure 4.27b for 15 K and 27 K, where the black lines are horizontal fits regarding the peak position of peaks A and B. Again, the dotted vertical lines define the transitions from the intermediate phase to phase 2 (green for 15 K, red for 27 K). The fits reveal the peak positions of $k_A = 0.067\,\text{Å}^{-1} \pm 0.002\,\text{Å}^{-1}$ and $k_B = 0.052\,\text{Å}^{-1} \pm 0.002\,\text{Å}^{-1}$, resulting in $L_A = 94\,\text{Å} \pm 3\,\text{Å}$ and $L_B = 121\,\text{Å} \pm 5\,\text{Å}$. The helix with length L_A fits into the MnSi layer 5.9 times, while the helix with length L_B fits only 4.6 times. **FWHM.** A second characteristic feature is the FWHM dropping from 0.025 to $0.01\,\text{Å}^{-1}$ with increasing magnetic field as depicted in Figure 4.27c for peak A. This is due either to increasing domains or to more definition of the spin structure with increasing magnetic field. Indeed, PNR measurements will show (Section 4.4.4) that an increasing number of spins align parallel or antiparallel to the increasing magnetic field, and thus the spin structures become more defined.

The FWHM of peak B shows a similar behavior, and is about $0.005\,\text{Å}^{-1}$ smaller. However, due to the reduced number of turns for helices with the increased length L_B one would have expected a broader FWHM. This can again be explained by the spin structure, which is even more defined for fewer helix turns, since the regions of spin rotation are also reduced and even more spins align parallel or antiparallel to the magnetic field.

Note that the error bars for the FWHM of peak A in phase 2 and of peak B in phase 1 are huge, since then always one peak is hidden in the shape of the other peak and fitting becomes more ambiguous.

Integrated Intensity. The intensity integrating both magnetic Bragg peaks within one sector as indicated in the detector image in Figure 4.21a is plotted as a function of magnetic field (Figure 4.28a) for 15 K and 27 K and as a function of temperature (Figure 4.28b) for 0.05 T and 0.4 T for data recorded at SANS1. The intensity drops when the magnetic field or the temperature are increased, as the magnetic state undergoes a phase transition to the ferromagnetic, the paramagnetic, or a different phase. That cannot be identified at this point. **Phase Diagram.** The above classified phases are illustrated in the B-T-phase diagram of Figure 4.29, in which the filled squares originate from data recorded at SANS1 and the open

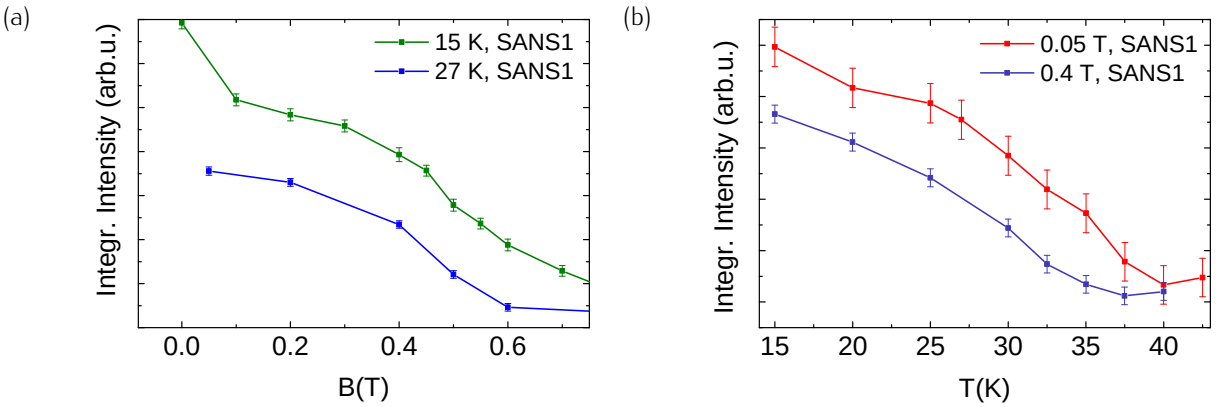

Fig. 4.28: *Intensity within one sector integrating both magnetic Bragg peaks of the SANS1 detector images plotted (a) vs. magnetic field for 15 K and 27 K and (b) vs. temperature for 0.05 T and 0.4 T. The magnetic signal drops with increasing temperature or field, which indicates a phase transition.*

squares from data recorded at NREX. The points associated with the phases are encoded via color ranging from black (phase) and red (intermediate phase) to green (phase 2) and additionally separated by lines, illustrating the boundaries. Data of gray squares did not show any magnetic signal. For an exact determination of the phase boundaries, different techniques, such as MOKE or Hall effect measurements need to be used, which was not within the scope of this thesis. Above phase 2, we expect, based on results obtained for bulk, a ferromagnetic phase and, above T_c, a paramagnetic phase. The data presented in the next section will provide more information.

To conclude, we observed three different magnetic phases, always with a periodic structure parallel to the surface normal. The length of this periodic structure, a helix, changes as a function of field with a wavevector $\boldsymbol{k_A} = 0.067\,\text{Å}^{-1} \pm 0.002\,\text{Å}^{-1}$ corresponding to a helix length of $L_A = 94\,\text{Å} \pm 3.0\,\text{Å}$ at low fields in phase 1 and of $\boldsymbol{k_B} = 0.052\,\text{Å}^{-1} \pm 0.002\,\text{Å}^{-1}$ corresponding to a helix length of $L_B = 118.5\,\text{Å} \pm 12.4\,\text{Å}$ at high fields in phase 2. The intermediate phase is a mixture of phases 1 and 2, representing a broad phase transition and containing different domains with both helix pitches. Bragg peaks with smaller k_H values cannot be identified, because they will overlap with the reflected spot located at low Q of $Q_z = 0.011\,\text{Å}^{-1}$ or $Q_z = 0.026\,\text{Å}^{-1}$ for GISANS, whereas for OSR, the minimum accessible Q_z is $0.028\,\text{Å}^{-1}$. Further, smaller k_H-vectors are due to longer helix lengths and therefore fewer helix turns, which causes the Bragg peak to become even broader and as a consequence less detectable.

Discrete helicoidal states for an in-plane field were also predicted in [12], as illustrated in Figure 4.6a. Here, the ground state helix length of 13.9 nm was much larger than our observed helix length in zero field.

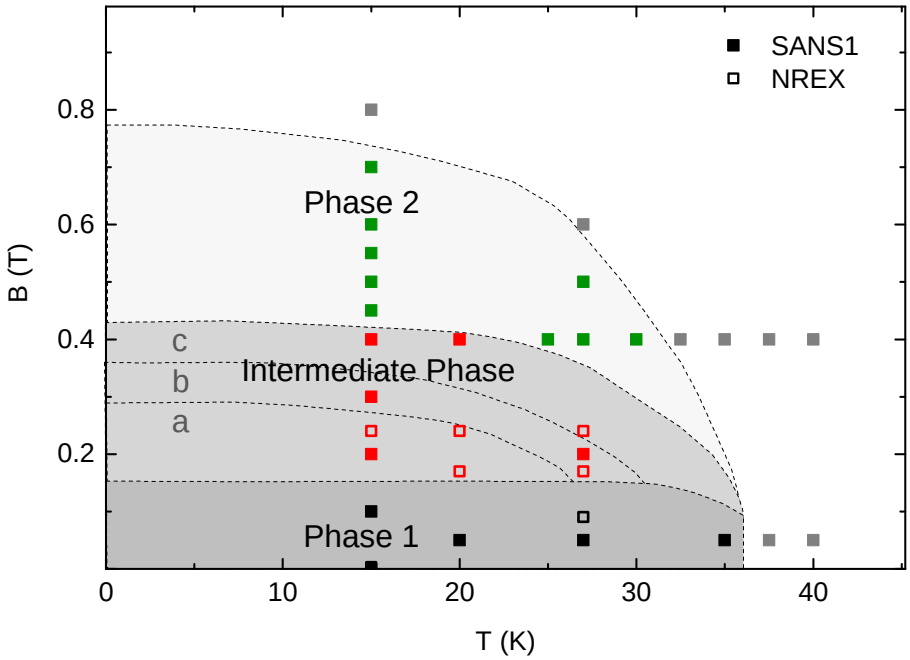

Fig. 4.29: Preliminary B-T phase diagram of sample SI121 with $d_{MnSi} = 553\,\text{Å}$ based on the data recorded at SANS1 (filled squares) and NREX (open squares). Phase 1 (black squares) and phase 2 (green squares) show magnetic Bragg peaks along MnSi<111> with $k_A = 0.067\,\text{Å}^{-1}$ and $k_B = 0.052\,\text{Å}^{-1}$, respectively. The intermediate phase (red squares) exhibits both magnetic Bragg peaks. Data indicated by gray squares do not show any magnetic signal.

4.4.4 Indirect Phase Determination using PNR

So far, we have investigated the direction of the magnetic wavevector of the helices and its behavior as a function of magnetic field and temperature. However, we have not presented any information about the direction or absolute value of the magnetization. Using PNR, which depends on the vertical magnetic profile in the sample (Section 2.2.2), we will show that as the magnetic fields increases, more and more spins align parallel or antiparallel to it. The combination of PNR and GISANS, or off-specular reflectivity, is therefore a powerful tool to determine the details of the magnetic structure. Again, we investigate sample SI121 with $d_{MnSi} = 553\,\text{Å}$. The setup at NREX is described in Section 4.3.3. Since PNR data have to be fitted, resulting sometimes in different equivalent models, the magnetic profile was obtained only indirectly. Although data interpretation is difficult, the PNR method is very sensitive to small magnetic moments. The magnetic field was again applied horizontally, i.e. in plane, but this time — in contrast to GISANS and OSR — perpendicular to $\boldsymbol{k_i}$.

Reflectivity Curves. By using a polarizer and an analyzer in front of and behind the sample, all four spin-flip channels of the reflected beam can be measured — again, as a function of Q_z, as is depicted in Figure 4.30 at 35 K for three different magnetic fields. The intensity

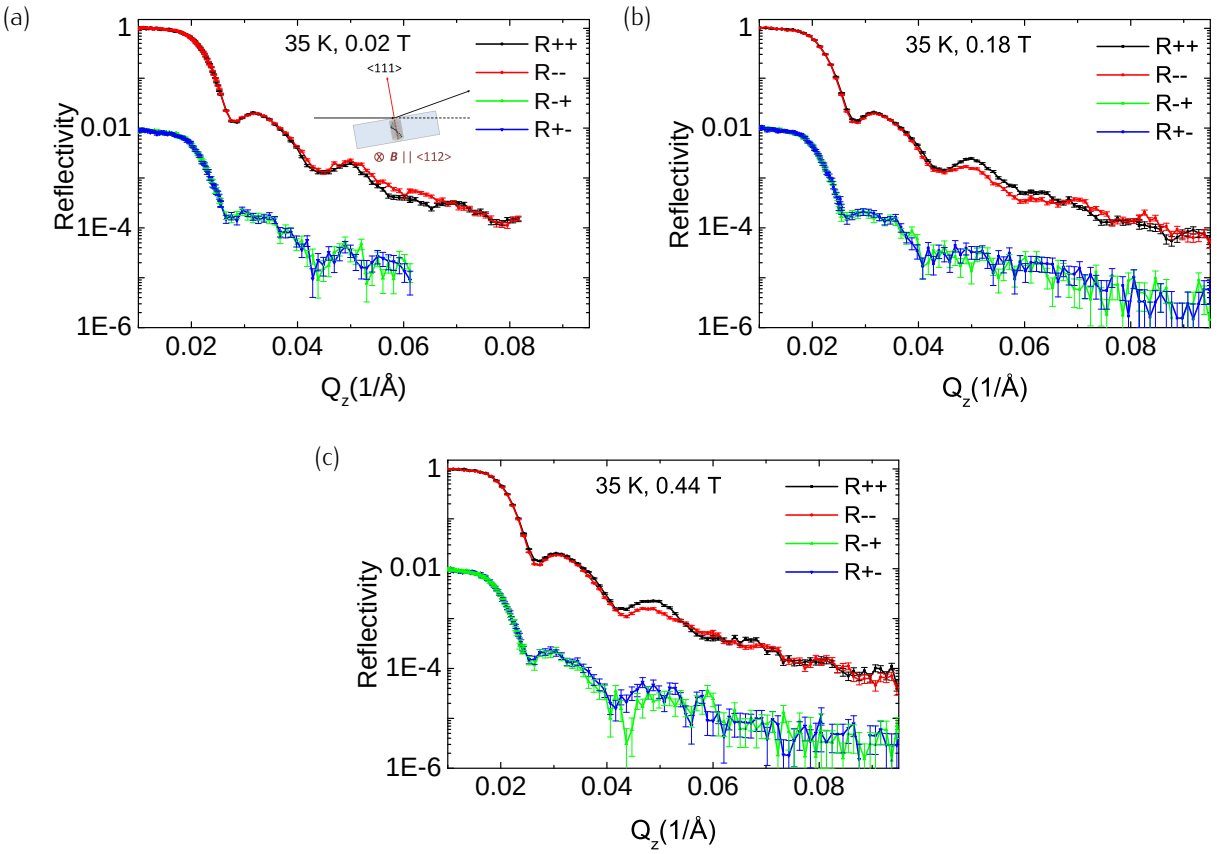

Fig. 4.30: *PNR at NREX: Reflectivity of sample SI121 (d_{MnSi} = 553 Å) vs. Q_z for all four spin channels measured at 35 K and (a) 0.02 T, (b) 0.18 T, and (c) 0.44 T. The intensities of the spin-flip channels R+- and R-+ replicated the curves of the non-spin-flip channels R++ and R-- but with an intensity by two orders of magnitude smaller, indicating that we measured only spin leakage. The difference between R++ and R-- implies a magnetic structure.*

in the spin-flip channels R+- and R-+, which are sensitive to the in-plane magnetization component perpendicular to the magnetic field, are two orders of magnitude smaller than the intensity in the non-spin-flip channels R++ and R--. The curves also replicate the shape of R++ and R--. This means that we only measured the spin leakage, which is due to the beam polarization of 97%. This is the case for all the measurements recorded at three magnetic field values, which, as I will show later, correspond to three different phases. Accordingly, there is either no in-plane magnetization component perpendicular to the magnetic field or it is cancelled out within one plane. A cancellation of this component can be explained by equally distributed right- and left-handed helices, since then the spin components of each z-plane cancel out in that direction, as is shown in Figure 4.8c. This is confirmed by Karhu *et al.*, who revealed right-handed and left-handed domains in the crystal structure by TEM [145] as well as no spin-flip signal in PNR measurements (Figure 4.8b) on a 26.7 nm sample for an in-plane magnetic field [147], too.

R++ and R−− are definitively different, showing a spin asymmetry. This is why the spins are aligned parallel or antiparallel to the magnetic field direction. The signal difference appears mainly between $0.04\,\text{Å}^{-1} < Q_z < 0.08\,\text{Å}^{-1}$ and does not remain constant in the total Q_z-range, hinting at a complicated magnetic structure rather than a ferromagnetic state. From GISANS and OSR measurements, we expect a helical or conical magnetic structure, whose k_H vectors lie in the range of the observed spin asymmetry. To obtain more information about the microscopic magnetic structure, we fitted the magnetic profile to the data. Owing to the lack of distinct features in the spin-flip channels, we continued the measurements without an analyzer in order to gain intensity. Consequently, we only discuss the spin asymmetry (SA) of R+ and R- or R++ and R−−, depending on what has been measured.

Spin Asymmetries. Figure 4.31 shows all spin asymmetries (Section 4.3.3) as a function of Q_z measured in magnetic fields between 30 mT and 0.44 T for 5 K and 35 K. For the purpose of clarity, error bars are only added to one curve of each figure. Figure 4.31a gives an overview of the SAs of all three phases at 35 K for magnetic fields $0\,\text{T} < B < 0.44\,\text{T}$. The magnetic field range at NREX was too small to reach a higher phase than phase 2, such as the ferromagnetic phase. The SAs in phases 1 and 2 are distinctly different. The position of the first dip (SA<0) does not change considerably from phase to phase, but the amplitude increases with increasing phase. The SA of phase 1 has a very pronounced dip at $Q_z = 0.057\,\text{Å}^{-1}$. For very small magnetic fields, this dip is sharp, and we refer to the corresponding state as regime 1a. By applying a larger magnetic field, the SA has a broader dip extended to smaller Q_z of $0.05\,\text{Å}^{-1}$, assigning it to regime 1b. The SA of the intermediate phase is very similar to the SA of phase 1, but increased at $Q_z = 0.06\,\text{Å}^{-1}$ to zero. At this Q_z value in phase 2, the SA is even greater but drops at $Q_z = 0.044\,\text{Å}^{-1}$. Due to the fact that the intermediate phase exhibits characteristic features of phase 1 and phase 2, it confirms the conclusion drawn from GISANS that is a mixed state.

Regimes 1a and 1b are summarized for 35 K in Figure 4.31c and for 5 K in Figure 4.31d. They all share a negative SA at $0.06\,\text{Å}^{-1}$. At 35 K, the curves measured at 30 mT and 0.02 T belong to regime 1a, with a higher SA at $0.05\,\text{Å}^{-1}$. The difference between regime 1a and 1b at this Q_z value is better defined at 5 K, where the curves of regime 1a seem to continuously shift to more negative values for increasing magnetic fields. In phase 1, a continuous shift with increasing field was also observed in the Bragg-peak intensity in Figure 4.27a, which was also more pronounced at low temperatures, i.e. 15 K.

The SAs in the intermediate phase at 35 K and 5 K (Figure 4.31e and f) are all very similar. Only the SA at 35 K and 0.27 T is a bit above zero, at $0.06\,\text{Å}^{-1}$, probably because it is close to the transition to phase 2. The SA at 5 K and 0.27 T shows a small peak at $Q_z = 0.058\,\text{Å}^{-1}$, but is smaller than zero, presumably being close to the transition to phase 1. The SA of phase 2 was only measured for 35 K (Figure 4.31b) and was positive at $0.06\,\text{Å}^{-1}$. At 5 K we ought to have measured at higher magnetic fields to reach the next phase, but this was not possible with the magnet used at NREX.

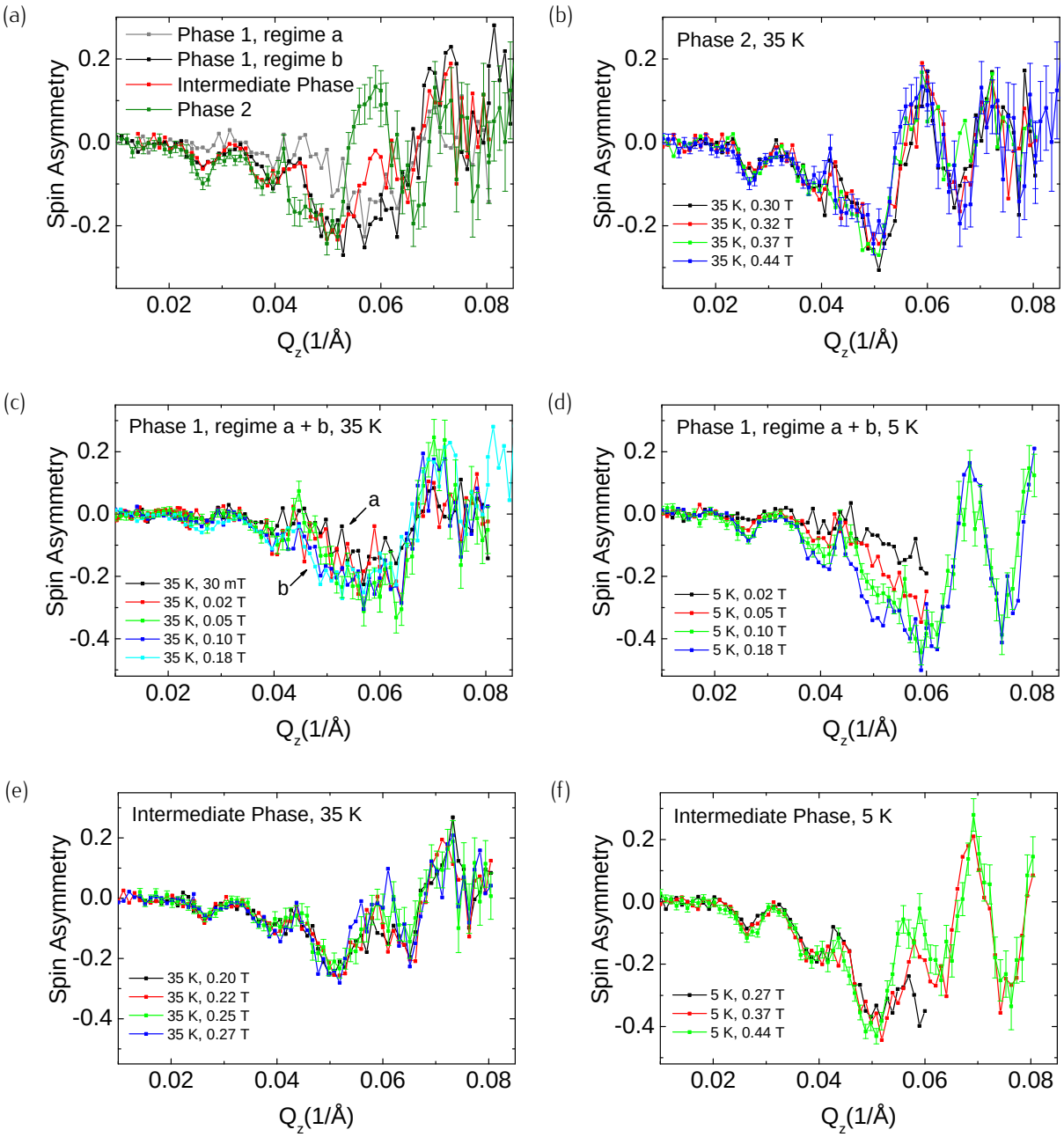

Fig. 4.31: *SA of sample SI121 (d_{MnSi} = 553 Å) calculated from PNR plotted vs. Q_z and measured at 35 K and 5 K for magnetic fields between 30 mT and 0.44 T. (a) Overview of different phases measured at 35 K. Spin asymmetries arranged by shape and phase: (b) phase 2 at 35 K, phase 1 (c) at 35 K and (d) at 5 K, the intermediate phase (e) at 35 K and (f) at 5 K.*

Figure 4.32 enables a direct comparison between the SAs of 5 K and 35 K recorded at the same magnetic fields of 0.18 T associated with phase 1 (Figure 4.32a) and in the intermediate phase, where we had to apply different fields (Figure 4.32b). In both cases, the SA is sharper

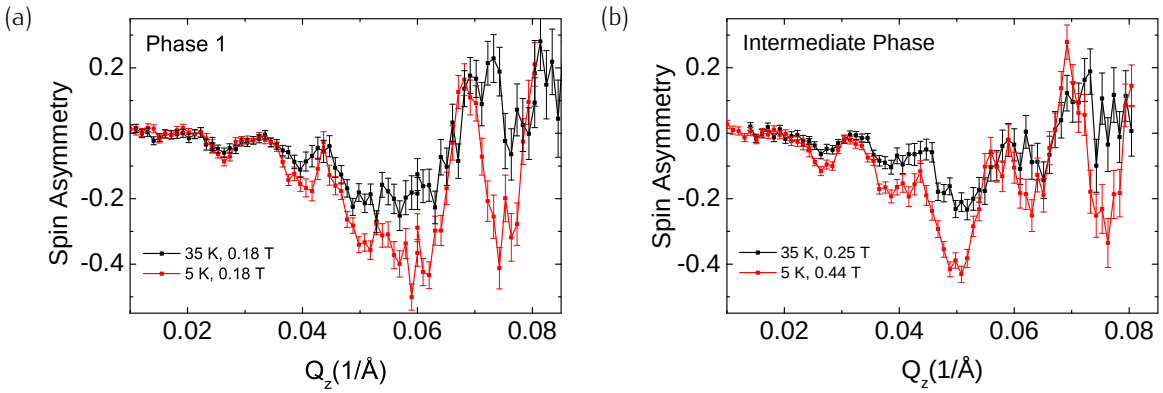

Fig. 4.32: *Comparison of the SA measured at 5 K and 35 K in (a) phase 1 and (b) the intermediate phase, with the amplitude of the measurement at 5 K higher than at 35 K.*

at 5 K than at 35 K, having higher amplitudes.

Phase Diagram. This classification of the phases is illustrated by adding the PNR data to the phase diagram of Figure 4.29, resulting in the phase diagram of Figure 4.33. It becomes apparent that the PNR data still shows a signal in phase 2, whereas GISANS data did not show a signal anymore. We therefore infer that PNR is far more sensitive. Consequently, the phase transition from phase 2 and to the ferromagnetic state B_c as well as T_c cannot be determined by GISANS. Instead it was determined by magnetometry using a SQUID-VSM by Shilei Zhang (University of Oxford) of a similar sample, which resulted in a T_c of 42.5 K (vertical blue line) and in $B_c < 0.95$ T (blue dots). Matthias Brasse determined 1.2 T$< B_c <$0.75 T for a nominal 10 nm and 30 nm sample by torque magnetometry [153] with the magnetic field canted to the surface normal by 15–45°. Due to the easy-plane anisotropy, these values are bit increased. Nevertheless, these values are in good agreement with the PNR data as well as with other publications [10, 13, 147].

This phase diagram looks very similar to the phase diagram published by Wilson *et al.* [10], as shown in Figure 4.7b. However, their indication of the phases is in variance with [11], although the phase boundaries above 25 K are similar. Those phase transitions were identified from kinks in dM/dH curves, which were measured as field sweeps for several temperatures. Below 25 K, the phase boundaries deviate strongly for increasing and decreasing field and do not fit to our data. Wilson *et al.* spotted a very narrow additional phase directly below the ferromagnetic phase stated for the total temperature region below T_c. In that range, we were not able to record data by PNR, since the accessible magnetic field range was too small. The value of T_c is in good agreement with the T_c range stated in [11] of 41.4–44.0 K for 12.8–29.8 nm samples.

Magnetization Models. Given the very similar profiles of the SA of each phase, it is sufficient to fit one curve of each phase. Since the intermediate phase is a mixture of phase 1 and phase 2, the magnetic depth profile of this phase should also be a superposition of phases 1

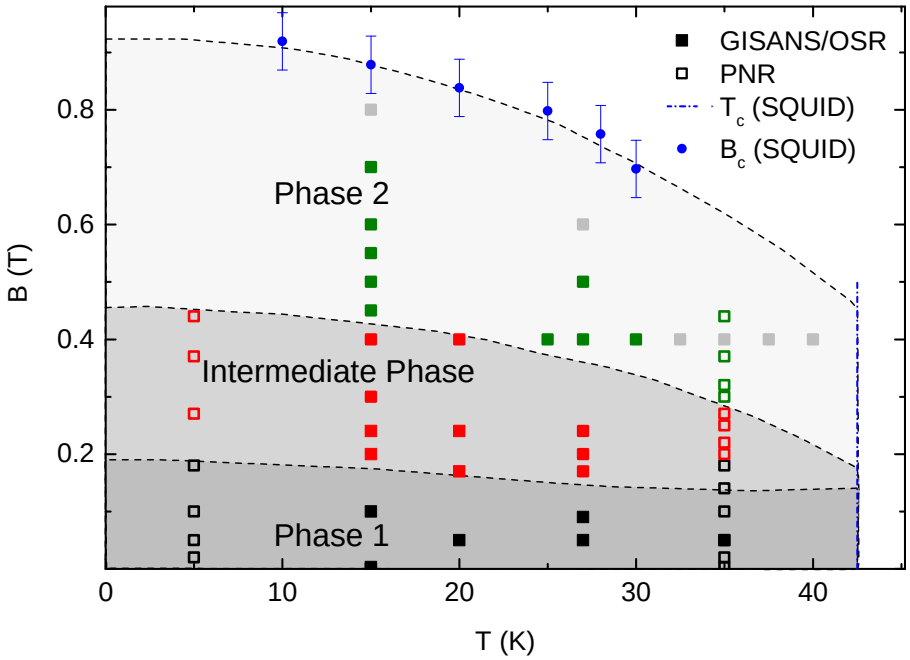

Fig. 4.33: B-T phase diagram of sample SI121 with $d_{MnSi} = 553\,Å$ based on the data recorded by GISANS or off-specular reflectometry (filled squares) and by PNR (open squares). Phase 1 (black squares) and phase 2 (green squares) show a magnetic Bragg peak along Q_z with $k_H = 0.067\,Å^{-1}$ and $k_B = 0.052\,Å^{-1}$, respectively. The intermediate phase (red squares)) exhibits both magnetic Bragg peaks. Data indicated by gray squares do not show any magnetic signal, which reveals that PNR is more sensitive than GISANS. Blue dots denote B_c as the critical field of the transition to the field polarized state and the blue dotted vertical line indicates the Curie temperature T_c. Both parameters were determined by Shilei Zhang (University of Oxford) for a similar sample using a SQUID-VSM. All data are in good agreement.

and 2. The ratio changes almost continuously, however, I will concentrate on the results of the fits for phase 1 at 35 K and 30 mT and for phase 2 at 35 K and 0.44 T in Figures 4.34a and b. The data is indicated by squares, while the fits are drawn as lines. Using SimulReflec [19] it was possible to simultaneously fit R++ and R-- as well as the SA. Owing to the large set of parameters, several fit solutions are possible. However, by restricting ourselves to a periodic structure, the number of reasonable fits is drastically reduced. The period, the amplitude, and the phase shift of the periodic magnetic depth profile are very sensitive to the fit quality.

The fits are shown in Figure 4.34c for phase 1 and in Figure 4.34d for phase 2. The squares illustrate the data and the line the fit, which is based on the same model as the fit of R++ and R--. This model, i.e. the magnetic moment as a function of MnSi depth z, is illustrated for both phases in Figure 4.34e. The magnetic model of phase 1 is a sine function with 5.5 turns, a period of $96\,Å \pm 5\,Å$, and an amplitude of $0.1\,\mu_B/atom$. A sinusoidal shape is expected for a helix, since we measure only the magnetization component parallel to the

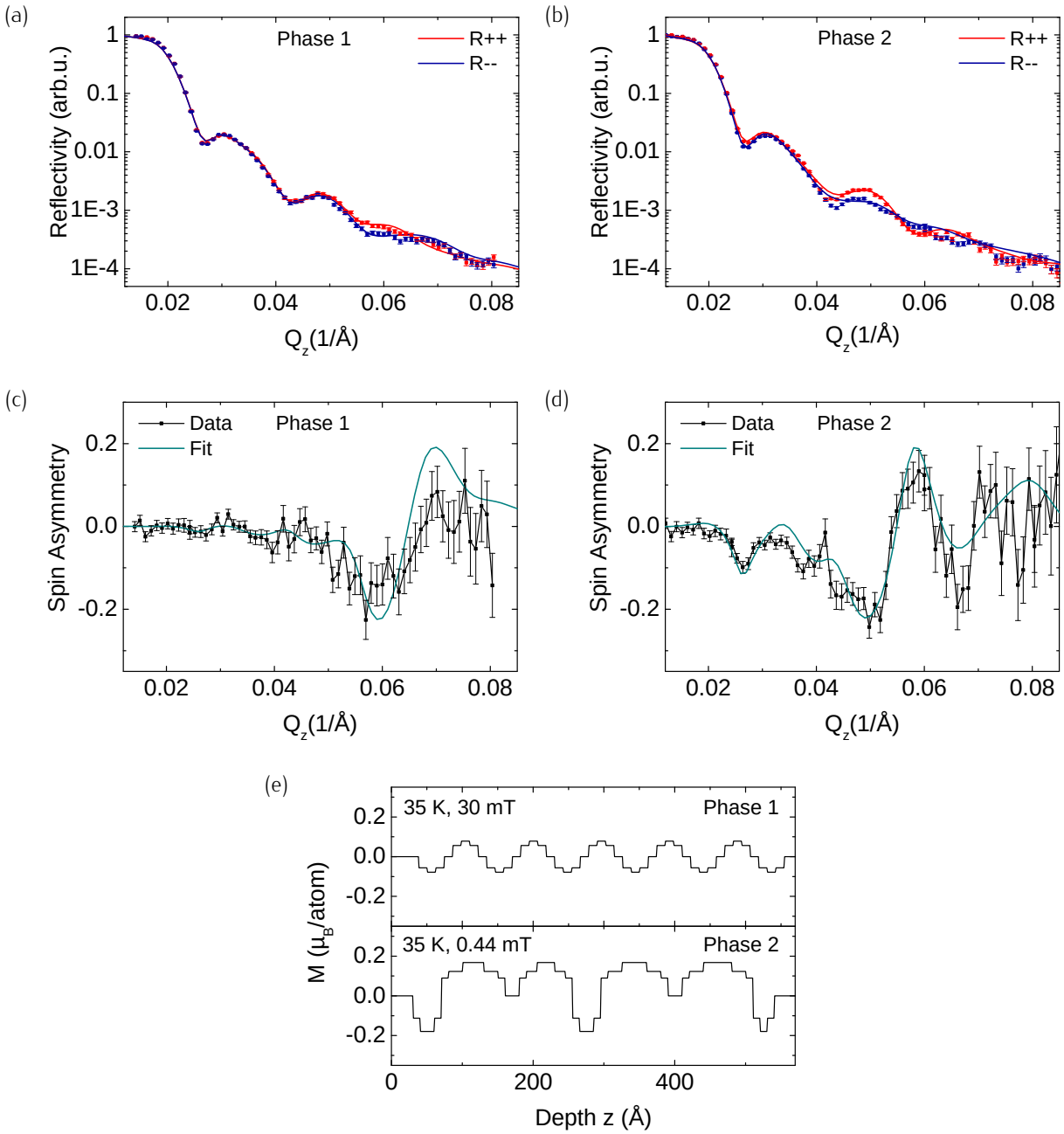

Fig. 4.34: *PNR data of SI121 (squares) for R++ and R-- with fits (lines) at 35 K and (a) 30 mT (phase 1) and (b) 0.44 T (phase 2). Corresponding SA data (squares) with fit (turquoise line) for (c) 35 K, 30 mT and (d), 35 K, 0.44 T. (e) Magnetic profile as a function of MnSi depth z, which results from the fits of R++, R--, and SA. The helix length increases from $L_A = 96\,\text{Å} \pm 5\,\text{Å}$ with 5.5 turns in phase 1 to $L_B = 120\,\text{Å} \pm 26\,\text{Å}$ with 4.5 turns and additional distortion of the sinusoidal shape in phase 2.*

magnetic field, which is the 2D projection of a helix. The model of phase 2 deviates from the pure sinusoidal shape, because more spins align parallel or antiparallel to the magnetic field with an increased amplitude of 0.17 $\mu_B/atom$. Removing the negative amplitudes of a periodic structure after the first and third turn improved the fit significantly. This profile could be due to the contribution of a second structure from different domains that is not visible in the GISANS measurement. We therefore regard the magnetic structure to consist of two periodic structures, appearing as the superposition of a short-wave and a long-wave profile. Compared to phase 1, the short-wave magnetic structure has only 4.5 turns and a longer period of 120 Å ± 26 Å. Therefore, it is in excellent agreement with GISANS and OSR, revealing the helix length of $L_A = 94$ Å ± 3 Å in phase 1 and $L_B = 121$ Å ± 5 Å in phase 2.

Wilson *et al.* [11] also fitted the SA measured at 5 K with a sinusoidal magnetization profile in zero field and a distorted sinusoidal shape together with a different periodicity for 0.2 T and 0.4 T. Further, they fitted the amplitude of the profile in μ_B/atom being twice as high as our results (Figure 4.9b), which is probably due to the much lower temperature. The difference may also be influenced by the different MnSi thickness of 26.7 nm investigated by Karhu *et al.*.

4.4.5 Comparison of Different Samples

In the previous sections, I presented the data of sample SI121 with a MnSi thickness of 553 Å ± 10 Å and a Cu capping layer of 351 Å ± 10 Å. The expected effect of an enhanced neutron scattering as a result of the Cu capping was not observed. In the following section, I want to discuss the influence of the MnSi thickness on the helix length and number of helix turns. We performed GISANS measurements at the SANS1 on sample SI008 with a MnSi thickness of 390 Å ± 10 Å and PNR measurements on sample SI048 with a MnSi thickness of 496 Å ± 10 Å. Both samples were grown without a capping layer. However, no major influence of the Cu capping is expected, since it is amorphous and nonmagnetic, and therefore has no impact on the MnSi crystal or magnetic structure.

Sample SI008. The setup of the GISANS measurement on sample SI008 was as depicted in Figure 4.15: $\boldsymbol{B}$ was aligned in plane and for $\omega = 0$ parallel to $\boldsymbol{k_i}$, but this time essentially parallel to MnSi <110>. Figure 4.35 directly compares the intensity profiles at 15 K and 0 T for samples SI121 and SI008. It is obvious that the intensity is twice as high for SI121 than for SI008. The intensities can be compared, since the reflected spot was detected at similar Q_z values of 0.0258 Å^{-1} for SI121 and 0.0227 Å^{-1} for SI008, and is therefore at a similar position on the rocking curve of the magnetic Bragg peak. The FWHM of the Bragg peak measured on sample SI008 is, with a value of 0.037 Å^{-1} ± 0.002 Å^{-1}, much greater than the FWHM of the Bragg peak determined from sample SI121 of 0.026 Å^{-1} ± 0.002 Å^{-1}. This is a direct consequence of the reduced MnSi thickness of sample SI008, resulting in fewer helix turns and , hence, a broader Bragg peak.

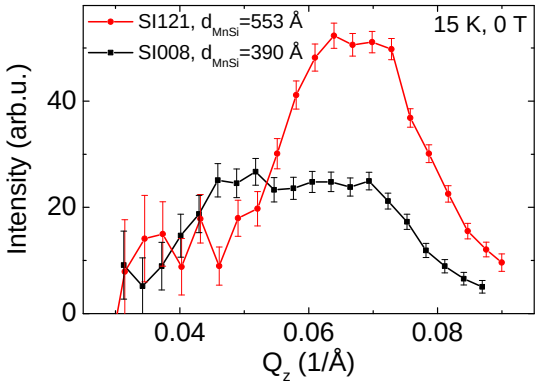

Fig. 4.35: Comparison of intensity profiles of the Bragg peak in phases 1 for sample SI121 and sample SI008 measured at 15 K and zero magnetic field. The Bragg peak of the thinner sample is broader and less intense.

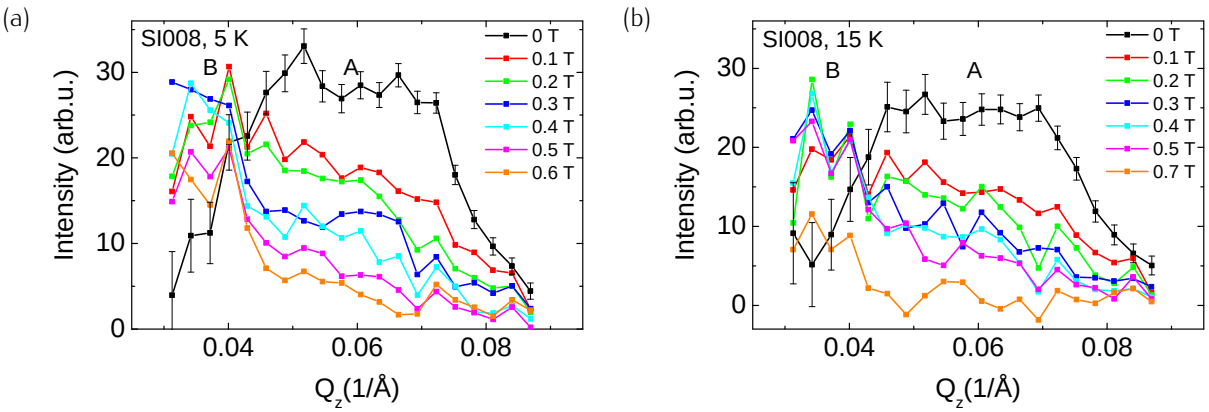

Fig. 4.36: All intensity profiles measured on sample SI008 (d_{MnSi} = 390 Å) at SANS1 (a) at 5 K and (b) 15 K for several magnetic fields between 0–0.7 T. Peak A dominates in zero field and drops continuously with increasing field.

Figure 4.36 shows all intensity profiles versus Q_z of the magnetic Bragg peaks measured on sample SI008 for 5 K and 15 K. The intensity of the Bragg peak of both figures is at the maximum for zero magnetic field. This phase corresponds to phase 1, with the position of Bragg peak A at $Q_z = 0.059\,\text{Å}^{-1} \pm 0.002\,\text{Å}^{-1}$. By applying a magnetic field of only 0.1 T, the intensity is reduced by 40% and an additional peak B appears at $0.037\,\text{Å}^{-1} \pm 0.003\,\text{Å}^{-1}$, with a higher intensity than peak A. Hence, the magnetic state has already changed to the intermediate phase. With a further increase of the magnetic field up to 0.5 T, the intensity of peak A drops continuously at both temperatures. The intensity of peak B remains constant for the field scan at 15 K but starts dropping for 0.5 T and 0.6 T at 5 K. By using the same criteria for phase 2 as for sample SI121, namely that peak A should have less than 50% of intensity of peak B, the profiles measured with magnetic fields at 0.3 T and higher are situated in phase 2. The intensity profile of 0.7 T at 15 K still shows a magnetic signal with intensity in peak B. Consequently, we did not reach the ferromagnetic state. The shapes of the profiles

for 5 K and 15 K are very similar, despite a slight drop of intensity, which demonstrates a good reproducibility of the measurement. The transition fields are reduced by about 0.15 T compared to SI121.

Sample SI048. The setup of the PNR measurement for sample SI048 was the same as for the PNR setup used for SI121: $\boldsymbol{B}$ was aligned in-plane and perpendicular to $\boldsymbol{k_i}$, but this time always parallel to MnSi <112>. Again, all data were recorded after ZFC, starting from at least 55 K. However, the very first data measured for 4 K at 30 mT, 0.1 T, and 0.34 T were recorded after heating up to only 35 K, since at this stage we believed this temperature to be above T_c. Additionally, these data have worse statistics owing to a shorter measurement time. All data were measured with a polarizer only. The reflectivities R+ and R- are depicted in Figure 4.37 as a function of Q_z at 27 K for 0.1 T (a), 0.22 T (b), and 0.44 T (c) — each measured in a different phase, as shown below. The Kiessig oscillations are more regular than the oscillations of Figure 4.30 of SI121, owing to the single layer MnSi without a copper capping layer. The curves measured for spin-up and spin-down clearly split as early as $Q_z = 0.015\,\text{Å}^{-1}$, indicating a considerable magnetic moment. To draw further conclusions,

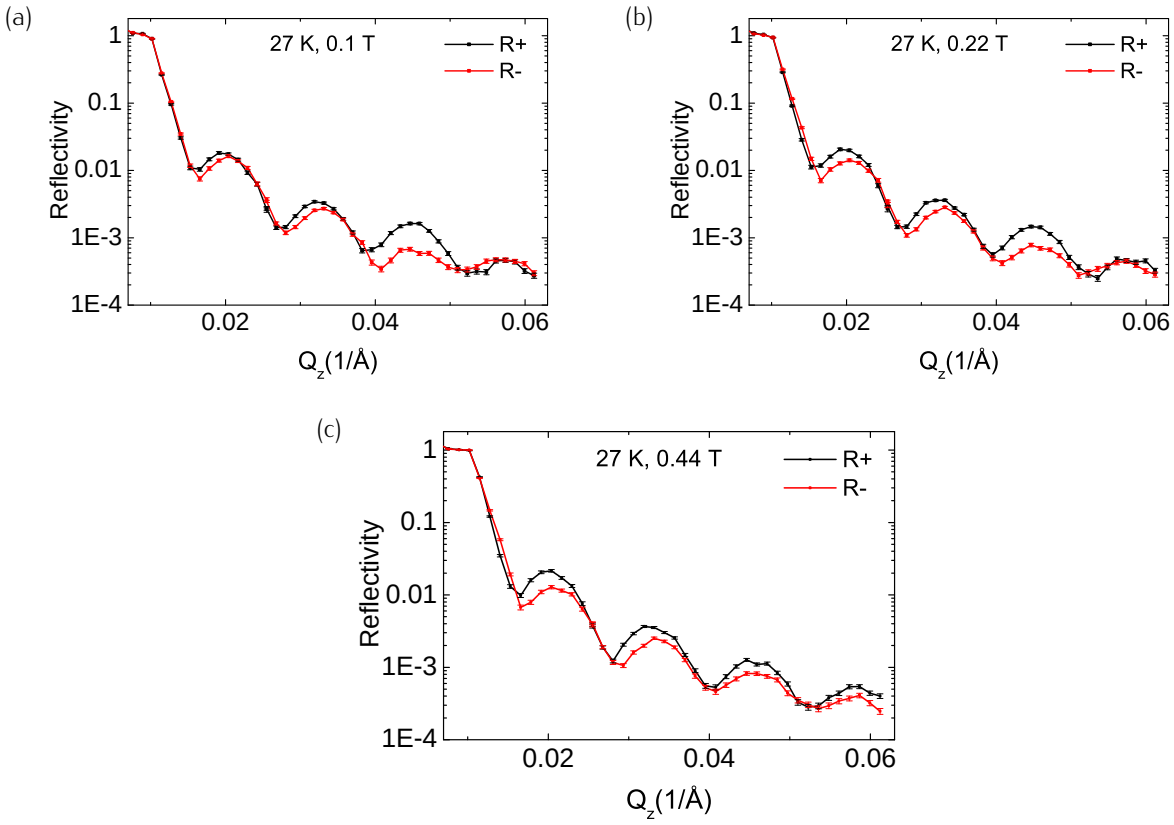

Fig. 4.37: PNR at NREX: R+ and R- reflectivities of SI048 (d_{MnSi} = 496 Å) measured at 27 K for (a) 0.1 T, (b) 0.22 T and (c) 0.44 T. The difference between R++ and R-- is a hint for a magnetic structure.

fitting is necessary.

Figure 4.38a gives an overview of the phases identified from the SA data. Like the reflectivity curves, the spin asymmetries are distinctly different from those of sample SI121 (Figure 4.31), since the copper capping layer of SI121 has a larger scattering length density compared to MnSi. Regime a in phase 1 features only a small SA at low Q_z values but a clear dip (SA<0) around 0.045 Å^{-1} and a small peak (SA>0) at 0.055 Å^{-1}. In regime b, the SA increases at all dips but remains constant at the peaks. In the intermediate phase, the curve increases at the first peak at 0.014 Å^{-1} and slightly at the first two dips. The transition to phase 2 is accompanied by an asymmetric broadening of the first two dips, a decrease of dip 3, and a decrease of the last peak, which shifts from 0.055 to 0.052 Å^{-1}.

The SAs measured for different B and T values in phase 1 are shown in Figure 4.38b. For the purpose of clarity, error bars are only added exemplarily for some SAs. The SA for 30 mT corresponds to regime a with a lower amplitude, while the spin asymmetries for 0.1 T correspond to regime b. Probably due to the larger error bars of the SA at 4 K caused by shorter counting time, an additional peak evolved at $Q_z = 0.046$ Å^{-1}, and thus we regard it as an outlier.

Figure 4.38c shows only the spin asymmetries of the intermediate phase at 4 K. The measurements of 0.27 T and 0.34 T were recorded in a shorter time than at 0.18 T, which results in more noisy curves. The rest of the curves recorded in the intermediate phase are illustrated in Figure 4.38d. The classification of the SA into the intermediate phase or phase 2 is not as straightforward as for sample SI121, because the SA only alters slightly and transitions more continuously from the intermediate phase into phase 2 with increasing field. For example, a part of the last peak of the curve measured at 27 K and 0.22 T has already dropped to zero at 0.056 Å^{-1}, but has not yet shifted to 0.052 Å^{-1}, and the amplitude of the last dip is already reduced. The curves of Figure 4.38e associated with phase 2 have not all undergone a broadening of dip 1 and dip 2, as for example, is the case for the curve at 27 K and 0,27 T. Nevertheless, compared to the intermediate phase, the last peak of all curves has shifted from 0.055 to 0.052 Å^{-1}. All the above introduced criteria for phase 2 are best fulfilled for 27 K and 0.44 T.

Some measurement points above 30 K were recorded with a shorter measurement time. Because the spin asymmetries at 0.18 T between 35 K and 39 K were similar, they were added up to reduce the noise and are depicted in Figure 4.38f. Together with the SA of 33 K, they have the characteristic peak at 0.055 Å^{-1} as well as the dip at 0.045 Å^{-1}, as in phase 1 and the intermediate phase. The first peak is much broader and the first dip less pronounced than expected for phases 1 to 2. Most conspicuous is the sharp dip at 0.033 Å^{-1} for 33 K. In contrast, the curve at 39 K and 0.41 T has a sharp peak at 0.03 Å^{-1} for 33 K. To confirm the existence of additional phases, one has to map this region in the phase diagram with higher statistics.

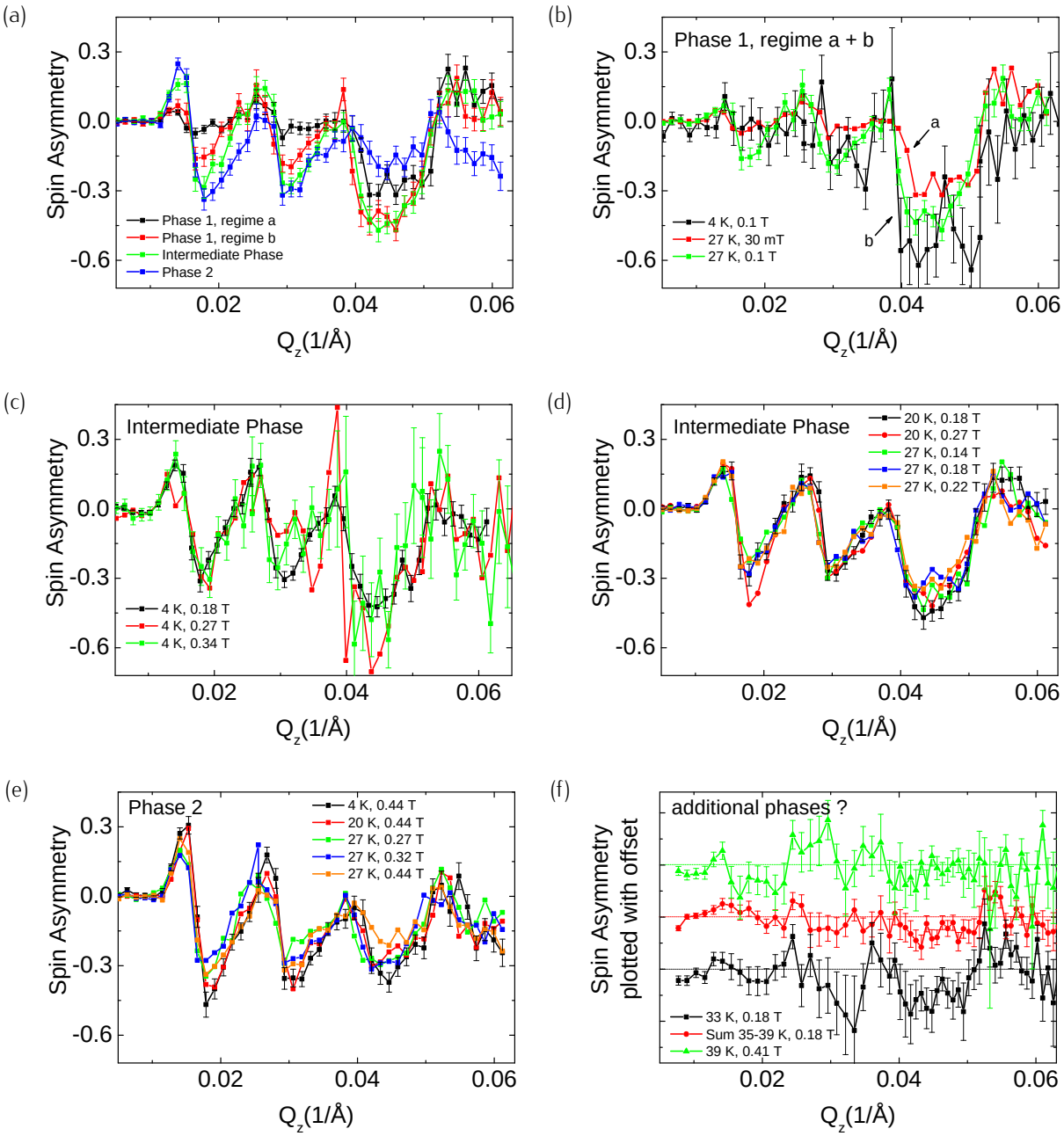

Fig. 4.38: *SA calculated from PNR of SI048 (d_{MnSi} = 496 Å) plotted versus Q_z and measured at 4 K, 20 K, and 27 K for magnetic fields between 30 mT and 0.44 T. (a) Overview of the different phases. Spin asymmetries arranged by shape and phase: (b) phase 1, the intermediate phase (c) at 4 K and (d) at 20–27 K, and (e) phase 2.*

The results are summarized in Figure 4.39 as a *B*-*T* phase diagram. For an estimation of the phase boundary to the ferromagnetic and paramagnetic states, I again used the same measurement results obtained via SQUID-VSM by Shilei Zhang (University of Oxford) from

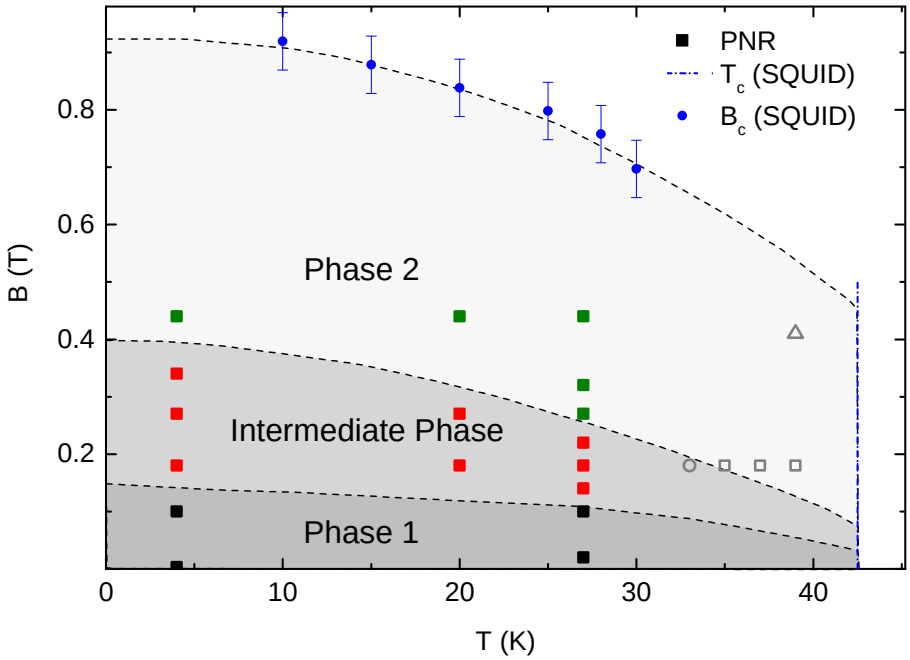

Fig. 4.39: *Phase diagram of sample SI048 with d_{MnSi} = 496 Å based on the data recorded by PNR. Data shown by black, red, and green squares indicate the phases from 1 to 2. Data indicated by gray open symbols show a magnetic signal, but cannot be attributed to one of the three phases. Blue dots denote B_c as transition to the FM state and the blue dotted vertical line marks T_c. Both were determined by Shilei Zhang (University of Oxford) for a similar sample using a SQUID-VSM.*

the sample with $d \approx 500$ Å, as shown in the phase diagram of sample SI121. From the magnetometry measurements of [147], we know that the transition to the ferromagnetic state remains fairly constant at 0.85 T±0.1 T for thicknesses above 18 nm. The data of each phase is again color-coded, with black indicating phase 1, red the intermediate phase, and green phase 2. The data above 30 K, which was not measured for long enough to identify the phases explicitly, are drawn as gray symbols, with different symbols indicating different SAs. The phase transitions occur at fields about 0.1 T higher for sample SI048 than for sample SI008. Figure 4.40 shows the fits of phases 1 and 2 from data measured at 27 K. The model, which was used for the fit of the reflectivity (Figure 4.40a) and of the SA (Figure 4.40b) is shown in Figure 4.40c. Due to the high number of fit parameters, several equivalent models fit well. As a result and owing to the GISANS results, we took only periodic functions into account. Phase 1a, measured at 30 mT, features a sinusoidal magnetic depth profile with 3.5 turns, with $L_A = 142$ Å ± 8 Å. Although the fit was not very sensitive to the exact shape, i.e. rectangular or sinus profile, it was very sensitive to the phase, the period, and the amplitude. By applying a higher field of 0.1 T corresponding to phase 1b, more and more spins align parallel to the magnetic field, resulting in a higher amplitude of the periodic structure, smaller regions of spin rotation and broader regions of positive magnetic moment. The amplitude increases

from $0.08\mu_B$ in phase 1a to $0.18\mu_B$ in phase 1b. By applying the maximum field of 0.44 T, the magnetic profile represents almost a constant magnetization of $0.3\mu_B$. However, the fit improves by inserting some sharp dips with negative magnetization. Good results can be obtained for one to four such interruptions, where, in particular, a dip at $z = 125$ Å resulted in a strong improvement of the fit. The other sharp dips did not have such an high impact on the fit. Since we expect a reduction of the repetitions by one compared to phase 1, we show the fit for two drops corresponding to 2.5 turns. Neither this fit nor the fits with more drops result in a real periodic function, as the drops are not equidistant. It is apparent that the first dip, which dominates the fit, is at the same depth as the minimum of the profiles of phase 1. This may originate from a pinning possibly stemming from a structural dislocation at this depth. Alternatively, this depth profile is a superposition of two periodic structures, as was already suspected for sample SI121. The mean period of the 2.5 oscillations is $L_B = 163\,\text{Å} \pm 60\,\text{Å}$.

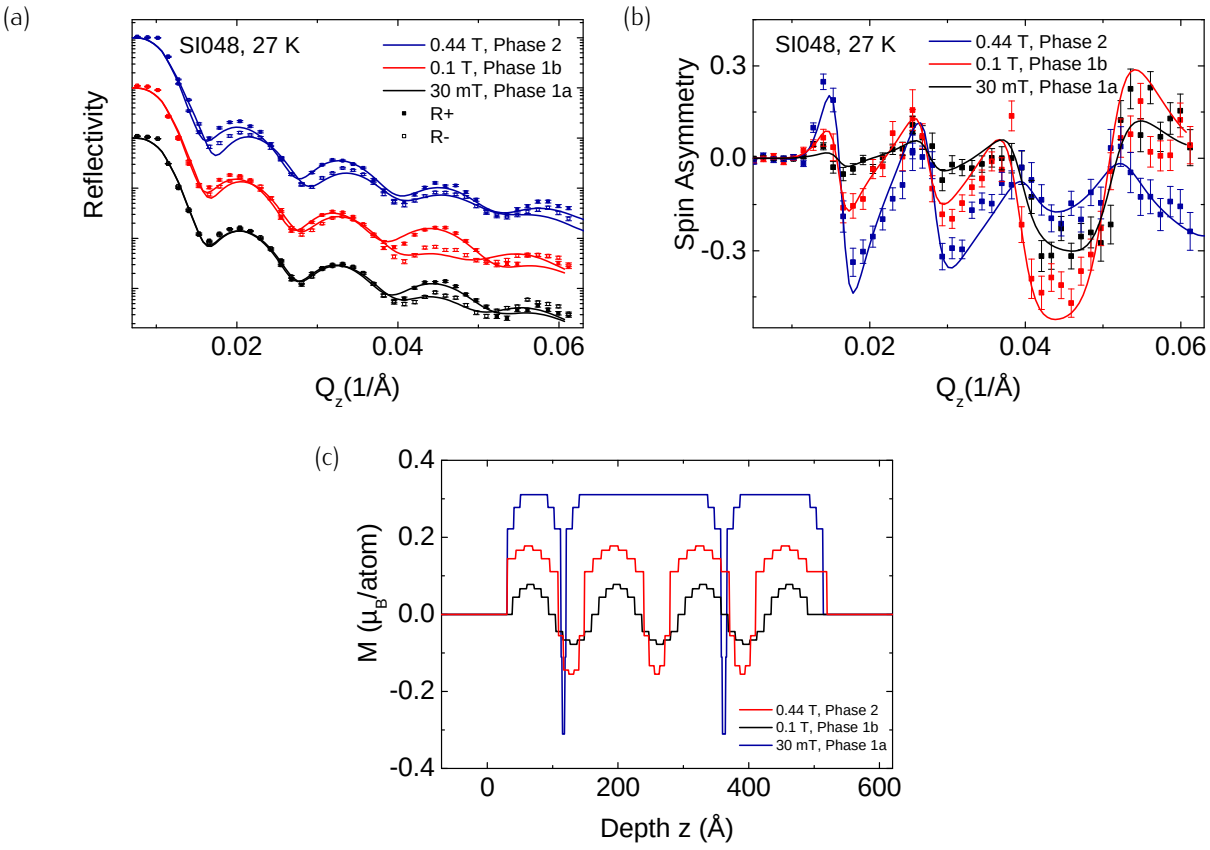

Fig. 4.40: *(a) Reflectometry data of SI048 ($d_{MnSi} = 496$ Å) for R+ (filled squares) and R- (open squares) with fits (lines) at 27 K and 30 mT (phase 1, regime a), 0.1 T (phase 1, regime b) and 0.44 T (phase 2). (b) Corresponding SA data (squares) with fits (lines). (c) Magnetic profile as a function of MnSi depth z, which results from the fits of R+, R-, and SA. With increasing magnetic field, more spins align parallel to the magnetic field and the helix length increases.*

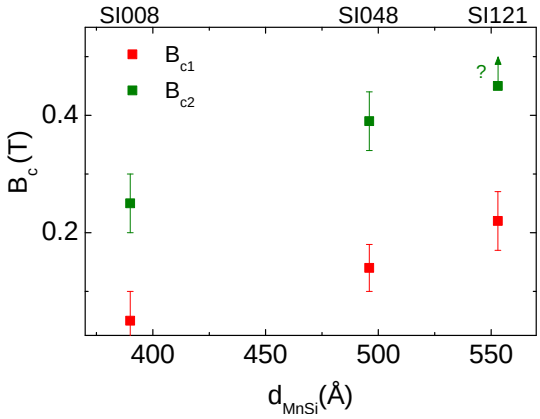

Fig. 4.41: *Critical fields of phase transitions as a function of MnSi thickness at 4-5 K: B_{c1} marks the transition from phase 1 to the intermediate phase and B_{c2} from the intermediate phase to phase 2. $B_{c2} > 0.44$ T of SI121 cannot be determined exactly owing to a lack of data points. At 15 K it was determined to $0.4 < B_{c2} < 0.45$.*

Thickness Dependence. Figure 4.41 compares the critical fields for the phase transition from phases 1 to 2 (B_{c2}) and from phase 2 to 3 (B_{c2}) for 4–5 K for all three samples. This shows a continuous and similar increase of B_{c1} and B_{c2} with increasing MnSi thickness from SI008 to SI121. Values of the k_H-vector and the helix length L_H are compared in Table 4.4. There is no trend of helix length in zero field, i.e. the ground state helix length L_A, as a function of MnSi thickness. The length appears to be the longest for the 496 Å sample and the shortest for the 553 Å sample, while the thinnest sample has a helix length lying in between the two. Overall, the helix length of phase 1 was found to be 94–142 Å. In contrast, a constant ground-state helix length was proposed by Karhu *et al.* [145] with a pitch of 13.9 nm.

While the number of helix turns is almost the same for SI008 and SI048 in both phases, it is about two times larger for the thickest sample SI121. Nevertheless, the helix turns reduce from phases 1 to 2 within the error bars by one integer for all samples. However, this property is quite speculative for sample SI048, which is only based on fit results of PNR data. Further, the interpretation of the intermediate phase originates from the assumption that the magnetic behavior is similar to the other two samples.

We did not find any strong indications of an influence of the copper layer of SI121. The properties are defined primarily by the MnSi thickness.

4.4.6 Summary and Discussion

We succeeded in getting a picture of the microscopic magnetic structure of epitaxial MnSi thin films as a function of in-plane magnetic field and temperature. This can be drawn as a phase diagram. In this section, I will firstly state the main results, discuss their meaning, and

Sample	d_{MnSi}	Phase	k_H direct	L_{direct}	$L_{indirect}$	Number of turns
SI121	(553 ± 10)Å	1	(0.067 ± 0.002)Å^{-1}	(94 ± 3)Å	(96 ± 5)Å	5.9 ± 0.5
		2	(0.052 ± 0.002)Å^{-1}	(121 ± 5)Å	(120 ± 26)Å	4.5 ± 0.4
SI008	(390 ± 10)Å	1	(0.059 ± 0.002)Å^{-1}	(107 ± 4)Å	-	3.6 ± 0.3
		2	(0.037 ± 0.003)Å^{-1}	(170 ± 15)Å	-	2.3 ± 0.3
SI048	(496 ± 10)Å	1	-	-	(142 ± 8)Å	3.5 ± 0.3
		2	-	-	(163 ± 60)Å	2.5(?)

Table 4.4: *Summary of k_H-vectors of the helices along MnSi<111>, determined directly by GISANS or OSR and indirectly by PNR for all samples.*

compare them to literature. Secondly, I will discuss the case for an out-of-plane field, as we performed measurements using this geometry that did not show any magnetic signal. Those measurements are presented in the Appendix.

The MnSi(111) films were grown epitaxially by Thorsten Hesjedal (University of Oxford) using MBE, with a vertical crystallite size of 240–300 Å (Section 4.2). The SLD profiles of the three samples appeared to be very similar, with a Si/MnSi roughness of 22–30 Å. On a similar sample, EBSD demonstrated that two chirality domains are present (Susannah Speller, University of Oxford). Analog results were obtained for the magnetic domains by PNR with an in-plane magnetic field. In these results, we did not observe any features in the spin-flip channels (Section 4.4.4). Consequently, the in-plane spins perpendicular to the magnetic field must cancel out. This finding suggests that right- and left-handed helices are equally distributed. A similar property for the magnetic as well as for the crystal domains of MnSi(111) films was observed in [145, 147] using TEM and PNR as already discussed in Section 4.1.4.

The neutron-scattering experiments were supported by magnetometry measurements performed by Shilei Zang (University of Oxford). The in-plane saturation magnetic field was determined to be around 0.9 T at 10 K, which is in good agreement to the saturation magnetic fields measured by Wilson *et al.* [10]. T_c with 42.5 K was determined to be similar to those values from literature [10, 13], but is larger compared to the bulk value of 29.5 K [8].

$\boldsymbol{B}$ in plane. By applying an in-plane magnetic field, we found k_H-vectors corresponding to spin helices directed along MnSi <111>, the surface normal (Section 4.4.1). Those k_H-vectors were identified along Q_z by Bragg peaks using GISANS, by Bragg sheets using OSR, and by the magnetic depth profile using PNR (Section 4.3). We found intensity along Q_x in the OSR measurement by measuring the magnetic Bragg sheets (Section 4.4.1), which represent the rocking curve and hence only the distribution of the helices with small tilts along the x-direction. The rocking curve of the Bragg peak cannot be measured, since its maximum is superimposed by the reflected spot (Section 4.3.2). Certainly, we can exclude any additional magnetic wavevectors in the y-direction provided $\boldsymbol{k_H}$ has a modulus in the accessible Q_y range with a similarly intense Bragg peak, since we also rocked in this direction by ±2° in the vertical configuration and by ±8° or ±4° in the horizontal configuration. In contrast, we cannot exclude a magnetic wavevector along the x-direction, which was the magnetic field

direction in the GISANS setup. This stems from the setup geometry used, for which the Bragg condition could not be obeyed for any wavevector aligned parallel to x.

An important result of this thesis is that the helix length, and therefore the number of helix turns, changes with magnetic field (Section 4.4.1). By increasing the magnetic field $\boldsymbol{B}$, more and more spins align parallel to $\boldsymbol{B}$. To achieve this, the magnetic structures favor a reduction of the spin rotation, resulting in longer helix length, as was predicted recently by Wilson *et al.* [11] (Figure 4.9a). It seems reasonable to surmise, that the helix length increases stepwise until only one half of the period remains before it shifts completely to the ferromagnetic state. However, Wilson *et al.* were not able to measure this behavior directly. We revealed that this transition happens by the formation of an intermediate phase, in which some domains still have helices with the shorter length of phase 1 and in other domains the helices already have the longer length associated with phase 2. The transition to more and more domains with longer wavelength occurs continuously with increasing magnetic field. This can be seen directly in the evolution the corresponding Bragg peaks recorded by GISANS and OSR (Section 4.4.3): phase 1 exhibited peak A, phase 2 peak B and the intermediate phase both peaks. In fact, the intermediate phase represents a broad phase transition from phase 1 to phase 2 and is no conventional phase with a thermodynamical phase transition. However, for a quantitative study, we defined reasonable criteria for its boundaries, as for example from the Bragg peak profiles: the lower boundary was defined by $I_B^{max} > 40\% \cdot I_A^{max}$, above which peak B increases, while peak A drops. The upper boundary was defined by $I_A^{max} > 50\% \cdot I_B^{max}$. The corresponding magnetic fields are the so-called critical fields. In the case of PNR, the phases were classified according to their SA shape (Section 4.4.4). This was in excellent agreement with the phases determined by GISANS and OSR.

We found that the magnetic phases are stable with respect to the cooling history or the in-plane magnetic field direction, but this was not tested for data close to a phase boundary (Section 4.4.2). Moreover, we were able to demonstrate that two different techniques used at two different instruments give the same results. This confirms the high reliability and reproducibility of the data.

We discovered that the number of turns reduces from phase 1 to phase 2, within error bars, with a step size of one, as can been seen from Table 4.4. The number of helix turns reduced from 5.9 to 4.5 for SI121, from 3.6 to 4.5 for SI008 and from 2.5 to 3.5 for SI048. The larger number of helix turns of SI121, compared to those of SI008 and SI048, is a result of the larger MnSi thickness. Integer or half-integer steps also occurred for the simulated field scan in [11] discussed in Section 4.1.4. Here, Wilson *et al.* calculated the critical fields for a sample with a thickness of 29.8 nm. Up to 0.22 T the helix made 2.0 turns, up to 0.46 T 1.5 turns, and above this value only 0.5 turns. The authors could fit this model to PNR data. Those phase transitions deviate from their measured phase transitions in a previous paper [10] (Figure 4.7b), in which they identified the phases differently, namely as a helical phase (phase 1), a mixed phase of helicoids and skyrmions (phase 2), and a pure skyrmion phase (phase 3). However, the phase transitions observed in [10] for a 26.7 nm sample fit quite well to the phase transitions we observed at least for $T > 25$ K for sample SI121 with a thickness

of 553 Å. Note that in the earlier paper, the identification of the phases was only based on theory. Their new theory of discrete states does not include an intermediate phase, as it can be identified in our GISANS measurements, and still does not deny the existence of a skyrmion lattice.

We discovered, that the spins do align more and more parallel or antiparallel to the in-plane magnetic field. This is thought to explain the change in helix length and can be seen in the magnetic depth profile obtained by PNR (Section 4.4.4). Whereas in zero magnetic field, the profile has a sinusoidal shape, as the field increases, the profiles become distorted, evolving plateaus with positive magnetization and a steep zero-crossing to small regions with negative magnetization. In addition, the magnetic moment per atom rises with increasing field up to $0.2\mu_B$ for sample SI121 and up to $0.3\mu_B$ for sample SI008. Similar profiles were fitted by Karhu *et al.* [147], but with a larger magnetic moment of maximum $0.4\mu_B$, as for bulk MnSi [107]. The PNR were measured at 5 K, whereas our data was recorded at 27 K and 35 K for sample SI008 and SI121, respectively. As a result, the differences in the magnetic moment can be explained by the decrease of magnetization for increasing temperature. This sinusoidal magnetic profile with low amplitude explains the small SA in zero field. By contrast, the Bragg peak in GISANS at zero field is most intense (Section 4.4.3). There are two possible reasons for this: In zero field most of the domains consist of the starting helix. It is possible that in the presence of a small magnetic field of some 10 mT is applied, first domains already change their helix length. These are too few to form a Bragg peak besides the first Bragg peak. Alternatively, the distortion of a uniform helix by a small magnetic field, with more spins aligning parallel to it, might already influence the Fourier transformation. In general, a continously intenstiy drop is expected for an increasing field until the Bragg peak has vanished in the ferromagnetic state. In addition, we know that the FWHM of the Bragg peaks drops for increasing magnetic fields. We explain this by the spin structure becoming more defined for parallel or antiparallel alignment to the magnetic field.

Another very important result is that the helix length and the critical fields of the phase transitions, determined by definition, are a function of MnSi thickness (Section 4.4.5). The critical fields increase with increasing thickness: B_{c1}, which marks the transition from phase 1 to the intermediate phase, increases, for example, at 4–5 K from 0.05 T±0.05 T for 390 Å to 0.22 T±0.05 T for 553 Å. Similarly, B_{c2}, which marks the transition from the intermediate phase to phase 2, increases from 0.25 T±0.05 T for 390 Å above 0.45 T for 553 Å.

The helix length of phase 1 deviates between 94 and 142 Å and of phase 2 between 121 and 163 Å. This contradicts Karhu *et al.* [145], who state the existence of a ground-state helix length of 13.9 nm for all thicknesses up to 40 nm.

It was suggested, as discussed above, that when the field is increased the helix repetitions are pushed out by steps of one integer or half-integer until the ferromagnetic state is reached [11]. We only observed, within error bars, steps of one integer. This could indeed occur for the thinner SI008 sample, where the turns above phase 2 have to be pushed out twice more to reach the ferromagnetic phase. Including the mixture phases would result in at least four additional phases. Unfortunately, we were not able to measure PNR in this region owing to

the limiting magnetic field. In the case of the 553 Å sample, there ought to be eight additional phases at high fields, with the helix turns reducing from 4.5 to 0.5 with intermediate phases in between. But given the small field range between the last measured point belonging to phase 2 and the ferromagnetic state determined by SQUID, this seems to be implausible. Note that Wilson *et al.* found the step size of helix turn jumps changing from 0.5 to 1 with increasing field. Therefore, we can no exclude that the helix turns maybe pushed out in even larger steps above phase 2. Alternatively, the region above phase 2 can be dominated by different phases, which cannot be observed in our GISANS and OSR experiments. PNR data revealed first hints, that phase 2 may partially consists of two different structures: At 0.44 T, the magnetic depth profiles of SI008 and SI121 measured at 27 K and 35 K, respectively, seem to be a superposition of two periodic structures. Hence, the magnetic structures at large magnetic fields are not totally clarified.

For this open question to be answered, the phases need to be investigated at larger magnetic fields in more detail. Given that GISANS becomes more and more difficult with fewer helix turns, I suggest performing PNR measurements. These turned out to be a powerful tool to discover small changes in the magnetic depth profile. To definitely prove the evolution of B_{c1} and B_{c2} as well as the helix length as a function of MnSi thickness definitely, one has to apply GISANS on SI048 to confirm the PNR model and PNR on SI008 to confirm the phase transitions. In addition, further investigations of MnSi samples with different thicknesses would help achieve a proper overview of the thickness dependence.

As also briefly mentioned above, GISANS is not sensitive to $\boldsymbol{k_H}$ parallel to $\boldsymbol{k_i}$. To exclude an additional magnetic Bragg peak with $\boldsymbol{k_H}$ parallel to the magnetic field, one would have to apply the in-plane field $\boldsymbol{B}$ perpendicular to $\boldsymbol{k_i}$. This would easily prove the existence of more complicated structures with either different populated domains or several different $\boldsymbol{k_H}$ vectors, as is expected for the skyrmion phase. Unfortunately, this measurement could not be realized at this time, as the FRM II neutron source has been shut down for several months, but it is scheduled for December 2014. However, nobody has found any indication for such a complicated structure in an in-plane field, and we would have noticed hints in the magnetic depth profiles obtained by PNR. There were some anomalies in the SA of sample SI048 above 30 K (Section 4.4.5), but these may equally stem from noise due to low acquisition times.

Although PNR, GISANS, and OSR are suitable methods to identify the phases, a detailed mapping of the phase diagram is time consuming. Different techniques need to be applied to define the exact phase transitions, enabling measurements to be accomplished on a much shorter time scale and to be freely accessible. Since we have identified the microscopic picture, such measurements could easily complete the details of the phase diagram.

$\boldsymbol{B}$ out of plane. So far we have only discussed measurements carried out in an in-plane field. We also conducted measurements with an out-of-plane field that did not deliver any magnetic signal. These measurements are presented in the Appendix. From this, we deduced some assumptions regarding the magnetic structure for an out-of-plane field. In the literature (Section 4.1.4), there are two contradictory predictions for MnSi(111) epitaxial films: Li *et al.* [13] showed TEM images of in-plane helices with a helix length of 8.5 nm and a hexagonal

skyrmion lattice in agreement with THE measurements by Yokouchi *et al.* [132]. In contrast, Karhu and Wilson *et al.* [12, 145] state the existence of a pure conical state with the helix aligned out of plane and a length of 13.9 nm. Note that we determined the helix to align out of plane along MnSi<111> at 0 T after ZFC from the paramagnetic state. This therefore seems to be the magnetic ground state of the system. This is in contradiction to Li *et al.* [13], who observed the helices in plane at 0 T using Lorentz TEM.

We performed GISANS measurements at SANS1 on SI121 with $\boldsymbol{k_i}$ parallel to $\boldsymbol{B}$ and perpendicular to the sample surface, as depicted in Figure 5.1a. If there had been a hexagonal skyrmion lattice perpendicular to the surface, as it is claimed by Li *et al.* [13], according to Bragg's law the hexagonal lattice would have lain directly in the scattering plane. We measured right in the center of Li's skyrmion phase, i.e. at 27 K and 0.5 T, but observed no Bragg peaks (Figure 5.1b). Although the magnetic structure may not be very well long-range ordered, as was stated by Li *et al.* [13], we still should have been able to see even a broad Bragg peak, since only 3.5 helix turns produced a Bragg peak in the helical phase. We therefore regard the existence of the conical phase in an out-of-plane field as being more likely.

To confirm the statement by Karhu *et al.* [145] and Wilson *et al.* [12] that a conical phase with $\boldsymbol{k_H}$ directed out-of-plane exists, GISANS measurements with $\boldsymbol{k_i}$ parallel to the surface, but $\boldsymbol{B}$ perpendicular to the surface have to be performed. In the case of long-range order, a Bragg peak along Q_z should be directly observed. This experiment is also planned as part of the beamtime scheduled in December 2014.

We applied PNR in an out-of-plane field measuring all spin channels (Figure 5.2a). We did not find any SA in the non-spin-flip channel, nor did we find features in the spin-flip channels (Figure 5.2b). We do not expect a SA of the non-spin-flip channels, since the neutron spin is parallel to the scattering wavevector Q_z. In contrast, the spin-flip channels are sensitive to all moments perpendicular to Q_z, i.e the in-plane moments. We measured at magnetic fields and temperatures similar to those at which Li *et al.* [13] or Wilson *et al.* [12] predicted or already measured the magnetic structures. We measured at 10 K and 0.25 T up to 0.1 $Å^{-1}$ and short measurements up to 0.037 $Å^{-1}$ between 0.10 and 0.28 T at five different fields at 10 K, and two different fields at 39 K. It is possible for the short measurements, that we could have missed the features, but not for the long measurement. Karhu *et al.* [145] also performed PNR with an out-of-plane field for all spin channels. They observed a small peak in the spin-flip signal after cooling the sample in a high in-plane magnetic field of 0.8 mT and providing a small in-plane magnetic field in the order of some mT during the actual out-of-plane measurement at 0.2 T. They attributed the peak to a conical state. The authors suspect the missing long-range order as being responsible for the necessity of this complicated field-cooling process.

There are several possible explanations for the lack of magnetic signal in our PNR signal:
1. We did not measure for long enough, losing the signal in the background.
2. The moments cancel out within one plane. This will happen in the case of a skyrmion lattice with three k_H-vectors lying in plane, as predicted by Li *et al.* [13]. This results in a constant magnetic depth profile and a cancellation of all in-plane spins as a result of the

spin rotation within one plane. This will also appear for helices with $\boldsymbol{k_H}$ in plane, as again observed by [13].
3. The magnetic structure does not show any long-range order but forms a glassy state, as already suspected by Li *et al.* [13] and Karhu *et al.* [145].

However, these explanations do not allow us to solve the contradiction. For Mnsi thin films in an out-of-plane field, the Zeeman energy competes with the easy-plane anisotropy as discussed in Section 4.1.5. Both energy contributions favor the opposite spin alignment. Therefore, one explanation for the contradiction could be that the out-of-plane field leads to a frustrated system, where different magnetic structures are possible — small changes in cooling history may be sufficient to yield totally different results. Li *et al.* do not write anything about the cooling history, and it is also odd that they only show three TEM images and determine their phase diagram by Hall measurements. However, the phase diagram was confirmed by Yokouchi *et al.* [132], who extracted the THE signal from the Hall measurements. Alternatively, the samples investigated by us, Li *et al.*, and Wilson *et al.* may possess different strains influencing the magnetic anisotropy. Furthermore, it is not clear, whether Li *et al.* and Yokouchi *et al.* used the MBE growth method or the SPE growth method for the sample investigated by Lorentz TEM, as they used both methods for different samples. The preparation of the samples, that are necessary for Lorentz TEM may also influence the magnetic anisotropies. Wilson, Monchesky *et al.* [12, 148] suggest artifacts in Lorentz TEM as being responsible for the results obtained by Li *et al.*, which in turn is disputed by Li *et al.* [149]. However, the theory of Wilson *et al.* is still not proved by a direct experimental method.

4.5 Conclusion

In this chapter of my thesis, I gave a literature review (Section 4.1), presented the samples (Section 4.2) and the neutron scattering techniques with an in-plane magnetic field (Section 4.3), and described the results obtained from three MnSi(111) thin film samples with different MnSi thicknesses (Section 4.4).

We were able to derive a detailed microscopic magnetic picture of epitaxial MnSi thin films in an in-plane field. This revealed helices aligned out of plane and showed the helix pitch to increase with increasing magnetic field. Similar properties were predicted in [11]. However, we were the first group to directly measure the k_H-vector of the magnetic structure in a B20 epitaxial film. In addition, we found that the helix length and the critical fields for the helix length transition change as a function of MnSi thickness.

It appears that the magnetic properties of thin films are totally different from bulk or free-standing crystal plates. From the literature study in Section 4.1.4, we infer that the shape anisotropy does not effect the magnetic structures. In contrast, finite size effects seem to dominate the magnetic properties in reduced dimensionality as is also the case in plates,

where an extended skyrmion phase was observed. In addition to the mechanisms in thin plates, strain is induced in epitaxial thin film owing to the lattice mismatch stemming from the growth, which was found to play a crucial role. This mechanism competes with the finite size and the Zeeman effect. For systems in which the Zeeman effect and the uniaxial anisotropy induced by strain favor the same spin structure, the finite size effect may be overcome. Two different magnetic structures are predicted for epitaxial MnSi thin films, when this is not the case: the skyrmion lattice together with an in-plane ground-state helix [13] and the pure conical phase [12]. For a complete understanding of the competition between the mechanisms, further investigations need to be done on the properties of MnSi thin films to find the reason for this contradiction.

Chapter 5

Conclusions and Outlook

In this work, I showed that polarized neutron reflectometry is a powerful tool to investigate the structural and magnetic properties of thin films. We found that ultrathin Fe layer can be grown either as pure bcc or with a large portion of fcc on a Cu(100) seed layer. Since the portion of the fcc Fe altered with Fe thickness, monitoring the magnetic and structural properties *in situ* during growth was of particular importance (Chapter 3). This would also have been important for MnSi thin films. I have shown that MnSi(111) thin films change the magnetic helix length as a function of MnSi thickness (Chapter 4). Therefore, it would be of enormous advantage to be able to measure the evolution of helix length directly during growth.

The disadvantages of low neutron flux compared to X-ray techniques can be overcome in the near future: We have already achieved measuring times of 15 min per spin state and layer using PNR in combination with the Selene concept (Section 3.2.2) at Amor (PSI). Particularly short measurement times are likely for *in-situ* measurements during growth, since the latter takes place within the order of seconds. *In-situ* growth chambers, e.g. MBEs, PLDS or sputtering chambers, easily installed at a neutron beamline or, better, integrated into a neutron beamline, are therefore of particular interest for monitoring the growth of thin films. Measurement times will be further reduced when the Selene setup is realized at the European Spallation Source (ESS) in Lund, Sweden. It is planned that the neutron source will start its operation in 2019 [155]. The concept of a reflectometer called ESTIA with the Selene concept was recently endorsed by the Scientific Advisory Committee of the ESS [156]. The high brilliance of the ESS together with longer Montel mirrors, which provide a larger footprint on the sample, will reduce the measurement times by a factor of 1000 [156]. Consequently, a comparable PNR measurement could take place within less than one second. This is on the same time scale as the growth and the evolution of the properties of the layers can then be monitored in real time.

The applications of this technique go far beyond the material systems investigated in this thesis. Several systems change their magnetic properties as a function of thickness. For example,

the interface between $LaAlO_3$ and $SrTiO_3$, exhibits superconductivity and ferromagnetism in a specific thickness range of the $LaAlO_3$ layer [157, 158]. The origins of these properties are not fully understood and research monitoring those properties during growth would be of great benefit.

Appendix

MnSi(111) Thin Films Measured in an In-Plane Magnetic Field

In Chapter 4, I only presented neutron data of MnSi(111) thin films with the magnetic field applied in plane. We also performed PNR and GISANS measurements in an out-of-plane magnetic field, which are presented in this section. These, however, did not reveal any magnetic signal. Possible reasons are discussed in Section 4.4.6.

GISANS. GISANS was performed on sample SI121 at SANS1, using a similar setup as described in Section 4.3.1. Here, we simply rotated the sample to place it on its edge such that the magnetic field and the incoming neutron beam are perpendicular to the sample plane, as shown in Figure 5.1a. The MnSi <111> direction was then parallel to $\boldsymbol{B}$ and $\boldsymbol{k_i}$. Again, the sample, together with the magnetic field, can be rocked using the angles χ and ω. Like for GISANS with an in-plane field applied, we performed rocking scans with $\Delta\chi = \pm 4°$ and

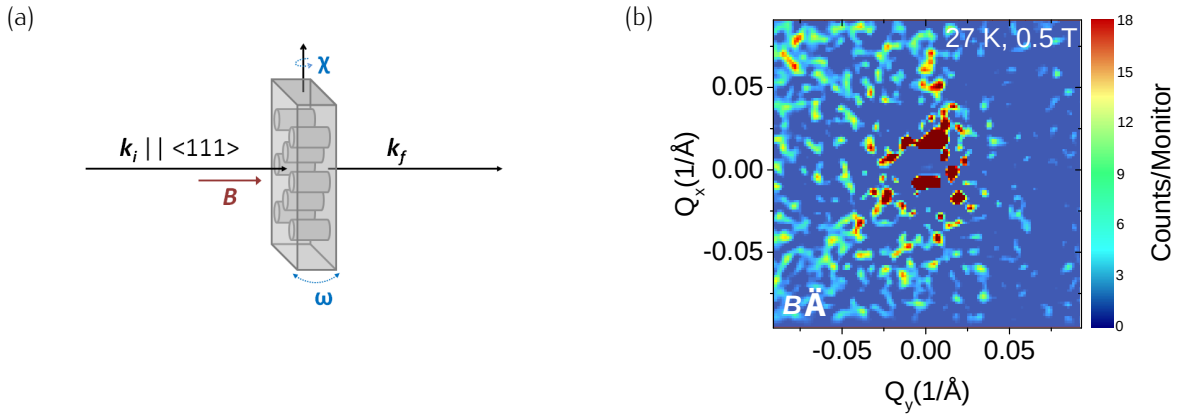

Fig. 5.1: *(a) GISANS setup with an out-of-plane field at SANS1. The MnSi sample is aligned with <111> || $\boldsymbol{k_i}$ || $\boldsymbol{B}$. (b) Intensity map of sample SI121 measured at 27 K, 0.5 T using the setup shown in (a).*

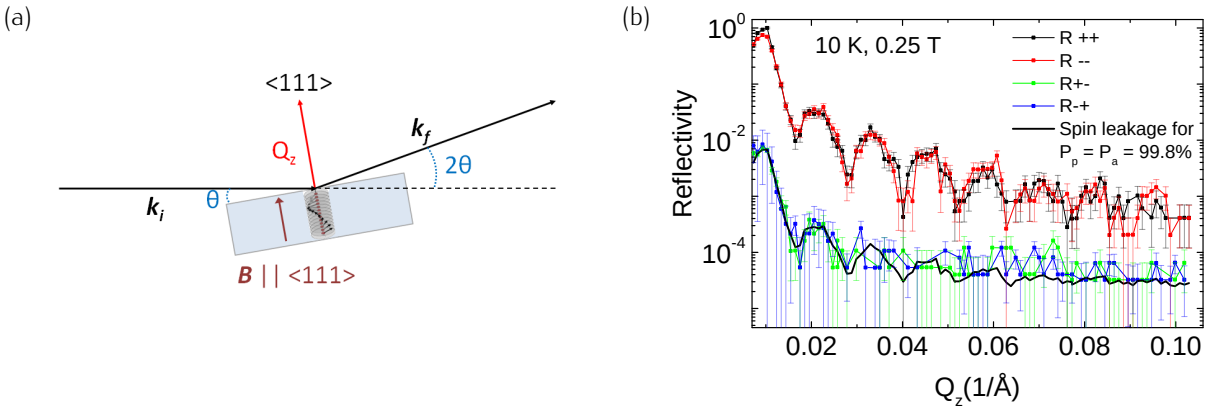

Fig. 5.2: *(a) PNR setup with MnSi <111>|| $\boldsymbol{B}$ at NREX. (b) PNR curves of sample SI048 measured at 10 K and 0.25 T for all spin channels as a function of Q_z together with a fit accounting for spin leakage.*

$\Delta\omega = \pm 2°$ to find a magnetic Bragg peak. With this setup, we searched for a skyrmion lattice, as was claimed to exist by Li *et al.* [13]. The intensity map recorded at 27 K and 0.5 T as a function of Q_x and Q_y is plotted in Figure 5.1b. There are no magnetic Bragg peaks visible.

PNR. PNR measurements were performed on SI048 at NREX using a polarizer and an analyzer to record all four spin channels. The setup with the magnetic field applied along the surface normal, i.e. MnSi <111> , is shown in Figure 5.2a. With this setup, we tried to measure $\boldsymbol{k_H}$ of a helical structure propagating along the surface normal as indicated in the figure. Figure 5.2b shows the reflectivity curves of all spin channels. The non-spin-flip channels R++ and R-- are, as expected, very similar, showing no SA as $\boldsymbol{Q} \parallel \boldsymbol{M}$. In this geometry, PNR is not sensitive to out-of-plane moments. In contrast, $\boldsymbol{Q} \perp \boldsymbol{M}$ is fulfilled for the spin-flip channels R+- and R-+, since in an out-of-plane field the spins are flipped for in-plane magnetization components. Thus, the spin-flip channels are sensitive to the magnetization. However, R+- and R-+ are two orders of magnitude smaller than the non-spin-flip channels and replicate those. Yury Khaydukov fitted the spin-flip channels by accounting for a polarization of polarizer and analyzer of 99.8%. This fitted the curves very well and indicates, that we measured only the spin leakage and no magnetic signal. For right- and left-hand helices, we would expect a magnetic peak in R+- and R-+ at the Q_z value of the helix wavevector, as was observed by Karhu *et al.* [145]. The corresponding discussion can be found in Section 4.4.6.

Bibliography

[1] L. Hammer, S. Müller, and K. Heinz, Fe/Cu(100) - a test case for the understanding of epitaxially grown magnetic thin films, Surface Science **569**, 1 (2004).

[2] M. Wuttig and X. Liu, *Ultrathin Metal Films: Magnetic and Structural Properties* (Springer, 2004).

[3] M. N. Baibich, J. M. Broto, A. Fert, F. N. Van Dau, F. Petroff, P. Etienne, G. Creuzet, A. Friederich, and J. Chazelas, Giant magnetoresistance of (001)Fe/(001)Cr magnetic superlattices, Phys. Rev. Lett. **61**, 2472 (1988).

[4] J. Coey, *Magnetism and Magnetic Materials* (Cambridge University Press, 2009).

[5] D. Li, M. Freitag, J. Pearson, Z. Q. Qiu, and S. D. Bader, Magnetic phases of ultrathin Fe grown on Cu(100) as epitaxial wedges, Phys. Rev. Lett. **72**, 3112 (1994).

[6] D. Qian, X. F. Jin, J. Barthel, M. Klaua, and J. Kirschner, Spin-density wave in ultrathin Fe films on Cu(100), Phys. Rev. Lett. **87**, 227204 (2001).

[7] J. Shen, H. Jenniches, C. Mohan, J. Barthel, M. Klaua, P. Ohresser, and J. Kirschner, In-plane anisotropy and reversed spin reorientation of fcc Fe ultrathin films on Cu(100) by pulsed-laser deposition, Europhys. Lett. **43**, 349 (1998).

[8] S. Mühlbauer, B. Binz, F. Jonietz, C. Pfleiderer, A. Rosch, A. Neubauer, R. Georgii, and P. Böni, Skyrmion lattice in a chiral magnet, Science **323**, 915 (2009).

[9] F. Jonietz, S. Mühlbauer, C. Pfleiderer, A. Neubauer, W. Münzer, A. Bauer, T. Adams, R. Georgii, P. Böni, R. A. Duine, K. Everschor, M. Garst, and A. Rosch, Spin transfer torques in MnSi at ultralow current densities, Science **330**, 1648 (2010).

[10] M. N. Wilson, E. A. Karhu, A. S. Quigley, U. K. Rößler, A. B. Butenko, A. N. Bogdanov, M. D. Robertson, and T. L. Monchesky, Extended elliptic skyrmion gratings in epitaxial MnSi thin films, Phys. Rev. B **86**, 144420 (2012).

[11] M. N. Wilson, E. A. Karhu, D. P. Lake, A. S. Quigley, S. Meynell, A. N. Bogdanov, H. Fritzsche, U. K. Rößler, and T. L. Monchesky, Discrete helicoidal states in chiral magnetic thin films, Phys. Rev. B **88**, 214420 (2013).

[12] M. N. Wilson, A. B. Butenko, A. N. Bogdanov, and T. L. Monchesky, Chiral skyrmions

in cubic helimagnet films: The role of uniaxial anisotropy, Phys. Rev. B **89**, 094411 (2014).

[13] Y. Li, N. Kanazawa, X. Z. Yu, A. Tsukazaki, M. Kawasaki, M. Ichikawa, X. F. Jin, F. Kagawa, and Y. Tokura, Robust formation of skyrmions and topological Hall effect anomaly in epitaxial thin films of MnSi, Phys. Rev. Lett. **110**, 117202 (2013).

[14] W. Bragg, The diffraction of short electromagnetic waves by a crystal, Proceedings of the Cambridge Philosophical Society **17**, 43 (1913).

[15] D. Sivia, *Elementary Scattering Theory* (Oxford University Press, 2011).

[16] Brigham Young University, http://www.cleanroom.byu.edu/ew_orientation.phtml, .

[17] L. G. Parratt, Surface studies of solids by total reflection of X-rays, Phys. Rev. **95**, 359 (1954).

[18] M. Tolan, *X-Ray Scattering from Soft-matter Thin Films* (Springer, 1999).

[19] Laboratoire Léon Brillouin CEA/CNRS Saclay, France, Software SimulReflec Version 1.72, http://www-llb.cea.fr/prism/programs/simulreflec/simulreflec.html, (2007).

[20] W. Kreuzpaintner, *Preparation and Characterisation of Magnetic Nanostructured Samples for Inelastic Neutron Scattering Experiments*, Ph.D. thesis, Universität Hamburg (2010).

[21] A.-J. Dianoux and G. Lander, *Neutron Data Booklet* (OCP Science, 2003).

[22] F. Ott and S. Kozhevnikov, Off-specular data representations in neutron reflectivity, Journal of Applied Crystallography **44**, 359 (2011).

[23] S. C. Abrahams, L. Guttman, and J. S. Kasper, Neutron diffraction determination of antiferromagnetism in face-centered cubic γ iron, Phys. Rev. **127**, 2052 (1962).

[24] L. Bergmann and C. Schäfer, *Lehrbuch für Experimentalphysik - Band 3, Festkörper* (Walter de Gruyter, 1992).

[25] F. J. Pinski, J. Staunton, B. L. Gyorffy, D. D. Johnson, and G. M. Stocks, Ferromagnetism versus antiferromagnetism in face-centered-cubic iron, Phys. Rev. Lett. **56**, 2096 (1986).

[26] C. S. Wang, B. M. Klein, and H. Krakauer, Theory of magnetic and structural ordering in iron, Phys. Rev. Lett. **54**, 1852 (1985).

[27] B. Roldan Cuenya, W. Keune, D. Li, and S. D. Bader, Enhanced hyperfine magnetic fields for face-centered tetragonal Fe(110) ultrathin films on vicinal Pd(110), Phys. Rev. B **71**, 064409 (2005).

[28] A. Hahlin, C. Andersson, J. H. Dunn, B. Sanyal, O. Karis, and D. Arvanitis, Structure and magnetism of ultrathin epitaxial Fe on Ag(100), Phys. Rev. B **73**, 134423 (2006).

[29] C. C. Kuo, W. Pan, Y. C. Chen, and M.-T. Lin, Exchange bias in Co/Fe/Fe_xMn_{1-x}/Cu(100) ultrathin films, Journal of Applied Physics **93**, 8743 (2003).

[30] M. Croft, D. Sills, and A. Sahiner, Fe-fcc layer stabilization in [111]-textured Fe/Pt multilayers, Nanostructured Materials **9**, 413 (1997).

[31] B. An, L. Zhang, S. Fukuyama, and K. Yokogawa, Growth and structural transition of Fe ultrathin films on Ni(111) investigated by LEED and STM, Phys. Rev. B **79**, 085406 (2009).

[32] T. Allmers and M. Donath, Magnetic properties of Fe films on flat and vicinal Au(111): Consequences of different growth behavior, Phys. Rev. B **81**, 064405 (2010).

[33] C. A. F. Vaz, J. A. C. Bland, and G. Lauhoff, Magnetism in ultrathin film structures, Reports on Progress in Physics **71**, 056501 (2008).

[34] S. Müller, P. Bayer, C. Reischl, K. Heinz, B. Feldmann, H. Zillgen, and M. Wuttig, Structural instability of ferromagnetic fcc Fe films on Cu(100), Phys. Rev. Lett. **74**, 765 (1995).

[35] J. Thomassen, F. May, B. Feldmann, M. Wuttig, and H. Ibach, Magnetic live surface layers in Fe/Cu(100), Phys. Rev. Lett. **69**, 3831 (1992).

[36] D. Qian, X. Jin, J. Barthel, M. Klaua, and J. Kirschner, Temperature-induced structure instability and magnetism of Fe/Cu(100), Phys. Rev. B **66**, 172406 (2002).

[37] A. Biedermann, R. Tscheliessnig, M. Schmid, and P. Varga, Local atomic structure of ultra-thin Fe films grown on Cu(100), Applied Physics A **78**, 807 (2004).

[38] M. T. Kief and W. F. Egelhoff, Growth and structure of Fe and Co thin films on Cu(111), Cu(100), and Cu(110): A comprehensive study of metastable film growth, Phys. Rev. B **47**, 10785 (1993).

[39] J. Giergiel, J. Shen, J. Woltersdorf, A. Kirilyuk, and J. Kirschner, Growth and morphology of ultrathin Fe films on Cu(001), Phys. Rev. B **52**, 8528 (1995).

[40] D. E. Fowler and J. V. Barth, Magnetic anisotropy of glide-distorted fcc and of bcc ultrathin Fe/Cu(001) films, Phys. Rev. B **53**, 5563 (1996).

[41] R. Vollmer and J. Kirschner, Influence of H_2 adsorption on magnetic properties of Fe films on Cu(001), Phys. Rev. B **61**, 4146 (2000).

[42] J. Shen, Z. Gai, and J. Kirschner, Growth and magnetism of metallic thin films and multilayers by pulsed-laser deposition, Surface Science Reports **52**, 163 (2004).

[43] T. Asada and S. Blügel, Total energy spectra of complete sets of magnetic states for fcc-Fe films on Cu(100), Phys. Rev. Lett. **79**, 507 (1997).

[44] E. G. Moroni, G. Kresse, and J. Hafner, Coherent epitaxy and magnetism of face-centred-cubic Fe films on Cu(100), Journal of Physics: Condensed Matter **11**, L35 (1999).

[45] Y.-m. Zhou, W.-t. Geng, and D.-s. Wang, Theoretical determination of the exchange interaction and magnetization energy in fcc-Fe/Cu(001) films, Phys. Rev. B **57**, 5029 (1998).

[46] Y. Tsunoda, Y. Nishioka, and R. Nicklow, Spin fluctuations in small γ-Fe precipitates, Journal of Magnetism and Magnetic Materials **128**, 133 (1993).

[47] D. Spišák and J. Hafner, Magnetic structure of ultrathin γ-Fe films on Cu(001): Spin waves versus collinear magnetic ordering, Phys. Rev. B **66**, 052417 (2002).

[48] D. J. Keavney, D. F. Storm, J. W. Freeland, I. L. Grigorov, and J. C. Walker, Site-specific Mössbauer evidence of structure-induced magnetic phase transition in fcc Fe(100) thin films, Phys. Rev. Lett. **74**, 4531 (1995).

[49] M. Zharnikov, A. Dittschar, W. Kuch, C. Schneider, and J. Kirschner, Interplay between structure and magnetism in Fe/Cu(100) upon temperature variation, Journal of Magnetism and Magnetic Materials **174**, 40 (1997).

[50] J. Rajeswari, H. Ibach, and C. M. Schneider, Large wave vector surface spin waves of the nanomartensitic phase in ultrathin iron films on Cu(100), EPL (Europhysics Letters) **101**, 17003 (2013).

[51] H. Magnan, D. Chandesris, B. Villette, O. Heckmann, and J. Lecante, Structure of thin metastable epitaxial Fe films on Cu(100): Reconstruction and interface ordering by coating, Phys. Rev. Lett. **67**, 859 (1991).

[52] K. Heinz, S. Müller, and L. Hammer, Crystallography of ultrathin iron, cobalt and nickel films grown epitaxially on copper, Journal of Physics: Condensed Matter **11**, 9437 (1999).

[53] A. Biedermann, Stability of the nanomartensitic phase in ultrathin Fe films on Cu(100), Phys. Rev. B **80**, 235403 (2009).

[54] A. Biedermann, R. Tscheließnig, M. Schmid, and P. Varga, Crystallographic structure of ultrathin Fe films on Cu(100), Phys. Rev. Lett. **87**, 086103 (2001).

[55] V. Myagkov, L. Bykova, and L. Solovyov, Fourfold in-plane magnetic anisotropy in epitaxial Fe(110)/Cu(001) and Fe(110)/Ni(001) bilayers, Journal of Magnetism and Magnetic Materials **322**, 1715 (2010).

[56] R. Naik, C. Kota, J. S. Payson, and G. L. Dunifer, Ferromagnetic-resonance studies of epitaxial Ni, Co, and Fe films grown on Cu(100)/Si(100), Phys. Rev. B **48**, 1008 (1993).

[57] F. Scheurer, R. Allenspach, P. Xhonneux, and E. Courtens, Magnetic coupling of structural microdomains in bcc Fe on Cu(001), Phys. Rev. B **48**, 9890 (1993).

[58] J. Thomassen, B. Feldmann, and M. Wuttig, Growth, structure and morphology of ultrathin iron films on Cu(100), Surface Science **264**, 406 (1992).

[59] A. Biedermann, R. Tscheliessnig, C. Klein, M. Schmid, and P. Varga, Reconstruction of the clean and H covered "magnetic live surface layer" of Fe films grown on Cu(100), Surface Science **563**, 110 (2004).

[60] C. Egawa, E. M. McCash, and R. F. Willis, Adsorption of hydrogen on thin fcc-iron films grown on Cu(100), Surface Science Letters **215**, L271 (1989).

[61] A. Berger, B. Feldmann, H. Zillgen, and M. Wuttig, Correlation between the microscopic and macroscopic magnetic properties in ultrathin Fe/Cu(100)-films, Journal of Magnetism and Magnetic Materials **183**, 35 (1998).

[62] G. G. Hembree, J. Drucker, S. D. Healy, K. R. Heim, Z. J. Yang, and M. R. Scheinfein, Field-induced metastable states in ultrathin films of fcc Fe/Cu(100), Applied Physics Letters **64**, 1036 (1994).

[63] D. Steigerwald, I. Jacob, and W. Egelhoff Jr., Structural study of the epitaxial growth of fcc-Fe films, sandwiches, and superlattices on Cu(100), Surface Science **202**, 472 (1988).

[64] R. Allenspach and A. Bischof, Magnetization direction switching in Fe/Cu(100) epitaxial films: Temperature and thickness dependence, Phys. Rev. Lett. **69**, 3385 (1992).

[65] D. P. Pappas, C. R. Brundle, and H. Hopster, Reduction of macroscopic moment in ultrathin Fe films as the magnetic orientation changes, Phys. Rev. B **45**, 8169 (1992).

[66] M. Weinelt, S. Schwarz, H. Baier, S. Müller, L. Hammer, K. Heinz, and T. Fauster, Structure of ultrathin Fe films on Cu(100) prepared by pulsed laser deposition, Phys. Rev. B **63**, 205413 (2001).

[67] G. Rauchbauer, A. Buchsbaum, H. Schiechl, P. Varga, M. Schmid, and A. Biedermann, Ultra-thin Fe films grown on Cu by pulsed laser deposition: Intermixing and bcc-like structures, Surface Science **602**, 1589 (2008).

[68] B. M. Clemens, T. C. Hufnagel, M. C. Kautzky, and J.-F. Bobo, Structural transformations during growth of epitaxial Fe(001) thin films on Cu(001) and Pt(001), *Symposium CC - Thin Films Stresses and Mechanical Properties VI*, MRS Proceedings **436** (1996), 10.1557/PROC-436-9.

[69] S. F. Cheng, A. N. Mansour, J. P. Teter, K. B. Hathaway, and L. T. Kabacoff, Structure and magnetic properties of magnetron-sputtered Fe/Cu multilayered thin films, Phys. Rev. B **47**, 206 (1993).

[70] S. Pizzini, F. Baudelet, D. Chandesris, A. Fontaine, H. Magnan, J. M. George, F. Petroff, A. Barthélemy, A. Fert, R. Loloee, and P. A. Schroeder, Structural characterization of Fe/Cu multilayers by X-ray absorption spectroscopy, Phys. Rev. B **46**, 1253 (1992).

[71] S. E. Khiraoui, M. Sajieddine, M. Hehn, S. Robert, O. Lenoble, C. Bellouard, M. Sahlaoui, and K. Benkirane, Magnetic studies of Fe/Cu multilayers, Physica B: Condensed Matter **403**, 2509 (2008).

[72] D. W. Lee, D. H. Ryan, Z. Altounian, and A. Kuprin, Structural and magnetic properties of Cu/Fe multilayers, Phys. Rev. B **59**, 7001 (1999).

[73] Y. Kozono, M. Komuro, S. Narishige, M. Hanazono, and Y. Sugita, Structures and magnetic properties of Fe/Cu multilayered films fabricated by a magnetron sputtering method, Journal of Applied Physics **61**, 4311 (1987).

[74] H. Jiang, T. Klemmer, J. Barnard, and E. Payzant, Epitaxial growth of Cu on Si by magnetron sputtering, J. Vac. Sci. Technol. A **16**, 3376 (1998).

[75] J. A. Dura and J. LaRock, A molecular beam epitaxy facility for *in situ* neutron scattering, Review of Scientific Instruments **80**, 073906 (2009).

[76] T. Nawrath, H. Fritzsche, F. Klose, J. Nowikow, and H. Maletta, *In situ* magnetometry with polarized neutrons on thin magnetic films, Phys. Rev. B **60**, 9525 (1999).

[77] T. Mairoser, *In-Situ Neutronen-Reflektometrie und Untersuchungen von EuO-Filmen*, Ph.D. thesis, Universität Augsburg (2013).

[78] MEIVAC, Owner's operation manual of the MAK sputtering sources, http://www.meivac.com .

[79] G. Galvez de la Puente, J. Guerra Torres, O. Erlenbach, M. Steidl, R. Weingärtner, F. D. Zela, and A. Winnacker, Determination of the sputter rate variation pattern of a silicon carbide target for radio frequency magnetron sputtering using optical transmission measurements, Materials Science and Engineering: B **174**, 127 (2010), advances in Semiconducting Materials.

[80] J. Stahn, Paul Scherrer Institut, Villigen, Swizzerland, TOF reflectometry at PSI: from an optical bench set-up to a new instrument concept with focus on small samples, Talk at JCNS instrumentation workshop, Tutzing, Germany (2011).

[81] F. Ott and A. Menelle, New designs for high intensity specular neutron reflectometers, The European Physical Journal Special Topics **167**, 93 (2009).

[82] J. Stahn, U. Filges, and T. Panzner, High intensity specular reflectometry - first experiments, (2011), arXiv:, 1102.2747 .

[83] J. Stahn, U. Filges, and T. Panzner, Focusing specular neutron reflectometry for small samples, The European Physical Journal - Applied Physics **58**, 11001 (2012).

[84] J. Stahn, Paul Scherrer Institut, Villigen, Switzerland, First tests with a model Selene-type neutron guide, Talk at IKON 4, Lund, Sweden (2013).

[85] M. Montel, The X-ray microscope with catamegonic roof-shaped objective, in: X-ray microscopy and microradiography, Elsevier (1957).

[86] O. Soltwedel, MLZ (FRM2), Garching, Germany, Private Communication (2013).

[87] P. Dumas, Y. J. Chabal, and G. S. Higashi, Coupling of an adsorbate vibration to a substrate surface phonon: H on Si(111), Phys. Rev. Lett. **65**, 1124 (1990).

[88] D. Gräf, M. Grundner, R. Schulz, and L. Mühlhoff, Oxidation of HF-treated Si wafer surfaces in air, Journal of Applied Physics **68**, 5155 (1990).

[89] S. S. Iyer, M. Arienzo, and E. de Frésart, Low-temperature silicon cleaning via hydrogen passivation and conditions for epitaxy, Applied Physics Letters **57**, 893 (1990).

[90] P. Ziegler, *Herstellung und Charakterisierung von dünnen Fe-Schichten*, Diploma thesis, Technische Universität München (2013).

[91] T. Drüsedau, M. Löhmann, F. Klabunde, and T.-M. John, Investigations on energy fluxes in magnetron sputter-deposition: implications for texturing and nanoporosity of metals, Surface and Coatings Technology **133-134**, 126 (2000).

[92] W. Kreuzpaintner, TUM, Physics Dep. E21, Garching, Germany, Private Communication (2014).

[93] A. L. Patterson, The Scherrer formula for X-ray particle size determination, Phys. Rev. **56**, 978 (1939).

[94] R. P. Leavitt and F. J. Towner, Determination of the lattice parameter and poisson ratio for AlAs via high-resolution X-ray-diffraction studies of epitaxial films, Phys. Rev. B **48**, 9154 (1993).

[95] D. Hogan and D. Dyson, Angles between planes in the hexagonal and tetragonal crystal systems, Micron (1969) **2**, 59 (1970).

[96] N. Paunović, Z. V. Popović, and Z. D. Dohšević-Mitrović, Superparamagnetism in iron-doped CeO_{2-y} nanocrystals, Journal of Physics: Condensed Matter **24**, 456001 (2012).

[97] S. Blundell, *Magnetism in Condensed Matter* (Oxford Master Series in Condensed Matter Physics, 2001).

[98] S. Fiedler, *Magnetische Momente massenselektierter CoPd und FePt Legierungscluster auf Ni/Cu(100) untersucht mittels XMCD*, Ph.D. thesis, Universität Hamburg (2010).

[99] R. Kampmann, M. Haese-Seiller, V. Kudryashov, B. Nickel, C. Daniel, W. Fenzl, A. Schreyer, E. Sackmann, and J. Rädler, Horizontal ToF-neutron reflectometer REFSANS at FRM-II Munich/Germany: First tests and status, Physica B: Condensed Matter **385-386, Part 2**, 1161 (2006), proceedings of the Eighth International Conference on Neutron Scattering.

[100] M. Enomoto, Enhanced phenomena in metals with electric and magnetic fields: II magnetic fields, Materials Transactions **46**, 1088 (2005).

[101] D. Schmitz, C. Charton, A. Scholl, C. Carbone, and W. Eberhardt, Magnetic moments of fcc Fe overlayers on Cu(100) and Co(100), Phys. Rev. B **59**, 4327 (1999).

[102] A. Neubauer, C. Pfleiderer, B. Binz, A. Rosch, R. Ritz, P. G. Niklowitz, and P. Böni, Topological Hall effect in the A phase of MnSi, Phys. Rev. Lett. **102**, 186602 (2009).

[103] C. Pappas, E. Lelièvre-Berna, P. Falus, P. M. Bentley, E. Moskvin, S. Grigoriev, P. Fouquet, and B. Farago, Chiral paramagnetic skyrmion-like phase in MnSi, Phys. Rev. Lett. **102**, 197202 (2009).

[104] T. Skyrme, A unified field theory of mesons and baryons, Nuclear Physics **31**, 556 (1962).

[105] A. Fert, V. Cros, and J. Sampaio, Skyrmions on the track, Nat Nano **8**, 152 (2013).

[106] R. Ritz, *Superconductivity and non-Fermi liquid behavior on the border of itinerant ferromagnetism*, Ph.D. thesis, Technische Universität München (2013).

[107] S. Mühlbauer, *Vortex lattices in superconducting niobium and skyrmion lattices in the chiral magnet MnSi investigated by neutron scattering*, Ph.D. thesis, Technische Universität München (2009).

[108] A. Bauer, *Investigations of itinerant antiferromagnets and cubic chiral helimagnets*, Ph.D. thesis, Technische Universität München (to be published in 2014).

[109] L. Landau and E. M. Lifshitz, *Electrodynamics of continous media* (Pergamon Press, Oxford, 1884).

[110] K. Everschor, *Manipulating magnetic structures in chiral metals by currents*, Diploma thesis, Universität zu Köln (2009).

[111] P. Bak and M. H. Jensen, Theory of helical magnetic structures and phase transitions in MnSi and FeGe, Journal of Physics C: Solid State Physics **13**, L881 (1980).

[112] Y. Ishikawa, G. Shirane, J. A. Tarvin, and M. Kohgi, Magnetic excitations in the weak itinerant ferromagnet MnSi, Phys. Rev. B **16**, 4956 (1977).

[113] C. Pfleiderer, G. McMullan, and G. Lonzarich, Critical behaviour at the transition from a magnetic to a nonmagnetic metallic state in MnSi as a function of hydrostatic pressure, Physica B: Condensed Matter **199-200**, 634 (1994).

[114] A. E. Petrova, V. N. Krasnorussky, T. A. Lograsso, and S. M. Stishov, High-pressure study of the magnetic phase transition in MnSi, Phys. Rev. B **79**, 100401 (2009).

[115] T. Schulz, R. Ritz, A. Bauer, M. Halder, M. Wagner, C. Franz, C. Pfleiderer, K. Everschor, M. Garst, and A. Rosch, Emergent electrodynamics of skyrmions in a chiral magnet, Nature Phys. **8**, 301 (2012).

[116] P. Milde, D. Köhler, J. Seidel, L. M. Eng, A. Bauer, A. Chacon, J. Kindervater, S. Mühlbauer, C. Pfleiderer, S. Buhrandt, C. Schütte, and A. Rosch, Unwinding of a skyrmion lattice by magnetic monopoles, Science **340**, 1076 (2013).

[117] T. Schwarze, J. Waizner, M. Garst, A. Bauer, H. Berger, A. Rosch, C. Pfleiderer, and D. Grundler, Universal helimagnon and skyrmion excitations in metallic, semiconducting, and insulating chiral magnets, unpublished (2013).

[118] M. Janoschek, F. Jonietz, P. Link, C. Pfleiderer, and P. Böni, Helimagnons in the skyrmion lattice of MnSi, Journal of Physics: Conference Series **200**, 032026 (2010).

[119] R. Ritz, M. Halder, M. Wagner, C. Franz, A. Bauer, and C. Pfleiderer, Formation of a topological non-Fermi liquid in MnSi, Nature (London) **497**, 231 (2013).

[120] C. Pfleiderer, D. Reznik, L. Pintschovius, H. v. Löhneysen, M. Garst, and A. Rosch, Partial order in the non-Fermi-liquid phase of MnSi, Nature (London) **427**, 227 (2004).

[121] N. Nagaosa and Y. Tokura, Topological properties and dynamics of magnetic skyrmions, Nat Nano **8**, 899 (2013).

[122] A. Tonomura, X. Yu, K. Yanagisawa, T. Matsuda, Y. Onose, N. Kanazawa, H. S. Park, and Y. Tokura, Real-space observation of skyrmion lattice in helimagnet MnSi thin samples, Nano Letters **12**, 1673 (2012).

[123] X. Z. Yu, Y. Onose, N. Kanazawa, J. H. Park, J. H. Han, Y. Matsui, N. Nagaosa, and Y. Tokura, Real-space observation of a two-dimensional skyrmion crystal, Nature **465**, 901 (2010).

[124] X. Z. Yu, N. Kanazawa, Y. Onose, K. Kimoto, W. Z. Zhang, S. Ishiwata, Y. Matsui, and Y. Tokura, Near room-temperature formation of a skyrmion crystal in thin-films of the helimagnet FeGe, Nat Mater **10**, 106 (2011).

[125] S. Seki, X. Z. Yu, S. Ishiwata, and Y. Tokura, Observation of skyrmions in a multiferroic material, Science **336**, 198 (2012).

[126] S. Heinze, K. von Bergmann, M. Menzel, J. Brede, A. Kubetzka, R. Wiesendanger, G. Bihlmayer, and S. Blugel, Spontaneous atomic-scale magnetic skyrmion lattice in two dimensions, Nat Phys **7**, 713 (2011).

[127] N. Romming, C. Hanneken, M. Menzel, J. E. Bickel, B. Wolter, K. von Bergmann, A. Kubetzka, and R. Wiesendanger, Writing and deleting single magnetic skyrmions, Science **341**, 636 (2013).

[128] M. Finazzi, M. Savoini, A. R. Khorsand, A. Tsukamoto, A. Itoh, L. Duò, A. Kirilyuk, T. Rasing, and M. Ezawa, Laser-induced magnetic nanostructures with tunable topological properties, Phys. Rev. Lett. **110**, 177205 (2013).

[129] S. X. Huang and C. L. Chien, Extended skyrmion phase in epitaxial FeGe(111) thin films, Phys. Rev. Lett. **108**, 267201 (2012).

[130] X. Yu, J. P. DeGrave, Y. Hara, T. Hara, S. Jin, and Y. Tokura, Observation of the magnetic skyrmion lattice in a MnSi nanowire by Lorentz TEM, Nano Letters **13**, 3755 (2013).

[131] H. Du, J. P. DeGrave, F. Xue, D. Liang, W. Ning, J. Yang, M. Tian, Y. Zhang, and S. Jin, Highly stable skyrmion state in helimagnetic MnSi nanowires, Nano Letters **0**, null (0).

[132] T. Yokouchi, N. Kanazawa, A. Tsukazaki, Y. Kozuka, M. Kawasaki, M. Ichikawa, F. Kagawa, and Y. Tokura, Stability of two-dimensional skyrmions in thin films of $Mn_{1-x}Fe_xSi$ investigated by the topological Hall effect, Phys. Rev. B **89**, 064416 (2014).

[133] N. A. Porter, G. L. Creeth, and C. H. Marrows, Magnetoresistance in polycrystalline and epitaxial FeSi thin films, Phys. Rev. B **86**, 064423 (2012).

[134] N. A. Porter, P. Sinha, M. B. Ward, A. N. Dobrynin, R. M. D. Brydson, T. R. Charlton, C. J. Kinane, M. D. Robertson, S. Langridge, and C. H. Marrows, Giant topological Hall effect in strained $Fe_{0.7}Co_{0.3}Si$ epilayers, (2013), arXiv:, 1312.1722 .

[135] P. Sinha, N. A. Porter, and C. H. Marrows, Strain-induced effects on the magnetic and electronic properties of epitaxial $Fe_{1-x}Co_xSi$ thin films, (2013), arXiv:, 1307.7301 .

[136] S.-Z. Lin, C. Reichhardt, and A. Saxena, Manipulation of skyrmions in nanodisks with a current pulse and skyrmion rectifier, Applied Physics Letters **102**, 222405 (2013).

[137] J. Iwasaki, M. Mochizuki, and N. Nagaosa, Current-induced skyrmion dynamics in constricted geometries, Nat Nano **8**, 742 (2013).

[138] H. Du, W. Ning, M. Tian, and Y. Zhang, Field-driven evolution of chiral spin textures in a thin helimagnet nanodisk, Phys. Rev. B **87**, 014401 (2013).

[139] L. Sun, R. X. Cao, B. F. Miao, Z. Feng, B. You, D. Wu, W. Zhang, A. Hu, and H. F. Ding, Creating an artificial two-dimensional skyrmion crystal by nanopatterning, Phys. Rev. Lett. **110**, 167201 (2013).

[140] E. Karhu, S. Kahwaji, T. L. Monchesky, C. Parsons, M. D. Robertson, and C. Maunders, Structure and magnetic properties of MnSi epitaxial thin films, Phys. Rev. B **82**, 184417 (2010).

[141] H. Suto, K. Imai, S. Fujii, S. ichi Honda, and M. Katayama, Growth process and surface structure of MnSi on Si(111), Surface Science **603**, 226 (2009).

[142] T. Suzuki, T. Lutz, B. Geisler, P. Kratzer, K. Kern, and G. Costantini, Surface morphology of MnSi thin films grown on Si(111), Surface Science **617**, 106 (2013).

[143] T. Takeuchi, Y. Hirayama, and M. Futamoto, Appearance of ferromagnetism at room temperature in MnSi films prepared by alternate deposition, Magnetics, IEEE Transactions on **29**, 3090 (1993).

[144] S. Higashi, P. Kocán, and H. Tochihara, Reactive epitaxial growth of MnSi ultrathin films on Si(111) by Mn deposition, Phys. Rev. B **79**, 205312 (2009).

[145] E. A. Karhu, S. Kahwaji, M. D. Robertson, H. Fritzsche, B. J. Kirby, C. F. Majkrzak, and T. L. Monchesky, Helical magnetic order in MnSi thin films, Phys. Rev. B **84**, 060404 (2011).

[146] D. Menzel, J. Engelke, T. Reimann, and S. Süllow, Enhanced critical fields in MnSi thin films, Journal of the Korean Physical Society **62**, 1580 (2013).

[147] E. A. Karhu, U. K. Rößler, A. N. Bogdanov, S. Kahwaji, B. J. Kirby, H. Fritzsche, M. D. Robertson, C. F. Majkrzak, and T. L. Monchesky, Chiral modulations and reorientation effects in MnSi thin films, Phys. Rev. B **85**, 094429 (2012).

[148] T. Monchesky, J. Loudon, M. Robertson, and A. Bogdanov, Comment on [13], Phys. Rev. Lett. **112**, 059701 (2014).

[149] Y. Li, N. Kanazawa, X. Yu, F. Kagawa, and Y. Tokura, Reply to comment [148], Phys. Rev. Lett. **112**, 059702 (2014).

[150] E. Karhu, *Structural and magnetic properties of epitaxial MnSi(111) thin films*, Ph.D. thesis, Dalhousie University, Halifax, Nova Scotia (2012).

[151] Y. Togawa, T. Koyama, K. Takayanagi, S. Mori, Y. Kousaka, J. Akimitsu, S. Nishihara, K. Inoue, A. S. Ovchinnikov, and J. Kishine, Chiral magnetic soliton lattice on a chiral helimagnet, Phys. Rev. Lett. **108**, 107202 (2012).

[152] M. N. Wilson, E. A. Karhu, D. P. Lake, A. S. Quigley, S. Meynell, A. N. Bogdanov, H. Fritzsche, U. K. Rößler, and T. L. Monchesky, Discrete helicoidal states in chiral magnetic thin films, (2013), arXiv:, 1305.5196 .

[153] M. Brasse, *Magnetization of correlated electron systems: MnSi thin films, CrB_2 single crystals and two-dimensional electron systems in MgZnO/ZnO*, Ph.D. thesis, Technische Universität München (2013).

[154] Charles Dewhurst, Institut Laue Langevin, Software Grasp Version 6.72, http://www.ill.eu/instruments-support/instruments-groups/groups/lss/grasp/home/, (2013).

[155] European Spallation Source, Lund, Sweden, http://europeanspallationsource.se/, (2014).

[156] P. Böni, TUM, Physics Dep. E21, Garching, Germany, Private Communication (2014).

[157] J. A. Bert, B. Kalisky, C. Bell, M. Kim, Y. Hikita, H. Y. Hwang, and K. A. Moler, Direct imaging of the coexistence of ferromagnetism and superconductivity at the $LaAlO_3/SrTiO_3$ interface, Nature Physics **7**, 767 (2011).

[158] G. Herranz, F. Sánchez, N. Dix, M. Scigaj, and J. Fontcuberta, High mobility conduction at (110) and (111) $LaAlO_3/SrTiO_3$ interfaces, Scientific Reports **2**, (2012).

Acknowledgment

Vielen Dank an ...

- Peter Böni für die Chance bei E21 promovieren zu dürfen, für seine immer offene Tür und große Hilfsbereitschaft.
- allen Mitarbeitern von E21 für die gute Stimmung und tolle Atmosphäre.
- Wolfgang Kreuzpaintner für seine große Hilfsbereitschaft und Unterstützung. Die gemeinsame Arbeit im Labor hat viel Spaß gemacht.
- Christoph Morkel für die sehr nette Zeit zusammen in unserem Büro. Danke für deine Hilfsbereitschaft und deine lustige Geschichten.
- Christian Pfleiderer für viele nützliche Diskussionen.
- Thomas Mairoser, Alexander Herrenberger und Andreas Schmehl für die gute Zusammenarbeit. Ihr habt mit der Konstruktion und dem Bau der Sputteranlage tolle Arbeit geleistet. Ich danke vor allem Thomas für seine Abrufbereitschaft während den letzten Messzeiten und seine Bemühungen auf der Suche nach Problemlösungen.
- Jean-Francois Moulin, Martin Hease-Seiler und Matthias Pomm für ihren unbändigen Einsatz während unseren Messzeiten an REFSANS, für nächtliche Ausflüge zum Instrument und tausend Überstunden!
- Yury Khaydukov for his great effort during beamtimes at NREX and lots of useful discussions. Und Olaf Softwedel für einen wichtigen Hinweis.
- Jochen Stahn für seine große Unterstützung und Hilfsbereitschaft an AMOR. And Panagiotis Korelis for his active support.
- Thorsten Hesjedal für seine MnSi Proben und vielen nützlichen Diskussionen. Shilei Zhang for the SQUID measurements.
- Uwe Filges und Tobias Panzner für die Strahlzeit an BOA.

- Patrick Ziegler, Sina Mayr und Christoph Reitinger für die Hilfe beim Umbau und aufwändige Installation der Sputteranlage an Amor.
- Astrid Mühlberg für ihre Geduld und ihre Mühe.
- Andreas Mantwill und Stefan Giemsa für schnelle Umsetzung von vielen kurzfristigen Aufträgen.
- meinen Mentor Wolfgang Häussler.
- Alfonso, Ioannis, Andi, Marco und Christoph S. für Messungen an MnSi und Diskussionen.
- Georg Brandl, Robert Georgii, Reinhardt Schwikowski und Klaus Seeman für die MIRA Strahlzeit.
- Amitesh Paul für seine XMCD und XAS Messungen und viele nützliche Diskussionen.
- Fritz Phillipp für mühsame TEM-Aufnahmen.
- Maximilian Weitz für seine Unterstützung. Unsere gemeinsame Schreibphase hat vieles leichter gemacht.